University of Chemistry and Technology, Prague

Vysoká škola chemicko-technologická v Praze

Habilitation thesis

Electric field-driven microfluidics and its applications in biomolecular assays

Zdeněk Slouka

2017

I hereby declare that I have worked out this thesis independently and listed all the resources employed as well as co-authors of the presented results.

Prague, February 28, 2017

Zdeněk Slouka

Abstract

Microfluidics is a relatively new scientific discipline having a tremendous potential to influence our everyday lives in the near future. It is often regarded as a discipline which offers unusual solutions to many engineering problems and on top of that it often enables to perform experiments or run processes which are impossible to do with our conventional techniques. One characteristic feature of microfluidics is the ability to integrate passive or active elements which allows one to control actively processes occurring in the microfluidic system. Integration of electrodes into microfluidic systems and application of electrical field on various microfluidic elements such as channels with characteristic dimensions in nanometer and micrometer scale, gels or membranes gives rise to many interesting phenomena such as electrical field-driven convection, electrical field-facilitated water splitting or recombination reaction or phenomena associated with property called ion selectivity as described in this thesis. The scientific field studying the effects of electrical field on spatial charge in electrolytes is called electrokinetics. Interestingly, the knowledge from the field of electrokinetics can be utilized in developing novel strategies and techniques for performing biomolecular assays. Biomolecules are usually charged, a trait allowing one to use electrical field to transport the biomolecules. The combination of simple migration of biomolecules in electrical field with electrokinetic phenomena occurring in microfluidic systems offers unprecedented capabilities in terms of biomolecule pre-concentration, separation or even detection as described. Electrokinetic microfluidic systems are sometimes viewed as alternative tools for biomolecular assays and their integration on a single chip allowed us to construct electrokinetic diagnostic or screening platforms.

Contents

Abstract iv

1 Introduction 1

2 Electrokinetic microfluidic systems – fundamentals 4

2.1 Electrolyte diode - system of large pH and electrical potential gradients [22] 4

2.2 Electrolyte diode – dynamics of closing and opening [31] 7

2.3 DC electroosmosis in microchannels – convective transport [32] 8

2.4 DC electroosmosis in nanochannels – ion selectivity, [39], [40] 10

2.5 Ion-exchange membranes – structure [52] 12

2.6 Ion-exchange membranes – electrokinetics [59], [60] 14

3 Electrokinetic microfluidic systems – applications 17

3.1 DNA/RNA membrane sensor – the core of the detection platforms [66, 75] 19

3.2 Technologies for preprocessing of analyzed samples [68] 20

3.2.1 Preconcentration and localization nucleic acids 21

3.2.2 Separation of nucleic acids from lysates 21

3.3 Membrane integrated platform for detection of miRNA 146a [68] 22

3.4 Nanoparticle-based nanomembrane platform [87] 23

3.5 Nanomembrane platform for detection of miRNA contained in exosomes [66] 24

4 Conclusions 25

References 27

List of appendices 32

1 Introduction

Microfluidics, as the name suggests, is a scientific field that deals with fluids spatially constrained in systems in which characteristic dimensions fall into the range from 1 to 1000 micrometers [1]. From the perspective of the useful dimensions, the characteristic dimensions are tens or hundreds of micrometers. There is a distinctive field where these dimensions are below 1 micrometer which is called nanofluidics [2].

Microfluidics is still considered a new scientific discipline that started to develop in the late nineties of the last century. It reflected the trend followed in other areas of human activities, the trend towards miniaturization. Especially semiconductor industry with lithographic processes allowing to create structures in the micrometer and soon after in the nanometer range was the key player in determining the pace of miniaturization [3]. Miniaturization gave the world new products characterized with higher performance and high reliability, often opening doors to until then impossible ventures. The progress in these other areas started to influence scientific disciplines which deals with fluids in chemical and biological systems. Development of chromatographic [4] and electrophoretic [5] separation techniques based on the use of thin capillaries or development of microarray technologies for profiling of gene expression can be named as examples of pioneering projects that launched the era of microfluidic systems.

Microfluidic systems, in their most encountered physical embodiment, are fluidic systems in the shape of simple chips containing channels with the width having the proper dimensions [6]. Today, approximately two decades after the birth of microfluidics, the strict requirement on the dimensions weakened and microfluidics is viewed in a different perspective. It is an engineering tool that offers a plethora of new phenomena and experimental solutions with often unprecedented consequences with respect to handling, controlling and processing of chemical or biological samples. By looking at the characteristic features and traits of microfluidics, one will see that hydrodynamics inside microfluidic channels almost exclusively exhibits laminar flow (characteristic Re numbers 0.1 - 10) which in turn implies that the main mechanism of mixing relies on diffusion. Turbulent flow, with obscure exceptions, does not occur in microfluidic systems due to spatial constraints [7]. These two features, pressure-driven convective flow in laminar regime and mixing controlled by diffusion, offer new ways for the old processes to be carried out or it provides new spatiotemporal environment for novel

processes or for processes difficult to achieve in common macroscopic systems [8]. However, at the same time, these two characteristics can be limiting in certain situations and need to be overcome. Microfluidics offers relatively easy techniques how to integrate other functionalities into the microfluidic systems. This is an aspect that immensely broadens the range of possible applications. Possibility of integration elevates microfluidic systems from simple channels with passive control over processes taking place inside to systems with elements that actively control and influence what is happening inside [9]. Today, one can recognize many distinctive fields of microfluidics such as optofluidics [10], digital microfluidics [11], paper-based microfluidics [12], etc. It is almost safe to say, that microfluidics has reached into all different scientific disciplines. One of the most mentioned words when it comes to microfluidics is a so called lab-on-a-chip system [6] sometimes also referred to as micro-total analysis systems [13]. The concept of lab-on-a-chip systems is based on taking individual steps of a given analysis commonly performed in an analytical or biomolecular lab, miniaturize them and eventually integrate them on a single chip usually having the size of a credit card. The credit-card sized chip shall then perform the whole analysis without the need of external interference. The lab-on-a-chip systems are anticipated to influence a whole range of human activities such as environmental and pollution control [14], food safety [15], medical diagnostics and screening [16], prevention of bioterrorists attacks [17], improve the quality of life in the developing world [18] etc. The ideas to have small smart platforms capable running quick tests outside well equipped laboratory have been around since the beginning of the new millennium. Especially in medicine a term point-of-care diagnostics [19] was coined and has attracted a lot of attention. Chips processing real human samples (saliva, blood, urine, tears, …) for detection (present or absent, yes or no) or even quantification of the amount of a given cell type or a given biomolecule possessing a diagnostic value would allow to do medical testing at the place of the patient treatment and to run quick preventive care screenings to intervene early in case of life threatening diseases such as cancer. Although these ideas are very compelling and the anticipation of the impact on human society is also reflected in the expected market value for point-of-care testing today worth of billions of US dollars, the introduction of point-of-care systems into our everyday lives has not materialized yet.

George Whitesides states in his reflection from 2006 [1]:

”*As a technology, microfluidics seems almost too good to be true: it offers so many advantages and so few disadvantages (at least in its major applications in analysis). But*

it has not yet become widely used. Why not? Why is every biochemistry laboratory not littered with 'labs on chips'? Why does every patient not monitor his or her condition using microfluidic home-test systems? The answers are not yet clear. I am convinced that microfluidic technology will become a major theme in the analysis, and perhaps synthesis, of molecules: the advantages it offers are too compelling to let pass. Having said that, the answers to questions concerning the time and circumstances required for microfluidics to develop into a major new technology are important not just for this field, but also for other new technologies struggling to make it into the big time."

Now, ten years later, a huge step towards bringing microfluidics to everyday use has been taken and there are many start-up companies working on developing functional prototypes and commercial products worldwide [20]. Still the mankind is waiting for the killer application, application that would mark off the beginning of point-of-care testing.

This habilitation thesis summarizes approximately ten years of my work on microfluidic systems. The common denominator that joins all the various investigated microfluidic systems is the DC electrical field. The DC electrical field has been applied on channels, membranes and gels integrated in microfluidic systems.

The scientific field dealing with application of electrical field on various fluidic systems and investigating phenomena resulting from interactions of the electrical field with spatial charge that localizes mostly at interfaces is regarded as electrokinetics [21]. As will be described in this thesis, electrostatic interactions between strong electrical field, mobile charged molecules and charges fixed on a solid support give rise to a plethora of interesting physical phenomena such as electrical field-induced flow or electrical field-enhanced water splitting reaction. The electrokinetic fundamentals have been studied in the context of microfluidics and also nanofluidics when the transition from micro- to nanofluidics brings the concept of ion selectivity. Ion selectivity is an inherent property of two seemingly disconnected systems namely fluidic nanochannels and ion-exchange membranes.

Later, the phenomena exhibited by the electrokinetic microfluidic systems were employed for processing, control and detection of certain biomolecules, mostly nucleic acids. The main underlying concept lies in utilizing the interactions of the charge borne by these molecules with the electrical field connected to the system. Integration of various electrokinetic elements allowing control and detection of nucleic acids on a single chip

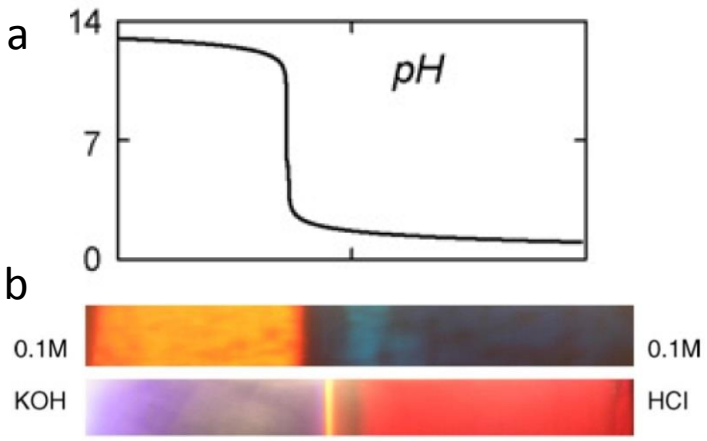

Figure 1: *a) pH profile in the electrolyte diode in the closed mode, b) experimental verification of the sharp pH gradient developing inside the gel. The pH dyes used were congo red (upper image) and thymol blue (bottom image). Thymol blue with two acid-base transitions allows to capture all three pH regions predicted by theory – alkaline (blue), neutral (yellow), and acidic (red).*

was a first proof-of-concept step in developing a commercial product intended as a point-of-care diagnostic platform.

This thesis is divided into two major chapters. The first one deals with experimental studies aimed at fundamentals of electrokinetic microfluidic systems and the later with applications of electrokinetics to biomolecular detection.

2 Electrokinetic microfluidic systems – fundamentals

2.1 Electrolyte diode - system of large pH and electrical potential gradients [22]

Very simple microfluidic system that is designed to exhibit behavior similar to that of a semiconductor diode can be constructed by connecting two channels, one containing KOH solution and the other HCl solution, with a thin gel layer [23] , [24], [25] which fulfills two functions. It prevents the two solutions from mutual convective mixing and at the same time it allows diffusion and migration of ionic species contained in the electrolytes. The migration of ionic components through the gel layer without any limitations such as those caused by ion selectivity exhibited for instance by ion-exchange membranes or resin particles is key for observing diode-like action. While the electrical field imposed on the systems in the sense of forward bias drives K^+ and Cl^- ions into the

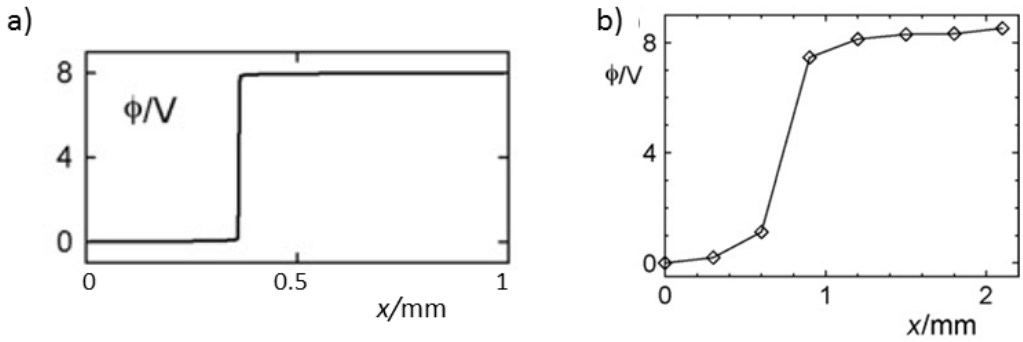

Figure 2: *Profiles of the electrical potential developed inside the gel layer in the closed mode: a) prediction of the mathematical modeling, b) experimental verification on a microfluidic chip integrated with an array of electrodes placed along the gel layer.*

gel layer rendering the gel highly conductive, the negative bias exerts the opposite force on the ions resulting in depletion of the gel layer of potassium and chloride ions and in turn filling the gel with H^+ and OH^- ions. H^+ and OH^- ions possess higher apparent mobilities than the other two aforementioned ions which would indicate higher conductance of the gel layer. However, if the concentrations of H^+ and OH^- do not correspond to equilibrium given by the water product, these two ions will be consumed in a reaction yielding water. Water is characterized by very low electrolytic conductivity which is the reason why negative bias applied on the system yields very low current. This behavior reflects in the current- voltage characteristic which has two distinctive regions: one corresponding to the positive bias with high slope (the physical meaning of the slope is conductance of the system) and one corresponding to the negative bias characterized with very low slope. Using the terminology of semiconductors, positive bias means connection in the open mode, negative bias in the closed mode. One compelling question arising in studying these systems concerns the spatial distribution of ion concentrations (and also pH) and electrical potential. The system was mathematically modelled as 1-dimensional system using non-equilibrium model based on finite rate of water dissociation/association reaction [26, 27]. The solution of the set of partial differential equation qualitatively confirmed the expected behavior of the diode in the closed and open mode and predicted very steep gradients of pH (concentrations of OH^- and H^+ ion) and electrical potential localized inside the gel (see Figs. 1 and 2). The zone of localized steep gradients is the place where the reaction of water formation occurs. This zone of water formation is very narrow (on the order of micrometers depending on the geometry

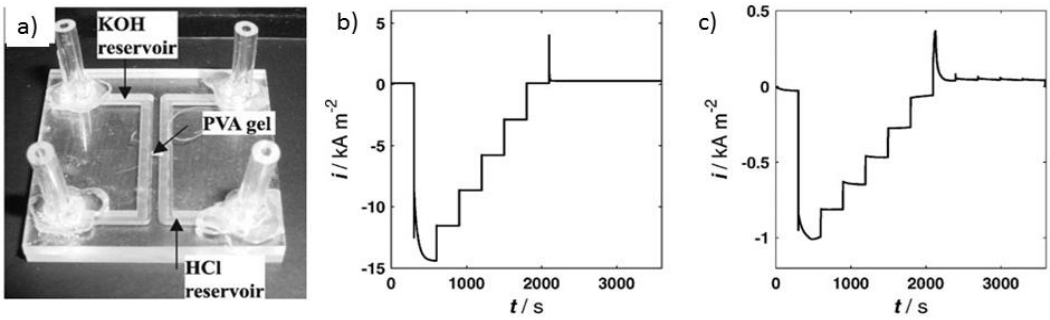

Figure 3: *Transients in electrical current associated with closing and opening the electrolyte diode: a) electrolyte diode realized as a two-channel microfluidic system bridge with a thin layer of polyvinyl alcohol gel, b) dynamics of the electrolyte diode predicted by mathematical modeling, c) dynamics of the electrolyte diode obtained experimentally. In figs. b and c the electrical current transient corresponding to opening and closing the diode occurs around the time of 200 s and 2000 s, respectively.*

of the system and the voltage applied) and divides the gel into three layers: (i) alkaline region in which the pH is approx. larger than 11, (ii) acidic region, in which the pH is approx. less than 3 and (iii) neutral region with the pH in between 3 and 11 (see Fig. 1). At the same time, this thin zone responsible for the low conductivity sustains very high electrical field reaching up to several MV/m and is responsible for generation of electrical double layer which is formed by the excess of H^+ ion on one side and OH^- ions on the other one. The formation of the electrical double layer inside homogeneous phase is very striking and unprecedented characteristic of this system. Electrical double layers, as will be described in the next sections, are generally localized at interfaces, most frequently solid-liquid interfaces. The question arose whether a gel layer can sustain such high electrical field and so steep gradients in pH. The question was resolved by (i) constructing a microfluidic system with a gel layer in which a pH indicator (congo red, thymol blue or fluorescein) was added, and (ii) constructing a system equipped with an array of electrodes to measure the electrical potential profile along the channel. In both cases the experimental systems provided a clear evidence of steep gradients that develop inside the gel layer [22] (Figs. 1,2). The values of electrical field evaluated experimentally were on the order of 10^4 - 10^5 V/m. All pH indicators evidenced sharp changes in pH value, however, they themselves contributed to the system behavior.

The system of electrolyte diode is interesting from the point of fundamental research but it does not have any practical applications. However, systems in which water splitting reaction or recombination occurs exist and the studies performed on the electrolyte diode may help in understanding the fundamentals of these practical systems. We can mention

generation of pH gradients in microfluidic channel by recombination of H^+ and OH^- later used for isoelectric focusing [28], [29] or bipolar membranes intentionally used to split water [30].

2.2 Electrolyte diode – dynamics of closing and opening [31]

This system, although very simple in its essence, shows very interesting dynamic behavior when connected in open or closed mode. Under zero voltage applied on the system, the gel layer separating the solutions of HCl and KOH fills with both K^+ and Cl^- ions and partially with OH^- and H^+ ions. OH^- and H^+ diffuse into the gel layer from the appropriate sides of the gel, encounter at a certain position in the gel (given by diffusion coefficients of H^+ and OH^- in the gel) and immediately reacts forming water. Therefore even under zero external voltage, the gel layer divides into three zones with different pH values. On switching on the positive bias (opening the diode), one can observe a very interesting transient in electrical current, which reaches maximum right after connecting the voltage, then it decreases, goes through a minimum and then it starts to increase again (Fig 3c around 300s). This seemingly erroneous behavior of the system was explained by mathematical modeling of the dynamics of the diode. The mathematical model was defined with the same set of equations as described previously and solved in the dynamic regime. The model predicted the same transients in electrical current as observed experimentally and allowed to analyze the evolution of concentration profiles for all ionic species inside the gel. The explanation of the observed transient is simply given by faster migration of H^+ and OH^- ions than that of K^+ and Cl^- ions. This implies that after connecting the voltage the gel layer first depletes of H^+ and OH^- ions that is reflected on the electrical current transient as a decrease followed by slow filling the gel layer with K^+ and Cl^- ions. The transport of K^+ and Cl^- ions into the gel layer is also hindered with the lack of corresponding counterions which are needed to fulfil the local condition of electroneutrality. The transient observed in closing the diode (connecting negative bias) is more straightforward. Maximum value of the electrical current is reached right after connecting the negative bias (Fig. 3c around 2000 s). The electrical current quickly drops to very low and virtually steady value. The explanation of this transient is in accordance with the explanation of the transient observed in opening the diode. The H^+ and OH^- migrate faster than the two remaining ions and, thus, are not hindered in their transport

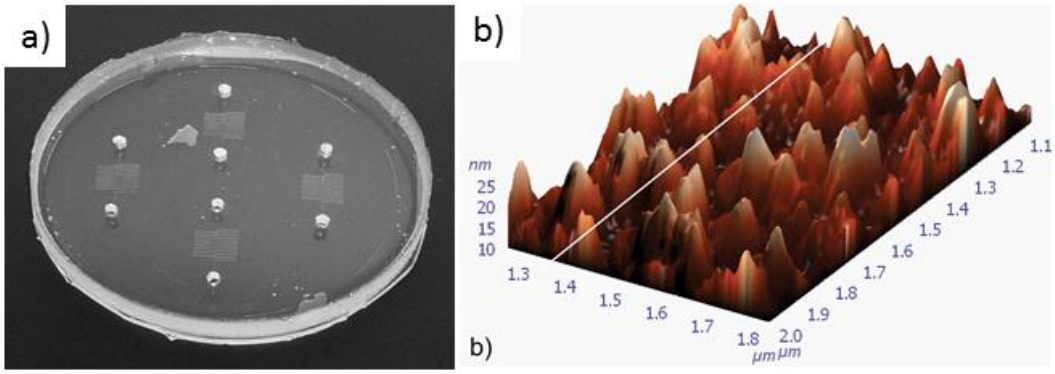

Figure 4: *a) Microfluidic chip made of native polydimethylsiloxane used to study the effect of bovine serum albumin on the electroosmotic flow. The channel dimensions are 75 mm in length, 40 μm in width and 25 μm in height. b) The surface of the polydimethyl siloxane with adsorbed layer bovine serum albumin analyzed by atomic force microscopy.*

into the gel. This in turn implies almost immediate reaction of water formation which is indicated by rapid decrease in the overall electrical current passing through the system.

2.3 DC electroosmosis in microchannels – convective transport [32]

Electrolyte diode connected in the closed mode is believed to sustain very high electrical field which in turn gives rise to an unexpected formation of electrical double layer inside a homogenous phase. Electrical double layers, however, occur naturally at interfaces [33]. In microfluidics, the typical interfaces are solid-liquid interfaces, for instance glass-water electrolyte interface. The silane groups present on the glass surface dissociate leaving the surface of the glass negative with a positive cloud of ions in the near vicinity. Several theoretical models for such electrical double layers have been developed. One of the theories divides the electrical double layer into two layers [34] (i) Stern layer having the dimension roughly corresponding to the size of counterions which strongly adsorb on the solid surface and are immobile and (ii) diffuse layer the dimension of which depends mainly on the concentration of the electrolyte (approx. 1 nm for 1M KCl and 1 μm for DI water). The diffuse layer contains both counter and co-ions to that fixed on the solid surface, however, there is an excess of counterions to render the whole system electroneutral. Application of the electrical field parallel to the solid surface results in net electrical force acting on ions within the diffuse part of the electrical double layer. Since there is an excess of counterions there is a preferential transport in the direction of counter-ion migration. The diffuse layer adjacent to the solid wall starts moving which subsequently sets in motion the bulk of the electrolyte through the omnipresent friction

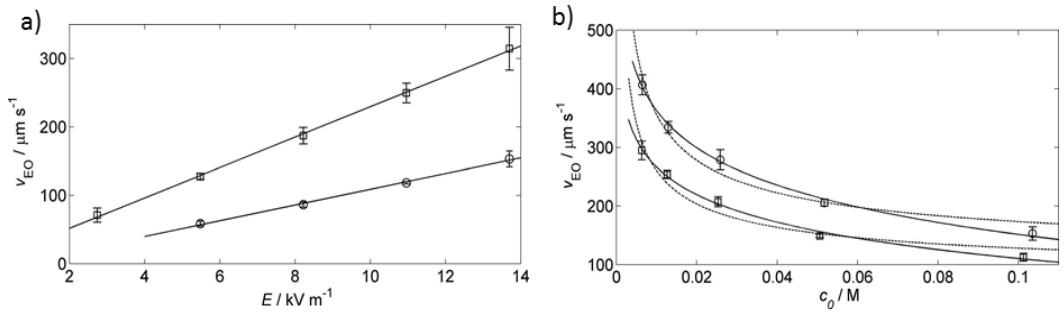

Figure 5: *a) The dependence of the electroosmotic flow velocity on the applied electrical filed under constant concentration of the electrolyte, b) the dependence of the electroosmotic flow velocity on the concentration of the electrolyte under constant applied electrical field. While the dependence on the electrical field is linear, which corresponds to theoretical predictions, the dependence on the concentration of the electrolyte is nonlinearly decreasing. The experimental data were best fitted with logarithmic function and theoretically explained as a combined effect of surface heterogeneity caused by adsorbed bovine serum albumin and changes in the Debye layer thickness that depends on the concentration of the used electrolyte.*

forces acting in flowing liquids [35]. This mechanism has been used for construction of electroosmotic microfluidic pumps [36], [37].

It is without any doubt that the surface of the microfluidic channel plays an important role in formation of the electrical double layers which in turn will have implication on the induced electroosmotic flow. Proteins are known to adsorb on many solid surfaces [38] and due to their ampholytic character, they may change the overall surface charge on the solid surface. At the same time, proteins are rather large molecules which may transform smooth surfaces into relatively rugged surfaces. This was shown by performing an AFM study of polydimethylsiloxane (PDMS) surfaces treated with a solution containing bovine serum albumin (Fig. 4b). While the average surface roughness of the native PDMS was 0.68 nm, this number increased to 4.28 nm for PDMS exposed to BSA solution. The BSA-treated PDMS surfaces were then characterized from the point of electrokinetic properties. The microfluidic chip for this measurement is depicted in Fig. 4a. Current-monitoring technique used for tracking the electroosmotic flow showed: (i) the electroosmotic flow velocity is linearly dependent on the electrical field (Fig. 5a), and (ii) the electroosmotic velocity nonlinearly decreases with increasing ionic concentration (Fig. 5b). This nonlinear decrease in electroosmotic velocity was well fitted with a logarithmic function.

The layer of BSA molecules adsorbed on solid surface has two implications: (i) they increase the surface roughness, and (ii) they partially screen off the fixed charge

originally present on the PDMS surface. These conclusions were supported with mathematical modelling that provided very good agreement with experimental data in case of assumption of heterogeneous distribution of the fixed charge on the PDMS wall. The analysis of the theoretical and experimental data gave an approximate coverage of the PDMS surface with BSA molecules to be 40%.

2.4 DC electroosmosis in nanochannels – ion selectivity, [39], [40]

DC electroosmosis can be used to transport electrolytes in microfluidic channels that are of proper dimension. In case of too large channels, small pressure differences at the two ends of the channel will result in pressure-driven convection that completely overtakes electroosmotic flow. In the other extreme, when the channel characteristic dimension is too small, new phenomena will set in. These new phenomena are associated with the fact that very tiny channels (less than 1 micrometer) may exhibit property called ion selectivity [39], [41]. Ion selectivity is a property that is common for seemingly disconnected areas such as microfluidics and nanofluidics [42] and electromembrane separation processes [43]. Ion selectivity is displayed by channels in which the inner dimension is comparable with the electrical double layer thickness. In other words, the channels in which electrical double layers overlap are ion selective. The thickness of the electrical double layer (Debye length) gives an approximate length scale of electrostatic forces exerted by the surface charge on the mobile ions in the "bulk" of the solution. These electrostatic forces allow mainly counter-ions to reside in ion selective channels and in case of application of external electrical field to migrate through them. As

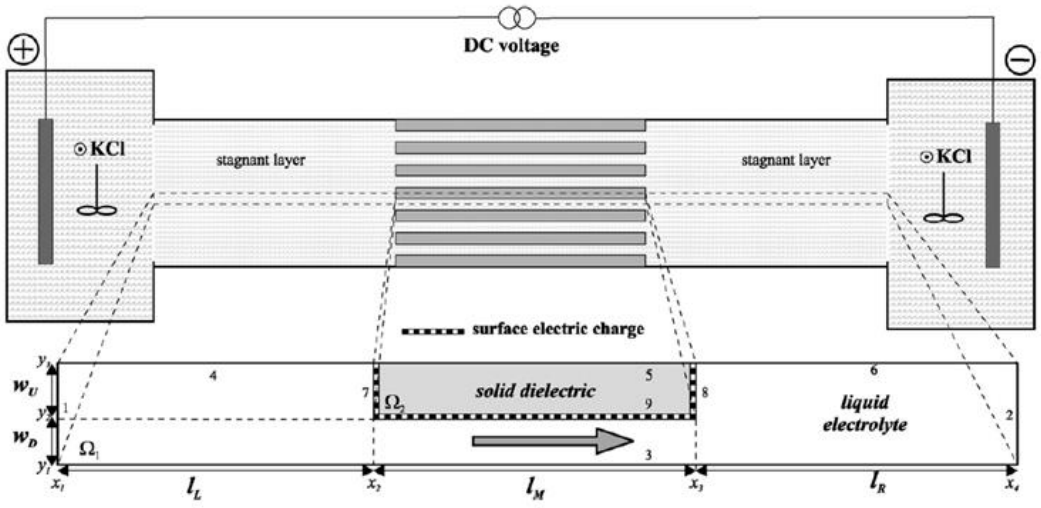

Figure 6: *Ion-exchange membrane modelled as a system of parallel nanochannels possessing ion selectivity.*

mentioned above, the thickness of the electrical double layer is influenced by the ionic strength of the solution which implies that a given channel (nanochannel) can be ion selective in diluted solutions and lose this property in highly concentrated solutions [44]. The ion selectivity is also displayed by ion-exchange membranes in which a so called fixed charge in the membrane usually bound on the polymeric scaffold determines the selectivity to given ions [39]. The difference between ion selective channels and membranes is in their physical embodiment. Sometimes, ion exchange membranes are geometrically approximated as systems of parallel ion-selective channels (Fig. 6) [40]. The implications of the ion selectivity on the electroosmotic flow are the following. Due to the preferential transport of the one type of ions through the ion selective channels, a region almost depleted of mobile ions develops on one side of the channel and at the same time a region enriched of ions occurs on the other side. This phenomenon is called concentration polarization [45, 46]. The depleted region is the place of high electrical field which is responsible for sustaining electrical double layer whose thickness is much larger than that predicted as Debye length (in equilibrium) [47]. The interaction of the electrical field with the charge in the extended electrical double layer can trigger electroconvection which eventually manifests itself as a vortex or an array of vortices [48]. Sometimes this electroconvection is denoted as electroosmosis of the second kind, in which the electrical field creates the electrical double layer on which it eventually acts [49]. The electroosmosis of the first kind refers to convective motion invoked by the electrical field acting on pseudo-equilibrium electrical double layers formed by electrical field of surface charge. Concentration polarization and vortex formation are reflected in current-voltage characteristics which are non-linear with three distinguishable regions

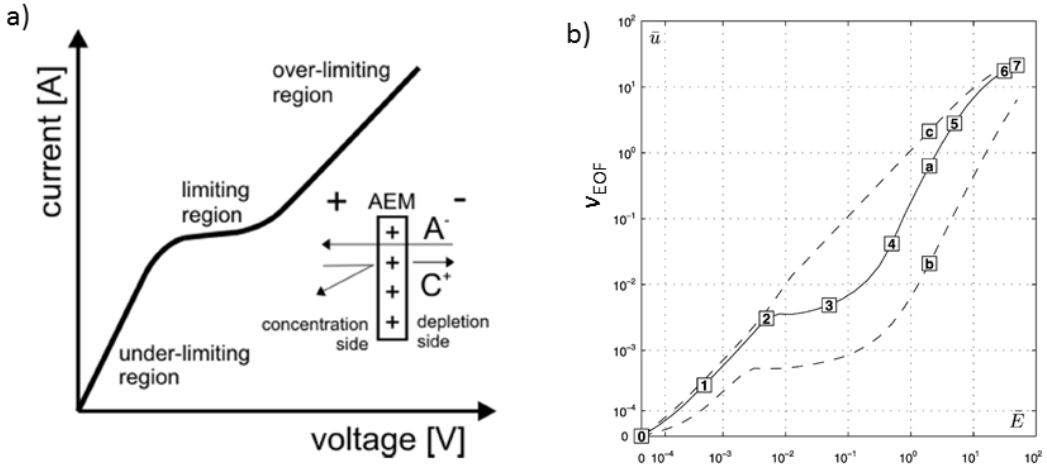

Figure 7: *Manifestation of ion selectivity on current-voltage characteristics and the dependence of electroosmotic velocity on the applied electrical field.*

[50], [51]: (i) underlimiting, (ii) limiting, and (iii) overlimiting (Fig. 7). The limiting region indicates generation of the depletion region (electrical current shows tendency to saturation), overlimiting region starts at the onset of the vortex. The vortex partially destroys the depletion region.

The electroosmotic flow through nanochannels is strongly affected by the formation of the depletion zone (Fig. 7b). While the dependence of the electroosmotic flow velocity on the voltage applied is linear in case of channels without ion selectivity (curve c), it is nonlinear in case of ion selective nanochannels (curves a, b). The character of this dependence strongly reminds one of the current-voltage characteristics. There is a tendency of the electroosmotic flow velocity to reach constant value independent of applied voltage which however does not happen and the velocity increases again after vortex on the depletion side of the channel sets in [40].

2.5 Ion-exchange membranes – structure [52]

Ion-exchange membranes are functional components of large industrial electromembrane separation units used in e. g. electrodialysis or electrodeionization [53]. They display the property of ion selectivity, i. e. they selectively transport ions with opposite charge to that one fixed (bound) in/on the membrane. Based on the type of the ions they transport selectively, one can distinguish anion and cation-exchange membranes [54]. There are many different types of the membranes having different composition and structure. One recognizes homogeneous and heterogeneous ion-exchange membranes. The homogenous ones are formed by a polymer heavily decorated with functional groups responsible for the bound charge and the heterogeneous ones usually contain three major components: (i) finely ground ion-exchange resin particles, (ii) polymeric binder, and (iii) polymeric mesh [55]. While the resin particles provide the membrane with function, the polymeric binder and mesh provide the membrane with mechanical stability. The structure of heterogeneous ion-exchange membranes is of tremendous importance since the amount of the functional component (ion-exchange resin) and the inert (polymeric binder and mesh) along with distribution of the functional component within the final membrane product determine the processing parameters of the final membrane [56] such as electrical resistance, mechanical and thermal stability, selectivity etc. Most of the heterogeneous membranes are produced in the following way. The resin and binder are blended together, slightly melted at elevated temperature and laminated in between two rollers while

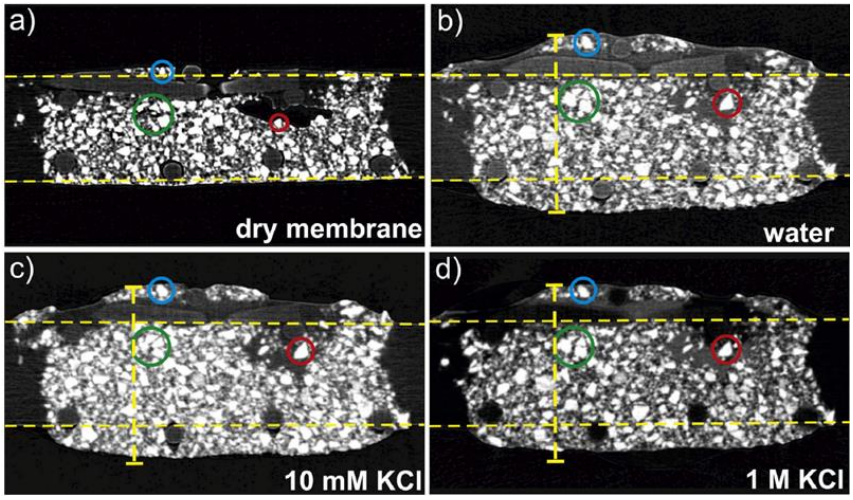

Figure 8: *The same cross-section of a cation-exchange membrane exposed to KCl solutions of different concentrations: a) dry membrane, b) swollen in DI water, c) swollen in 10 mM KCl, and d) swollen in 1M KCl. The analysis of swelling and shrinkage of the cation exchange membrane was done by micro-computed tomography.*

polymeric mesh is added on both sides of the membrane. The membranes are usually stored in dry state and are soaked in a given solution before use. The exposure of the membrane to water solution is accompanied with swelling [57] which in turn is characterized with profound structural changes inside the membrane (Fig 8).

X-ray tomography is a technique that allows one to obtain internal 3D structure of composite systems (or multiphase system) [58]. The technique in the most common arrangement exposes sample under investigation to X-ray and obtains 2D image capturing transmitted light. After scanning the sample from different angles, one can assemble recorded transmission images into a 3D structural model of the system. The use of this technique for determining the 3D structure of polymeric samples swollen in water electrolyte presents significant challenge. This is given by large X-ray absorption of water electrolyte comparable to polymers which in turn decreases the contrast and resolution of the tomography. One way around this problem is to let the sample swell in a given electrolyte and run the scanning in saturated water vapors. Saturated water vapors prevent any drying of the membrane and thus any structural and volumetric changes of swollen samples.

Such a technique was used to analyze structural changes of a heterogeneous cation exchange membrane caused by its swelling and to investigate the effect of concentration of KCl solution on the degree of swelling (Fig. 8). The tomography of the membrane showed the presence of the three major components, i. e. ion-exchange resin particles,

polymeric binder and polymeric fibers. Surprisingly, dry membrane also contained relatively large amount of air pockets that fill with appropriate solution on swelling. These air pockets present in the membrane may significantly decrease the membrane performance. One of the key conclusions of the study was the observation that ion-exchange resin particles are the only functional components that undergo swelling or shrinkage and any other structural changes in the membrane are result of the initial action of particles. Our quantitative analysis of obtained data revealed a correlation between the volume of the particles in the membrane, overall volume of the membrane and the concentration of the KCl solution in which the membrane had been soaked. These data were fitted with a logarithmic function that can be used as an empirical equation predicting volumetric changes caused by changes in concentration of salt solutions.

2.6 Ion-exchange membranes – electrokinetics [59], [60]

Ion-exchange membranes possess the property of ion selectivity that manifests itself in the same way as in systems of ion-selective channels. The ability to preferentially transport counterions gives rise to the concentration polarization of the membrane when connected in DC field. The formation of depletion and concentration zones in the electrolytes adjacent to the membrane has a characteristic signature on the current-voltage curve, i. e. the tendency of the electrical current to saturate after reaching its limiting value. However, the current almost never saturates and an inflection appears on the curve leading to overlimiting current. The processes behind the occurrence of the overlimiting current are more complex than those in case of ion-selective channels. Beside the vortex formation due to electroconvection, also water splitting, natural convection or exaltation effect [61],[62] may contribute to the transport of ions into the depleted region resulting in partial destruction of the depletion zone. The existence of depletion and concentration regions was experimentally verified in a simple two-channel microfluidic system with an integrated cation exchange membrane. While pressure-driven flow applied on the depleted side of the membrane significantly affected the current-voltage characteristics (e. g. the value of limiting current density), the flow on the concentration side of the membrane had essentially no effect on this curve [60]. This observation proves that the behavior of ion-exchange membranes is controlled by the processes taking place on the depletion side. Heterogeneity of the membranes, especially random alternation of conductive ion-exchange resin and nonconductive polymeric components (binder and

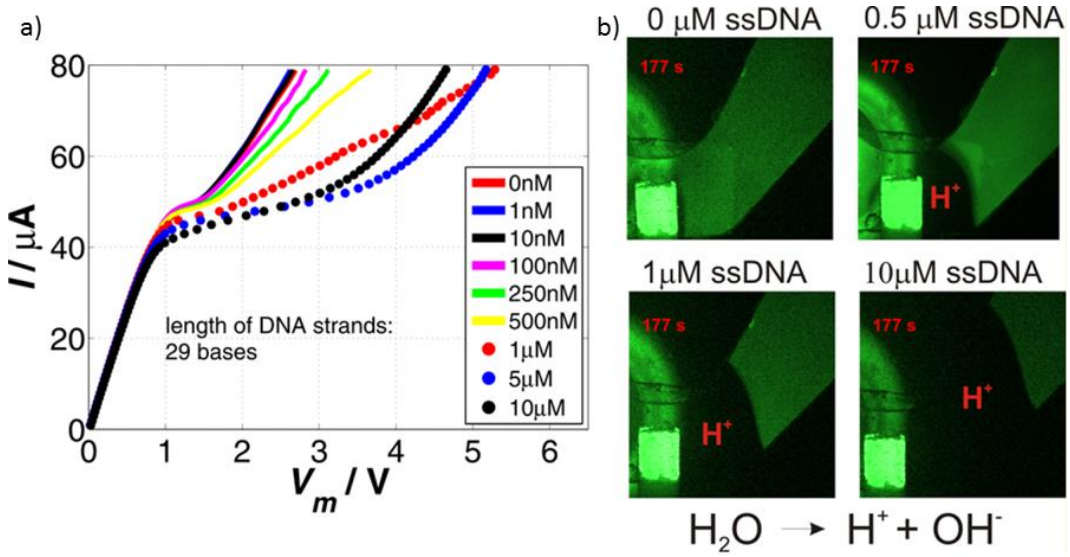

Figure 9: *The effect of long negatively charged biopolymer (ssDNA) on the behavior of an anion-exchange membrane: a) current-voltage characteristics measured at different concentrations of ssDNA, b) detection of H^+ ion produced in water splitting reaction at the interface between membrane and the adsorbed DNA through changes in intensity of fluorescence. Both figures show concentration-dependent behavior of the system that can be interpreted as follow. Higher concentrations of DNA result in formation of bipolar junction significantly enhancing water splitting.*

fibers) on its surface, implies that the active ion-exchange area will be different from the overall area of the ion-exchange membrane in contact with the desalinated solution. Transient times which represent the times required for the membrane to develop depletion region in a stagnant layer of electrolyte under a constant current load can be used to estimate the fraction of conductive domains on the surface of the membrane. This fraction was found to be 0.6 pointing at very high heterogeneity of the membrane. This number correlates well with the volumetric fraction of ion-exchange resin in a cation exchange membrane analyzed by micro-computed tomography [52].

Ion-exchange membranes are used to remove usually small ions from various electrolytes. These electrolytes often include complex samples of biological origin or coming from food industry, e. g. desalination of whey. These samples contain much larger molecules bearing various charges. It is known that processing of these samples in electrodialysis cell causes problems with fouling of the membranes [63]. Fouling of the membranes is a result of interactions of membranes with large molecules causing their strong adsorption. A thin layer of deposited molecules can adversely affect the performance of the membranes usually due to large increase in the resistance. Interestingly, the adverse effects might involve processes that one would not expect, for example, enhancement of

water splitting reaction, thus generation of H^+ or OH^- at the interface between the membrane and adsorbed molecules [59].

Anion exchange membranes are membranes that easily exchange anions. There is a limit in the size of counterions capable of entering ion exchange membrane and passing through it [64]. As mentioned before, the functional component of heterogeneous ion exchange membranes is exchange resin which is mostly highly crosslinked copolymer of styrene and divinylbenzene functionalized with functional groups providing fixed charge. The internal structure of the copolymer is given by randomly crosslinked polymers and will have characteristic dimensions on the order of nanometers after swelling. When such ion resin encounters large molecules of the opposite charge, the strong electrostatic attraction will facilitate adsorption of the molecule on the resin surface, however, such molecules will not be able to penetrate through the particle due to steric effects. Such a behavior was observed in a system of positively charge heterogeneous anion-exchange membranes and single stranded DNA molecules of various lengths [59]. DNA molecules are negatively charged under biologically relevant pH values owing to the presence of phosphate groups on the sugar-phosphate backbone. Lengths (number of nucleotides) of the ssDNA as well as the concentration of the DNA showed to have strong effect on the current-voltage characteristics. After analysis of the experimental data, the major conclusions of the experiments were: (i) the determining factor of the effect of DNA on the current-voltage characteristics is the concentration of the charge borne by the DNA molecule, i. e. the concentration of phosphate groups, (ii) the slope (electrical conductance) of the overlimiting region decreases, reaches its minimum and then sharply increases again with increasing DNA concentration, (iii) limiting current decreases with increasing DNA concentrations (Fig. 9a). All the conclusions point at the fact that DNA molecules create a so called bipolar junction after their adsorption on the anion-exchange membrane. The quality of the bipolar junction is concentration dependent. At lower concentrations, the DNA suppresses a mechanism that is mainly responsible for the occurrence of the overlimiting current on the bare membrane (no DNA adsorbed). At larger concentrations a new mechanism takes over the control of the overlimiting current. On running fluorescent observations of the processes taking place on the membrane, we identified these two mechanisms to be electrokinetic vortex and water splitting reaction (see Fig. 9b).

3 Electrokinetic microfluidic systems – applications

Connection of DC electric field to various types of microfluidic systems gives rise to plethora of phenomena which when tuned and controlled properly can be employed for a bit unexpected applications such as detection of charged molecules [65], [66], their preconcentration [67] or separation from biological samples of high complexity [68]. Most of these phenomena have been described in the previous section dealing with fundamentals of electrokinetic microfluidic systems. Here, the most important ideas behind the use of electrokinetics for development of a microfluidic platform intended as an automated platform for detection of certain biomolecules will be summarized.

Most of the biomolecules bear some charge that is present on the biomolecule at the biologically relevant pH values. One of the best examples is molecules of nucleic acids (DNA, RNA). Nucleic acids are composed of three major building blocks: (i) 4 different types of nucleotides, (ii) 5-carbon sugar, and (iiii) phosphate groups. The sugar molecules and phosphate groups create a so called sugar-phosphate backbone on which a sequence of nucleotides is covalently attached. The phosphate groups become negatively charged dissociate by stripping off one hydrogen cation. The charge on the molecules can be used as a nonspecific handle for those molecules if one exploits DC electrical field as a ”hand” which can grab the charged molecules and moves them around. One of the typical applications of applying DC electrical field on nucleic acids is gel electrophoresis. In this biomolecular assay agarose gel is used as a separation environment through which nucleic acid molecules migrate towards positively charged electrode and separate in the dependence on their size (linear size) [69]. The tacit prerequisite for successful separation is that the linear charge density on nucleic acid molecules is approximately constant. This is true since today’s electrophoretic systems can separate molecules differing by one nucleotide in length usually in conjunction with using some tags [70].

To efficiently control the transport of nucleic acid, or even employ the native charge on their sugar-phosphate backbone to detect their presence in a sample, one needs to find proper tools. It may be a little bit surprising, that such tools can even be ion-exchange membranes and the behavior they display on applying DC electrical field. The fouling of membranes with large molecules of opposite charge having characteristic signatures on the measured current-voltage curves can be ingeniously employed for sensing those molecules. This type of sensing does not require any artificial tags [71] (e. g. fluorescent molecule [72]). The creation of depletion and concentration regions around ion-exchange

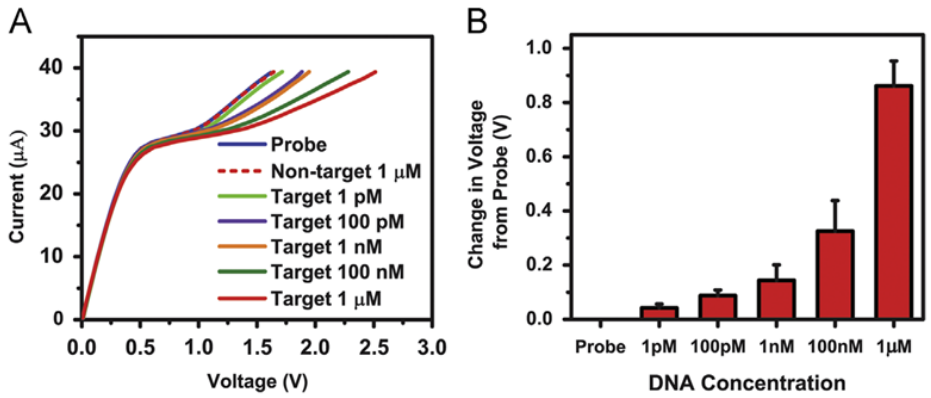

Figure 10: *Specific detection of a 27-nucleotide long ssDNA on the sensor made of anion-exchange membrane. a) Current-voltage characteristics are dependent on the concentration of the target. The increase in the concentration of the target results in larger shift of the overlimiting region when compared to the baseline. b) Quantification of the voltage shift as a function of the target concentration. The experiments were performed in triplicates and show dynamic range for the detection spanning 6 orders of magnitude.*

membranes results in formation of high and low electrical field regions which when designed properly can be used for preconcentration and localization of charged molecules. The enhanced transport of biomolecules significantly accelerates hybridization assay [73]. As described earlier, the ion-exchange membranes display a property of ion-selectivity which is a result of synergic effects of an electrical charge bound on the polymeric scaffold of ion-exchange resin and the characteristic internal dimensions being on the order of nanometers. The internal characteristic dimension is important from the point of length scales over which the bound charge can exert electrostatic forces on the mobile ions inside the resin. This combination of electrostatic interactions between the fixed charge and the charge on mobile molecules along with spatial restrictions of the internal porous resin structures makes ion-exchange membranes ideal as selective sieves for large molecules of the same charge. At the same time, this can be a reason of significant fouling of membranes in electrodialytic cells [74].

The next sections describe how the aforementioned phenomena exhibited by heterogeneous ion-exchange membranes have been used to develop an integrated platform for specific detection of nucleic acid fragments extracted from samples of biological origin. The platform can be thought of as an example of point-of-care diagnostic or screening platform that would allow physicians to run test on patient samples directly in their offices without the need of sending them off to equipped laboratories.

3.1 DNA/RNA membrane sensor – the core of the detection platforms [66, 75]

As mentioned in section 2.6, large molecules can interact with ion-exchange membranes and cause their fouling. This has been shown in case of negatively charged nucleic acids and positively charged anion-exchange membranes in which nucleic acids, although being counterions, cannot pass through the membrane and accumulate at its surface. This electrostatically-enhanced adsorption manifests itself in changes in current-voltage characteristics on which two main qualitative effects are observed. The overlimiting region deviates from that one of the baseline (no nucleic acids) and the limiting current decreases. Interestingly, when one does the same experiments with nucleic acids and negatively charged cation-exchange membranes, no such behavior is observed. The presence of the charge having opposite sign to that fixed in the membrane is thus important for detecting the presence of nucleic acids on the membrane. The quantification of the results with respect to the nucleic acid concentration and length (number of nucleotides) showed that anion exchange membrane is sensitive to the opposite charge borne by phosphate groups and quantitative changes on the current-voltage curves are proportional to the concentration of this charge.

The anion-exchange membranes are thus sensors of opposite charge borne by large molecules that cannot pass the membrane due to steric effects. This sensing is, however, nonspecific. The same changes on current-voltage characteristics will be induced by other large, negatively charged molecules (e. g. trypan blue). To render the sensing specific, one has to: (i) functionalize the membrane with probes having the ability to capture specific molecules of interest and (ii) develop a washing protocol which will remove all nonspecifically adsorbed molecules.

We developed a functionalization protocol for covalent linkage of single stranded DNA probes on the membrane. This protocol is based on photochemistry of carboxylated benzophenone followed by linkage of the DNA probe with amine-modified end. The sequence of nucleotide of the ssDNA probe is complementary to the ssDNA or RNA target. The sensor was tested on the detection of miRNA146a that has been implicated in development of oral cancer, and RNA samples of pathogenic Escherichia Coli O157:H7, Dengue virus, and Brucella (Fig. 10 a). The membrane sensor is thus generic sensor

capable of detection essentially any single stranded fragment of nucleic acids. The limit of detection for 27 long-nucleotide target was 1pM (Fig. 10 b).

3.2 Technologies for preprocessing of analyzed samples [68]

Preprocessing of real biological samples is usually a required step without which the downstream processing and final detection of the target molecule would be impossible [76] [77] [78] [79]. Both RNA and DNA molecules reside inside cells. To analyze these molecules one has to rupture the cell membranes/walls to get access to the inner environment. This process of disrupting cells is called cell lysis. Lysate of cells contains besides the target to be detected a lot of other molecules, cell debris etc. which indicate possible problems with respect to detection of the target. First, cell debris and other molecules can interact with the sensor and in extreme case even to damage the sensor irreversibly. Second, the ratio of the number of target molecules to the number of other molecules is very low, which means that the target is screened off by these molecules, an effect that makes the target invisible to the sensor.

The main reasons for developing technologies that process and pretreat real biological samples, are to simplify the sample, i. e. to separate the molecules of interest from the rest of the sample and to accelerate the transport of separated molecules towards the sensor. This increases the incidence rate of probe-target encounter and thus successful hybridization [80] [81] [82].

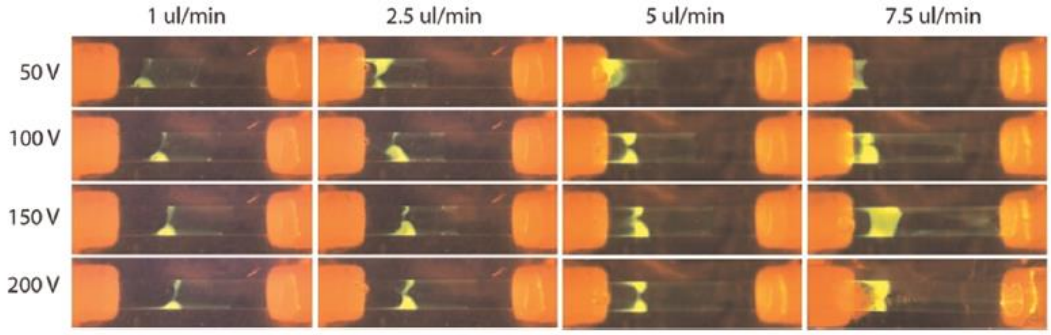

Figure 11: *Preconcentration of fluorescently labeled ssDNA in a microfluidic channel integrated with two cation exchange membranes under different experimental conditions. The preconcentration occurs as a result of balance between the convective flow (applied from right to left) and electrical force exerted on ssDNA molecules acting in the opposite direction. The electrical force increases from right to left due to simultaneous creation of depletion and concentration zones in the channel. The position of the preconcentration slug of molecules is mainly determined by these two experimental parameters: the flow rate through the channel and the voltage applied on the system.*

3.2.1 Preconcentration and localization nucleic acids

Two cation-exchange membranes placed on top of a single microfluidic channel and connected in series to a DC power supply will generate non-homogenous electrical field inside the channel. This non-homogeneous field generates as a result of depletion and concentration regions that simultaneously occur in the channel on either of the membranes, respectively. The non-homogeneous electrical field will exert electrical force on charged molecules that will increase from the concentration to the depletion region. Applying flow through the channel in such a way that it will force the molecules to move against the electrical force will result in preconcentration of the charged molecules at the location where the effect of the electrical force and the flow cancel each other. The side effect of the preconcentration of the large charge molecules is simultaneous desalination of the flowing solution. The electrolyte leaving the chip has properties of almost pure water. Very similar effect is observed at nanochannel – microchannel junctions and is referred to as ion concentration polarization [83].

As mentioned above, two major parameters affect the localization and preconcentration of the molecules. This claim is supported with a parametric study in which the effect of voltage (strength of the electrical field) and flow rate on the preconcentration was studied (Fig. 11). While increasing voltage applied on the system pushes the slug of fluorescently labeled ssDNA molecules further away from the membrane with depletion region (from left to right), the increasing flow rate has the opposite effect.

3.2.2 Separation of nucleic acids from lysates

Gel electrophoresis is very simple and efficient technology for separation of nucleic acids into bands. Although the separation of individual nucleic acids based on their size usually requires their cleaning, the idea of using electrical field to separate these molecules from cell debris and most of the proteins is attractive. In Fig.12a, one can see a microfluidic chip for preferential separation of short nucleic acids from cell lysate by means of on-chip electrophoresis. The efficacy of this technique is depicted in Fig 12 b. This set of images captures electrophoretic extraction of fluorescently labeled ssDNA molecule spiked into lysate of an oral cancer cell line. While all fluorescence is localized in the sample chamber at the beginning of the experiment, the connection of DC electrical field for about 10 minutes causes the fluorescently labeled molecules to move through the gel

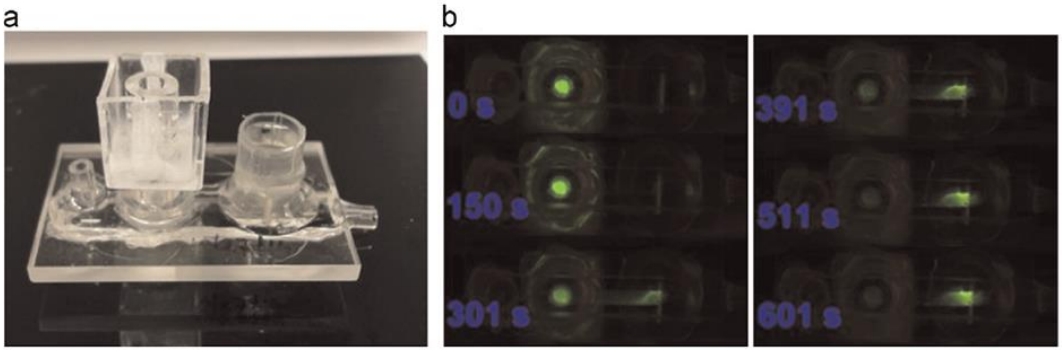

Figure 12: *Electrophoretic separation of short nucleic acids from a lysate: a) experimental microfluidic chip used for the electrophoretic separation of short nucleic acid from lysates, b) dynamics of the electrophoretic loading of short fluorescently labeled nucleic acids spiked into a lysate of oral cancer cells.*

layer at the bottom of the sample chamber into the channel and further towards a cation exchange membrane at which the molecules localize. The cation exchange membrane serves as a filter for nucleic acids since it prevents these molecules from leaving the channel and migrating to the positively charged electrode. This is due to combined effects of electrostatic repulsions and steric limitations.

3.3 Membrane integrated platform for detection of miRNA 146a [68]

Fast detection of a molecule possessing some diagnostic value in real samples coming directly from a patient requires integration of several steps that need to be carried out on a single chip operating ideally without external interference [84, 85]. The membrane technologies presented above were integrated on a chip of the size of a microscopic glass (Fig. 13a,b) slide and its functionality was tested on a modeling system of an oral cancer cell line of oral squamous cell carcinoma (OSSC) [86]. OSSC line was genetically modified to overexpress miRNA 146a which was the target of the detection. miRNA 146a is known to be associated with some types of the oral cancer types. The parental line known not to express this miRNA 146a was used as a negative control. The whole protocol for running the analysis is as follows: (i) prepare the chip for analysis, (ii) measure the baseline of the membrane sensor, (iii) perform the electrophoretic extraction of negatively charged molecules from the lysed sample, (iv) preconcentrate molecules at the membrane sensor, (v) incubation followed by washing, (vi) detection of the hybridization events. Successful discrimination of the parental line from the genetically modified cell line is documented in Fig 13 c in which the current-voltage curve measured for the target cell line provides approximately shift of 0.5 V with respect to the current –

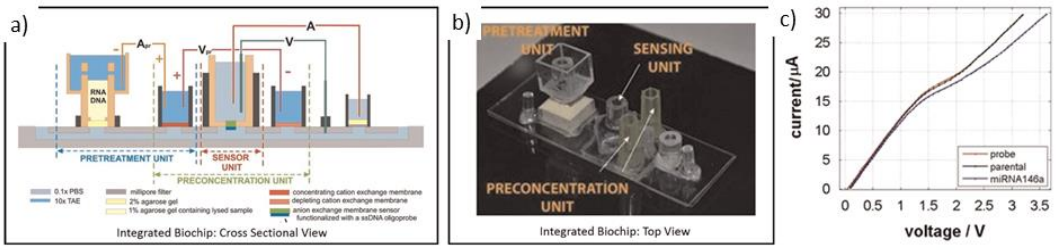

Figure 13: *Integrated platform for detection single stranded nucleic acids from cell lysates: a) schematics showing the individual functional units integrated on a microfluidic chip with the size corresponding to a microscopic glass slide. The three major functional units are: pretreatment unit, preconcentration unit, and sensing unit, b) the actual realization of the microfluidic chip with labels showing the three units, c) detection of miRNA146a molecule from a genetically modified oral cancer cell line of OSSC (oral squamous cell carcinoma) to overexpress the particular miRNA.*

voltage curve representing the probe while current-voltage curve for the parental line coincides with the one for the probe.

3.4 Nanoparticle-based nanomembrane platform [87]

Phenomena related to concentration polarization occurring on ion-exchange membranes when under DC current load can also be used to control transport processes in a gel layer which in turn can be employed to accelerate hybridization assay between a target and two probes functionalized on the surface of gold nano-beads. These two probes are against the two ends of the target. Such hybridization crosslinks the nanobeads creating much larger objects that can be easily identified. Aggregation of nanoparticles to detect pieces of single stranded DNA are commonly used both in cross-linking [88] and non-cross-linking mode [89]. The use of the concentration side of the membrane significantly facilitates the hybridization due to spatial restriction of all the components participating in the hybridization assay (target, nanobeads functionalized with two probes) at the same location. One achieves the stacking at the membrane upon applying DC electrical field driving the nanobeads (negatively charged) and the target (also negatively charged) to the membrane (Fig. 15b). After allowing the target to hybridize on the appropriate probes, the polarity of the electrical field is reversed causing creation of depletion region on the corresponding side of the membrane. Since the channel is filled with gel, no vortex can be formed and the depletion region expands in the course of time. The expanding depletion zone pushes all non-crosslinked particles away from the membrane while those crosslinked ones remain at the membrane due to steric effects (Fig. 15 c). The creation of

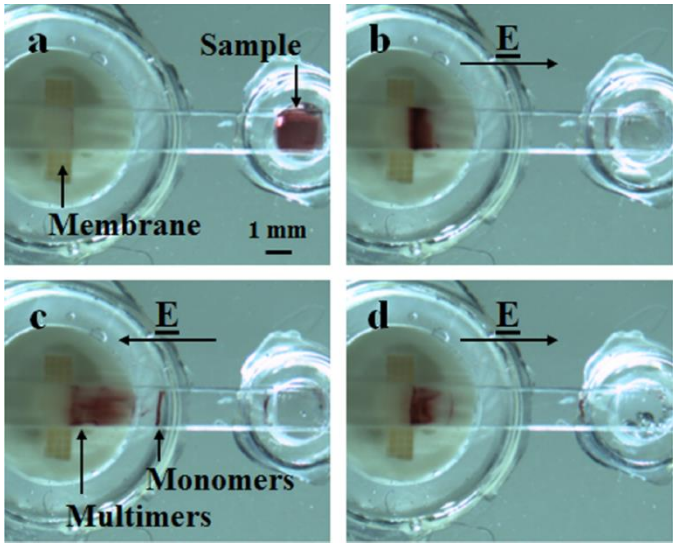

Figure 14: *Detection of ssDNA or RNA molecules by cross-linking gold nanoparticles functionalized with probes complementary to either end of the target. The detection rate is enhanced by utilization of depletion and concentration zones generated in a gel filling microfluidic channel. a) sample containing gold nanoparticles and potential target, b) electrical field transports nanoparticles and the target to the membrane where they accumulate, c) reversed polarity creates depletion zone whose front pushes non-crosslinked nanoparticles away, d) electrical field repacks the crosslinked nanoparticles at the membrane for quantification.*

the two bands thus provides qualitative information about the presence of the target and their mutual intensity about the quantity of the target (Fig. 15 d).

3.5 Nanomembrane platform for detection of miRNA contained in exosomes [66]

Exosomes are small vesicles used to transport some cargo of given biomolecules on the intercellular level. Cancer cells have been shown to produce more exosomes than normal cells [90] and there is some evidence indicating that exosomes coming from cancerous tissue with their unique molecular composition are implicated in metastasis of the cancer [91]. The increased production of exosomes can, by itself, have some diagnostic value [92]. However, the knowledge of the internal composition can increase the precision of the cancer detection and diagnosis, e. g. by pinpointing the location of the cancerous tissue. One type of the molecules present in the exosomes is miRNA molecules, short (22-24 nucleotides) single stranded RNA molecules that regulate protein expression on the posttranscriptional level. The expression level of different miRNA molecules have been shown to change dramatically when comparing healthy and cancerous tissues. They

are, thus, believed to be very good biomarkers of cancer [93]. In the future, screening of exosomes isolated e. g. from blood may enable fast detection of the presence of cancerous cells. The detection of given miRNA from exosomes present several challenges: (i) isolation of small exosomes (30-200 nm) from blood and their preconcentration is difficult, (ii) exosomes have to be lysed and the released cargo collected, (iii) successful diagnosis requires not only detection of the presence of a given molecule but also its quantification. In [66], we combined nanomembrane detection technology with the lysis of the exosomes caused by surface acoustic wave (SAW). SAW is a wave generated on the surface of a piezoelectric crystal by alternating current applied through an interdigitated electrode transducer and it is a very good alternative to traditional chemical or surfactant lysis methods. The target of the detection was miRNA has-miR-550-002410 contained in exosomes coming from pancreatic cancer cells (PANC1 cell line). The limit of detection was 2 pM.

4 Conclusions

This habilitation thesis introduces the reader into the world of electrokinetic microfluidic systems. These are fluidic systems in which liquids are confined in spaces with characteristic dimensions between 1 and 1000 micrometers and are subjected to the electrical field. The field of electrokinetics and microfluidics is experiencing tumultuous development both in the area of fundamental research and applications. This habilitation thesis reflects this trend to a large extent.

The first part of the thesis described several electrokinetic microfluidic systems which are very similar in their physical embodiment. DC electrical field is applied across an element that is investigated, i. e. a membrane, gel or a channel. However, the observed behavior is different from many aspects, which is given by the properties unique to each system. While the system of the electrolyte diode requires the permeation layer (gel) contain as little of the fixed charge as possible not to be ion selective, the other two systems (channels and membranes) systems are systems in which fixed charge plays a major role. In the case of channels, the charge fixed on the channel walls participates in formation of electrical double layers, which is a prerequisite for the electroosmotic flow to occur. In ion exchange the fixed charge stands behind the property of ion selectivity. The experimental investigation of these systems showed many phenomena that included (i) formation of large gradients in electrical potential both at interfaces and inside

homogeneous phase, (ii) water recombination reaction and water splitting reaction both enhanced by very strong electrical fields, (iii) electrokinetic flows caused by the action of the electrical field on both equilibrium electrical double layer (electroosmosis of the first kind) and nonequilibrium electrical double layer (electroosmosis of the second kind).

Although such fundamental studies may seem to only be an effort to answer some interesting academic questions without any aspiration to impact our everyday life, the reverse is true. The phenomena exhibited by the electrokinetic microfluidic systems have been, are and will be used for processing and simplification of complex biological samples to prepare it for biomolecular analysis. The processing of the sample included electrophoretic separation of nucleic acids from lysates, their localization and preconcentration at membranes with either depletion or concentration regions around them. The biomolecules, namely single stranded nucleic acids, were then specifically detected on an anion-exchange membrane functionalized with a DNA probe complementary to the sequence of the detected target. The working principles of these microfluidic techniques were based on a few facts (i) nucleic acids are negatively charged, (ii) electrical field can be used to transport charged molecules, and (iii) electrokinetic phenomena displayed by electrokinetic microfluidic systems can be used to control the transport charged molecules and even detect charge borne by specific molecules. The integration of several technologies on a single chip allowed us to distinguish genetically modified oral cancer cell line from its parental line. This proof-of-principle experiment laid a basis for development of a platform for detection of oral cancer from the biomolecular composition of oral rinses. The nanomembrane sensor was also used to detect a miRNA implicated in development of pancreatic cancer. This miRNA was contained in exosomes produced by the pancreatic cancer cells.

References

1. Whitesides, G.M., *The origins and the future of microfluidics.* Nature, 2006. **442**(7101): p. 368-373.
2. Bocquet, L. and E. Charlaix, *Nanofluidics, from bulk to interfaces.* Chemical Society Reviews, 2010. **39**(3): p. 1073-1095.
3. Bruning, J.H., *Optical Lithography... 40 years and holding - art. no. 652004.* Optical Microlithography XX, Pts 1-3, 2007. **6520**: p. 52004-52004.
4. Bartle, K.D. and P. Myers, *History of gas chromatography.* Trac-Trends in Analytical Chemistry, 2002. **21**(9-10): p. 547-557.
5. Woolley, A.T. and R.A. Mathies, *Ultra-High-Speed DNA-Sequencing Using Capillary Electrophoresis Chips.* Analytical Chemistry, 1995. **67**(20): p. 3676-3680.
6. Weigl, B.H., R.L. Bardell, and C.R. Cabrera, *Lab-on-a-chip for drug development.* Advanced Drug Delivery Reviews, 2003. **55**(3): p. 349-377.
7. Squires, T.M. and S.R. Quake, *Microfluidics: Fluid physics at the nanoliter scale.* Reviews of Modern Physics, 2005. **77**(3): p. 977-1026.
8. deMello, A.J., *Control and detection of chemical reactions in microfluidic systems.* Nature, 2006. **442**(7101): p. 394-402.
9. Ismagilov, R.F., *Integrated microfluidic systems.* Angewandte Chemie-International Edition, 2003. **42**(35): p. 4130-4132.
10. Fan, X.D. and I.M. White, *Optofluidic microsystems for chemical and biological analysis.* Nature Photonics, 2011. **5**(10): p. 591-597.
11. Samiei, E., M. Tabrizian, and M. Hoorfar, *A review of digital microfluidics as portable platforms for lab-on a-chip applications.* Lab on a Chip, 2016. **16**(13): p. 2376-2396.
12. Li, X., D.R. Ballerini, and W. Shen, *A perspective on paper-based microfluidics: Current status and future trends.* Biomicrofluidics, 2012. **6**(1).
13. Kovarik, M.L., et al., *Micro Total Analysis Systems for Cell Biology and Biochemical Assays.* Analytical Chemistry, 2012. **84**(2): p. 516-540.
14. Delattre, C., et al., *Macro to microfluidics system for biological environmental monitoring.* Biosensors & Bioelectronics, 2012. **36**(1): p. 230-235.
15. Neethirajan, S., et al., *Microfluidics for food, agriculture and biosystems industries.* Lab on a Chip, 2011. **11**(9): p. 1574-1586.
16. Rivet, C., et al., *Microfluidics for medical diagnostics and biosensors.* Chemical Engineering Science, 2011. **66**(7): p. 1490-1507.
17. Gluodenis, T. and S. Harrison, *Homeland security and bioterrorism applications: detection of bioweapon pathogens by microfluidic-based electrophoretic DNA analysis.* MLO Med Lab Obs, 2004. **36**(2): p. 34-8.
18. Yager, P., et al., *Microfluidic diagnostic technologies for global public health.* Nature, 2006. **442**(7101): p. 412-418.
19. St John, A. and C.P. Price, *Existing and Emerging Technologies for Point-of-Care Testing.* Clin Biochem Rev, 2014. **35**(3): p. 155-67.
20. Volpatti, L.R. and A.K. Yetisen, *Commercialization of microfluidic devices.* Trends Biotechnol, 2014. **32**(7): p. 347-50.
21. Ramos, A.n. and International Centre for Mechanical Sciences., *Electrokinetics and electrohydrodynamics in microsystems*. CISM courses and lectures. 2011, Wien ; New York: Springer. 297 p.
22. Svoboda, M., et al., *Direct evidence of concentration and potential profiles in the electrolyte diode.* Chemical Engineering Journal, 2008. **135**: p. S203-S209.

23. Hegedus, L., et al., *Polarization Phenomena in Hydrogel Membranes - Experimental Realization of an Electrolyte Diode.* Ach-Models in Chemistry, 1995. **132**(1-2): p. 207-224.
24. Hegedus, L., et al., *Nonlinear effects of electrolyte diodes and transistors in a polymer gel medium.* Chaos, 1999. **9**(2): p. 283-297.
25. Hegedus, L., et al., *Electrolyte transistors: Ionic reaction-diffusion systems with amplifying properties.* Journal of Physical Chemistry A, 1998. **102**(32): p. 6491-6497.
26. Lindner, J., D. Snita, and M. Marek, *Modelling of ionic systems with a narrow acid base boundary.* Physical Chemistry Chemical Physics, 2002. **4**(8): p. 1348-1354.
27. Snita, D., et al., *Nonlinear behaviour of simple ionic systems in hydrogel in an electric field.* Faraday Discussions, 2001. **120**: p. 53-66.
28. Cheng, L.J. and H.C. Chang, *Microscale pH regulation by splitting water.* Biomicrofluidics, 2011. **5**(4).
29. Cheng, L.J. and H.C. Chang, *Switchable pH actuators and 3D integrated salt bridges as new strategies for reconfigurable microfluidic free-flow electrophoretic separation.* Lab on a Chip, 2014. **14**(5): p. 979-987.
30. Desharnais, B.M. and B.A.G. Lewis, *Electrochemical water splitting at bipolar interfaces of ion exchange membranes and soils.* Soil Science Society of America Journal, 2002. **66**(5): p. 1518-1525.
31. Slouka, Z., et al., *Transient behavior of an electrolytic diode.* Physical Chemistry Chemical Physics, 2007. **9**(39): p. 5374-5381.
32. Schrott, W., et al., *Study on surface properties of PDMS microfluidic chips treated with albumin.* Biomicrofluidics, 2009. **3**(4).
33. Attard, P., *Electrolytes and the Electric Double Layer*, in *Advances in Chemical Physics*. 2007, John Wiley & Sons, Inc. p. 1-159.
34. Stern, O., *Zur theorie der elektrolytischen doppelschicht.* . Z.Elektrochem.Angew.Phys.Chem., 1924. **30**: p. 508-516.
35. Wang, X.Y., et al., *Electroosmotic pumps and their applications in microfluidic systems.* Microfluidics and Nanofluidics, 2009. **6**(2): p. 145-162.
36. Chen, Z., P. Wang, and H.C. Chang, *An electro-osmotic micro-pump based on monolithic silica for micro-flow analyses and electro-sprays.* Analytical and Bioanalytical Chemistry, 2005. **382**(3): p. 817-824.
37. Zeng, S.L., et al., *Fabrication and characterization of electroosmotic micropumps.* Sensors and Actuators B-Chemical, 2001. **79**(2-3): p. 107-114.
38. Nakanishi, K., T. Sakiyama, and K. Imamura, *On the adsorption of proteins on solid surfaces, a common but very complicated phenomenon.* Journal of Bioscience and Bioengineering, 2001. **91**(3): p. 233-244.
39. Slouka, Z., S. Senapati, and H.C. Chang, *Microfluidic Systems with Ion-Selective Membranes.* Annual Review of Analytical Chemistry, Vol 7, 2014. **7**: p. 317-335.
40. Postler, T., et al., *Parametrical studies of electroosmotic transport characteristics in submicrometer channels.* Journal of Colloid and Interface Science, 2008. **320**(1): p. 321-332.
41. Sollner, K., *Recent Advances in the Electrochemistry of Membranes of High Ionic Selectivity.* Journal of the Electrochemical Society, 1950. **97**(7): p. C139-C151.
42. Sparreboom, W., A. van den Berg, and J.C.T. Eijkel, *Transport in nanofluidic systems: a review of theory and applications.* New Journal of Physics, 2010. **12**.
43. Strathmann, H., A. Grabowski, and G. Eigenberger, *Ion-Exchange Membranes in the Chemical Process Industry.* Industrial & Engineering Chemistry Research, 2013. **52**(31): p. 10364-10379.
44. Yossifon, G., et al., *Nonlinear current-voltage characteristics of nanochannels.* Physical Review E, 2009. **79**(4).

45. Chang, C.C., C.P. Yeh, and R.J. Yang, *Ion concentration polarization near microchannel-nanochannel interfaces: Effect of pH value.* Electrophoresis, 2012. **33**(5): p. 758-764.
46. Krol, J.J., M. Wessling, and H. Strathmann, *Concentration polarization with monopolar ion exchange membranes: current-voltage curves and water dissociation.* Journal of Membrane Science, 1999. **162**(1-2): p. 145-154.
47. Yossifon, G. and H.C. Chang, *Selection of Nonequilibrium Overlimiting Currents: Universal Depletion Layer Formation Dynamics and Vortex Instability.* Physical Review Letters, 2008. **101**(25).
48. Chang, H.C., G. Yossifon, and E.A. Demekhin, *Nanoscale Electrokinetics and Microvortices: How Microhydrodynamics Affects Nanofluidic Ion Flux.* Annual Review of Fluid Mechanics, Vol 44, 2012. **44**: p. 401-426.
49. Barany, S. and N. Mishchuk, *Electrokinetic phenomena of the second kind: Theory, experiment, applications.* Abstracts of Papers of the American Chemical Society, 1999. **218**: p. U427-U428.
50. Rubinstein, I. and L. Shtilman, *Voltage against Current Curves of Cation-Exchange Membranes.* Journal of the Chemical Society-Faraday Transactions Ii, 1979. **75**: p. 231-246.
51. Nandigana, V.V.R. and N.R. Aluru, *Understanding anomalous current-voltage characteristics in microchannel-nanochannel interconnect devices.* Journal of Colloid and Interface Science, 2012. **384**: p. 162-171.
52. Svoboda, M., et al., *Swelling induced structural changes of a heterogeneous cation-exchange membrane analyzed by micro-computed tomography.* Journal of Membrane Science, 2017. **525**: p. 195-201.
53. Strathmann, H., *Electrodialysis, a mature technology with a multitude of new applications.* Desalination, 2010. **264**(3): p. 268-288.
54. Xu, T.W., *Ion exchange membranes: State of their development and perspective.* Journal of Membrane Science, 2005. **263**(1-2): p. 1-29.
55. Tanaka, Y., *1 - Preparation of Ion Exchange Membranes*, in *Ion Exchange Membranes (Second Edition)*. 2015, Elsevier: Amsterdam. p. 3-28.
56. Balster, J., et al., *Morphology and microtopology of cation-exchange polymers and the origin of the overlimiting current.* Journal of Physical Chemistry B, 2007. **111**(9): p. 2152-2165.
57. Duan, Q.J., S.H. Ge, and C.Y. Wang, *Water uptake, ionic conductivity and swelling properties of anion-exchange membrane.* Journal of Power Sources, 2013. **243**: p. 773-778.
58. Stock, S.R., *MicroComputed Tomography: Methodology and Applications.* Microcomputed Tomography: Methodology and Applications, 2011: p. 1-331.
59. Slouka, Z., et al., *Charge Inversion, Water Splitting, and Vortex Suppression Due to DNA Sorption on Ion-Selective Membranes and Their Ion-Current Signatures.* Langmuir, 2013. **29**(26): p. 8275-8283.
60. Svoboda, M., et al., *Cation exchange membrane integrated into a microfluidic device.* Microelectronic Engineering, 2009. **86**(4-6): p. 1371-1374.
61. Belova, E.I., et al., *Effect of anion-exchange membrane surface properties on mechanisms of overlimiting mass transfer.* Journal of Physical Chemistry B, 2006. **110**(27): p. 13458-13469.
62. Zabolotsky, V.I., V.V. Nikonenko, and N.D. Pismenskaya, *On the role of gravitational convection in the transfer enhancement of salt ions in the course of dilute solution electrodialysis.* Journal of Membrane Science, 1996. **119**(2): p. 171-181.
63. Lindstrand, V., G. Sundstrom, and A.S. Jonsson, *Fouling of electrodialysis membranes by organic substances.* Desalination, 2000. **128**(1): p. 91-102.

64. Choi, J.H. and S.H. Moon, *Pore size characterization of cation-exchange membranes by chronopotentiometry using homologous amine ions.* Journal of Membrane Science, 2001. **191**(1-2): p. 225-236.
65. Senapati, S., et al., *A Nanomembrane-Based Nucleic Acid Sensing Platform for Portable Diagnostics.* Microfluidics: Technologies and Applications, 2011. **304**: p. 153-169.
66. Taller, D., et al., *On-chip surface acoustic wave lysis and ion-exchange nanomembrane detection of exosomal RNA for pancreatic cancer study and diagnosis.* Lab on a Chip, 2015. **15**(7): p. 1656-1666.
67. Ko, S.H., et al., *Nanofluidic preconcentration device in a straight microchannel using ion concentration polarization.* Lab on a Chip, 2012. **12**(21): p. 4472-4482.
68. Slouka, Z., et al., *Integrated, DC voltage-driven nucleic acid diagnostic platform for real sample analysis: Detection of oral cancer.* Talanta, 2015. **145**: p. 35-42.
69. Lee, P.Y., et al., *Agarose Gel Electrophoresis for the Separation of DNA Fragments.* Jove-Journal of Visualized Experiments, 2012(62).
70. Anada, T., et al., *The separation of oligodeoxynucleotides having a single-base difference by affinity capillary electrophoresis using oligodeoxynucleotide-polyacrylamide conjugate.* Electrophoresis, 2002. **23**(14): p. 2267-2273.
71. Star, A., et al., *Label-free detection of DNA hybridization using carbon nanotube network field-effect transistors.* Proceedings of the National Academy of Sciences of the United States of America, 2006. **103**(4): p. 921-926.
72. Liu, B. and G.C. Bazan, *Homogeneous fluorescence-based DNA detection with water-soluble conjugated polymers.* Chemistry of Materials, 2004. **16**(23): p. 4467-4476.
73. Kim, S.J., Y.A. Song, and J. Han, *Nanofluidic concentration devices for biomolecules utilizing ion concentration polarization: theory, fabrication, and applications.* Chemical Society Reviews, 2010. **39**(3): p. 912-922.
74. Suwal, S., A. Doyen, and L. Bazinet, *Characterization of protein, peptide and amino acid fouling on ion-exchange and filtration membranes: Review of current and recently developed methods.* Journal of Membrane Science, 2015. **496**: p. 267-283.
75. Senapati, S., et al., *An ion-exchange nanomembrane sensor for detection of nucleic acids using a surface charge inversion Phenomenon.* Biosensors & Bioelectronics, 2014. **60**: p. 92-100.
76. Abdelgawad, M., M.W.L. Watson, and A.R. Wheeler, *Hybrid microfluidics: A digital-to-channel interface for in-line sample processing and chemical separations.* Lab on a Chip, 2009. **9**(8): p. 1046-1051.
77. Watson, M.W.L., M.J. Jebrail, and A.R. Wheeler, *Multilayer Hybrid Microfluidics: A Digital-to-Channel Interface for Sample Processing and Separations.* Analytical Chemistry, 2010. **82**(15): p. 6680-6686.
78. Bhattacharyya, A. and C.A. Klapperich, *Microfluidics-based extraction of viral RNA from infected mammalian cells for disposable molecular diagnostics.* Sensors and Actuators B-Chemical, 2008. **129**(2): p. 693-698.
79. Chen, C., et al., *Microfluidic isolation and transcriptome analysis of serum microvesicles.* Lab on a Chip, 2010. **10**(4): p. 505-511.
80. Giordano, B.C., et al., *On-line sample pre-concentration in microfluidic devices: A review.* Analytica Chimica Acta, 2012. **718**: p. 11-24.
81. Persat, A. and J.G. Santiago, *MicroRNA Profiling by Simultaneous Selective Isotachophoresis and Hybridization with Molecular Beacons.* Analytical Chemistry, 2011. **83**(6): p. 2310-2316.
82. Lin, C.C., J.L. Hsu, and G.B. Lee, *Sample preconcentration in microfluidic devices.* Microfluidics and Nanofluidics, 2011. **10**(3): p. 481-511.
83. Wang, Y.C., A.L. Stevens, and J.Y. Han, *Million-fold preconcentration of proteins and peptides by nanofluidic filter.* Analytical Chemistry, 2005. **77**(14): p. 4293-4299.

84. Huang, F.C., C.S. Liao, and G.B. Lee, *An integrated microfluidic chip for DNA/RNA amplification, electrophoresis separation and on-line optical detection.* Electrophoresis, 2006. **27**(16): p. 3297-3305.
85. Chin, C.D., et al., *Microfluidics-based diagnostics of infectious diseases in the developing world.* Nature Medicine, 2011. **17**(8): p. 1015-U138.
86. Shah, S.S., et al., *Current Technologies and Recent Developments for Screening of HPV-Associated Cervical and Oropharyngeal Cancers.* Cancers (Basel), 2016. **8**(9).
87. Marczak, S., et al., *Induced nanoparticle aggregation for short nucleic acid quantification by depletion isotachophoresis.* Biosens Bioelectron, 2016. **86**: p. 840-8.
88. Mirkin, C.A., et al., *A DNA-based method for rationally assembling nanoparticles into macroscopic materials.* Nature, 1996. **382**(6592): p. 607-609.
89. Sato, K., K. Hosokawa, and M. Maeda, *Rapid aggregation of gold nanoparticles induced by non-cross-linking DNA hybridization.* Journal of the American Chemical Society, 2003. **125**(27): p. 8102-8103.
90. Zhang, X., et al., *Exosomes in cancer: small particle, big player.* Journal of Hematology & Oncology, 2015. **8**.
91. Azmi, A.S., B. Bao, and F.H. Sarkar, *Exosomes in cancer development, metastasis, and drug resistance: a comprehensive review.* Cancer and Metastasis Reviews, 2013. **32**(3-4): p. 623-642.
92. Soung, Y.H., et al., *Exosomes in Cancer Diagnostics.* Cancers (Basel), 2017. **9**(1).
93. Paranjape, T., F.J. Slack, and J.B. Weidhaas, *MicroRNAs: tools for cancer diagnostics.* Gut, 2009. **58**(11): p. 1546-54.

List of appendices

1. Svoboda, M., et al., *Direct evidence of concentration and potential profiles in the electrolyte diode.* Chemical Engineering Journal, 2008. **135**: p. S203-S209.

2. Slouka, Z., et al., *Transient behavior of an electrolytic diode.* Physical Chemistry Chemical Physics, 2007. **9**(39): p. 5374-5381.

3. Schrott, W., et al., *Study on surface properties of PDMS microfluidic chips treated with albumin.* Biomicrofluidics, 2009. **3**(4).

4. Slouka, Z., S. Senapati, and H.C. Chang, *Microfluidic Systems with Ion-Selective Membranes.* Annual Review of Analytical Chemistry, Vol 7, 2014. **7**: p. 317-335.

5. Postler, T., et al., *Parametrical studies of electroosmotic transport characteristics in submicrometer channels.* Journal of Colloid and Interface Science, 2008. **320**(1): p. 321-332.

6. Svoboda, M., et al., *Swelling induced structural changes of a heterogeneous cation-exchange membrane analyzed by micro-computed tomography.* Journal of Membrane Science, 2017. **525**: p. 195-201.

7. Slouka, Z., et al., *Charge Inversion, Water Splitting, and Vortex Suppression Due to DNA Sorption on Ion-Selective Membranes and Their Ion-Current Signatures.* Langmuir, 2013. **29**(26): p. 8275-8283.

8. Svoboda, M., et al., *Cation exchange membrane integrated into a microfluidic device.* Microelectronic Engineering, 2009. **86**(4-6): p. 1371-1374.

9. Taller, D., et al., *On-chip surface acoustic wave lysis and ion-exchange nanomembrane detection of exosomal RNA for pancreatic cancer study and diagnosis.* Lab on a Chip, 2015. **15**(7): p. 1656-1666.

10. Senapati, S., et al., *An ion-exchange nanomembrane sensor for detection of nucleic acids using a surface charge inversion Phenomenon.* Biosensors & Bioelectronics, 2014. **60**: p. 92-100.

11. Slouka, Z., et al., *Integrated, DC voltage-driven nucleic acid diagnostic platform for real sample analysis: Detection of oral cancer.* Talanta, 2015. **145**: p. 35-42.

12. Marczak, S., et al., *Induced nanoparticle aggregation for short nucleic acid quantification by depletion isotachophoresis.* Biosensors & Bioelectronics, 2016. **86**: p. 840-848.

ELSEVIER

Chemical Engineering Journal 135S (2008) S203–S209

Chemical Engineering Journal

www.elsevier.com/locate/cej

Direct evidence of concentration and potential profiles in the electrolyte diode

M. Svoboda, Z. Slouka, J. Lindner*, D. Šnita

Department of Chemical Engineering, Institute of Chemical Technology, Technická 5, 166 28 Prague 6, Czech Republic

Abstract

Electrolyte diode is an electrochemical microsystem showing complex nonlinear behaviour due to interactions of diffusion, migration and chemical reactions. In our recent works we have developed a mathematical model of the electrolyte diode which predicted steep concentration and potential profiles on a spatial interval of several micrometers in the closed mode. The main aim of this work is the experimental verification of the concentration and potential profiles predicted by the model. In this work two techniques for direct observation of spatial concentration and potential profiles in the electrolyte diode are presented. Two different methods were used: (i) visualization of the acid–base boundary using acid–base indicators and (ii) direct measurements of electric potential profiles using the array of microelectrodes. As the presence of an indicator changes the properties of the system, there is a good agreement between modelling and experimental results only at relatively low values of external potential difference. Results of the other method confirm the model predictions in broad range of external potential difference values.

Keywords: Electrolyte diode; Electrochemical microsystems; Acid–base equilibria

1. Introduction

The electrolyte diode is a system consisting of two electrolyte reservoirs (in our case, one containing HCl solution, the other containing KOH solution) separated by a permeation layer (membrane) or by a capillary (microchannel) suppressing the convective flow, while the diffusion and migration flows can pass through. When an external electric field is connected in a proper way, diode-like action can be observed [1]. In the open mode, potassium and chloride ions are driven into the permeation layer, forming a zone of relatively high conductivity with high current density proportional to the potential difference of the external electric field (cf. Figs. 1a and 3a–h). Almost linear profiles of concentrations and of electric potential are established and the behaviour of the system is similar to that of a spatially homogeneous conducting layer. When the polarity of the external electric field is reversed (cf. Fig. 1b), a narrow zone of almost pure water is formed in the permeation layer; the conductivity is very low there (cf. Fig. 3m–t).

Typical experimental current-voltage characteristics similar to those of a semiconductor diode is shown in Fig. 2a, typical time course of the electric current during measurement of the current-voltage characteristics can be seen in Fig. 2b. The convention used in this work is that the KOH and HCl reservoirs are on the left-hand side and the right-hand side, respectively, as it can be seen in Fig. 1. Thus, the negative values of the external electric potential difference (defined as $U = \phi^{\text{right}} - \phi^{\text{left}}$) mean that the diode is in the open mode ($U < 0$) and vice versa.

As a combination of two electrolyte diodes, an electrolyte transistor has been constructed [2]. Nonlinear behaviour (oscillations, bistability) has been observed in both systems [3].

The function of the electrolyte diode can be verified by measurement of current-voltage characteristics. The current-voltage characteristics gives us only integral information about the behaviour of the system inside the permeation layer, for more detailed studies we would need to know the profiles inside the permeation layer.

2. Mathematical modelling

In our previous studies [4,5] we have presented the mathematical model suitable also for description of the electrolyte diode. We have developed two versions of the model, using different assumptions. All modelling results mentioned in this paper are obtained from the "non-equilibrium" model where finite rates of the water dissociation and recombination reactions are con-

* Corresponding author. Tel.: +420 220 443 296; fax: +420 220 444 320.
E-mail address: jiri.lindner@vscht.cz (J. Lindner).

1385-8947/$ – see front matter © 2007 Elsevier B.V. All rights reserved.
doi:10.1016/j.cej.2007.07.027

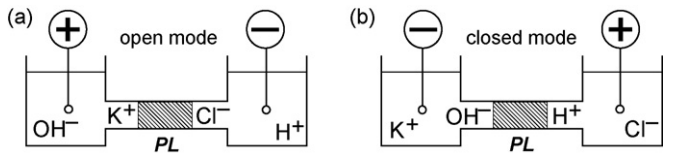

Fig. 1. Principle of the electrolyte diode; the two different regimes – the open (a) and the closed mode (b) – are shown. The permeation layer (PL) is hatched.

sidered. The local electroneutrality assumption is not used here. For a detailed discussion of the model please cf. our papers [4,5], another application of the model has been presented in [6].

The non-equilibrium model (in spatially one-dimensional form as used in this work) consists of mass balances of all ionic components present in the system (K^+, Cl^-, H^+, OH^-):

$$\frac{\partial c_{K^+}}{\partial t} = -\frac{\partial}{\partial x}\left(-D_{K^+}\frac{\partial c_{K^+}}{\partial x} - D_{K^+}c_{K^+}\frac{\partial \phi}{\partial x}\frac{F}{RT}\right) \quad (1)$$

$$\frac{\partial c_{Cl^-}}{\partial t} = -\frac{\partial}{\partial x}\left(-D_{Cl^-}\frac{\partial c_{Cl^-}}{\partial x} + D_{Cl^-}c_{Cl^-}\frac{\partial \phi}{\partial x}\frac{F}{RT}\right) \quad (2)$$

$$\frac{\partial c_{H^+}}{\partial t} = -\frac{\partial}{\partial x}\left(-D_{H^+}\frac{\partial c_{H^+}}{\partial x} - D_{H^+}c_{H^+}\frac{\partial \phi}{\partial x}\frac{F}{RT}\right) - r_1 \quad (3)$$

$$\frac{\partial c_{OH^-}}{\partial t} = -\frac{\partial}{\partial x}\left(-D_{OH^-}\frac{\partial c_{OH^-}}{\partial x} + D_{OH^-}c_{OH^-}\frac{\partial \phi}{\partial x}\frac{F}{RT}\right) - r_1 \quad (4)$$

and of the Poisson's equation for the electric potential profile evaluation

$$\frac{\partial^2 \phi}{\partial x^2} = -\frac{q}{\varepsilon} = -\frac{F}{\varepsilon}(c_{H^+} - c_{OH^-} + c_{K^+} - c_{Cl^-}) \quad (5)$$

Here $c_i(t, x)$ is the concentration of the ith component, t is the time, x is the spatial coordinate, D_i is the diffusion coefficient of the ith component, $\phi(t, x)$ is the electrostatic potential, q is the electric charge density, F is the Faraday's constant, R is the molar gas constant, T is the absolute temperature, ε is the permittivity, respectively.

The symbol r_1 stands for the reaction rate of water dissociation $H^+ + OH^- \leftrightarrow H_2O$:

$$r_1 = k_1(c_{H^+}c_{OH^-} - K_W), \quad (6)$$

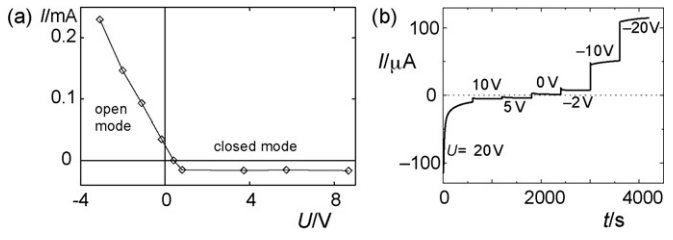

Fig. 2. (a) Typical experimental current-voltage characteristics of the electrolyte diode. (b) The dynamics of the diode: after change of the external electric potential difference, a new stationary state (characterized by constant value of the electric current passing through the system in this figure) is established usually within a few minutes except the initial change (from 0 to 20 V).

here k_1 is the reaction rate constant of the water recombination, K_W is the equilibrium constant of the water dissociation.

We have used the following set of parameters: concentrations of both HCl and KOH in the reservoirs are equal to 0.1 M. Diffusion coefficients of ionic components we have used correspond to the values in dilute aqueous solutions: $D_{H+} = 9.31 \times 10^{-5}\,cm^2\,s^{-1}$, $D_{OH-} = 5.28 \times 10^{-5}\,cm^2\,s^{-1}$, $D_{K+} = 1.96 \times 10^{-5}\,cm^2\,s^{-1}$, $D_{Cl^-} = 2.03 \times 10^{-5}\,cm^2\,s^{-1}$. The value of Faraday constant $F = 96484.56\,C\,mol^{-1}$, the gas constant $R = 8.314\,J\,mol^{-1}\,K^{-1}$. Water product (equilibrium constant) $K_W = 10^{-14}\,M^2$, the rate constant of water recombination $k_1 \cong 1.3 \times 10^{11}\,M^{-1}\,s^{-1}$. The dielectric constant $\varepsilon = \varepsilon_0\varepsilon_r$, where ε_0 is the permittivity of vacuum ($\varepsilon_0 = 8.854 \times 10^{-12}\,C^2\,J^{-1}\,m^{-1}$) and $\varepsilon_r = 78.5$ is the relative permittivity of water.

In a general case we have a set of five partial differential equations (PDEs) of which four are of a parabolic type (mass balances) and one is of an elliptic type (the Poisson equation). In stationary simulations the accumulation term in parabolic equations is equal to zero and thus the set of five elliptic PDEs represents the description of the system. The profiles presented in this paper are results of stationary simulations. Constant values of the electric potential and constant concentrations of both electrolytes are used as the boundary conditions, linear profiles of system variables (concentrations, electric potential) are used as the initial estimate.

The simulation results (cf. Fig. 3) have shown steep gradients of concentrations, potential, charge density and other characteristic quantities (changes of several orders of magnitude) on a spatial interval of several micrometers (also called the acid–base boundary, cf. Fig. 4) when the diode is in the closed mode. This makes the numerical solution of the model equations rather difficult. The model then can be used for description of a broad class of ionic systems, where dissociation reactions, diffusion and migration take place simultaneously, inducing complex nonlinear effects.

An approximate analytical solution has been also derived recently [3,7]. In this case, the diode is divided into three zones (alkaline, neutral and acidic) and the profiles are calculated for each zone apart, using the quasielectroneutrality and quasiequilibrium assumptions [7].

The main aim of this work is qualitative experimental verification of the simulation results. The quantitative comparison would require much more sophisticated model with even more difficult numerical solution. Among others, the quantitative model should take into account changes of diffusion coefficients of ions in the permeation layer with increasing gel density (cf., e.g., [10]), effects of ionic strength, interactions with fixed charges contained in the gel or at the walls of the channel, electrode reactions, etc.

We have developed and tested an experimental device for measuring the electric potential profile inside the electrolyte diode. For verification of the concentration profiles, absorbance pH indicators were used to visualize the changing concentration of H^+ and OH^- ions along the electrolyte diode.

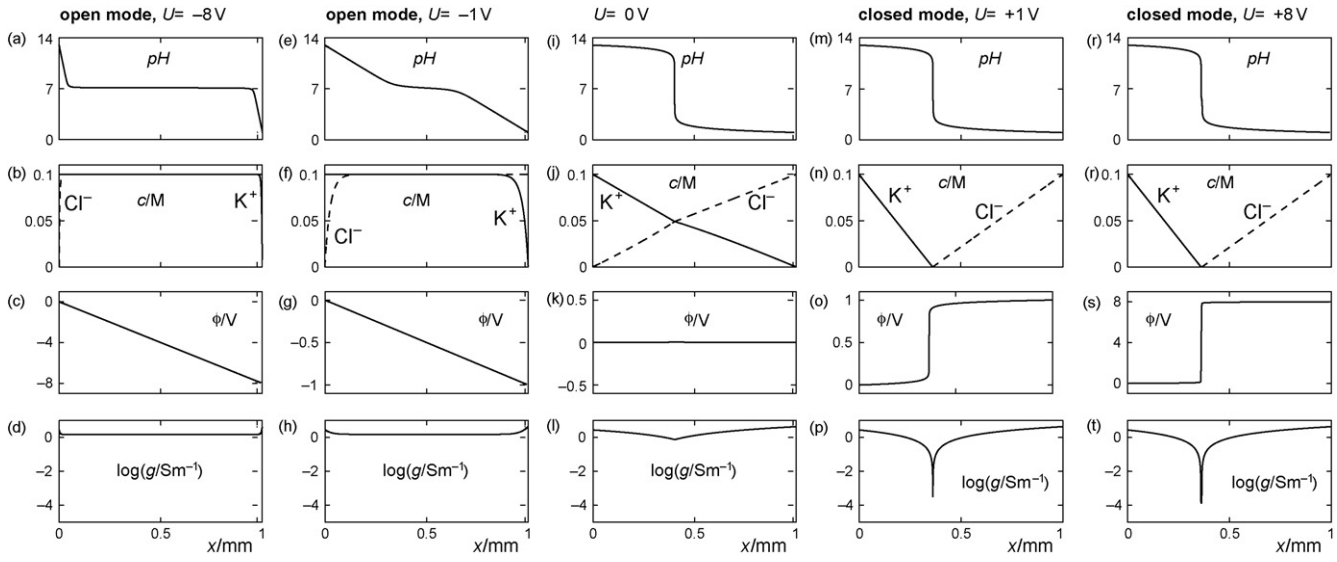

Fig. 3. Computed profiles of pH, concentrations of K^+ and Cl^- ions, electric potential ϕ, and logarithm of conductivity $\log(g)$ for external potential differences $U = -8$ and -1 V in the open mode (a–d, e–h, respectively), $U = 0$ V (i–l), and $U = +1$ V and $U = +8$ V in the closed mode (m–p, r–t, respectively).

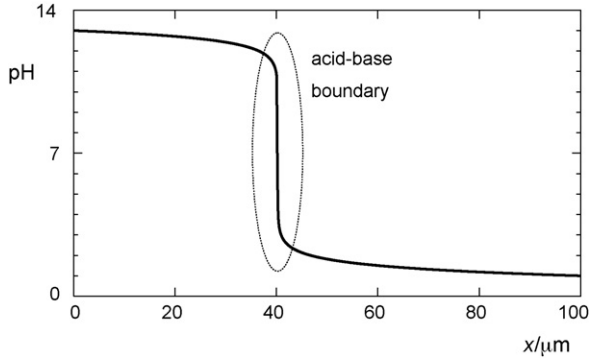

Fig. 4. Computed profile of pH (defined as $-\log_{10}[H^+]$) in the closed mode for the electrolyte diode of the total length 100 μm for boundary concentrations of HCl and KOH equal to 0.1 M and $U = 1$ V.

3. Experimental setup

3.1. Device A: Electrolyte diode in a tubular microreactor

There are various possibilities of the experimental realization of the electrolyte diode, some of them have been published by Noszticzius and co-workers [1]. For experiments with acid–base indicators presented in this work we have developed a tubular microreactor made from Tygon tubing, where the permeation layer has been made from a cylinder-shaped hydrogel (dimensions $W \times L$ were 100–450 μm × 2–3 mm, i.e., the crossflow area between 1×10^{-8} and 1×10^{-7} m^2 approximately) as it can be seen in Fig. 5. Fresh electrolyte solutions are introduced to the inner tube, then the electrolyte passes to the surface of the permeation layer and finally, the electrolyte is led out of the device, as denoted by the arrows.

Relatively low volume of the permeation layer, comparing to the traditional experimental setup of Noszticzius and co-workers [1], means lower residence time of the electrolyte and shorter time necessary to reach the steady state. Concentrations of both the KOH and HCl solutions used were 0.1 M. The platinum wires were used both as measuring and working electrodes in all experiments, using the four-electrodes setup. The electrolyte is fed via a thin PTFE tube, using the ISMATEC peristaltic pump.

As the separating layer mostly the poly-vinyl-alcohol (PVA) gel has been used as it has good mechanical properties, good stability both in acidic and alkaline solutions, high transparency and the lowest fixed charge from the common hydrogels. The PVA gel has been prepared accordingly to the recipe published by Noszticzius and co-workers [1] in the two steps: (i) the stock solution (approximately 30%, w/w of PVA in water) has been prepared from the monomer of nominal molecular weight 31,000 (Fluka order No. 81381), (ii) 2 ml of glutardialdehyde solution (1%, w/w, prepared from the stock Fluka order No. 49630) and 1 ml of 5 M HCl solution have been added to 4 g of the PVA stock solution under continuous stirring. The polymerization is rather fast, the gel should be put into a form within 30 s after mixing. The polymerized gel can be dried out and kept in the dry state for a long time. The dry gel piece is then inserted into the device, and when the water is added, the gel swells and its original volume is restored. Before experiment, the gel plug is washed with 1 M KOH solution to neutralize remaining acidic groups fixed in the polymer chain. For some experiments we have used also the Agar gel as its preparation is easier. The 4% (w/w) agar solution is heated under continuous stirring to its boiling temperature. The gel solidifies as the temperature decreases, yet liquid solution of

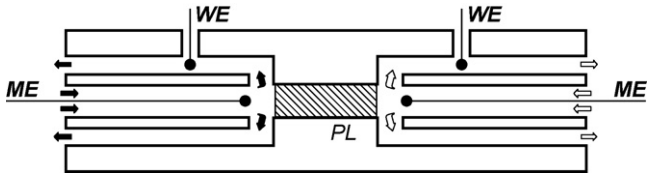

Fig. 5. Electrolyte diode as the tubular microreactor. The hatched part is the permeation layer (PL), measuring electrodes (ME) are located in the inlets of fresh electrolytes, working electrodes (WE) are placed in the electrolyte outlets.

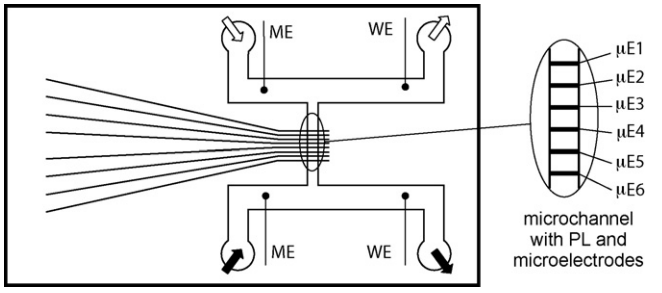

Fig. 6. Scheme of the electrolyte diode with a set of measuring microelectrodes (μE) in the central microchannel with permeation layer (PL). In the experimental Device B eight measuring microelectrodes has been used. Additional pair of measuring (ME) and one pair of working (WE) electrodes are placed in the electrolyte inlets and outlets, respectively.

the gel is introduced into a form. Similarly to the PVA gel, the Agar gel can be dried out and after inserting to its location inside the experimental apparatus it swells in the presence of water to its original volume. This device has been used for experiments with acid–base indicators.

3.2. Device B: Electrolyte diode with electrode array in the permeation layer

For other type of experiments we have developed an alternative construction of the electrolyte diode (cf. Fig. 6). The central microchannel with the permeation layer was approximately 250 μm wide, 400 μm deep and 2–3 mm long. Whole device is fabricated by micro-milling from polystyrene wafers. After fabrication of the channels, the individual plates are connected by thermal bonding. Platinum wires are used both as the working and measuring electrodes. For the measurements of the potential profile at the electrolyte diode, the central microchannel is equipped with additional microelectrodes (Pt wires with diameter of 100 μm) in the distance of 300–400 μm from each other. The device B has been used for measurements of electric potential distribution.

3.3. Supplementary experimental equipment

In both electrolyte diode arrangements described above the electrolytes have been pumped to the inlet channels from reservoirs by a peristaltic pump. Keithley source meter model 2400 was used as the external voltage source, Keithley multimeter model 2700 was used for measurement. Both devices were connected to a computer via GPIB interface. Whole process was controlled by a specially developed subroutine under Matlab environment (cf. Fig. 7). For optical observation of the central part of the diode in some experiments, the microscope Olympus BX51WI has been used. Computer-controlled digital camera Olympus C5050Z has been attached to the microscope. The camera is capable to take high-resolution images automatically in preset intervals down to 5 s.

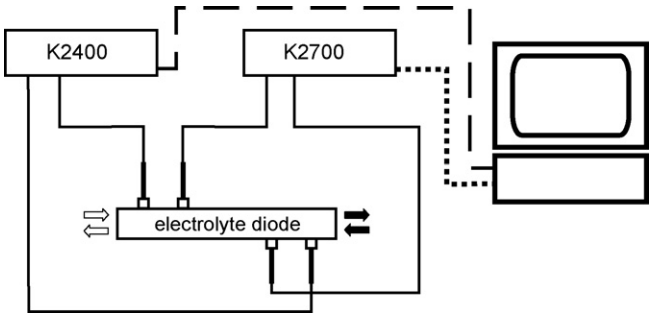

Fig. 7. Connection of the electrolyte diode to the electrolyte inlets and outlets (white and black arrows), potential source (K2400) and multimeter (K2700).

4. Experimental results

4.1. Measuring of the potential course

Experimental course of electric potential has been measured in the diode (Device B) with permeation layer (gel plug) approximately 2.1 mm long which has been equipped with set of eight platinum microelectrodes (cf. Fig. 6). In the open mode, the potential profile is almost linear (Fig. 8a) as it has been predicted by the model (cf. Fig. 3c and g). The major part of the total potential change in the closed mode can be observed left to the central part of the diode (Fig. 8b). The potential profiles predicted by the model are similar (cf. Fig. 3o and s). Experimental results qualitatively correspond well to the model predictions. Quantitative variations can be found as the model does not include the effects of the gel permeation layer on transport of ions.

4.2. Visualization of the acid–base boundary

The steep change of pH inside the electrolyte diode in the closed mode led to the idea to use an acid–base indicator and observe its absorbance change under a microscope. There are several limitations for the choice of a suitable indicator: (i) it should have a distinct colour, absorbance or fluorescence change, in an ideal case between pH 6 and 8, (ii) it should be well soluble both in acidic and alkaline solutions, and (iii) it should not be rapidly washed out of the gel. Also the concentration of the dye should be as low as possible as the ionic forms of indicators can affect the behaviour of the electrolyte diode. Possible problems with the use of an acid–base indicator are, e.g., the dependency of the indicator behaviour on the ionic strength and washing-out of the indicator out of the permeation layer of the electrolyte diode [8].

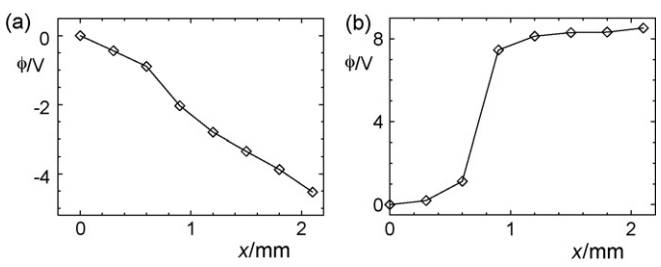

Fig. 8. Potential course in the electrolyte diode (a) in the open mode, (b) in the closed mode.

Preliminary experiments have shown that the most suitable (although still not ideal) indicators for our purposes are congo red and thymol blue. Congo red possesses the colour change around pH 4 from the red (acidic) to the blue (alkaline) form. Thymol blue has two colour changes: with increasing pH, the first colour change is around pH 2 from the red to the yellow, the second one is around pH 9 from the yellow to the blue. We have added a small amount of the indicator to the gel during preparation. The total concentration of the dye in the gel was not higher than 10^{-2} M approximately. No indicator has been present in the electrolyte inlets.

The main advantage of the congo red is its almost neglectable rinsing out of the PVA gel. This is probably caused by various weak and strong interactions of the dye with the gel, the congo red in higher concentrations can be used even as the cross-linking agent for the PVA gel [9]. Under the conditions of our experiments, congo red was well retained in the PVA gel, however, its ability to exhibit a colour change with changing pH has not been affected.

The two colour changes of the thymol blue (at pH 2 and 9 approximately) makes this dye a promising marker of steep pH gradients expected to develop in the electrolyte diode.

4.3. Different behaviour of the electrolyte diode with an addition of the dye

As the molecules of acid–base indicators are of ionic character, they can affect charge transport through the electrolyte diode. Their mobility in the gel is, however, significantly decreased due to (i) larger molecule comparing to other ions present in the system (H^+, OH^-, K^+ and Cl^-), (ii) spatial limitations of the gel matrix and (iii) possible interactions with polymer chains. Experimental and modelling study on the decrease of the effective diffusivity of ions in PVA hydrogel has been published recently [10]. In our experiments the addition of an acid–base indicator at higher concentrations generally increases the conductivity of the gel especially in the closed mode, nevertheless, the diode-like UI characteristics is qualitatively retained as it can be seen in Fig. 9 for the pure diode and the diode with addition of thymol blue in the PVA gel (using Device A).

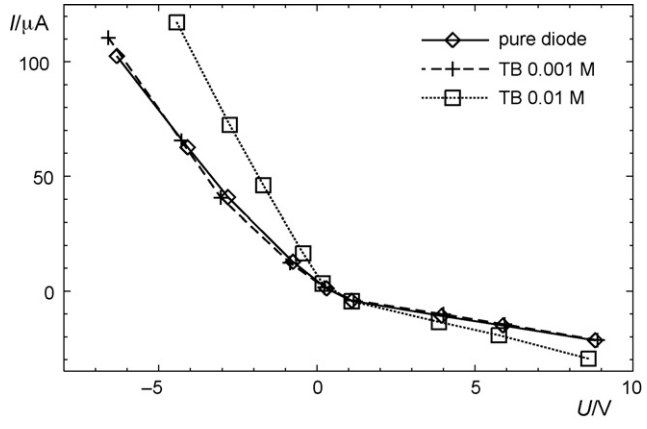

Fig. 9. The current-voltage characteristics of the electrolyte diode with addition of thymol blue (TB).

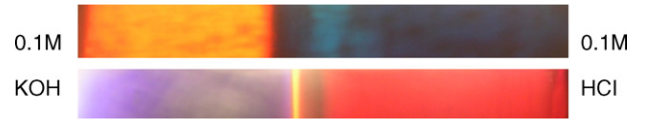

Fig. 10. Position of the acid–base boundary visualized by congo red and thymol blue (the upper and bottom image, respectively) when no external electric field is applied to the system. The images have been converted to the greyscale with enhanced contrast for printed edition, to see original colours please cf. the on-line edition.

4.4. Experimental observations

First set of experiments with the electrolyte diode (Device A) with acid–base indicators has been carried out without the external electric field ($U = 0$ V). Under this condition, the pH profile in the permeation layer of the electrolyte diode is similar to that in the closed mode as the acid–base boundary (the zone with significant change of pH and other variables) is rather narrow (cf. Fig. 3i, m, and r). The acid–base boundary can be found left from the center of the diode, closer to the reservoir with the alkaline electrolyte. This is caused by different mobility of H^+ and OH^- ions. Experimental results confirm this prediction: both with congo red as well as with thymol blue the colour change corresponding to the change of pH can be found left to the center of the diode closer to the inlet of the alkaline electrolyte (cf. Figs. 3i and 10).

When a negative potential difference is applied, i.e., the diode works in the open mode, the zone of the bright colour (corresponding to the pH between 2 and 9 in the case of thymol blue) expands according to the predictions of the model (cf. Figs. 3a, e and 11), the only difference is the disappearance of the red-coloured zone at higher voltages (−10 V in Fig. 11).

When positive potential difference is applied, i.e., when the diode goes to the closed mode, the colours change as it can be seen in Fig. 12. While in simulations of the pure diode (without addition of indicators) the position of the acid–base boundary almost does not change, in experiments (here shown for thymol blue) the bright zone (yellow in reality) corresponding to the zone between pH values 2 and 9 approximately is moving to the left and also it is broadening. The left dark field (cf. Fig. 12, bottom, blue in reality) disappears for voltages above 1.9 V.

Fig. 11. Experimental results for negative external potential difference (i.e., the diode in the open mode) for thymol blue in Agar gel. For potential difference −5 V the left dark field marks the area of pH above 9, the lighter central part (yellow in reality) denotes the area with pH value between 9 and 2 approximately, the dark right border of the image (red in reality) denotes pH below 2. When the external potential difference U has been set to −10 V, the red-coloured area disappeared. The images have been converted to the greyscale with enhanced contrast for printed edition, to see original colours please cf. the on-line edition.

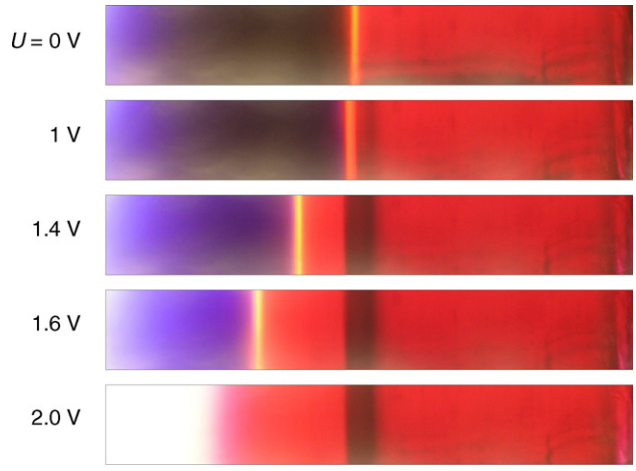

Fig. 12. Experimental results for increasing external potential difference (i.e., shifting the diode into the closed mode) for thymol blue in Agar gel. The acid–base boundary (represented by the bright strip between the two dark fields) is shifted to the left. The images have been converted to the greyscale with enhanced contrast for printed edition, to see original colours please cf. the on-line edition.

The results of the experiments with the acid–base indicator both in the closed and open mode suggest that the acid–base transient zone (between pH values 2 and 9 approximately) is shifted out of the permeation layer at higher potential differences. The explanation of this behaviour is not easy as it is a result of complex interactions of several processes. One effect which should be taken into account are the acid base equilibria of the indicator. In the case of thymol blue, up to five different forms of the indicator can be found, according to Kolthoff et al. [11]: the blue form I^{2-}, yellow or colourless forms HI^{-} and H_2I (two different conformations), and the red form H_3I^{+} (cf. Fig. 13). When external potential difference is applied, ionic forms of the indicator migrate according to their charge. They can change their charges when entering the zone of different pH and also they can be washed out of the permeation layer when they reach the border of the permeation layer. Another effect which should be considered is possible different diffusivity of different ionic forms in the permeation layer, as well as possible interactions of the ionic forms with the gel (e.g., with ionic groups of the opposite charge fixed in the gel structure).

At low external potential differences (in absolute values, up to 1 V in the closed mode and up to 5 V in the open mode) the correspondence of the experimental results with the model predictions is quite good.

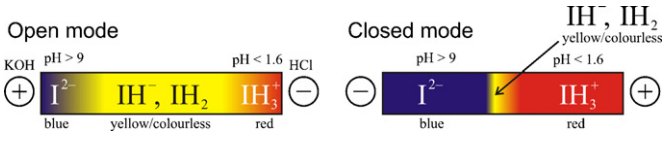

Fig. 13. Ionic forms of the thymol blue in the permeation layer. The images have been converted to the greyscale with enhanced contrast for printed edition, to see original colours please cf. the on-line edition.

5. Conclusions

We have verified experimentally the existence of steep electric potential and concentration gradients of ionic components around the acid–base boundary in the electrolyte diode. One of the methods used involved the addition of an acid–base indicator into the system. The ionic nature of indicator molecules can affect the behaviour of the electrolyte diode. At low potential differences, formation of a narrow zone with a distinctive change of pH has been observed in the closed mode, in the open mode the acid–base zone broadens as predicted by the mathematical model. At higher values of the external potential difference, the behaviour of the electrolyte diode differs from the predictions of the model (describing the "pure" diode without an acid–base indicator): experiments have shown the movement of the transient acid–base zone to the border or out of the permeation layer. This behaviour is probably caused (i) by participation of indicator particles in charge transport in the permeation layer (the isoelectric focusing can be one of the effects), (ii) by acid–base equilibria of different ionic forms of the indicator, as well as (iii) by interaction of the indicator particles with the gel matrix. The detailed explanation of the influence of the indicator would require additional experimental and modelling studies. We are working on the extension of our recently published [4] non-equilibrium model of the electrolyte diode with mass balances and acid–base equilibria of ionic forms of the acid–base indicator.

Another experimental technique used was the measurement of the electric potential profile in the electrolyte diode. The steep potential change around the acid–base boundary located near the alkaline electrolyte reservoir has been found as predicted in the results of mathematical modelling. The significant advantage of this measurement is the possibility to measure the potential profiles also with higher external voltages (we have successfully tested the external voltages up to 20 V; even higher voltages are possible to use, the problem is formation of bubbles on the working electrodes especially in the open mode, where the current passing through the permeation layer is significantly higher).

The earlier works concentrated on the measurement of overall current-voltage curves. We are trying to explain the behaviour of the systems with more detailed approach, as the advanced microtechnology methods allow us to study the system by direct methods inside. The electrolyte diode is an example of relatively simple microsystem with steep spatial gradients. The methodics developed here can be used for studies of similar microfluidic systems using the external electric field.

In the next work we plan further decrease of dimensions of the electrolyte diode and its integration into a more complex microfluidic device as a functional part.

Acknowledgements

This work has been supported by the Grant Agency of the Czech Republic (Project No. 104/03/D005). Authors also would like to thank to Professor Noszticzius and his colleagues from Technical University in Budapest for inspiration and cooperation.

References

[1] L. Hegedüs, Z. Noszticzius, A. Papp, A.P. Schubert, M. Wittmann, Polarization phenomena in hydrogel membranes. Experimental realization of an "electrolyte diode", ACH Models Chem. 132 (1995) 207–224.

[2] L. Hegedüs, N. Kirschner, M. Wittmann, Z. Noszticzius, Electrolyte transistors: ionic reaction—diffusion systems with amplifying properties, J. Phys. Chem. A 102 (1998) 6491–6497.

[3] L. Hegedüs, N. Kirschner, M. Wittmann, P. Simon, Z. Noszticzius, Nonlinear effects of electrolyte diodes and transistors in a polymer gel medium, CHAOS 9 (1999) 283–297.

[4] J. Lindner, D. Šnita, M. Marek, Modelling of ionic systems with a narrow acid–base boundary, Phys. Chem. Chem. Phys. 4 (2002) 1348–1354.

[5] D. Šnita, M. Pačes, J. Lindner, J. Kosek, M. Marek, Nonlinear behaviour of simple ionic systems in hydrogel in an electric field, Faraday Discuss. 120 (2001) 53–66.

[6] K. Iván, P.L. Simon, M. Wittmann, Z. Noszticzius, D. Šnita, Electrolyte diodes with weak acids and bases. II. Numerical model calculations and experiments, J. Chem. Phys. 123 (2005) 164510.

[7] K. Iván, P.L. Simon, M. Wittmann, Z. Noszticzius, Electrolyte diodes with weak acids and bases. I. Theory and an approximate analytical solution, J. Chem. Phys. 123 (2005) 164509.

[8] J. Lin, Recent development and applications of optical and fiber-optic pH sensors, Trends Anal. Chem. 19 (2000) 541–552.

[9] N.J. Atkin, R.M. Abeysekera, D.H. Chenery, A.W. Robards, Induced changes of polymer organization in a gel of poly(vinyl alcohol) crosslinked by congo red, J. Polym. Sci. – Part B: Polym. Phys. 39 (2001) 1471–1483.

[10] F. Fergg, F.J. Keil, Diffusion and reactions of multicomponent electrolytes in poly(vinylalcohol) hydrogels—modeling and experiment, Chem. Eng. Sci. 56 (2001) 1305–1315.

[11] I.M. Kolthoff, M.K. Chantooni Jr., S. Bhowmik, Acid–base indicator constants in acetonitrile, Anal. Chem. 39 (1967) 315–320.

Transient behavior of an electrolytic diode

Zdeněk Slouka, Michal Přibyl,* Dalimil Šnita and Tomáš Postler

Received 14th May 2007, Accepted 13th July 2007
First published as an Advance Article on the web 3rd August 2007
DOI: 10.1039/b707197c

The transient behavior of an electrolytic diode system was studied. A gel-like electrolytic diode was incorporated in a capillary microfluidic chip. The microfluidic platform guaranteed a constant composition of solutions on the diode boundaries. The current responses of the electrolytic diode to step-like changes of the imposed DC electric voltage were measured. Some of these transients were accompanied by a short-time overshoot of electric current density. In order to explain this phenomenon, a mathematical model of the electrolytic diode system was developed. Dynamical analysis of the model equations confirmed the existence of the electric current overshoots. Because the results of the experimental and the numerical transient studies were quite similar, we have explained the physical meaning of three selected overshoots by means of an analysis of the reaction-transport processes inside the electrolytic diode system. The transient experiments carried out in this study indicate that our physical concept of the electrolytic diode system presented in previous papers is correct.

Introduction

The electrolytic diode system can be considered as an electrochemical analogue to a semiconductor diode due to a similar qualitative behavior. Electrical conductors in the electrolytic diode are formed by water solutions of strong acids and strong bases. The transfer of an electric charge is then mediated by the transport of ionic components. The open and closed modes of the electric diode are realized by appropriate orientation of an imposed external electric field.[1]

In our study, solutions of hydrochloric acid and potassium hydroxide are separated by a thin layer of polyvinyl alcohol (PVA) gel. The ionic species are transported by the diffusion and electromigration mechanisms. The convective transport is suppressed in the gel matrix, Fig. 1a. If a DC voltage is imposed on the system, two qualitatively different regimes of the electrolytic diode are observed. In the open mode, see Fig. 1b, potassium and chloride ions are pumped into the gel and hydrogen and hydroxyl ions are transported out of the system. A solution of potassium chloride with a high value of electrolytic conductivity is formed inside the system. If the orientation of the imposed electric field is reversed, the electrolytic diode switches into the closed mode. Then, hydrogen and hydroxyl ions migrate into the PVA gel. The fast water recombination reaction occurs in the zone where these ions meet. It results in the formation of a very thin water layer that is characterized by an extremely low electrolytic conductivity, Fig. 1c. This zone with a large pH gradient is called as an acid–base boundary.[2]

The first ideas about the electrolytic diode come from the seventies of the last century.[3] The first qualitative experiments were carried out by Schubert *et al.*[4] Experiments with an electrolytic diode system incorporated into the PVA gel was first reported in the nineties.[1] In this experimental arrangement, where cylinder-like and ring-like forms of the PVA gel were used, the authors obtained diode-like current–voltage characteristics. The effects of a fixed electric charge in the PVA gel on the electrolytic diode behavior was also studied.[5] The authors proved that the fixed electric charge has a negative sign. The fixed charge holds the counterions in the gel and thus increases the electric current density in the diode above the values predicted theoretically. The authors also derived an expression for the evaluation of the fixed electric charge concentration in the gel from the slopes of current–voltage characteristics. Polarization curves of a diode-like system where potassium hydroxide and hydrochloric acid were

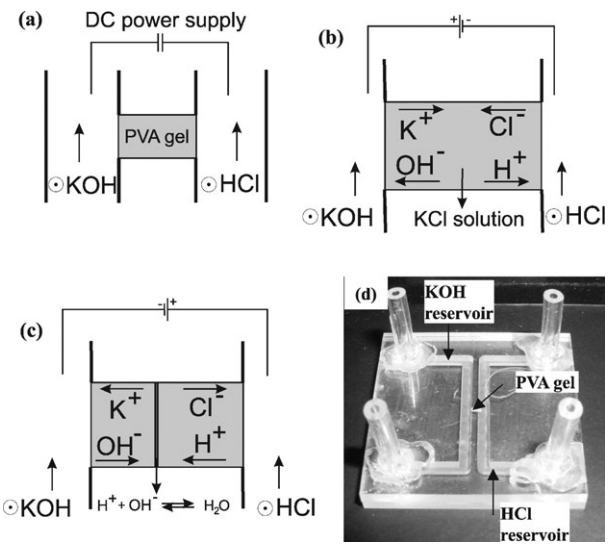

Fig. 1 (a) Scheme of the electrolytic diode, (b) electrolytic diode in the open mode, (c) electrolytic diode in the closed mode, (d) experimental microchip.

Department of Chemical Engineering, Institute of Chemical Technology, Prague, Technická 5, 166 28 Praha 6, Czech Republic. E-mail: pribylm@vscht.cz; Fax: +420 2 2044 4320; Tel: +420 2 2044 3168

replaced by diluted solutions of potassium chloride were also investigated.[6] By the analysis of the polarization curves, the presence of the negative electric charge was again confirmed.

Electrolytic diode systems were theoretically studied in several papers.[2,7,8] In the closed mode, Hegedus *et al.*[7] divided the electrolytic diode system into three regions: acidic, alkaline, and neutral. The reaction-transport processes were modeled separately in each domain. The model was then used for an analysis of the nonlinear effects exhibited by an electrolytic diode system contaminated with potassium chloride. Merkin *et al.*[8] derived a more rigorous model. The ionic electromigration is described by Nernst–Planck equation and the assumption of the local electroneutrality is employed. The results of the numerical analysis verified the existence of the three zones considered in the paper.[7] Snita *et al.*[9] and Lindner *et al.*[2] developed a mathematical model in which the distribution of electric potential is described by Poisson equation. A finite rate of the water dissociation and recombination is also considered. Stationary analysis of the model predicted the existence of large spatial gradients of electric potential, ionic concentrations, and electrolytic conductivity in the closed mode.

Electrochemical transistors have also been studied. Hegedus *et al.*[10] found out that it is impossible to construct an electrochemical analogue of a semi-conductor transistor with the use of ion exchange membranes. However, they developed this analogue by means of electrolytic diodes. In this device, the transistor-like action was observed.

Nonlinear phenomena in electrolytic transistors and diodes were studied experimentally.[7] Excitability and oscillation behavior were found in one type of the transistors. In the electrolytic diode studied, a hysteresis loop in the current–voltage characteristics was obtained when potassium chloride (contaminant) was added into the hydrochlorid acid solution.

An electrolytic diode system with a weak acid (acetic acid) and a weak base (ammonium hydroxide) was investigated experimentally and theoretically by Ivan *et al.*[11,12] This system preserves the diode-like behavior, however, no large gradients of electric potential and ionic concentrations were observed.

In this work, the dynamical behavior of an electrolytic diode is studied. First, the method of fabrication of the electrolytic diode microsystem is described. In the next section, a Poisson–Nernst–Planck mathematical model used in the numerical analysis is derived. The results of the experimental and numerical transient analyses are then compared and discussed. Our findings are summarized in the last section.

Experimental

Gel preparation

The PVA gel was prepared from 1 g of 30% w/w solution of PVA (Fluka, 81381) in water, 0.25 ml of 2% glutardialdehyde (Fluka, 49630) solution in water, 0.5 ml of water and 0.25 ml of 5 M hydrochloric acid. The mixture was pumped into a silicon tube with the internal diameter 500 μm. After gel solidification, the silicon tube was inserted in hexane. When the silicon tube swelled, the PVA gel was pulled out. The remaining acidic groups in the gel matrix were neutralized by 1 M solution of potassium hydroxide. The PVA gel was finally dried in the ambient air.

Microchip fabrication

The electrolytic diode system consisted of two thin polystyrene plates (40 × 40 × 2 mm). A microcapillary (1 mm length, 0.25 mm width, and 0.20 mm depth) connecting two flow-through reservoirs (1.6 mm width, 1 mm depth) was milled on one plate. The dried PVA gel was inserted into the microcapillary. Four holes (2.4 mm diameter) for tubing (Tygon) were drilled in the other plate. The polystyrene plates were precisely aligned and the microchip was assembled by means of temperature bonding. Then, the tubing was glued into the holes by Acrifix 192 (Degussa), Fig. 1d. Finally, two pairs of platinum electrodes were inserted in the microchip.

Experimental procedure

A four-wire remote sensing was used in the experiments. One pair of electrodes (the source electrodes) imposes the DC electric field on the system. The other pair (the sensing electrodes) enables to measure the electric potential drop imposed on the microcapillary. This wiring ensures a precise control of the voltage applied on the electrolytic diode boundaries. The source electrodes were placed in the outlets of the reservoirs. The pair of sensing electrodes was inserted in the reservoir inlets. In this arrangement, the products of electrochemical reactions (*e.g.*, bubbles) were continuously washed away. Hence the electrode processes did not affect the behavior of the electrolytic diode system. Keithey 2400 was used as a source unit.

Solutions of 0.1 M potassium hydroxide and 0.1 M hydrochloric acid were continuously dosed into the flow-through reservoirs by a peristaltic pump (Ismatec). The flow rate was set to 0.25 ml min^{-1} in order to ensure constant conditions on the boundaries of the PVA gel.

For selected sequences of the applied voltage, the dynamical responses represented by the electric current passing through the electrolytic diode system were recorded.

Mathematical model and numerical analysis

The mathematical model describes reaction-transport processes in a long and thin microcapillary (Fig. 2). In such an effectively one-dimensional system, the molar balances of ionic

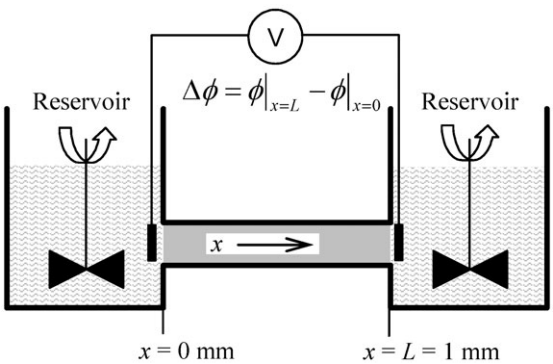

Fig. 2 Scheme of the reaction system described by the mathematical model. L is the length of the gel matrix.

components can be written as

$$\frac{\partial c_n}{\partial \tau} = -\frac{\partial j_n}{\partial x} + r_n, \quad n = \mathrm{H^+}, \mathrm{OH^-}, \mathrm{K^+}, \mathrm{Cl^-} \qquad (1)$$

where c_n, j_n, and r_n are the molar concentrations, the molar fluxes, and the source terms of the ionic species, respectively. The symbols τ and x denote time and the spatial coordinate, respectively. Only four ions are considered in the electrolytic diode system: potassium and hydrogen cations and chloride and hydroxyl anions. Potassium and chloride ions are not involved in any chemical reaction. Hydrogen and hydroxyl ions are consumed and produced in the water recombination and dissociation reactions. The source terms are expressed by eqn (2)

$$r_{\mathrm{H^+}} = r_{\mathrm{OH^-}} = k_w(K_w - c_{\mathrm{H^+}} c_{\mathrm{OH^-}}), \quad r_{\mathrm{K^+}} = r_{\mathrm{Cl^-}} = 0, \qquad (2)$$

where k_w and K_w are the kinetic and the equilibrium constants of the water recombination, respectively. The molar flux of the ionic components in a dilute water solution is given by the Nernst–Planck equation

$$j_n = -D_n\left(\frac{\partial c_n}{\partial x} + \frac{z_n F}{RT} c_n \frac{\partial \phi}{\partial x}\right), \quad n = \mathrm{H^+}, \mathrm{OH^-}, \mathrm{K^+}, \mathrm{Cl^-} \qquad (3)$$

where ϕ is electric potential. The symbols D_n, z_n, c_n, F, R, T denote the ionic diffusivities, the ionic charge numbers, the ionic molar concentrations, Faraday's constant, the molar gas constant, and temperature, respectively. Temperature was assumed to be a constant.

The distribution of electric potential in a medium with a spatially homogeneous dielectric constant can be computed from Poisson's equation

$$\frac{\partial^2 \phi}{\partial x^2} = -F \sum_n z_n c_n/(\varepsilon_0 \varepsilon_r), \quad n = \mathrm{H^+}, \mathrm{OH^-}, \mathrm{K^+}, \mathrm{Cl^-} \qquad (4)$$

where ε_0 and ε_r are the vacuum permittivity and the dielectric constant of the environment, respectively.

Dirichlet's boundary conditions for the ionic concentrations and electric potential were used

$$\begin{gathered} c_{\mathrm{K^+}}|_{x=0} = 0.1 \text{ kmol m}^{-3}, \quad c_{\mathrm{K^+}}|_{x=L} = 0 \text{ kmol m}^{-3}, \\ c_{\mathrm{Cl^-}}|_{x=0} = 0 \text{ kmol m}^{-3}, \quad c_{\mathrm{Cl^-}}|_{x=L} = 0.1 \text{ kmol m}^{-3}, \\ \phi|_{x=0} = 0\,\mathrm{V}, \quad \Delta\phi = \phi|_{x=L} - \phi|_{x=0}. \end{gathered} \qquad (5)$$

Here $\Delta\phi$ is the electric potential difference imposed on the electrolytic diode, see Fig. 2. $\Delta\phi$ is related to the zero reference value on the left boundary ($x = 0$ mm). Hence for $\Delta\phi < 0$ V and $\Delta\phi > 0$ V, the electrolytic diode is in the open and closed mode, respectively. This convention is kept through the entire text. Potassium hydroxide ($c_{\mathrm{KOH}} = 0.1$ kmol m^{-3}) and hydrochloric acid ($c_{\mathrm{HCl}} = 0.1$ kmol m^{-3}) were assumed to be on the left and on the right boundary ($x = L$), respectively. Because the electroneutrality condition and the water equilibrium should be satisfied there, the molar concentrations of hydroxyl and hydrogen ions on the boundaries were computed with the use of eqn (6) and (7)

$$0 = \sum_n z_n c_n, \; n = \mathrm{H^+}, \mathrm{OH^-}, \mathrm{K^+}, \mathrm{Cl^-} \qquad (6)$$

$$K_w = c_{\mathrm{H^+}} c_{\mathrm{OH^-}}. \qquad (7)$$

Table 1 Model parameters

Parameter	Description	Value
$D_{\mathrm{Cl^-}}$/m^2 s^{-1}	Diffusivity of chloride ions	2.03×10^{-9}
$D_{\mathrm{H^+}}$/m^2 s^{-1}	Diffusivity of hydrogen ions	9.31×10^{-9}
$D_{\mathrm{K^+}}$/m^2 s^{-1}	Diffusivity of potassium ions	1.96×10^{-9}
$D_{\mathrm{OH^-}}$/m^2 s^{-1}	Diffusivity of hydroxyl ions	5.28×10^{-9}
F/C mol^{-1}	Faraday's constant	9.6487×10^4
k_w/m^3 mol^{-1} s^{-1}	Kinetic constant of water recombination	1.3×10^8
K_w/mol^2 m^{-6}	Ionic product of water	1×10^{-8}
L/mm	microcapillary length	1
R/J mol^{-1} K^{-1}	Molar gas constant	8.314
T/K	Temperature	298
$Z_{\mathrm{Cl^-}}$	Charge number of chloride ions	-1
$Z_{\mathrm{H^+}}$	Charge number of hydrogen ions	1
$Z_{\mathrm{K^+}}$	Charge number of potassium ions	1
$Z_{\mathrm{OH^-}}$	Charge number of hydroxyl ions	-1
ε_0/F m^{-1}	Vacuum permittivity	8.854×10^{-12}
ε_r	Water dielectric constant	78.5

The values of the model parameters are summarized in Table 1.

The numerical analysis of the mathematical model, eqn (1)–(5), was carried out by means of an algorithm that combines the standard Femlab procedures[13] and a recently developed empirical procedure for dynamical adaptation of a nonequidistant mesh based on the estimation of transport times.[14] The Femlab procedures employ the finite element method for the space discretization. The Lagrange quadratic elements were used in this study. The standard Femlab solver *daspk*[15] designed for the dynamical analysis of large systems of stiff differential-algebraic equations was employed. The *daspk* solver is based on the use of the backward differentiation formulae. The dynamical meshing method expands a dense mesh in the neighborhoods of localized large gradients of concentrations and electric potential, and estimates the mesh adaptation interval. The size of the neighborhoods and the re-meshing intervals are dynamically controlled.

Results and discussion

Two types of experiments were carried out. The first one, called *transients closed → open mode*, was realized in the following way: the electrolytic diode system was first kept in the steady state ($\Delta\phi = 0$ V) for 300 s. Then, the system was quickly switched to the closed mode ($\Delta\phi = 10$ V) by the step-like manner and, subsequently, the sequence of the electric potential differences was applied: 8, 6, 4, 2, 0, −2, −4, −6, −8, −10 V. Each voltage was imposed for 300 s. During the entire experiment, the electric current was measured.

In the experiments called *transients open → closed mode*, the electrolytic diode system was first kept in the steady state ($\Delta\phi = 0$ V) for 300 s. Then, the system was quickly switched to the open mode ($\Delta\phi = -10$ V) and the sequence of the electric potential difference was applied: −8, −6, −4, −2, 0, 2, 4, 6, 8, 10 V.

The numerical analysis was carried out identically to the experiments. The quick voltage changes were realized by a linear decrease or increase of the voltage applied on the right

boundary of the computational domain. The duration of the voltage change was set to 0.1 s.

Transients closed → open mode

Current–voltage characteristics. The computed and the experimentally measured current responses are plotted in Fig. 3a and 3b, respectively. The values of the electric current density are close to zero in the closed mode (300 s $< t <$ 1800 s) because potassium and chloride ions are pumped out of the PVA gel and the recombination reaction between hydrogen and hydroxyl ions forms a thin region with an extremely low electrolytic conductivity. The initial switch from $\Delta\phi = 0$ to 10 V is accompanied by a rapid and a short-time (few seconds) increase in the electric current density.

As the electrolytic diode switches to the open mode ($t >$ 2100 s), potassium and chloride ions are pumped into the gel, electrolytic conductivity is high everywhere, and the electric current density increases (in absolute values) with the growing difference of the electric potential $|\Delta\phi|$ according to Ohm's law.

The corresponding current–voltage characteristics are plotted in Fig. 3d and 3e. These dependencies are similar to those obtained by the stationary analysis[2] except for the initial transient.

The values of the electric current density obtained by numerical simulation are approximately by one order of magnitude higher than those experimentally measured. In the simulations, the ionic diffusivities in water were considered. However, the effective ionic diffusivities in the PVA gel are smaller than those in water due to a high gel density. This density is given by the composition of the gel and by the gel preparation procedure. The prepared shrunken gel inserted into the microcapillary swells but the degree of the swelling is limited by the microcapilary dimensions. It is probably the main reason of the observed discrepancy.

The electric current density i is computed from equation

$$i = F\sum_n z_n j_n, \quad n = \mathrm{H^+}, \mathrm{OH^-}, \mathrm{K^+}, \mathrm{Cl^-} \tag{8}$$

where the intensity of molar flux j_n is linearly proportional to the ionic diffusivity according to eqn (3). In a rough approximation, it can be assumed that the ratio of the diffusivities in water and in the PVA gel is the same for all considered ions

$$k = D_n^{\mathrm{W}}/D_n^{\mathrm{PVA}}, \quad n = \mathrm{H^+}, \mathrm{OH^-}, \mathrm{K^+}, \mathrm{Cl^-} \tag{9}$$

where k is the proportionality constant. Then, the electric current density in the PVA gel, i^{PVA}, can be estimated from

$$i^{\mathrm{PVA}} = i^{\mathrm{W}}/k, \tag{10}$$

where i^{W} is the electric current density in water.

The proportionality constant was evaluated by fitting the numerically obtained current responses to the experimental data together for the *closed → open mode transients* and the *open → closed transients*. It was determined that k is approximately equal to 14.9.

In the next step, the current response was again computed for the diffusivities calculated by means of eqn (9). The corresponding transients and the current–voltage characteristics are shown in Fig. 3c and 3f. The time courses of the electric current density in Fig. 3b and 3c are in a good qualitative and quantitative agreement. The current–voltage characteristics plotted in Fig. 3e and 3f are also similar.

Transient response $\Delta\phi$ = 0 V → 10 V. The transient response of the electrolytic diode system at t = 300 s was

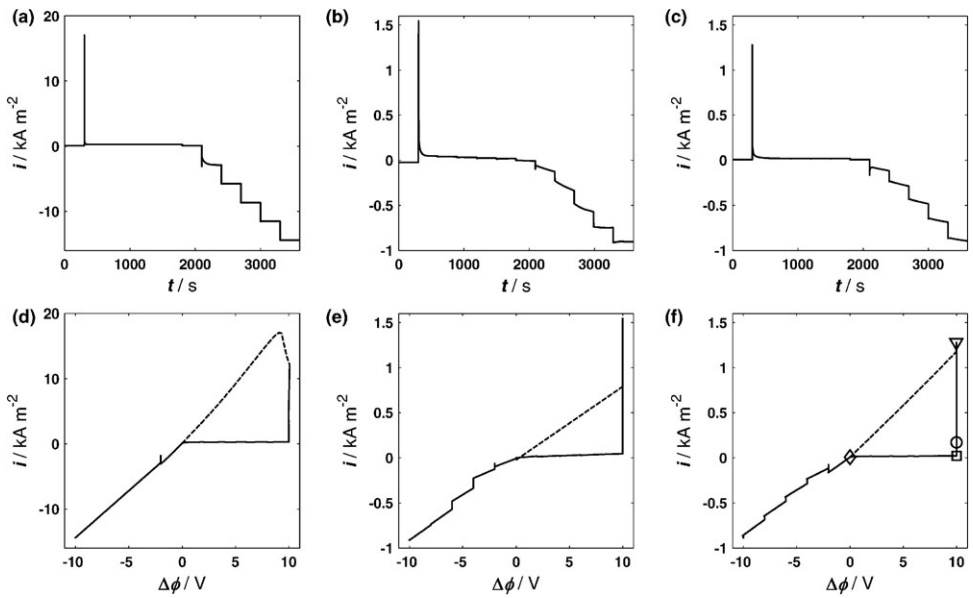

Fig. 3 *Transients closed → open mode.* (a) The computed electric current density transient with the ionic diffusivities for water, (b) the measured electric current density transient, (c) the computed electric current density transient with the adjusted ionic diffusivities (k = 14.9), (d) the computed current–voltage characteristics with the ionic diffusivities for water, (e) the measured current–voltage characteristics, (f) the computed current–voltage characteristics with the adjusted ionic diffusivities (k = 14.9). The dashed lines in (d)–(f) represent the initial transient from the steady state ($\Delta\phi$ = 0 V) to the closed mode ($\Delta\phi$ = 10 V). The diamond, triangle, circle, and square in (f) correspond to the states of the electrolytic diode system at t = 300, 300.5, 305.1 and 600.1 s, respectively.

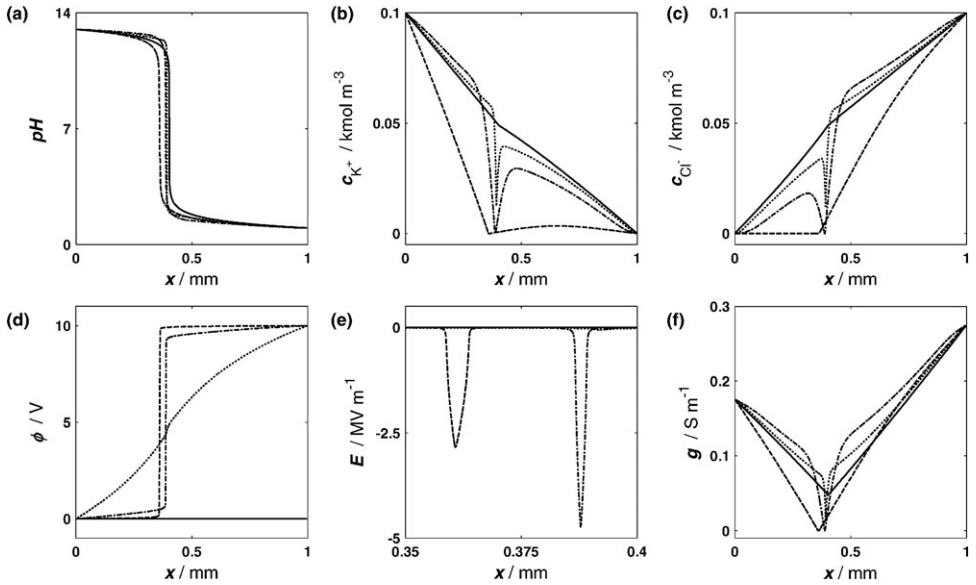

Fig. 4 Analysis of the initial transient from the steady state $\Delta\phi = 0$ V to the closed mode $\Delta\phi = 10$ V. The spatial profiles of: (a) pH value, (b) concentration of potassium ions, (c) concentration of chloride ions, (d) electric potential, (e) electric field intensity, and (f) electrolytic conductivity are plotted. The solid, dotted, dash-dotted, and dashed lines correspond to the profiles at $t = 300$, 300.5, 305.1 and 600.1 s, respectively.

analyzed in detail. The system is in the steady state ($\Delta\phi = 0$ V) before the sudden change of the imposed difference of electric potential to $\Delta\phi = 10$ V. The steady state[2] can be characterized by: (i) a localized pH gradient; (ii) high concentrations of potassium and chloride ions; (iii) flat profiles of electric potential and electric field intensity E;

$$E = -\frac{\partial\phi}{\partial x}, \qquad (11)$$

and (iv) a relatively high value of the electrolytic conductivity, g, everywhere in the PVA gel (see the solid line in Fig. 4)

$$g = F^2 \sum_n z_n^2 D_n c_n/(RT).\ n = \mathrm{H^+}, \mathrm{OH^-}, \mathrm{K^+}, \mathrm{Cl^-} \qquad (12)$$

As the difference of electric potential is switched to $\Delta\phi = 10$ V, the electric current density quickly increases according to Ohm's law (dashed line in Fig. 3e and 3f). At the same time, the ions with higher electric mobilities (H^+ and OH^-) are intensively pumped into the central part of the gel where they form water (dotted line in Fig. 4). The water region is characterized by a low value of electrolytic conductivity. In this region, the imposed electric field attains the maximal intensity in order to satisfy Kirchoff's current law. It substantially enhances the coulombic force acting on the ions with the lower electric mobilities (K^+ and Cl^-). These ions are then intensively pumped out of the water region where local minima of electrolytic conductivity and concentrations of the bigger ions are observed (dash-dotted line in Fig. 4). As the concentrations of potassium and chloride ions decrease in the gel, the electric current density returns to a value close to zero (Fig. 3f). At time 600.1 s, the electrolytic diode system almost attains a new steady state with (i) a localized maximum of electric field intensity $|E| \approx 2.5$ MV m^{-1} and (ii) a minimum of electrolytic conductivity (the dashed line in Fig. 4).

Transients open → closed mode

Current–voltage characteristics. The computed and the experimentally measured current responses are plotted in Fig. 5a,b. In the open mode, the electric current density is directly proportional to the applied voltage difference, Fig. 5d–e. However, the initial transient ($\Delta\phi = 0$ V → −10 V) is accompanied by a temporal overshoot of electric current density. In absolute values, the electric current density firstly increases, then decreases for about 5 s and, finally, again increases. This response of the electrolytic diode system was repeatedly observed in the experiments and also verified by the numerical analysis (Fig. 5a,b and 5d–e).

When $\Delta\phi$ was altered from 0 V to 2 V, *i.e.*, the system was switched to the closed mode, a significant temporal increase of the electric current density was recorded.

Because the values of the electric current density obtained experimentally and numerically differ by more than one order of magnitude, a new transient response and a current–voltage characteristics were computed (Fig. 5c, 5f). Before the computation, the ionic diffusivities were modified according to eqn (9) with $k = 14.9$. The obtained time course of electric current density (Fig. 5c) is quite similar to the experimental one (Fig. 5b). However, if the applied difference of electric potential was equal to −10, −8, −6 V, the computed values of the electric current density do not reach the experimental ones (in absolute values). One of the possible explanations of this phenomenon can be based on the fact that the effect of the Stokes's radii was not taken into account in eqn (9). The decrease in the effective diffusivities in a porous matrix is more significant for the bigger ions (K^+ and Cl^-) than for the smaller ones (H^+ and OH^-).[16] Hence, the effective diffusivities in the PVA gel should individually be found for each ionic component. Unfortunately, one transient computation, *e.g.*, construction of Fig. 5, usually takes more than one day.

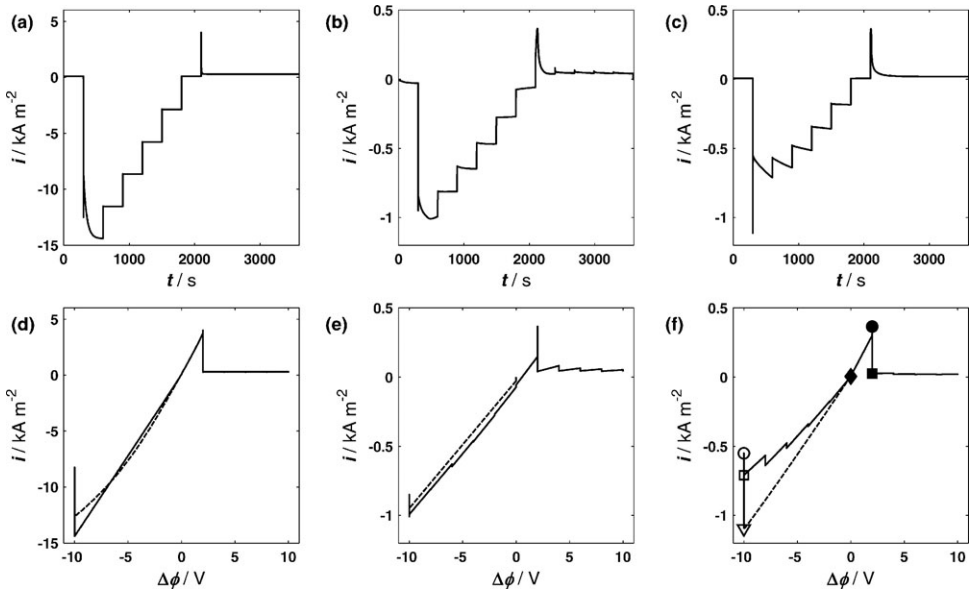

Fig. 5 *Transients open → closed mode.* (a) The computed electric current density transients with the ionic diffusivities for water, (b) the measured electric current density transient, (c) the computed electric current density transient with the adjusted ionic diffusivities ($k = 14.9$), (d) the computed current–voltage characteristics with the ionic diffusivities for water, (e) the measured current–voltage characteristics, (f) the computed current–voltage characteristics with the adjusted ionic diffusivities ($k = 14.9$). The dashed lines in (d)–(f) represent the initial transient from the steady state ($\Delta\phi = 0$ V) to the open mode ($\Delta\phi = -10$ V). The filled diamond, empty triangle, empty circle, and empty square in (f) correspond to the states of the electrolytic diode system at $t = 300$, 300.1, 305.2 and 600.1 s, respectively ($\Delta\phi = 0$ V → -10 V). The filled diamond, filled circle, and filled square in (f) correspond to the states of the system at $t = 1800.6$–2100.6, 2109.1 and 2400.7 s, respectively ($\Delta\phi = 0$ V → 2 V).

A possible presence of the fixed electric charge in the PVA gel can be the other reason for the observed discrepancy. Ivan *et al.*[6] found that the volume concentration of the bound negative electric charge in a PVA gel (30% w/w) is about 1×10^{-3} kmol m^{-3}. Because no electric charge should be fixed in a pure PVA gel, it has to be brought in the matrix by ionic contaminants such as carboxylic groups. The presence of the fixed charge results in (i) a significant change of ionic distributions and in (ii) the electroosmotic transport of the electrolyte. Both these effects can substantially vary the ionic fluxes, and thus, the observed values of electric current density.

The two remarkable dynamical responses of the electrolytic diode will be analyzed in the next section: (i) $\Delta\phi = 0$ V → -10 V, and (ii) $\Delta\phi = 0$ V → 2 V.

Transient response $\Delta\phi = 0$ V → -10 V. Spatial profiles of the dependent variables were computed for selected points (depicted by symbols in Fig. 5f) on the current–voltage characteristics. The initial steady state ($\Delta\phi = 0$ V) is represented by the solid line in Fig. 6. The electrolytic conductivity is high everywhere in the system. Hence immediately after the sudden change of the imposed difference of electric potential (dotted line in Fig. 6), the electric current density increases according to Ohm's law (in absolute values). Hydrogen and hydroxyl ions are intensively transported out of the PVA gel. A region with a pH value close to 7 is formed in the central part of the gel (dash-dotted line in Fig. 6a). It means that this region contains a solution of potassium chloride in water. Potassium and chloride ions are intensively transported by the electromigration mechanism into the PVA gel, however, the electroneutrality condition should be satisfied everywhere, eqn (6). In the central part of the gel, the chloride ions are exclusively equilibrated by potassium ions (dash-dotted line in Fig. 6b,c). As the bigger ions (K^+ and Cl^-) are transported more slowly into the gel than the smaller ions (H^+ and OH^-) out of the gel, electrolytic conductivity decreases on average (dash-dotted line in Fig. 6f), which results in a temporal decrease of the electric current density (in absolute values). The bigger ions are then gradually pumped into the gel. Thus the electrolytic conductivity and electric current density again increase (dashed line in Fig. 6). Finally, the system slowly approaches a steady state that is characterized by an almost linear profile of the electric potential, *i.e.*, the electric field intensity is approximately constant within the gel.

Transient response $\Delta\phi = 0$ V → 2 V. In the current–voltage characteristics, this transient looks similar to the transient $\Delta\phi = 0$ V → 10 V. However, now the transient does not start from the steady state. At $t = 1800.6$ s, the electrolytic diode system is switched from the open mode to the state without any imposed difference of the electric potential: $\Delta\phi = -2$ V → 0 V. Immediatelly after this switch, the state of the system is characterized by the solid line in Fig. 7, *i.e.*, (i) the neutral pH value is in the gel centre, (ii) the concentrations of the bigger ions are high everywhere except in the boundary regions, (iii) the profiles of the electric potential and electric field intensity are flat, and (iv) the electrolytic conductivity is relatively high and uniform in the system. After the next 300 s ($t = 2100.6$ s), the concentrations of potassium and chloride ions and the electrolytic conductivity still remain high in the system due to slow diffusion transport of the bigger ions out of the gel

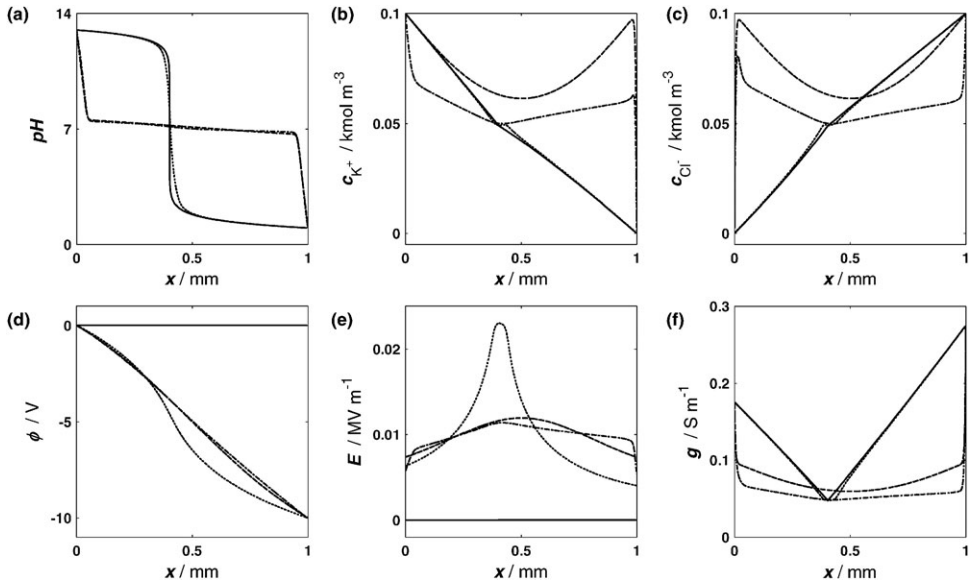

Fig. 6 Analysis of the initial transient from the steady state $\Delta\phi = 0$ V to the open mode $\Delta\phi = -10$ V. The spatial profiles of: (a) pH value, (b) concentration of potassium ions, (c) concentration of chloride ions, (d) electric potential, (e) electric field intensity, and (f) electrolytic conductivity are plotted. The solid, dotted, dash-dotted, and dashed lines correspond to the profiles at $t = 300$, 300.1, 305.2 and 600.1 s, respectively.

(dotted line in Fig. 7). The other characteristics are almost identical to those in the steady state ($\Delta\phi = 0$ V).

As the imposed difference of the electric potential is switched to 2 V, the electric current density temporally increases according to Ohm's law (dash-dotted line in Fig. 7). Hydrogen and hydroxyl ions are transported into the PVA gel. Close to the gel centre, a water region with a low electric conductivity is formed. The bigger ions are transported out of the electrolytic diode. As the electromigration flux of these ions is highest in the water region due to a locally growing electric field intensity, two maxima and one minimum are then observed on their concentration profiles (dash-dotted line in Fig. 7b,c). The temporal accumulation of the bigger ions in the non-water regions results in a local increase of potassium and chloride concentrations above those on the boundaries. The concentrations of potassium and chloride ions then gradually decrease, the electrolytic conductivity approaches a zero value in the water region and a local maximum of the electric field intensity (in absolute values) is observed there. These processes lead to closing the electrolytic diode.

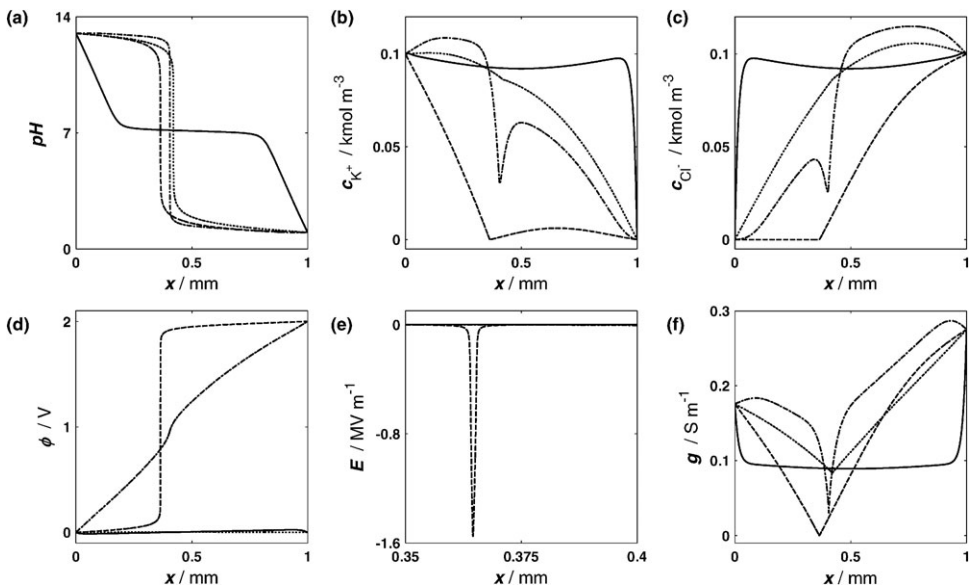

Fig. 7 Analysis of the transient from the $\Delta\phi = 0$ to 2 V. The spatial profiles of: (a) pH value, (b) concentration of potassium ions, (c) concentration of chloride ions, (d) electric potential, (e) electric field intensity, and (f) electrolytic conductivity are plotted. The solid, dotted, dash-dotted, and dashed lines correspond to the profiles at $t = 1800.6$, 2100.6, 2109.1 and 2400.7 s, respectively.

Conclusions

The developed microfluidic format of the electrolytic diode enables to carry out reproducible transient experiments with well-defined boundary conditions. We have found that some of the experimentally observed dynamical responses to a step-like change of the imposed difference of the electric potential are accompanied by short-time overshoots of the electric current density. In order to explain this effect, we have used the Poisson–Nernst–Planck mathematical model[2,9] to describe the reaction-transport processes in the electrolytic diode. Because the transients are accompanied by extremely large moving gradients of the ionic concentrations and the electric potential, an adaptive mesh algorithm for the numerical analysis of the model equations had to be employed.[14] The dynamical analysis of the model proved the existence of these short-time overshoots of the electric current density. The computed and measured transients were qualitatively comparable. However, the values of the electric current density obtained experimentally were about one order of magnitude smaller than those given by the mathematical model. We have suggested that this phenomenon is caused by smaller values of the ionic diffusivities in the used PVA gel than those in water environment. Hence, we indirectly estimated the diffusivities in the PVA gel from comparison of the experimental and numerical data. Then, we recalculated the time courses. It was found out that the recomputed transients from the closed to the open mode fit qualitatively and also quantitatively the experimental data. The recalculated time course of the transients from the open to closed mode is in good qualitative agreement with the experimental data, however, the absolute values differ. We have proposed two possible explanations of this discrepancy: (i) the decrease of ionic diffusivities in a porous matrix depends on the particular Stokes radius of an ion, (ii) the presence of a fixed electric charge in the PVA gel.

The mathematical model was then used as a tool for the explanation of the short-time overshoots of the electric current density. The origin of the overshoots is a result of the reaction-transport processes such as: (i) the formation of a thin water region by the water recombination reaction, Fig. 4 and 7, (ii) the intensive electromigration transport of the hydrogen and hydroxyl ions tightly bound up with the ionic distributions of the bigger ions *via* the Poisson equation. This can lead to a temporary decrease in the electrolytic conductivity in the entire gel medium, Fig. 6, or a short-time accumulation of the bigger ions in the certain regions, Fig. 7.

As the computed transients agree with experiments, we expect that the development of the concentration and potential fields depicted in Fig. 4, 6 and 7 will be very close to reality. Moreover, the performed transient analysis proved the stability of the steady states that had been predicted earlier by a stationary numerical analysis of the electrolytic diode model.[2]

Our findings thus expand the knowledge on the electrolytic diode systems, especially on the transient behavior. Because the electrolytes and ions are often transported by an external electric field in a variety of microfluidic and related applications such as electrokinetic addressing and dosing,[17] electro-osmotically driven bioassays,[18] fuel cells[19,20] or other membrane processes,[21] the results and methodologies of the transient analysis can be possibly exploited there.

Acknowledgements

The authors are thankful for support by the Ministry of Education, Youth and Sports of the Czech Republic, Grant No. MSM 6046137306 and the Ministry of Industry and Trade of the Czech Republic, Grant No. Pokrok 1H-PK/24.

References

1 L. Hegedus, Z. Noszticzius, A. Papp, A. P. Schubert and M. Wittmann, *ACH Models Chem.*, 1995, **132**, 207–224.
2 J. Lindner, D. Snita and M. Marek, *Phys. Chem. Chem. Phys.*, 2002, **4**, 1348–1354.
3 Z. Noszticzius and A. Schubert, *Periodica Polytechnica Ser. Chem. Eng.*, 1973, **17**, 165–177.
4 A. Schubert and Z. Noszticzius, *Periodica Polytechnica Ser. Mech. Eng.*, 1977, **21**, 279–283.
5 L. Hegedus, M. Wittmann, N. Kirschner and Z. Noszticzius, *Prog. Colloid Polym. Sci.*, 1996, **102**, 101–109.
6 K. Ivan, N. Kirschner, M. Wittmann, P. L. Simon, V. Jakab, Z. Noszticzius, J. H. Merkin and S. K. Scott, *Phys. Chem. Chem. Phys.*, 2002, **4**, 1339–1347.
7 L. Hegedus, N. Kirschner, M. Wittmann, P. Simon, Z. Noszticzius, T. Amemiya, T. Ohmori and T. Yamaguchi, *Chaos*, 1999, **9**, 283–297.
8 J. H. Merkin, P. L. Simon and Z. Noszticzius, *J. Math. Chem.*, 2000, **28**, 43–58.
9 D. Snita, M. Paces, J. Lindner, J. Kosek and M. Marek, *Faraday Discuss.*, 2001, **120**, 53–66.
10 L. Hegedus, N. Kirschner, M. Wittmann and Z. Noszticzius, *J. Phys. Chem. A*, 1998, **102**, 6491–6497.
11 K. Ivan, P. L. Simon, M. Wittmann and Z. Noszticzius, *J. Chem. Phys.*, 2005, **123**, 164509.
12 K. Ivan, M. Wittmann, P. L. Simon, Z. Noszticzius and D. Snita, *J. Chem. Phys.*, 2005, **123**, 164510.
13 *Femlab 2.3, Reference manual*, Comsol AB, Stockholm, 2002.
14 M. Pribyl, D. Snita and M. Kubicek, *Comput. Chem. Eng.*, 2006, **30**, 674–685.
15 P. N. Brown, A. C. Hindmarsh and L. R. Petzold, *Siam J. Sci. Comput.*, 1994, **15**, 1467–1488.
16 W. Y. Gu, H. Yao, A. L. Vega and D. Flagler, *Ann. Biomed. Eng.*, 2004, **32**, 1710–1717.
17 M. Pribyl, D. Snita and M. Marek, *Chem. Eng. J.*, 2005, **105**, 99–109.
18 M. Pribyl, V. Knapkova, D. Snita and M. Marek, *Microelectron. Eng.*, 2006, **83**, 1660–1663.
19 P. R. Pathapati, X. Xue and J. Tang, *Renewable Energy*, 2004, **30**, 1–22.
20 R. M. Rao and R. Rengaswamy, *Chem. Eng. Sci.*, 2006, **61**, 7393–7409.
21 P. Sistat and G. Pourcelly, *J. Membr. Sci.*, 1997, **123**, 121–131.

Study on surface properties of PDMS microfluidic chips treated with albumin

Walter Schrott, Zdeněk Slouka, Petr Červenka, Jiří Ston, Marek Nebyla, Michal Přibyl, and Dalimil Šnita

Citation: Biomicrofluidics **3**, 044101 (2009); doi: 10.1063/1.3243913
View online: http://dx.doi.org/10.1063/1.3243913
View Table of Contents: http://scitation.aip.org/content/aip/journal/bmf/3/4?ver=pdfcov
Published by the AIP Publishing

Study on surface properties of PDMS microfluidic chips treated with albumin

Walter Schrott, Zdeněk Slouka, Petr Červenka, Jiří Ston, Marek Nebyla, Michal Přibyl,[a] and Dalimil Šnita
Department of Chemical Engineering, Institute of Chemical Technology, Prague 16628, Czech Republic

(Received 10 July 2009; accepted 13 September 2009; published online 12 October 2009)

Electrokinetic properties and morphology of PDMS microfluidic chips intended for bioassays are studied. The chips are fabricated by a casting method followed by polymerization bonding. Microchannels are coated with 1% solution of bovine serum albumin (BSA) in Tris buffer. Albumin passively adsorbs on the PDMS surface. Electrokinetic characteristics (electro-osmotic velocity, electro-osmotic mobility, and zeta potential) of the coated PDMS channels are experimentally determined as functions of the electric field strength and the characteristic electrolyte concentration. Atomic force microscopy (AFM) analysis of the surface reveals a "peak and ridge" structure of the protein layer and an imperfect substrate coating. On the basis of the AFM observation, several topologies of the BSA-PDMS surface are proposed. A nonslip mathematical model of the electro-osmotic flow is then numerically analyzed. It is found that the electrokinetic characteristics computed for a channel with the homogeneous distribution of a fixed electric charge do not fit the experimental data. Heterogeneous distribution of the fixed electric charge and the surface roughness is thus taken into account. When a flat PDMS surface with electric charge heterogeneities is considered, the numerical results are in very good agreement with our experimental data. An optimization analysis finally allowed the determination of the surface concentration of the electric charge and the degree of the PDMS surface coating. The obtained findings can be important for correct prediction and possibly for robust control of behavior of electrically driven PDMS microfluidic chips. The proposed method of the electro-osmotic flow analysis at surfaces with a heterogeneous distribution of the surface electric charge can also be exploited in the interpretation of experimental studies dealing with protein-solid phase interactions or substrate coatings. © *2009 American Institute of Physics.* [doi:10.1063/1.3243913]

I. INTRODUCTION

Polydimethylsiloxane (PDMS) is a favorite material for microfluidic chip fabrication due to its properties such as high optical transparency, biocompatibility, or undemanding microfabrication.[1–3] Electro-osmotic flow (EOF) is often employed in PDMS and other microchips for various biomicrofluidic applications.[4] The knowledge of electro-osmotic characteristics is then essential for microchip design and process control.

Electro-osmotic characteristics[5] (electro-osmotic mobility and zeta potential) of PDMS were obtained by many researchers who used various measurement techniques. Current monitoring

[a]Corresponding author Michal Přibyl Institute of Chemical Technology, Prague, Technická 5, 166 28 Praha 6, Czech Republic. Fax:+420 2 2044 4320; Tel: +420 2 2044 3168; E-mail: pribylm@vscht.cz

technique is one of the most exploited;[6–13] however, other techniques such as amperometric detection method,[14] cyclic voltametry,[15] imaging of a caged fluorescent dye,[16,17] and particle tracking technique[18] were also employed.

Data published in the literature differ significantly. This fact results from both various surface treatments of the PDMS chips (oxygen plasma treatment, possible adsorption from an electrolyte, use of coatings) and various compositions of electrolytes (*p*H, concentration). Electro-osmotic mobilities in a native PDMS were reported to be smaller than those where the PDMS surface was oxidized by plasma treatment.[9] The surface properties of the oxidized PDMS change in time as well as the values of the electro-osmotic mobilities that significantly decrease when the treated surface is exposed to air.[9] The electrokinetic characteristics slightly differ if the microchannel PDMS network is sealed against either another PDMS layer or a glass layer.[9,11]

PDMS was also chemically modified to enhance the EOF intensity. For instance, Luo *et al.*[19] added undecylenic acid to the PDMS prepolymer and the EOF mobility rose up to 7.6×10^{-8} $m^2\ V^{-1}\ s^{-1}$. When Vickers *et al.*[15] hydrophilized PDMS by an extraction process followed by air plasma treatment, the EOF mobility increased up to 6.8×10^{-8} $m^2\ V^{-1}\ s^{-1}$. Roman *et al.*[20] fabricated microchips with SiO_2 particles homogeneously distributed within the PDMS polymer matrix having the EOF mobility equal to 8.3×10^{-8} $m^2\ V^{-1}\ s^{-1}$. Choi *et al.*[7] modified the PDMS surface by cetyltrimethylammonium bromide which even reversed the EOF, i.e., changed the fixed electric charge polarity. Bao *et al.*[14] reported the influence of various cations contained in phosphate buffer solutions on the electro-osmotic velocity in a PDMS channel. They also attributed the EOF emergence to the cation and anion adsorption on PDMS walls.

Nonlinear dependences of the electro-osmotic mobility on ionic strength were experimentally obtained by Spehar *et al.*[11] The authors fitted the experimental data with two functions

$$\mu_{EO} = k_1 \log(I) + k_0, \tag{1}$$

$$\mu_{EO} = k_0 + k_1 I^{-0.5}, \tag{2}$$

where μ_{EO} and I are the EOF mobility and the ionic strength, respectively. Equation (1) provided a better fit. The dependence of the electro-osmotic mobility on the ionic strength can be explained by a change of the zeta potential. Kirby *et al.*[21] derived two approximate relations expressing the zeta-potential dependence on ionic strength. The first relation bears the logarithm form and is valid for high values of zeta potentials. The second one follows the inverse square root dependence and is applicable for low values of zeta potentials (up to 25 mV).

Because PDMS microchips find their use in a variety of bioapplications, a few papers were aimed at the electro-osmotic transport of buffers containing biomacromolecules.[6,10,22] These molecules often interact with the PDMS surface due to hydrophobic interactions generally resulting in a decrease of EOF intensity. For instance, the presence of bovine serum albumin (BSA) in transported electrolytes decreased the electro-osmotic velocity in microsystems made from twelve different plastic substrates.[10] Zhou *et al.*[22] evaluated the EOF mobility in a BSA treated PDMS microchannel to be 1.7×10^{-8} $m^2\ V^{-1}\ s^{-1}$. We summarized some available data on the electro-osmotic mobilities in various PDMS devices in Table I.

In this paper, we describe techniques for fabrication of multi-channel microchips from PDMS and methods for determination of their electrokinetic and morphological properties. A non-slip mathematical model of the electro-osmotic flow in a representative part of the microchips is then derived. In the next step, we report experimentally obtained dependencies of the EOF characteristics on the electrolyte concentration and the electric field strength. Finally, the obtained experimental results are confronted with the theoretical ones in the view of the surface concentration of the fixed electric charge and the morphology of the PDMS surface treated by BSA.

TABLE I. Electro-osmotic mobilities in PDMS systems.

Source	PDMS	EOF mobility [$\times 10^{-8}$ m^2 V^{-1} s^{-1}]	Conditions
Spehar[11]	native, reversibly sealed to PDMS	2.3	*N*-(2-acetamido)-2-aminoethanesulfonic acid, *p*H=7.8, *I*=90 mM
Spehar[11]	native, reversibly sealed to glass	2.8	*N*-(2-acetamido)-2-aminoethanesulfonic acid, *p*H=7.8, *I*=90 mM
Ren[9]	native, reversibly sealed to PDMS	1.1	phosphate buffers, *I*=15 mM, *p*H=7
Ren[9]	oxidized, irreversibly sealed to PDMS	3.7	phosphate buffers, *I*=15 mM, *p*H=7
Ocvirk[39]	native, reversibly sealed to PDMS	4.5	1 mM phosphate and 10 mM KCl, *p*H=8
Ocvirk[39]	native, reversibly sealed to PDMS	6.4	1 mM phosphate, 10 mM KCl, 1000 μM sodium dodecyl sulfate, *p*H=9
Luo[19]	addition of 0.5% w undecylenic acid, sealed to PDMS	7.6	19 and 20 mM HEPES buffer, *p*H=8.5
Vickers[15]	extracted in organic solvents, oxidized, irreversibly sealed to PDMS	6.8	20 mM TES buffer, *p*H=7.0, (*N*-tris(hydroxymethyl)methyl-2-aminoethanesulfonic acid)
Vickers[15]	native, sealed to PDMS	4.1	20 mM TES buffer, *p*H=7.0
Roman[20]	addition of SiO_2 particles	8.3	1 mM sodium phosphate, 10 mM KCl, *p*H=8.3
Roman[20]	native	4.2	1 mM sodium phosphate, 10 mM KCl, *p*H=8.3
Choi[7]	surficial modified by cetyltrimethylammonium bromide (CTAB)	−5.0	100 mM Tris, 20 mM boric acid, *p*H=9.3, 0.2 mM CTAB
Zhou[22]	native, reversibly sealed to PDMS	1.7	30 mM phosphate buffer, 10 μg ml^{-1} BSA, *p*H=6.9

II. EXPERIMENTAL

A. PDMS chip fabrication

Four meandering microchannels (75 mm × 40 μm × 25 μm) with a reservoir at each end were designed on a single microchip, Fig. 1. The chip was fabricated by means of PDMS casting against a SU8 master. The microchannels were enclosed by bonding to a pre-polymerized PDMS layer. This procedure avoided plasma treatment which alters the surface properties of PDMS.

The SU8 master (mold) was fabricated as follows: A phosphor bronze substrate was cleaned in a diluted nitric acid (68% acid and water in the volume ratio 1:2), washed in deionized water and acetone and finally dried in an oven for 30 min at 100 °C. After cooling to the laboratory temperature, 25 μm high layer of SU8–2025 (MicroChem) was spin coated on the substrate. This layer was pre-baked for 20 min at 100 °C on a hot plate, exposed through a mask, post-baked for

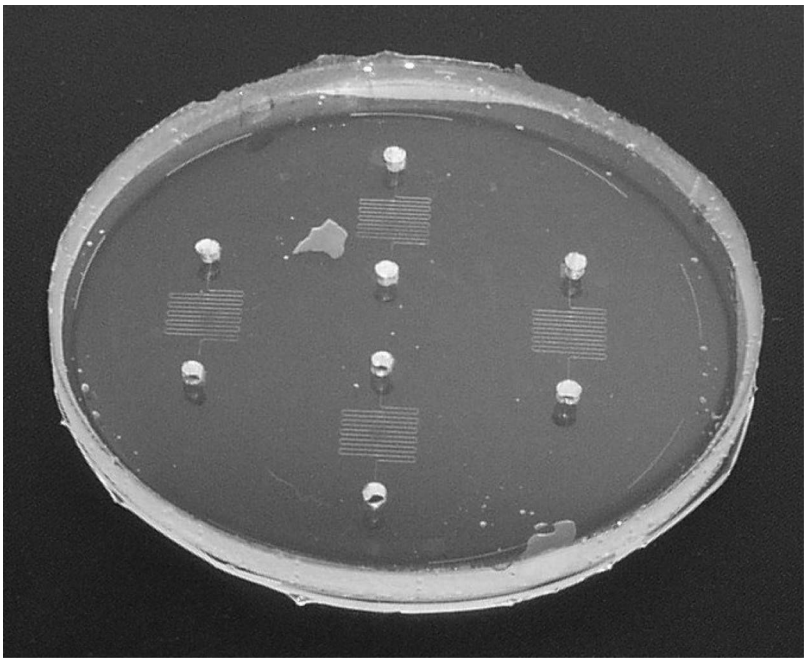

FIG. 1. PDMS microchip.

4 min at 100 °C and developed. PDMS (Sylgard 184, Dow Corning) was prepared by thorough mixing the pre-polymer and the curing agent in the weight ratio 10:1. After degassing, PDMS was poured onto the SU8 master and again degassed. Then the PDMS layer was placed in a drier at 70 °C for 60 min. The cured PDMS was peeled off the master and the holes for electrolyte delivery were punched at required locations. The PDMS surface was finally cleaned with isopropylalcohol and dried with nitrogen. Another PDMS slab was prepared on a glass substrate and pre-polymerized at 90 °C for 9 min. The two PDMS layers were brought in contact and placed in a drier for 30 min to finish the microchip fabrication. A very good irreversible sealing of the two PDMS layers was obtained.

B. Electrokinetic characteristics

The current monitoring technique[23,24] was used to evaluate the electro-osmotic characteristics of the PDMS substrate coated with BSA. The used Tris-BSA buffer (Sigma T-6789, 50 mM Tris, 138 mM NaCl, 2.7 mM KCl, pH=8,1% bovine serum albumin) contains several electroneutral molecules, tris(hydroxymethyl)aminomethane cation (pK_a=8.1), anion forms of BSA (pI=4.6),[25] Na^+, K^+, Cl^-, H^+ and OH^-. Consideration of all these compounds and their dissociation interactions brings strong difficulties in the analysis of transport processes. Because the NaCl concentration (138 mM) in the Tris-BSA buffer is much higher than the concentrations of the other ions, we assumed that the Tris-BSA buffer approximately behaves like the uni-univalent Na^+Cl^- electrolyte. Hence the expression "electrolyte concentration" used in the following experimental and modeling sections refers to NaCl concentration in the electrolytes.

The current monitoring technique is based on the measurement of the electric current flowing through a microcapillary under a constant difference of the electric potential. If the electrolyte concentration varies at the microcapillary inlet, the averaged electrolyte conductivity in the microcapillary changes together with the observed electric current.

The experimental procedure, which we used in our study, can be shortly described as follows: (i) the microchannel was filled with the blocking buffer Tris-BSA (10 min) to coat the PDMS surface, (ii) the channel was filled with Tris-BSA buffer of a chosen concentration c_1, (iii) a constant DC voltage $\Delta\Phi_T$ was imposed on the channel, (iv) when a constant electric current

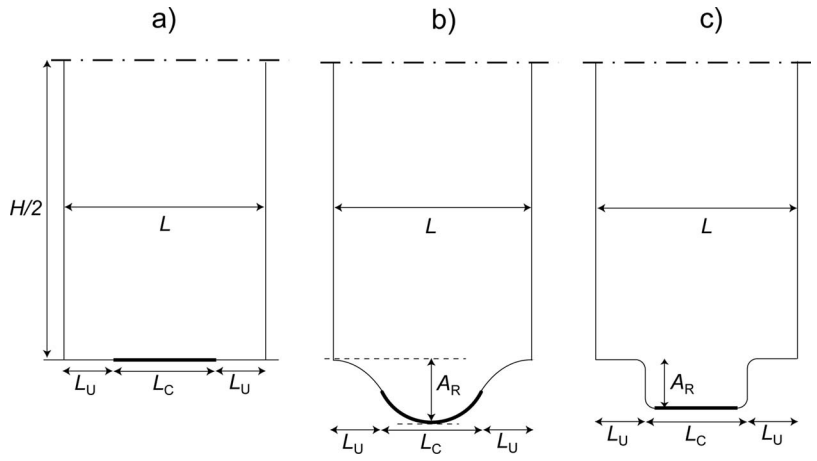

FIG. 2. Geometries of the computational domains, $H=25$ μm, $L=100$ nm: a) flat surface, b) ruffled surface represented by quadratic Bézier curves, A_R is the roughness amplitude, c) step-like surface with the rounding radius 1 nm. L_C and L_U represent the lengths of the charged and uncharged surfaces, respectively. The thick solid line denotes surface areas with a fixed electric charge.

response was obtained, Tris-BSA buffer with concentration of $c_2=2c_1$ was introduced into the inlet (anode) reservoir, (v) the duration of the electric current increase $\Delta\tau$ was measured. We also define the characteristic electrolyte concentration of this experiment $c_0 \equiv (c_1+c_2)/2$.

The EOF mobility μ_{EO} can be evaluated from

$$v_{EO} = \mu_{EO} E, \tag{3}$$

where v_{EO} and E are the net flow velocity and the electric field strength, respectively. Assuming a linear distribution of the electric potential along the channel (constant E)

$$E \approx -\Delta\Phi_T / L_T, \tag{4}$$

the EOF mobility is given by

$$\mu_{EO} = -L_T^2/(\Delta\tau\,\Delta\Phi_T), \tag{5}$$

where L_T is the microchannel length. Zeta potential ζ is related to the EOF mobility via the Smoluchowski equation[5,26]

$$\mu_{EO} = -\zeta\varepsilon/\eta \tag{6}$$

where η and ε are the dynamic viscosity and the electrolyte permittivity, respectively.

C. AFM surface characterization

PDMS samples were analyzed by the NTEGRA-Prima AFM system (NT-MDT). Diamond-like carbon tips with diameter 1–3 nm (NT-MDT, NSG01-DLC) were used. The measurements were carried out in a semi-contact mode in air.

Two types of PDMS samples were characterized: (i) uncoated PDMS and (ii) PDMS coated with BSA. To prepare the coating, the PDMS surface was covered by the blocking Tris-BSA buffer for 10 min. In the next step, the surface was dried and cleaned by a compressed air.

III. MATHEMATICAL MODEL

As the experimental microchips contain long channels with constant surface properties, the electrokinetic transport can be studied only in a short "representative" segment of the channels, Fig. 2. We assume that the width of the channel is large enough in order to describe the problem

TABLE II. Fixed model parameters.

Parameter	Description	Value
ε	electrolyte permittivity	6.95×10^{-10} F m^{-1}
η	electrolyte viscosity	8.91×10^{-4} Pa s
F	Faraday's constant	96487 C mol^{-1}
R	molar gas constant	8.314 J mol^{-1} K^{-1}
T	temperature	298 K
D_+	cation diffusivity	1.5×10^{-9} m^2 s^{-1}
D_-	anion diffusivity	2×10^{-9} m^2 s^{-1}
L_T	total capillary length	7.5×10^{-2} m
L	length of the capillary segment	1×10^{-7} m
A_R	roughness amplitude	8.56×10^{-9} m

as two-dimensional. Three different geometries of the channel surface are considered: Perfectly flat with homogeneous or heterogeneous distribution of the fixed electric charge (a), ruffled with heterogeneous distribution of the fixed electric charge (b), and step-like with heterogeneous distribution of the fixed electric charge (c). The choices of the surface geometries are discussed in the result section.

The mathematical model is based on the approach used in works.[27,28] The velocity $\mathbf{v}$ and pressure p fields are described by the Stokes equation[29] (Reynolds number is close to zero) containing the coulomb force term and by the continuity equation for an incompressible Newtonian fluid

$$\nabla p + q\,\nabla\Phi = \eta\nabla^2\mathbf{v}, \quad \nabla\cdot\mathbf{v} = 0, \tag{7}$$

where Φ and q are the electric potential and the volume concentration of the mobile electric charge, respectively. The electric potential field in a system with a constant electrolyte permittivity ε is described by the Poisson equation in the form

$$\nabla^2\Phi = -q/\varepsilon. \tag{8}$$

Sodium (subscript $+$) and chloride (subscript $-$) ions are dominant in the used Tris buffers. If concentrations of the other ions are neglected, the volume concentration of the electric charge is given by

$$q = F(c_+ - c_-), \tag{9}$$

where F and $c_\pm$ are the Faraday constant and the molar ion concentrations, respectively. The concentration fields can be evaluated using the steady state molar balances of ions in dilute electrolytes

$$\nabla\cdot\mathbf{J}_\pm = \nabla\cdot\left(\mathbf{v}c_\pm - D_\pm\nabla c_\pm \mp \frac{D_\pm F}{RT}c_\pm\nabla\Phi\right) = 0, \tag{10}$$

where the total ion flux intensities, $\mathbf{J}_+$ and $\mathbf{J}_-$, are given by the sum of the convective, diffusion and electromigration contributions. The symbols $D_\pm$, R and T denote the ion diffusivities, the molar gas constant and temperature, respectively. The values of the fixed model parameters are listed in Table II.

The symmetric boundary conditions were used on the symmetry axis (the top part of the segments). The periodic boundary conditions were applied on the inlet and outlet boundaries (the left and right parts of the segments) except for the electric potential for which

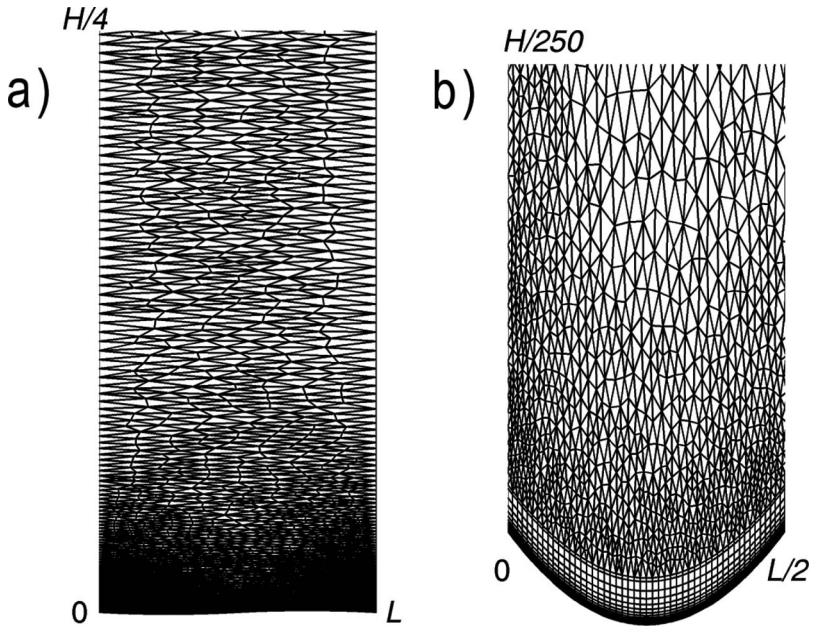

FIG. 3. Mesh of finite elements used for the ruffled geometry: a) one quarter of the computation domain, b) mesh detail above the bottom boundary.

$$\Phi|_{\text{inlet}} = \Phi|_{\text{outlet}} + \Delta\Phi_L, \tag{11}$$

where $\Delta\Phi_L$ is a change of the electric potential per the segment length L. We assume approximately linear distribution of the electric potential (a constant electric field strength along the microchannel), i.e., $E=-\Delta\Phi_L/L$. Thus, if the capillary length L_T, the total potential difference imposed on the capillary $\Delta\Phi_T$, and the segment length L are known, the parameter $\Delta\Phi_L$ can be easily estimated from $\Delta\Phi_L \approx \Delta\Phi_T L/L_T$. The non-slip boundary conditions for the velocity and the normal molar flux intensities equal to zero were considered on the dielectric surface (the bottom part of the segment)

$$\mathbf{v}|_{\text{wall}} = 0, \quad \mathbf{n}\cdot\mathbf{J}_{\pm}|_{\text{wall}} = 0, \tag{12}$$

where $\mathbf{n}$ is the normal vector to the surface. The following boundary conditions were chosen for the electric potential

$$\mathbf{n}\cdot\nabla\Phi|_{\text{charged wall}} = -\sigma/\varepsilon, \quad \mathbf{n}\cdot\nabla\Phi|_{\text{uncharged wall}} = 0, \tag{13}$$

where σ is the surface concentration of the fixed electric charge. Zero reference pressure and electric potential were considered at one point of the segment.

This set of model equations was numerically solved using the nonlinear stationary solver of the Comsol Multiphysics software. Because the proposed mathematical model describes transport phenomena in the entire spatial domain including the extremely thin region with a nonzero concentration of the electric charge (so called electric double layer—EDL), a hybrid triangle-rectangle spatial discretization was developed. The rectangle finite elements with various aspect ratios (up to 500) were used in EDL and the triangle elements in the rest of the domain, Fig. 3. Purely triangle meshes with a high element density were exploited for the step-like surface geometry. The main characteristics of all meshes are summarized in Table III. It can be seen that the finite element density across EDL is extremely high in order to capture the concentration and potential gradients.

TABLE III. Mesh parameters.

Geometry	Mesh type	No. elements	Min. step [nm]	Max. step [nm]	Max. aspect ratio (rectangle)
Flat	hybrid	12800	0.002	15	500
Ruffled	hybrid	12800	0.002	15	500
Step-like	triangle	25400	0.08	50	-

Numerical solutions were validated with the use of an analytical solution for the perfectly flat segment.[5] If one studies the electro-osmotic flow in a cylindrical microchannel, an exact solution can be found in.[30] Mesh convergence studies were carried out for the other segments with surface heterogeneities to avoid significant numerical errors.

The mathematical model was used for estimation of the parameter σ. The "optimal" parameter value was identified by minimizing a penalty function defined as the sum of squares of deviations between the experimentally and numerically obtained points on concentration dependencies of the electro-osmotic mobility.

IV. RESULTS AND DISCUSSION

A. AFM characterization

The root mean square (RMS) surface roughness of the uncoated PDMS was 0.85 nm and the average roughness was 0.68 nm.

An example of the AFM image of the coated PDMS surface is plotted in Fig. 4. BSA molecules do not regularly cover the PDMS surface. The protein layer has a "peak and ridge" structure that was observed, for example, when BSA adsorbed on treated[31] or untreated[32] polystyrene (PS) or gold.[33] The maximal vertical height of our protein layer is about 15 nm. BSA molecules have ellipsoid shape with characteristic dimensions 14 nm $\times$ 4 nm $\times$ 4 nm.[32] Thus BSA can adsorb in two limit orientations: (i) the "end-on" with the characteristic height 14 nm or (ii) the "side-on" with the characteristic height 4 nm.[32,33] It seems that no orientation is preferred on the PDMS substrate because one can observe peaks of various heights, Fig. 4. Width of the peaks attains hundreds of nanometers. Hence, we assume that larger peaks are formed by BSA aggregates. Huang and Gupta[34] suggested that the aggregate formation can be caused by protein unfolding upon the BSA adsorption. Then the internal hydrophobic domains are available for a close binding of other BSA molecules.

Figure 4 shows that there is a large uncovered part of the PDMS surface among BSA molecules/aggregates. This part forms approximately one half of the whole surface. According to an image analysis of the obtained 3D data, we determined the percentage of the uncoated part to be equal to 57%. This is surprising with respect to the fact that the BSA concentration in the Tris-BSA buffer is high (1%). A similar observation was published by Butler *et al.*[35] They used immunoglobulins and other proteins. The authors suggested that adsorption of proteins on PDMS can be locally difficult because small air bubbles can be bound on the polymer surface.

AFM images reveal important facts. The EDL formation is prevented at the PDMS surface covered by the BSA molecules because the fixed electric charge is shielded by this protein. Further, the RMS roughness increased from 0.85 nm to 5.34 nm and the average roughness from 0.68 nm to 4.28 nm on the coated PDMS surface. It means that the immobilized BSA molecules also increase the hydrodynamic resistance at the PDMS surface.

Hence, we suggest three possible arrangements characterizing a representative part of the coated PDMS surface, Fig. 2. In our concept, the covered part of the PDMS surface does not contribute to the formation of the mobile electric charge in the electrolyte, i.e., the concentration of the fixed electric charge in the covered parts is considered to be zero.

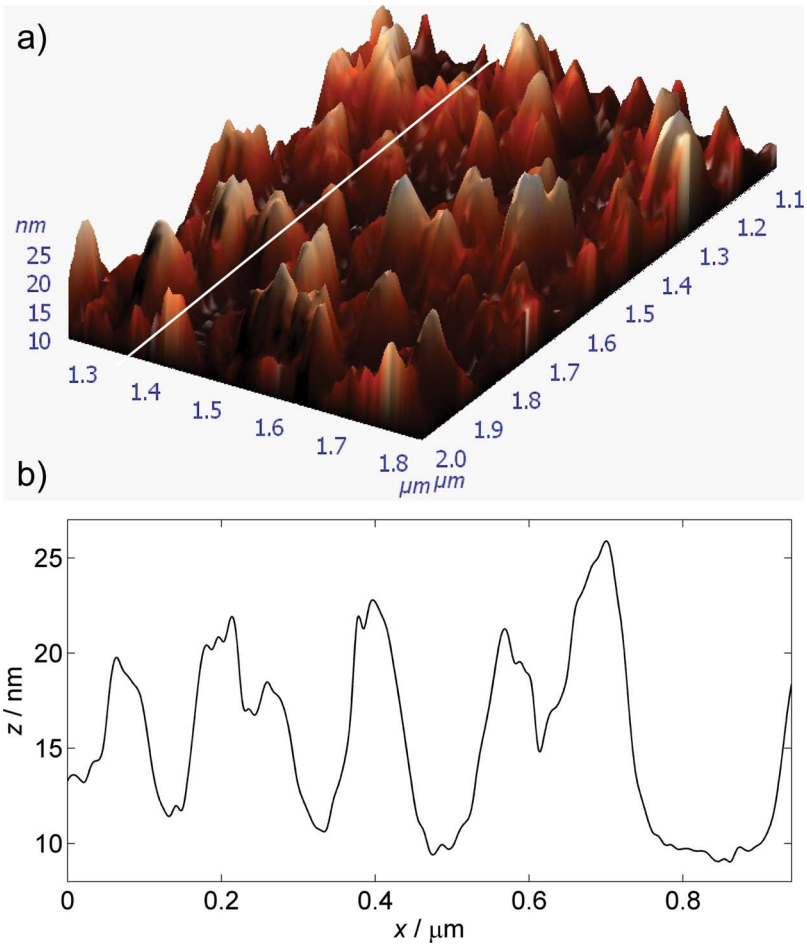

FIG. 4. AFM images of the surface coated with BSA: a) 3D image of a representative sample of the surface, b) height profile of the sample that corresponds to white line in a).

B. Electrokinetic properties

An example of a typical experiment used for the electro-osmotic velocity evaluation is shown in Fig. 5. The used electric current monitoring technique enables to clearly determine the duration of the electrolyte transport along the entire length of the microchannel. The electric current increase is not linear. In all experiments, we observed that the current response is a convex function of time. The origin of this finding was theoretically revealed and discussed in work.[24]

1. Electric field strength characteristics

Experiments aimed at the evaluation of the electro-osmotic mobility and zeta potential were performed for two different characteristic electrolyte concentrations. The obtained dependencies are linear in the considered interval of the electric field strength, Fig. 6. Each experimental point is represented by the arithmetic mean of the net velocity obtained from five independent measurements. 90% confidence intervals are also plotted. With the use of Eq. (5), the electro-osmotic mobility was evaluated to be $(1.08 \pm 0.02) \times 10^{-8}$ $m^2\ V^{-1}\ s^{-1}$ and $(2.35 \pm 0.06) \times 10^{-8}$ $m^2\ V^{-1}\ s^{-1}$ for the higher (c_0=0.104 M) and the lower (c_0=0.010 M) characteristic concentration, respectively. From Eq. (6), the corresponding zeta-potentials are $-(13.8 \pm 0.3)$ mV and $-(30.1 \pm 0.8)$ mV. The obtained values are in agreement with the data reported by Zhou *et al.*[22] for a PDMS substrate treated by BSA.

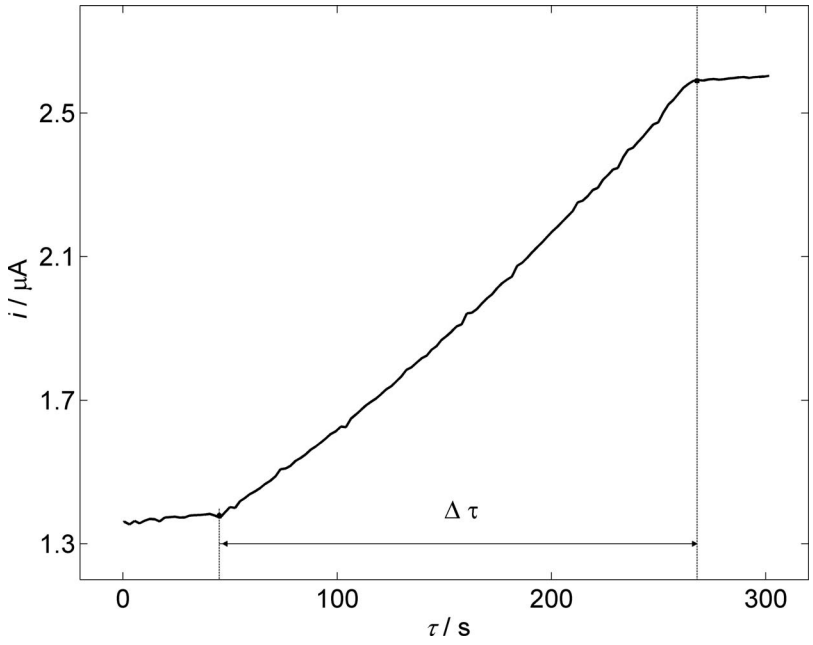

FIG. 5. Measurement of the electro-osmotic velocity: Electric current time course. Duration of the electric current increase is equal to $\Delta\tau$, E=13.7 kV m^{-1}, c_0=0.013 M.

2. Concentration dependencies

In the next step, dependencies of the net velocity on the electrolyte concentration were measured for two imposed electric field strengths, Fig. 7. Each point again represents the arithmetic mean of five independent measurements. The net velocity nonlinearly decreases with increasing concentration for the both electric field strengths. The zeta-potential and electro-osmotic mobility vary with increasing concentration from −38 mV to −13 mV and from 3.0×10^{-8} m^2 V^{-1} s^{-1} to 1.0×10^{-8} m^2 V^{-1} s^{-1}, respectively.

The experimental results were fitted with two functions, Eq. (1) and (2), as suggested by Spehar *et al.*[11] Our results are in agreement with data published in their work. The concurrence is both qualitative (the shape of the dependence, confidence of the two fits) and quantitative (the range of concentrations and the corresponding electro-osmotic mobilities).

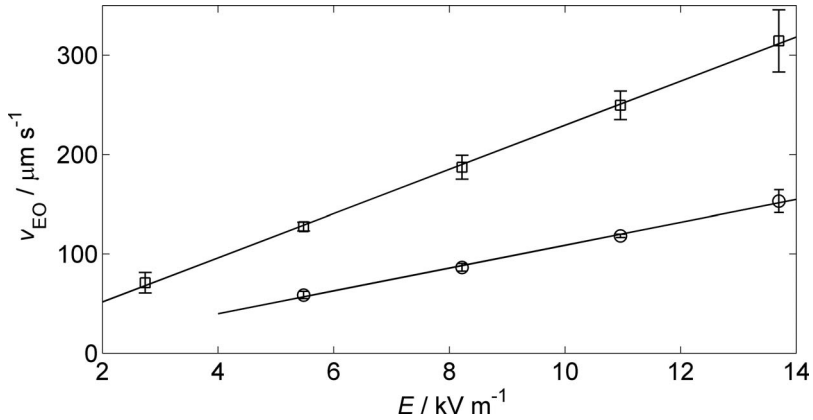

FIG. 6. Dependencies of the electro-osmotic flow velocity on the electric field strength. Circles: c_0=0.104 M, squares: c_0=0.010 M. The solid lines denote linear fits of the experimental data.

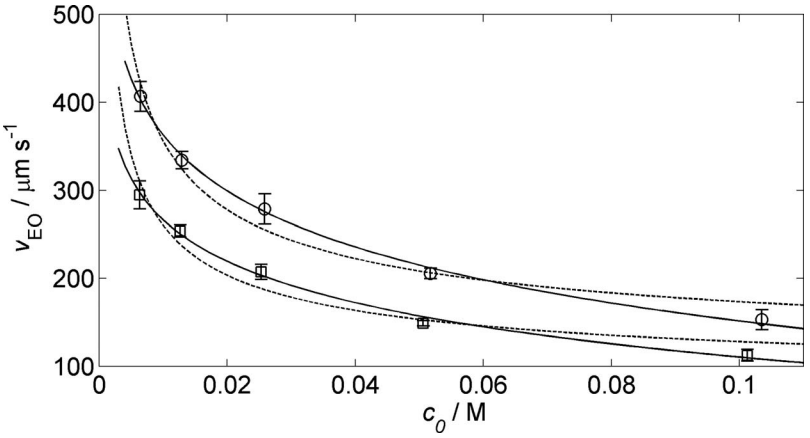

FIG. 7. Dependencies of the electro-osmotic flow velocity on the characteristic electrolyte concentration. Circles: $E=13.7$ kV m^{-1}, squares: $E=11.0$ kV m^{-1}. The solid and the dotted lines denote nonlinear fits of the experimental data according to the relations, Eq. (1) and Eq. (2), respectively.

It can be seen that the logarithm dependence, Eq. (1), fits the experimental points significantly better than the inverse square root function, Eq. (2), for the both electric field strengths. This fact is consistent with the finding that the logarithmic dependence is mostly applicable for low electrolyte concentrations, e.g., $c_0 < 100$ mM on silica.[21] On the other hand, the obtained value of the zeta-potential is suspiciously low (close to 25 mV). According to the theory, the experimental data should be fitted better by the inverse square root function. Hence, we decided to find possible origins of this discrepancy.

C. Effect of electric charge heterogeneities

The entire surface of the PDMS substrate cannot contribute to the electro-osmotic transport of the electrolyte due to the immobilized BSA molecules. Considering the homogeneous distribution of the electric charge along the PDMS surface [$L_C=100$ nm, $L_U=0$ nm, Fig. 2(a)], the dependence of the net velocity on the characteristic concentration c_0 can be evaluated with the use of an exact expression. It gives the relation between the zeta potential and the electric charge surface concentration[5]

$$\zeta = \frac{2RT}{F}\operatorname{arcsinh}\left(\frac{\sigma\lambda F}{2RT\varepsilon}\right), \tag{14}$$

which can be substituted into Eq. (6). The symbol λ denotes the Debye length that is proportional to the inverse square root of the characteristic electrolyte concentration

$$\lambda = \left(\frac{RT\varepsilon}{2c_0F^2}\right)^{0.5}. \tag{15}$$

We further consider that the surface concentration of the fixed electric charge on PDMS is approximately constant on the studied interval of the electrolyte concentrations. The optimal σ value can be then found by the optimization procedure (see the section Mathematical model). It can be observed that Eq. (14) is not able to satisfactorily fit the experimental data, see the dotted line in Fig. 8.

Hence, we consider that the PDMS surface can be divided into two parts, Fig. 2(a). One part represents the surface where no BSA molecules are immobilized (L_C), i.e., the surface electric charge concentration should be similar as on the non-treated PDMS substrate. The other part

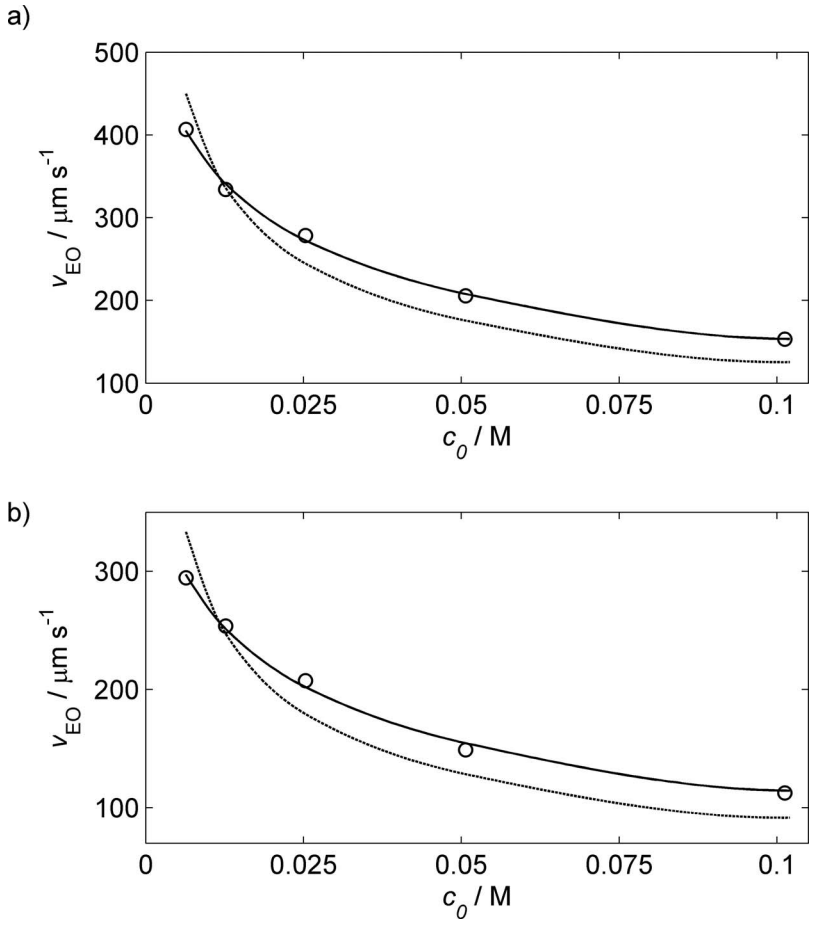

FIG. 8. Dependencies of the electro-osmotic flow velocity on the characteristic electrolyte concentration for the flat geometry Fig. 2(a). a) $E=13.7$ kV m^{-1}, circles: Experiments, solid line: $L_C=62$ nm, $\sigma=-1.80\times10^{-2}$ C m^{-2}, dotted line: $L_C=100$ nm, $\sigma=-0.884\times10^{-2}$ C m^{-2}, b) $E=11.0$ kV m^{-1}, circles: Experiments, solid line: $L_C=57$ nm, $\sigma=-1.83\times10^{-2}$ C m^{-2}, dotted line: $L_C=100$ nm, $\sigma=-0.805\times10^{-2}$ C m^{-2}.

represents the surface where BSA molecules occupy the PDMS surface (L_U). In this region, we assume that $\sigma\rightarrow0$ C m^{-2}. A two parametric optimization procedure was then carried out to identify the proper L_C and σ values.

As shown in Fig. 8, the dependence of the net velocity obtained by the numerical analysis of the model with the electric charge heterogeneity can perfectly fit the experimental data. The fixed electric charge is effectively located on about 60% of the PDMS surface (57%–62%). This finding is also in good agreement with the AFM observation (approximately 57% of uncoated surface). The local electric charge concentration on the charged part of PDMS (the L_C domain without BSA) is then about -1.8×10^{-2} C m^{-2}. The charge concentration averaged over the entire PDMS surface (computed as the weighted arithmetic mean) is about -1.1×10^{-2} C m^{-2}.

D. Effects of the surface roughness

The AFM analysis revealed that the surface roughness of the PDMS with the adsorbed BSA molecules is several times higher than that of the native PDMS. To study the effect of the surface roughness on the electro-osmotic flow numerically, we approximated the real surface profile with: (i) ruffled surface represented by Bezier curves of the second order, Fig. 2(b), and (ii) step-like surface with rounded corners, Fig. 2(c). In both cases the height of the peaks corresponded to the double of the average surface roughness measured by AFM. We again considered that the BSA

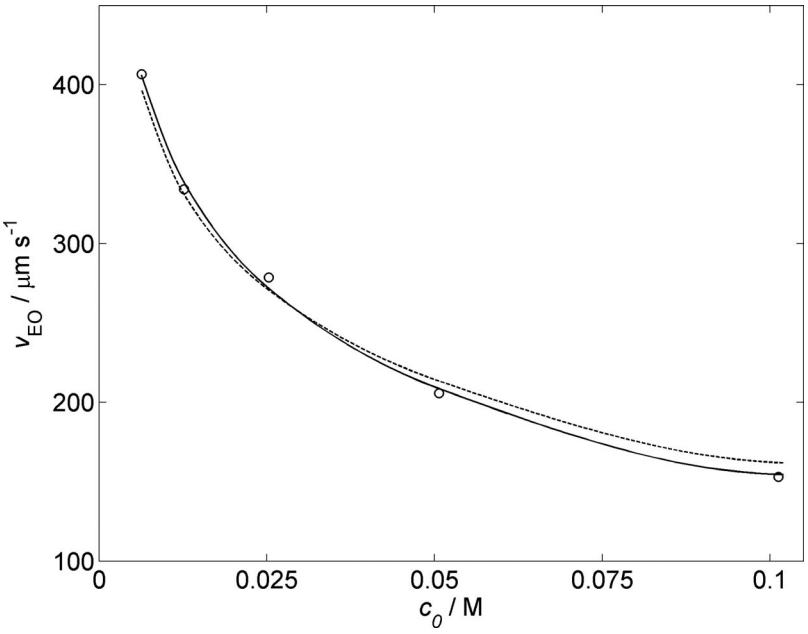

FIG. 9. Dependencies of the electro-osmotic flow velocity on the characteristic electrolyte concentration for the ruffled surface (solid line) and the step-like surface (dotted line). $E=13.7$ kV m^{-1}, circles: Experiments; solid line $L_C=74$ nm, $\sigma=-2.5\times10^{-2}$ C m^{-2}; dotted line: $L_C=89$ nm, $\sigma=-3.1\times10^{-2}$ C m^{-2}.

molecules cover a certain part of the PDMS surface which then cannot contribute to the EOF flow. Therefore, the same parametric optimization procedures as the above were performed to find out the values of the fixed electric charge σ and the length of the charged surface L_C. The length L_U corresponds to the half width of the peaks (Fig. 2).

The results of the optimization procedure are plotted in Fig. 9. It can be found that the modeled curve for the ruffled geometry fits the experimental data better than the curve for the step-like geometry. The local surface concentration of the electric charge σ and the length of the charged surface L_C for the ruffled surface were -2.5×10^{-2} C m^{-2} and 74 nm, respectively, for the step-like geometry -3.1×10^{-2} C m^{-2} and 89 nm, respectively. These results predict the fraction of the surface covered by BSA to be 26% or 11%, respectively.

The values of the optimized parameters (L_C, $|\sigma|$) are much higher for the ruffled and step-like geometry than those for the flat geometry. The results obtained for the flat geometry are also in a good agreement with the AFM observation. One of the possible explanations of this fact relies on a limited potential of the spatially two-dimensional models. The AFM picture of the PDMS layer coated with BSA shows that there are "valleys" among the immobilized protein molecules. As the surface electric charge is located dominantly in these valleys, the charged electrolyte (in EDL) is forced to flow among the protein molecules but not over them. The typical Debye layer thickness for the used electrolytes is about 1 nm (it depends on the used electrolyte concentration) but the vertical dimensions of the immobilized protein can exceed 10 nm. Thus the ruffled and step-like geometries cannot describe the real electrolyte behavior at the coated surface. The classical electro-osmosis probably emerges only in the valleys whereas zero flow is induced at the protein surface. In our opinion, the flat geometry with heterogeneous distribution of the electric charge can predict such behavior because this geometry linearly combines the charged and uncharged parts on the flat surface but no vertical flow over the uncharged proteins is forced. For a better understanding of the above described problem, spatially three-dimensional models reflecting the real geometry of the coated PDMS surface should be developed. In such models, the entire flow pattern can be probably obtained and analyzed.

E. Effective electric charge of BSA

In the previous analysis, we assumed that the immobilized BSA molecules do not contribute to the electro-osmotic flow, i.e., the effective surface electric charge of the BSA molecule is close to zero. Because the experiments were carried out at $p\mathrm{H}=8$, which is quite above the isoelectric point of BSA ($pI \sim 4.6$), the BSA molecules have to be negatively charged. Böhme and Scheler showed that the effective electric charge number of BSA under $p\mathrm{H}=8$ is about -12.[36] The corresponding surface charge density on a BSA molecule is then approximately -5×10^{-2} C m^{-2} (the characteristic BSA diameter equal to 6 nm was considered). Under such conditions, the BSA immobilization should accelerate the electro-osmotic flow at the PDMS surface.

This is in a clear contradiction with our findings. We carried out control experiments in order to compare the electro-osmotic mobility in the PDMS chip with and without the BSA coating under the same conditions (Tris buffer, $p\mathrm{H}=8$, $c_0=0.104$ M, $E=13.7$ kV m^{-1}). The obtained electro-osmotic mobilities were equal to $(1.08 \pm 0.02) \times 10^{-8}$ m^2 V^{-1} s^{-1} for the BSA coated PDMS and to $(2.56 \pm 0.03) \times 10^{-8}$ m^2 V^{-1} s^{-1} for the native PDMS. The decrease of the electro-osmotic mobility after the protein treatment indicates that the average surface charge density significantly reduced. It seems that the mobility decrease after a protein treatment is a common feature of many plastics.[10,22,37] The generally accepted explanation of this phenomenon is given in monograph.[38] In a stronger electrolyte, the counter-ions from the electrolyte firmly bind (the counter-ions are thus immobile) by the electrostatic interaction to the ionized groups of proteins that then behave as electroneutral molecules. We should note that the Böhme and Scheler experiments[36] were carried out in deionized water.

The previous discussion implies that our assumption on the zero effective electric charge of the immobilized BSA is correct.

V. CONCLUSIONS

The electrokinetic and surface properties of the PDMS chips treated with BSA molecules were investigated. The electro-osmotic mobilities and zeta potentials were evaluated from the electro-osmotic velocity vs. electric field strength dependencies giving the values $(1.08 \pm 0.02) \times 10^{-8}$ m^2 V^{-1} s^{-1} and $-(13.8 \pm 0.3)$ mV for the electrolyte concentration of 0.104 M and $(2.35 \pm 0.06) \times 10^{-8}$ m^2 V^{-1} s^{-1} and $-(30.1 \pm 0.8)$ mV for the electrolyte concentration of 0.010 M. The observed effect of electrolyte concentration on the electro-osmotic velocity was further studied in detail. The experimental dependence of the electro-osmotic velocity on the electrolyte concentration was nonlinear and well fitted with a logarithmic function.

The AFM analysis of the native and the BSA treated PDMS chips showed an increase in the average surface roughness from 0.68 nm to 4.28 nm and also significant heterogeneities of the protein layer. This observation implied that (i) the increased surface roughness offers a higher resistance to the electro-osmotic flow, and (ii) the BSA molecules cover only a part of the PDMS surface and partially shield the fixed electric charge. These implications were supported by the fact that the theoretical dependence of the EOF velocity on the electrolyte concentration derived for a flat surface with a homogeneous distribution of the surface electric charge did not satisfactorily fit the experimental data.

Assumption of the existence of the heterogeneously distributed surface electric charge gave a better fit of the experimental data for all the studied geometries. However, different values of the electric charge surface density and the fraction of the surface covered by the BSA molecules were predicted for the suggested geometries. When compared to the AFM analysis, the flat surface geometry with the heterogeneous distribution of the electric charge seems to provide the most realistic results giving the value of the local surface charge density of -0.018 C m^{-2} and the fraction of the surface coated with BSA of 40%.

The obtained results give us a deeper insight into the processes in the vicinity of the PDMS surface coated by BSA. One can expect that a similar behavior will be typical for other proteins on various substrates. The precise electro-osmotic dosing of samples and washing buffers is one of

the crucial steps of many lab-on-a-chip bioassay applications (heterogeneous immunoassays etc.). We showed that the developed mathematical model can help to precisely predict and possibly control the sample dosing under various electrolyte concentrations.

The use of knowledge about the microchannel surface properties and the advanced mathematical model for the explanation of the concentration dependencies of the electro-osmotic characteristics is the main novelty of this paper.

ACKNOWLEDGMENTS

The authors thank for the support of the research by the grant of the Grant Agency of Czech Academy of Science KAN208240651 and by the grant of Ministry of Education, Youth and Sport of the Czech Republic MSM 6046137306.

[1] S. K. Sia and G. M. Whitesides, Electrophoresis **24**, 3563 (2003).
[2] J. M. K. Ng, I. Gitlin, A. D. Stroock, and G. M. Whitesides, Electrophoresis **23**, 3461 (2002).
[3] T. Fujii, Microelectron. Eng. **61–62**, 907 (2002).
[4] J. M. Edwards, M. N. Hamblin, H. V. Fuentes, B. A. Peeni, M. L. Lee, A. T. Woolley, and A. R. Hawkins, Biomicrofluidics **1**, 014101 (2007).
[5] H. Ohshima and K. Furusawa (Marcel Dekker, New York, 1998).
[6] Z. A. Almutairi, T. Glawdel, C. L. Ren, and D. A. Johnson, International Mechanical Engineering Congress and Exposition 2007, Vol 11 Pt a and Pt B: Micro and Nano Systems 893 (2008).
[7] H. Choi, K. B. Lee, K. R. Yoon, I. S. Choi, S. I. Woo, K. Choi, S. C. Lee, and Y. Kim, Bull. Korean Chem. Soc. **25**, 560 (2004).
[8] S. Dasgupta, A. A. S. Bhagat, M. Horner, I. Papautsky, and R. K. Banerjee, Microfluidics and Nanofluidics **5**, 185 (2008).
[9] X. Q. Ren, M. Bachman, C. Sims, G. P. Li, and N. Allbritton, J. Chromatogr. B Analyt. Technol. Biomed. Life Sci. **762**, 117 (2001).
[10] H. Shadpour, H. Musyimi, J. F. Chen, and S. A. Soper, J. Chromatogr. A **1111**, 238 (2006).
[11] A. M. Spehar, S. Koster, V. Linder, S. Kulmala, N. F. de Rooij, E. Verpoorte, H. Sigrist, and W. Thormann, Electrophoresis **24**, 3674 (2003).
[12] A. Sze, D. Erickson, L. Q. Ren, and D. Q. Li, J. Colloid Interface Sci. **261**, 402 (2003).
[13] R. Venditti, X. C. Xuan, and D. Q. Li, Microfluidics and Nanofluidics **2**, 493 (2006).
[14] N. Bao, J. J. Xu, Q. Zhang, J. L. Hang, and H. Y. Chen, J. Chromatogr. A **1099**, 203 (2005).
[15] J. A. Vickers, M. M. Caulum, and C. S. Henry, Anal. Chem. **78**, 7446 (2006).
[16] D. Ross, T. J. Johnson, and L. E. Locascio, Anal. Chem. **73**, 2509 (2001).
[17] D. Ross and L. E. Locascio, Anal. Chem. **75**, 1218 (2003).
[18] S. Devasenathipathy, J. G. Santiago, and K. Takehara, Anal. Chem. **74**, 3704 (2002).
[19] Y. Q. Luo, B. Huang, H. Wu, and R. N. Zare, Anal. Chem. **78**, 4588 (2006).
[20] G. T. Roman, T. Hlaus, K. J. Bass, T. G. Seelhammer, and C. T. Culbertson, Anal. Chem. **77**, 1414 (2005).
[21] B. J. Kirby and E. F. Hasselbrink, Electrophoresis **25**, 187 (2004).
[22] F. Zhou, W. Wang, W. Y. Wu, J. R. Zhang, and J. J. Zhu, J. Chromatogr. A **1194**, 221 (2008).
[23] X. H. Huang, M. J. Gordon, and R. N. Zare, Anal. Chem. **60**, 1837 (1988).
[24] W. Schrott, M. Pribyl, J. Stepanek, and D. Snita, Microelectron. Eng. **85**, 1100 (2008).
[25] G. Sagvolden, I. Giaever, and J. Feder, Langmuir **14**, 5984 (1998).
[26] R. F. Probstein, *Physicochemical hydrodynamics: An Introduction*, 2nd ed. (Wiley and Sons, New York, 1994).
[27] T. Postler, Z. Slouka, M. Svoboda, M. Pribyl, and D. Snita, J. Colloid Interface Sci. **320**, 321 (2008).
[28] Z. Slouka, M. Pribyl, D. Snita, and T. Postler, Phys. Chem. Chem. Phys. **9**, 5374 (2007).
[29] W. M. Deen, *Analysis of Transport Phenomena* (Oxford University Press, New York, 1998).
[30] S. H. Chang, Biomicrofluidics **3**, 012802 (2009).
[31] M. M. Browne, G. V. Lubarsky, M. R. Davidson, and R. H. Bradley, Surf. Sci. **553**, 155 (2004).
[32] J. E. Puskas, Y. Dahman, and A. Margaritis, Biomacromolecules **5**, 1412 (2004).
[33] M. Tencer, R. Charbonneau, N. Lahoud, and P. Berini, Appl. Surf. Sci. **253**, 9209 (2007).
[34] Y. W. Huang and V. K. Gupta, J. Chem. Phys. **121**, 2264 (2004).
[35] J. E. Butler, E. P. Lu, P. Navarro, and B. Christiansen, J. Mol. Recognit. **10**, 36 (1997).
[36] U. Bohme and U. Scheler, Chem. Phys. Lett. **435**, 342 (2007).
[37] Y. L. Gao, G. Q. Hu, F. Y. H. Lin, P. M. Sherman, and D. Q. Li, Biomed. Microdevices **7**, 301 (2005).
[38] W. B. Blanch and D. S. Clark, *Biochemical Engineering* (Marcel Dekker, New York, 1997).
[39] G. Ocvirk, M. Munroe, T. Tang, R. Oleschuk, K. Westra, and D. J. Harrison, Electrophoresis **21**, 107 (2000).

Microfluidic Systems with Ion-Selective Membranes

Zdenek Slouka, Satyajyoti Senapati, and Hsueh-Chia Chang

Department of Chemical and Biomolecular Engineering, University of Notre Dame, Notre Dame, Indiana 46556; email: zslouka@nd.edu, ssenapat@nd.edu, hchang@nd.edu

Annu. Rev. Anal. Chem. 2014. 7:317–35

First published online as a Review in Advance on April 14, 2014

The *Annual Review of Analytical Chemistry* is online at anchem.annualreviews.org

This article's doi: 10.1146/annurev-anchem-071213-020155

Keywords

biosensing, depletion, electrokinetics, limiting current, molecular concentration

Abstract

When integrated into microfluidic chips, ion-selective nanoporous polymer and solid-state membranes can be used for on-chip pumping, pH actuation, analyte concentration, molecular separation, reactive mixing, and molecular sensing. They offer numerous functionalities and are hence superior to paper-based devices for point-of-care biochips, with only slightly more investment in fabrication and material costs required. In this review, we first discuss the fundamentals of several nonequilibrium ion current phenomena associated with ion-selective membranes, many of them revealed by studies with fabricated single nanochannels/nanopores. We then focus on how the plethora of phenomena has been applied for transport, separation, concentration, and detection of biomolecules on biochips.

1. INTRODUCTION

In recent years, the advancement of nanofabrication techniques has allowed the construction of nanostructures that are the workhorses of a new scientific discipline dealing with fluids confined in nanospaces—nanofluidics. They have catalyzed thorough investigations of electrokinetic phenomena in nanofluidic systems on the application of electric fields [alternative or direct current (DC)] and have revealed many unexpected and surprising phenomena. At this nanoscale confinement, surface charges and hydrodynamic slip phenomena at the channel walls often dictate the behavior of the whole system. The most important driving phenomenon is ion selectivity, when the transverse channel dimension is smaller than the Debye length, which can lead to large mobile ion concentration gradients, internal/external ion enrichment, extended polarized layers, surface electroconvection, water splitting, nonlinear ion current circuitry, current rectification, etc.

The concept of ion selectivity emerged long before nanofluidics, but nanofluidic research has greatly advanced our understanding of its effects. More than 70 years ago, ion-selective membranes started to be used in industrial water treatment processes such as electrodialysis and electrodeionization (1). These membranes are natural nanostructures because they contain nanopores decorated with surface charges. They are, however, much easier to synthesize and integrate into microfluidic systems than artificial nanostructures. In this review, we describe how knowledge garnered from artificial nanofluidic systems has led to new membrane-based microfluidic systems for the pumping, manipulation, preconcentration, and detection of biomolecules. Because they are inexpensive and can be easily integrated or inserted into a microfluidic chip, they are ideal for disposable point-of-care medical diagnostic biochips. They often offer better performance in limit of detection, sensitivity, selectivity, and target number than the cheaper paper-based devices and, unlike paper devices, can process large biomolecules such as chromosomal DNA.

Ion selectivity of such membranes also stipulates that the current is controlled by ion currents and not electron currents in electrodes or charge transfers by electrochemical reactions. As such, the membrane sensors are stable/reproducible and less sensitive to the presence of redox agents in the sample, and they do not require the fabrication of micro- or nanoelectrode sensors. Hence, membrane microfluidic devices are much more robust and inexpensive than electrochemical sensing devices.

2. CONCEPTS AND PHENOMENA

2.1. The Concept of Ion Selectivity

We offer only a cursory exposition of ion selectivity. It is currently an intensely researched topic, and interested readers are referred to several recent reviews (2–7). The concept of ion selectivity was formulated in the first half of the twentieth century and was later nicely described in a technical review by K. Sollner (8) in 1950. Sollner summarized the facts known about a material called collodion used to prepare porous membranes. He referred to those membranes as an electronegative membrane with preferential cation permeability, where the charge selectivity comes from acidic impurities present on the pores of the membrane. His technical review was based on a few previous papers by Meyer (9), Teorell (10, 11), and Donnan (12). Both Meyer and Teorell proposed the fixed charge theory of electrochemical membranes while Donnan worked out a theory of membrane equilibria. In the aforementioned review, Sollner (8, p. 141C) states the following:

> In the case of membranes of high and, in limiting cases, of ideal ionic selectivity—more correctly membranes which under a given set of circumstances are of ideal ionic selectivity—the picture becomes

fairly simple. The pores are so narrow that the fixed charged wall groups prevent, by electric repulsion, the permeation of any ions of the same sign. The movement of the counter ions of the fixed charged groups alone is, therefore, the cause of all electrical effects observed with these membranes.

This statement essentially covers all the conditions that are required to observe ion selectivity. First, we need a fixed charge bound on a solid support and second, the space over the fixed charge has to be restricted to a distance at which the fixed charge has some effect. Although the first requirement is usually fulfilled by the dissociation of surface functional groups [or some other charging mechanism (13)] after soaking in a water solution, the second requirement can be estimated by evaluation of a so-called Debye length characterizing an electrical double layer that forms at the charged interfaces.

2.2. Electrical Double Layer

Due to the presence of some inherent functional groups on a solid surface, a fixed charge is established on the surface of the solid plate, rendering the plate either positively or negatively charged. The electrostatic interactions cause the free ions to rearrange by attracting the oppositely charged ions to the plate, creating an electrical double layer. The concentration of those oppositely charged ions (counterions) in this electrical double layer must be equal to the concentration of the fixed charge so that the system still obeys the electroneutrality condition. However, due to thermal fluctuation (diffusion in a continuum theory), the mobile counterions occupy a layer, the electric double layer, of finite thickness. The classical theory for electrical double layer can be found in standard texts (13, 14). The potential and concentration profiles of co- and counterions in the electrical double layer can be derived from the Poisson-Boltzman equation where a Debye screening length appears as a natural parameter. This Debye length is dependent on the ionic strength of the working buffer solution. Calculating the distance over which an excess of counterions over coions exists in the solution as a function of the electrolyte concentration reveals why nanospaces are necessary to provide ion selectivity. In nanospaces/nanochannels, the electrical double layers overlap, which makes them ion selective; e.g., counterions easily pass through, whereas coions are repelled. The Debye length is not the only factor important for ion selectivity. The concentration of the fixed charge is also an important parameter affecting ion selectivity (15, 16). Systems with low concentrations of the fixed charge exhibit only weak ion selectivity even though Debye layers overlap. In a recent review (17), a new quantity, volumic surface charge, was introduced. This quantity relates the surface charge density to the section height of a planar microchannel, which could be thought of as a measure of ion selectivity. In any case, it is clear that the concentration of the mobile ions and hence the ion current conductivity in the nanochannel are controlled by surface charge. As such, the channel ion conductivity is as much as 10 times higher than the bulk conductivity outside the channel, depending on the bulk ionic strength.

3. ION-EXCHANGE MEMBRANES

3.1. Membrane Ion Current Circuits

Ion-exchange membranes are extensively used in many industrial applications, such as deionization or electrodialysis (1). There are many different types of ion-exchange membranes that can be classified according to their properties (18). Homogeneous ion exchange membranes (e.g., Nafion membranes) are made of coherent ion exchanger gel, whereas heterogeneous membranes contain ion-exchange particles embedded in an inert binder (**Figure 1*b***) (19). Most of these membranes

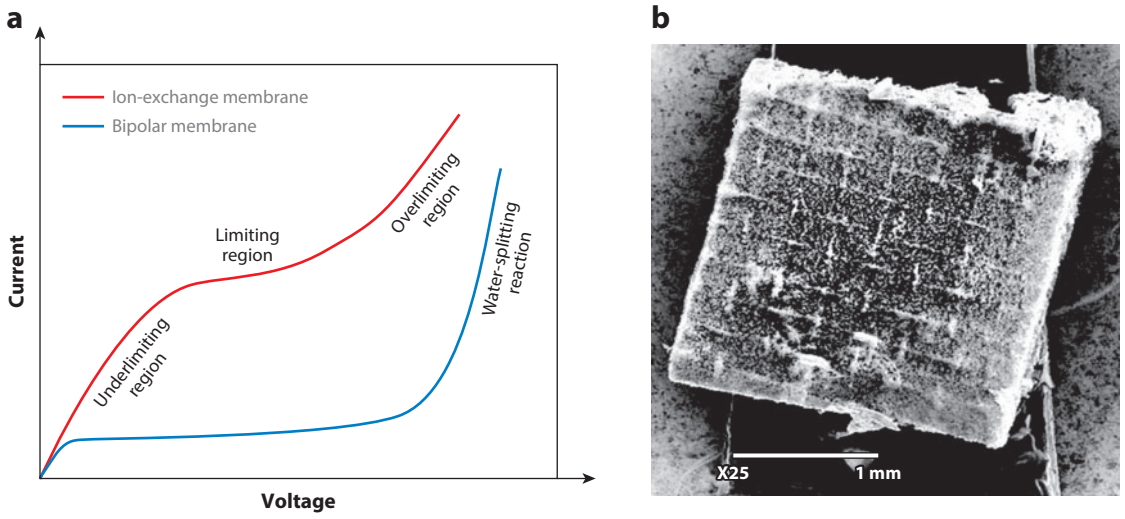

Figure 1

(*a*) Typical schematic representation of current voltage curves for an ion-exchange membrane (*red*) and bipolar membrane in the reverse bias (*blue*). (*b*) Scanning electron microscope image of a commercial heterogeneous polymeric membrane.

use sulfone anion ($R\text{-}SO_3^-$) for cation-exchange membranes and quaternary ammonium cation [$R\text{-}N^+(CH_3)_3$] for anion-exchange membranes as a fixed charge. Both groups are chemically very stable and capable of functioning properly over a large range of pH values. The charge borne by functional groups in nanochannels (SiO_2, Al_2O_3, COOH), however, can easily be neutralized in acid-base reactions, making the ion selectivity of nanochannels strongly pH dependent (20–22). The surface charge densities of ion-exchange membranes (23) and nanochannels (24) are usually on the order of mC/m^2. The pore size of those membranes prevents transport of molecules having molecular weights greater than 60–100 g/mol (25), a property that makes the membranes ion selective even for solutions with high ionic strength. For nanopores, however, the right solution with the proper ionic strength is absolutely necessary. Ion selectivity can be easily lost when solutions of high ionic strength are used (26–30). However, imparting the ion selectivity to the nanochannel by decreasing the ionic strength can be accompanied by a pH shift (31).

Although these ion-exchange membranes are mainly used in large-scale industrial processes for water treatment, they have also been integrated in microfluidic systems either to study fundamental electrokinetic processes (32–35) or to act as functional elements such as pH actuators (36) or biomolecule preconcentrators (37). One of the most interesting features of ion-exchange membranes is a nonlinear current voltage curve (CVC) (**Figure 1*a***) where two ohmic regions are connected through a limiting region, a behavior that was observed more than 60 years ago (38).

The origin of this nonlinearity is due to different transport numbers of mobile ionic species in the ion-selective membrane and surrounding electrolyte. At low voltages connected to the system, the electrical current is directly proportional to the voltage, which is referred to as the underlimiting region on the CVC. The ohmic resistance in this linear region can arise from the resistance outside the membrane or across the membrane, depending on the relative magnitude of each. However, with increasing voltage, the conductivity jump across the membrane begins to deplete bulk ions on one side of the membrane (depletion side) and enrich it on the other (**Figure 2*a***). The depletion layer near the membrane surface soon becomes the current controlling region of the system. At a certain critical voltage, the concentration of ions in the depletion region drops to almost

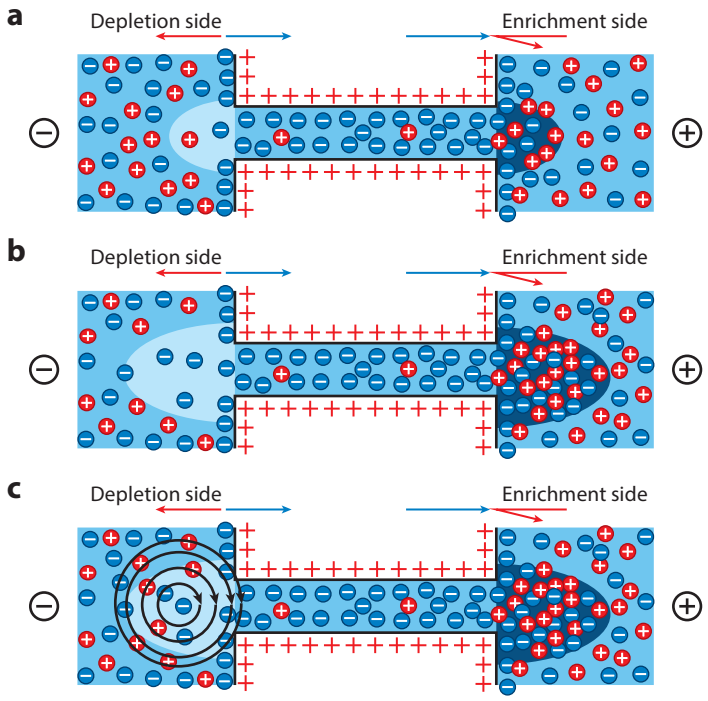

Figure 2

Schematics of the situation around an ion-exchange medium in an (*a*) underlimiting, (*b*) limiting, and (*c*) overlimiting region.

zero, and the current starts to saturate (**Figure 2*b***). This region on the CVC appears as a limiting region. This behavior was described by the concentration polarization theory (39). However, experimental data showed that with increasing voltage an inflection occurs on that curve, giving rise to a second linear region called the overlimiting region. This overlimiting region is a mystery and has been attributed to many possible effects: (*a*) electroconvection, (*b*) water splitting, (*c*) the exaltation, (*d*) natural convection, or (*e*) changes in ion selectivity (40–44). All these effects can contribute to the overlimiting current depending on the experimental setup. However, electroconvection in the depletion region is considered the main mechanism of the overlimiting current (**Figure 2*c***), as it was recently captured in real-time fluorescent experiments with both ion-selective nanochannels (28) and membranes (33, 35). Placing an agar gel in the depletion region is known to suppress the overlimiting current (45), which is also consistent with the electroconvection mechanism.

This electroconvection explained by Rubinstein et al.'s (43) microvortex instability essentially destroys the depletion region by mixing it with the electrolyte bulk. Vortices occurring on the depletion side of the membrane were confirmed using both theoretical analysis (46, 47) of the system and numerical solution of full Navier-Stokes/Poisson-Nernst-Planck models (15, 48–50). Similar CVC with three regions associated with underlimiting, limiting, and overlimiting currents have also been reported for a single nanopore (22, 29, 51). The overlimiting region was caused by Rubinstein's electroconvection instability, which arrested the growth of the depletion region (28). Yossifon & Chang (52) even observed two limiting regions when charged particles were added to the system and created a second ion-selective layer. This gave rise to the second overlimiting region. It was further shown that the pore geometry and the depth of the connecting chamber can have a profound effect on CVC (51). Yossifon et al. (53) showed that changing the width of

a nanochannel (from 2.5 mm down to 50 μm) can lead to the loss of the limiting region on the CVC, even though a pair of vortices caused by induced charged electroosmosis was still observed at the entrance to the nanochannel. Such a linear CVC is often reported for small symmetrical nanochannels as well (21, 54), unless a fixed charge at the entrance to the nanopore has a sign opposite of that inside the nanopore (54), which leads to saturation of the current. The generation of depletion and enrichment regions around nanopores has frequently been observed and used for preconcentration of large molecules (55). A quantitative model (56) and full numerical models (57) of a single nanopore connected to microchambers have confirmed concentration polarization and formation of depletion and enrichment regions around the nanopores. Interestingly, no vortices were observed in systems where a nanochannel with developed ion concentration polarization was used for preconcentration. Systems in which a small piece of a Nafion membrane was used instead, however, revealed vortices in the depletion region (37, 58).

Interestingly, ion-permselective particles (59, 60) were also shown to exhibit depletion and enrichment behavior accompanied by obscure and complex electrokinetic vortices (60). The origin of these microvortices is different from those predicted by Rubinstein's instability theory, as was summarized in a review by Chang et al. (61).

3.2. Bipolar Membranes

By stacking cation- and anion-exchange membranes, we create a so-called bipolar membrane. Bipolar membranes behave as ion-diodes with a strong rectification effect—the ion current is very different for forward and reverse biases. The forward bias causes the formation of an ion-enriched region at the bipolar junction and exhibits a linear CVC ohmic curve (**Figure 3*a***). With reverse bias, the ions are depleted from the bipolar junction, and the local electric field increases with decreasing ionic strength (**Figure 3*b***). At a sufficiently high voltage, the electric field at the bipolar junction becomes sufficiently high to split water, and the junction becomes an ionic reactor that continuously generates H^+ and OH^- ions (36, 62–65). The resulting water-splitting current produces an overlimiting current that is higher than any other mechanism, including that due to electroconvection by the microvortex instability.

3.3. Electroosmotic Flow Across Membranes and Backpressure

There have been very few studies on the importance of electroosmotic (EO) flow to ion flux across ion-selective membranes, but it is generally agreed that it is significant for membranes with larger pores (>10 nm). However, the pumping action of nanoporous membranes, particularly solid-state silica membranes in capillaries, has been well studied in the past decade (66). EO flow through a nanoporous membrane is fed into an open microfluidic channel. To ensure flow balance, a large backpressure builds up at the membrane/channel interface such that a pressure-driven flow can be driven downstream along with a pressure-driven backflow in the membrane to reduce the EO flow. Such EO pumping is ideal for driving flow in a biochip, as it involves no moving parts and can be driven by miniature power sources. However, it is extremely inefficient and was thought to be insufficient to overcome the large hydrodynamic resistance of microchannels on a chip. Paul et al. (67) first realized that this shortcoming of EO flow can be eliminated if a nanoporous ion-selective membrane is inserted into the microfluidic channel as a pumping section. The inefficiency of EO flow is caused by the electroneutral bulk being driven by an electric body force confined to the nanoscale space charge region within one Debye length λ of the charged surface, where it is balanced by a large hydrodynamic shear. With a nanopore smaller than the Debye length, this unfavorable force budget would be eliminated. However, a nanopore much

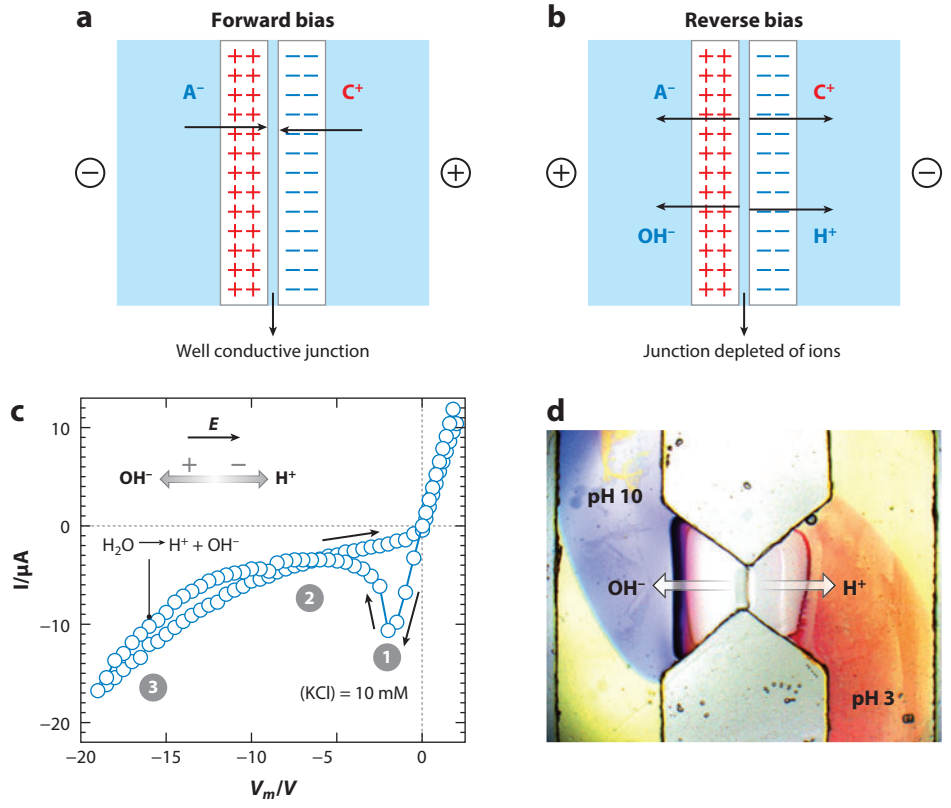

Figure 3

Schematic representation of a bipolar membrane connected in the (*a*) forward and (*b*) reverse bias. "+" and "−" signs represent the surface charge of the membranes. (*c*) I-V curve measured by Cheng & Chang (36) in the reverse bias region showing large overlimiting current and hysteresis. The spike at −2V during the backward scan is due to residual ions from water splitting in the bipolar membrane. Equilibration to the limiting current at −5V occurs after the depletion of residual ions. The numbers 1, 2, and 3 represent the hysteresis, saturation, and water-splitting regimes, respectively. (*d*) Image of pH-sensitive dye across the bipolar membrane showing ejection of H^+ and OH^- ions.

smaller than the Debye length would then produce excessive hydrodynamic stress, higher than even that within a Debye layer in a larger channel. Hence, an optimum EO pump would have a pore size that is roughly the same as λ of the medium—a weakly ion-selective medium. To ensure continuous flow into a downstream microchannel, a pressure maximum would then develop at the end of the nanoporous EO pump region, such that a backpressure reduces the high EO flow in the nanoporous pump and drives a pure pressure-driven flow in the microchannel. In the past 15 years, such nanoporous EO pumps have been developed by packing nanoparticles, fabricating polymer frits or nanoporous alumina in a chip, and sol-gel chemistry synthesis with an on-chip pressure as high as a few atmospheres for the most mechanically strong pumps (68–72). In **Figure 4*a***, we show the scanning electron microscope (SEM) image of a nanoporous silica monolith that has been synthesized by sol-gel chemistry in a silica microcapillary and the large pressure (2 atm) it can sustain at the end of the monolith (**Figure 4*b***). Such large backpressures can drive flow downstream in open channels or even sustain robust electrosprays at the end of the chip such that the electric field both supplies on-chip EO pumping and generates the electrospray (73).

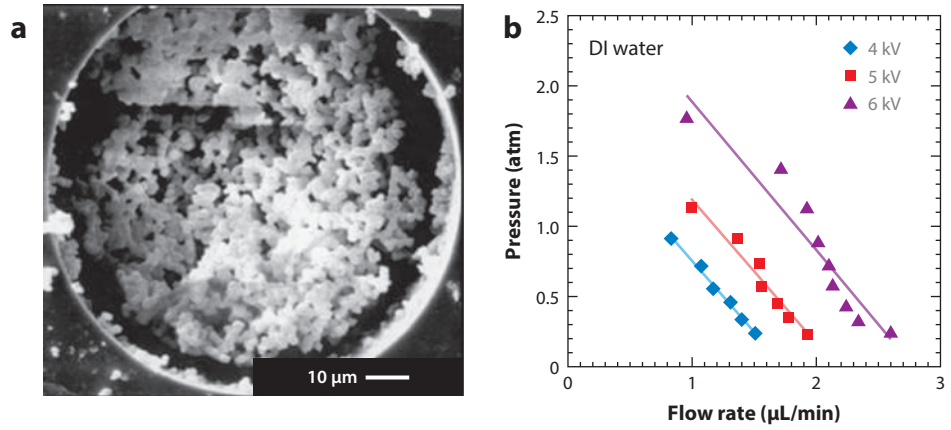

Figure 4

(*a*) Scanning electron microscope image of a nanoporous silica membrane in a glass capillary. Image by Wang et al. (71). (*b*) The no-load pump curve measured by compressing an air bubble at the end of a closed capillary shows a maximum pressure of several atmospheres. Abbreviation: DI, distilled.

3.4. Mixing By Nanoporous Granules

Ion depletion/enrichment across the membrane and vortices in the depleted region that are shown in **Figure 2** for a flat membrane or nanoslot can also be seen across a spherical ion-exchange granule (**Figure 5**). However, the mechanism for the vortices is not due to the Rubinstein instability but to a Dukhin mechanism because of a tangential field around the granule (60). These vortices can be used to enhance the assay time of many transport-limited biological reactions (74).

3.5. Sensitivity to Surface Molecules and Membrane Biosensors

Both the depletion region responsible for the limiting current and the microvortices responsible for the overlimiting current in **Figure 2** are very close to the membrane surface. In fact, the extended polarized region responsible for the microvortex Rubinstein instability is only slightly larger than the Debye length λ, at roughly 100 nm. Hence, the presence of large biomolecules such as DNA can suppress the microvortices and reduce the overlimiting current. This suppression should be even more pronounced if the DNA is of opposite charge from the membrane, such that the depletion and extended space charge regions cannot fully develop. However, at high coverage by an oppositely charged surface molecule, a monolayer may develop, and a bipolar membrane can form. The water-splitting mechanism of **Figure 3** would then reverse the trend and significantly enhance the overlimiting current. This inversion in the overlimiting current suppression was indeed found in a recent report by Slouka et al. (33). As seen in **Figure 6**, negatively charged ssDNAs physisorbed onto positively charged anion-exchange membranes produce two different shifts in the overlimiting current—reducing it at low concentrations but enhancing it at high concentrations. Evidence of water splitting was also seen in the latter case by using pH-sensitive dye. This experiment immediately suggests the possibility of biosensing, if probes can be functionalized onto the depletion side of the membrane. Such a membrane sensor technology would work at the high voltage overlimiting current region but not at the mV region typical for electrochemical sensing techniques. Moreover, this works because ion currents are involved and hence the sensors are not sensitive to redox agents in the sample.

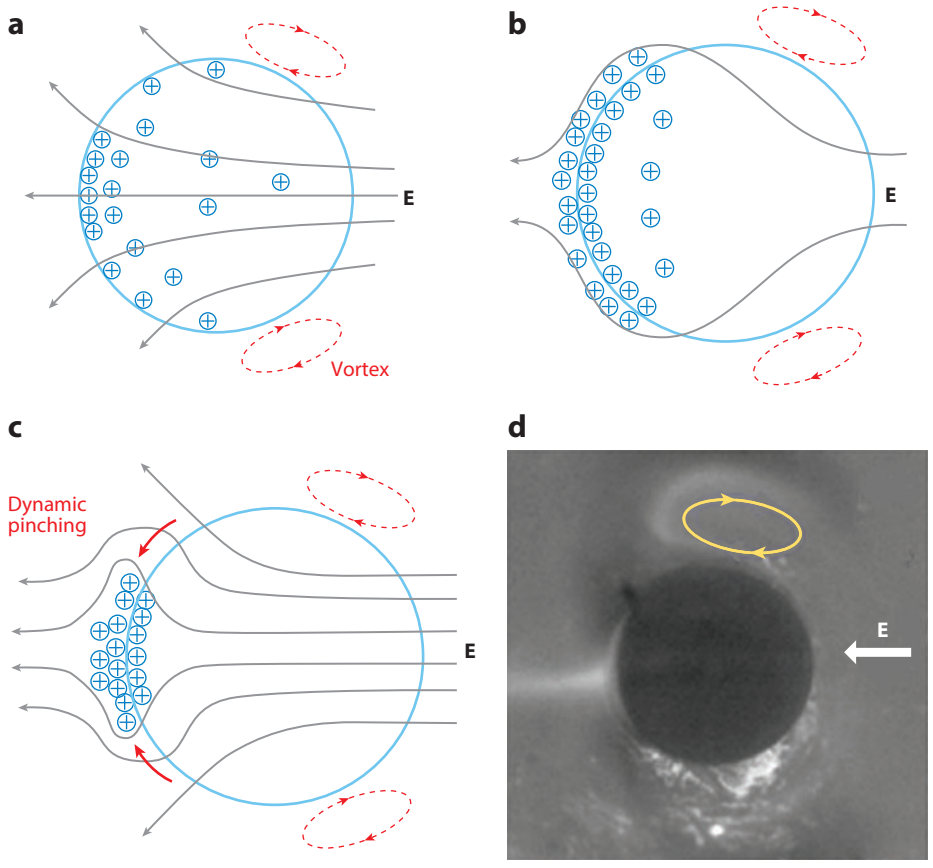

Figure 5

Ion enrichment at one pole of an ion-exchange granule and vortex pair generation at the other pole when an electric field is applied across an ion-selective granule (74). (*a*) Convective charging of the granule by asymmetric vortices at the right. (*b*) Saturation of the double layer by counterions exiting the granule and field screening. (*c*) Dynamic double-layer pinching toward the ejection pole. (*d*) A real image showing the polar ejection and the asymmetric vortices on the other hemisphere.

3.6. Rectification in Nanopores

A phenomenon associated with ion selectivity of nanochannels, which has not been observed for ion-exchange membranes, is rectification observed for nanochannels with a certain type of asymmetry (75, 76). This asymmetry can be caused by the geometry of the nanopores [e.g., a conical shape (21) or a nanopore connected to asymmetric chambers (77, 78)], concentration (79), and pH (80) gradient imposed on the nanochannel or a sudden change in surface charge (24). These asymmetries cause the ion selectivity to vary along the nanochannel in two ways: either (*a*) from strong to weak ion selectivity to the same type of ions (nanochannels with an asymmetry in geometry or with a concentration gradient) or (*b*) two regions of the nanochannel have ion selectivity to cations and anions (nanochannels with a pH gradient or with a change in polarity of the surface charge), respectively.

In conical nanopores, the diameter of the pore increases, thus rendering the tip ion selective, whereas the larger opening does not possess that strong ion selectivity (81). The cause for

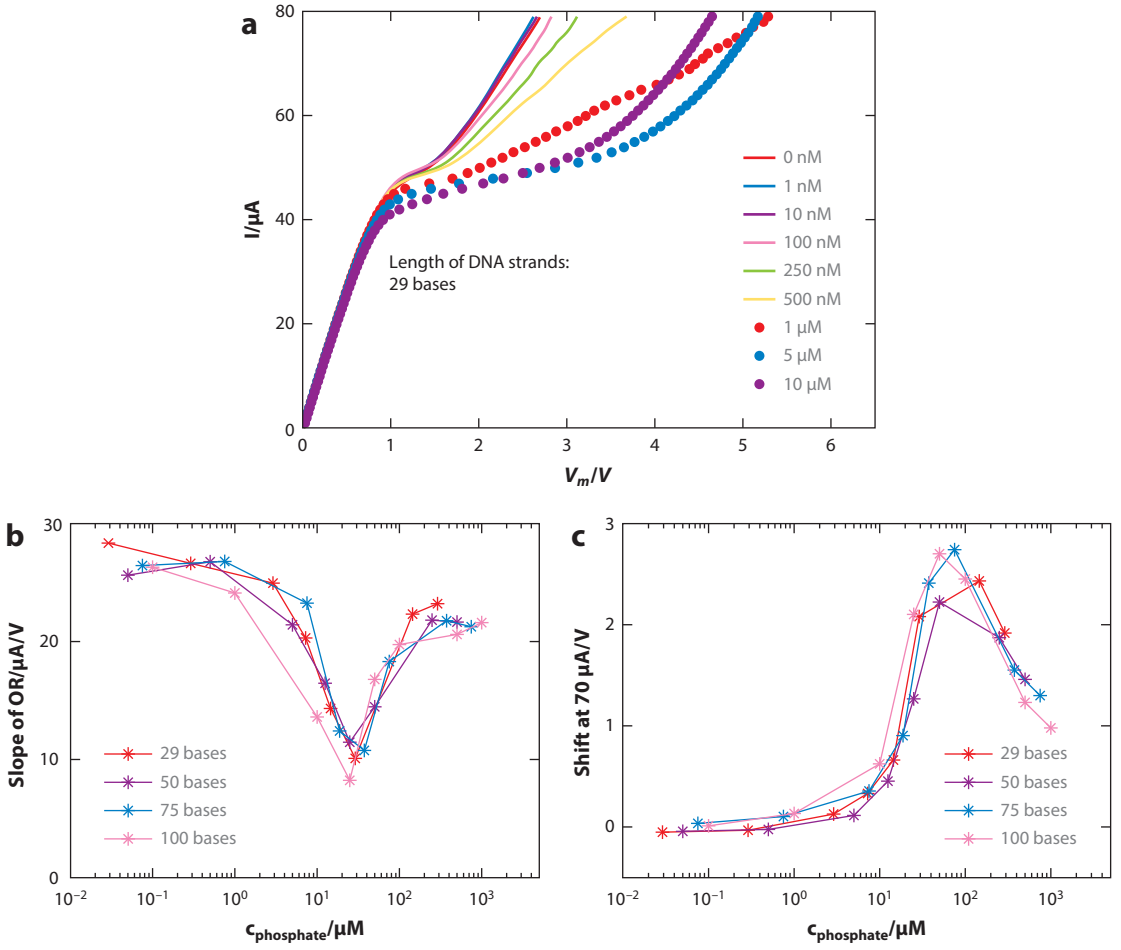

Figure 6

Current voltage curve of an anion-exchange membrane with physisorbed ssDNA (29 nucleotides long) present at different concentrations. (*a*) A reduction in the overlimiting current occurs below 1 μM, but an upward shift develops beyond this critical target concentration. (*b*) Slope of the OR. (*c*) Shift at 70 μA plotted against the concentration of the phosphate groups bound on each DNA sample. Abbreviation: OR, overlimiting region.

rectification in these channels is not yet fully understood (21), but formation of enrichment and depletion regions in the body of the conical nanopore can explain this behavior. The formation of enrichment and depletion regions in the conical nanopore was confirmed by simulations (82) as well as experiments with a fluorescent dye (83). However, the effect of a the surface charge concentration relative to the bulk ionic strength can be very important for conical nanopores (16) and can lead to a curious rectification inversion phenomenon across a critical concentration. Bipolar nanopores with a change in the surface charge (positive and negative) present a group of nanopores similar to bipolar membranes (84, 85). These systems reach the highest rectification factor, and the explanation of this behavior is straightforward. Although a high conductivity region develops in the nanochannel for a forward bias, a low conductivity region is responsible for low currents in the reverse bias connection (86, 87). Interestingly, Cheng & Guo (24) observed

a breakdown of the bipolar nanofluidic diode, which was attributed to a water-splitting reaction occurring at the interface between negatively charged silica and positively charged alumina. The rectification curve was also observed for biological nanopores with imposed pH gradient (80) or engineered nanopores that possess spatially separate regions of opposite charge (88). Cheng & Guo (79) studied the effect of a concentration gradient imposed on homogeneous silica nanochannels. The concentration gradient causes the nanochannel to have different Debye lengths at both ends, which is then responsible for rectification. Although for the forward bias the depletion develops at the low concentration side of the nanochannel and the nanochannel loses its ion selectivity, the reverse bias depletes the ions on the high concentration side of the nanochannel, which enhances the ion selectivity of the nanochannel. These effects result in the formation of high conductive and low conductive solutions in the nanochannel. It is possible that such rectification mechanisms of nanochannels can produce new membrane biosensors, if they are transferred to membranes; the asymmetric charge distribution is the most promising one. They could also be used to improve single pore stochastic sensing (89–92).

4. APPLICATIONS

We review several microfluidic technologies that have been developed based on the phenomena described in the previous sections, culminating in an integrated chip that combines several such technologies. These components pump the sample through the chip (see **Figure 4**), concentrate analytes at certain sensors, mix the reactants, and detect specific molecular targets. Because they are all based on ion currents, it is unnecessary to have microelectrodes within the chip. All electrical connections can be inserted through easily fabricated salt bridges through orifices that also allow fluid exchange.

4.1. Analyte Concentration

The ion depletion at the limiting current region can span across the entire microchannel and be used to prevent convection of charged molecules into the depletion zone, thus trapping them at the upstream edge of the depleted region. Han's group has fabricated nanochannels and proton-hopping Nafion membranes to allow effective concentration of analytes (55, 93, 94). Ion-selective membranes allow easier fabrication of such on-chip analyte concentration modules. As shown in **Figure 7*a***, a cation-exchange membrane UV-polymerized in a microslot bridging two microfluidic channels can induce deionization under voltage biases. The ion-depletion region functioning as an energy barrier traps the molecule passing across it in an electroosmotic flow tangential to the membrane on the side. The UV-curable ion-selective membrane offers superior concentration efficiency and processability to that of prior works using microfabricated nanochannels or Nafion resins. Unlike the 100-nm-thick nanochannels and surface-patterned Nafion thin films, the proposed membrane slot has the same depth as the microfluidic channel, yielding a large junction area. The large cross-sectional area provides greater ion current and better control of ion depletion in the microchannels. Therefore, preconcentration can be achieved in a few seconds. The fluorescence image in **Figure 7*b*** shows the concentration of labeled molecules by two to three orders of magnitude in 10 s from a solution being pumped by electroosmosis from the left to right in the top microfluidic channel, after 10 V is applied across the membrane. Moreover, the UV-curable ion-selective membrane adheres well to glass surfaces functionalized with acrylate-terminated silane, whereas Nafion has poor adhesion to most solid surfaces and the process is more operator dependent.

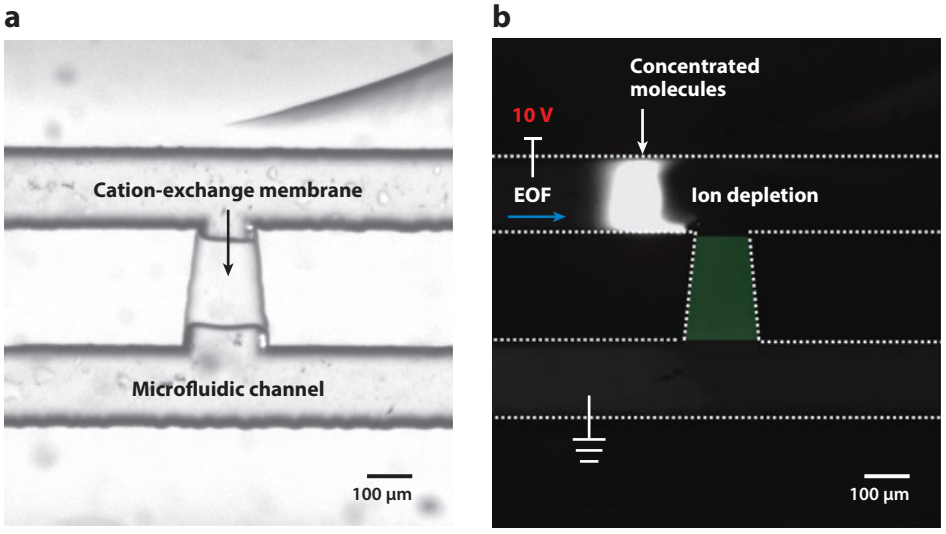

Figure 7

(*a*) A UV cured cation-exchange membrane embedded in a microfluidic channel. (*b*) The membrane produces a depletion region to concentrate charged dye molecules by two to three orders of magnitude in a flowing stream. The scale bars in the images indicate 100 μm. Abbreviation: EOF, electroosmotic flow.

4.2. Integrated Membrane Point-of-Care Diagnostic Unit

Ion concentration polarization on ion-exchange membranes can be employed for separation, concentration, and detection of biomolecules similarly to ion-selective channels. One of the main challenges that researchers often encounter is device fabrication with ion-exchange membranes. These membranes are generally incompatible with the materials traditionally used for fabrication of microfluidic systems. One of the major reasons is the swelling of the membranes when exposed to water solutions. The increase in volume after swelling of the membranes is approximately 50%, and the swelling forces are enormous (like charge repulsion of the fixed functional groups). However, the proper functioning of these membranes requires tight sealing within a microfluidic system so that no current can bypass the membrane. We solved this challenge by using molding resins that allow the tight embedding of these membranes in some functional elements that can be later integrated on a microfluidic chip.

Because ion-exchange membranes develop depletion and enrichment regions when a DC electrical field is applied, we used these effects and a novel nucleic acid sensing mechanism to construct an integrated point-of-care diagnostic platform that integrates three functionally independent units, as illustrated in **Figure 8*a***. The chips are fabricated through thermal bonding of polycarbonate sheets that have been cut to form internal microchannels and orifices for the insertion of the electrode salt bridges, flow tubing, and sample filters. This three-dimensional architecture with vertical integration allows precise control of all the membrane ion circuits on the chip by an external electronic instrumentation, with the ion currents as sensing variables as well as control variables.

The first unit is a pretreatment unit that allows extraction of negatively charged biomolecules (DNA and RNA mainly) from cell lysates through a thin layer of agar gel (**Figure 9*a***), whose working principle is similar to gel electrophoresis. The negatively charged nucleic acid molecules accumulate on the enrichment side of a cation-exchange membrane, which prevents the negatively

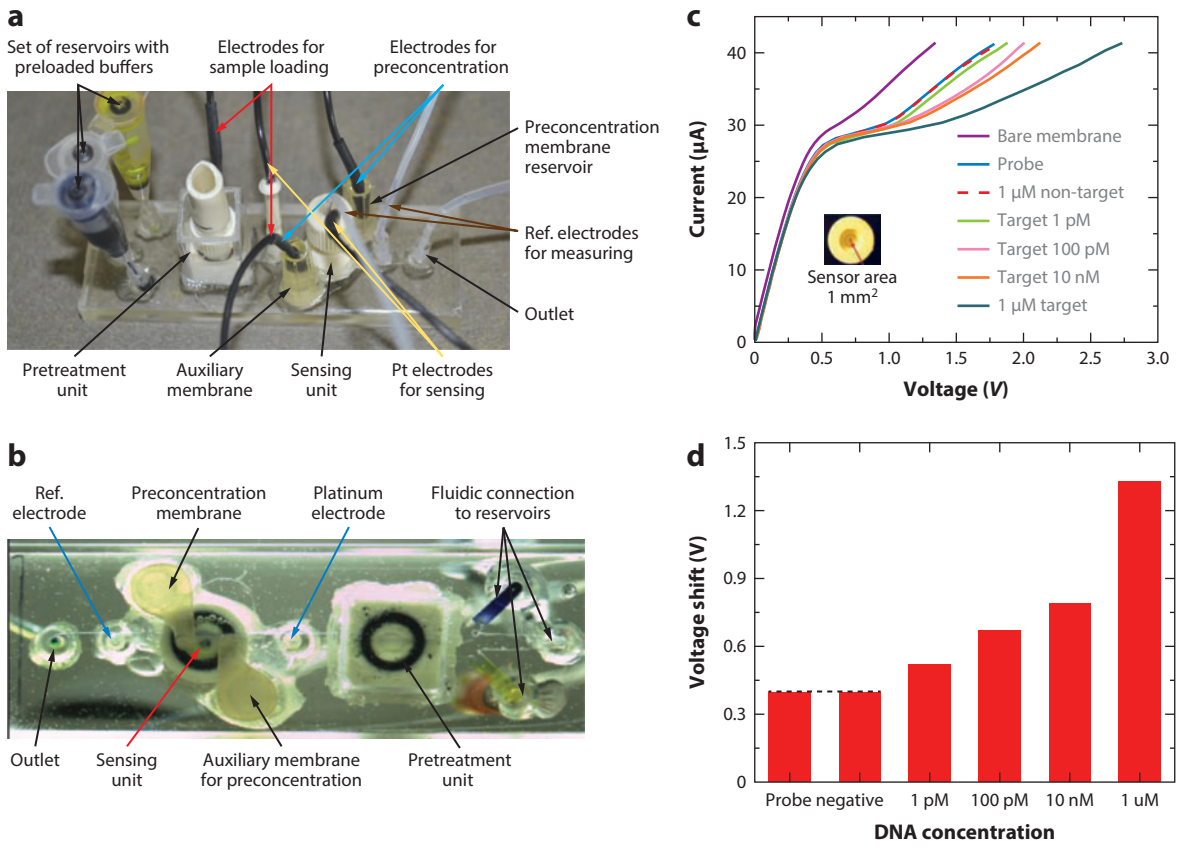

Figure 8

(*a*) Top and (*b*) bottom view of an ion-exchange-membrane-based integrated point-of-care diagnostic platform. pM to μM concentrations of target DNA are added to the same sensor to evaluate the dynamic range. (*c*) Results show an improvement in the sensor sensitivity down to 1 pM concentration by reducing the sensor area to 1 mm^2 (*inset*). (*d*) Histogram showing changes in potential (from bare membrane) at different DNA concentrations.

charged molecules to leave the main channel by both electrostatic repulsion and the sieving effect. When those negatively charged molecules are loaded into the main channel, another unit called the preconcentration unit collects and concentrates all the loaded molecules at a specific location in the main channel (**Figure 9*b***). The preconcentration unit consists of two cation-exchange membranes. One membrane creates a depletion region within the main channel that functions as an ionic filter and the other is just an auxiliary membrane that allows us to connect the electrical field to a specific part of the main channel. The position of the preconcentration slug can be controlled by counterbalancing the convective flow and depletion driven by the voltage applied on the system.

This feature which decouples the control of the flow rate and the extension of depletion makes our platform unique. By positioning the preconcentration slug right at a detection unit, we can achieve very fast detection of target nucleic acids. The detection unit is based on a charge inversion phenomenon that occurs when negatively charged nucleic acid molecules adsorb on a positively charged anion-exchange membrane. The charge inversion brings about two main effects: (*a*) It suppresses vortices on the membrane and (*b*) it enhances a water-splitting reaction at an interface

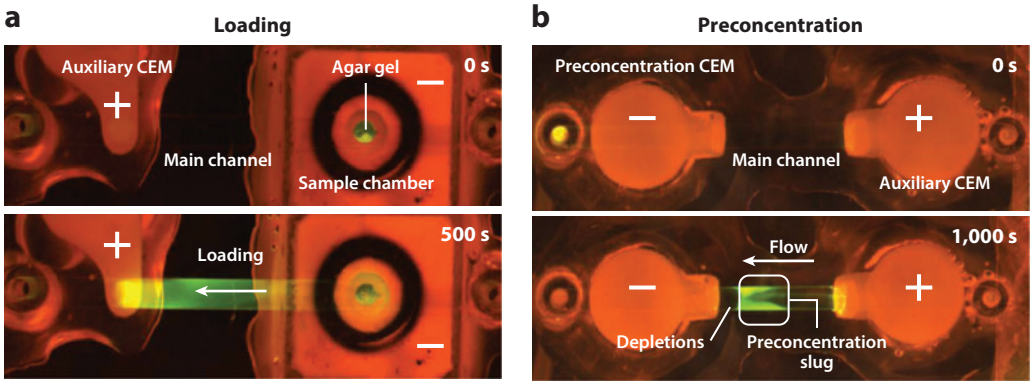

Figure 9

(*a*) Loading of fluorescently labeled DNA from a sample chamber and accumulation of the DNA on the enrichment side of the CEM. (*b*) Preconcentration of fluorescently labeled DNA. Abbreviation: CEM, cation-exchange membrane.

between the positive membrane and negatively charged molecules that behaves as a bipolar junction. In turn, this behavior is reflected in the CVC, where the limiting region prolongs, and the overlimiting region shifts toward higher voltages. This shift in the overlimiting region of the CVC indicates the presence of negatively charged molecules on a membrane surface. When such a membrane is first functionalized with a target-specific short oligoprobe, it makes the sensor specific to that target pathogen. Any shift in the CVC will indicate the successful capture of target nucleic acid by increasing the net negative charge on the membrane surface with a hybridization event. An example of a nucleic acid detection signal is plotted in **Figure 8*c***, which shows pM to μM

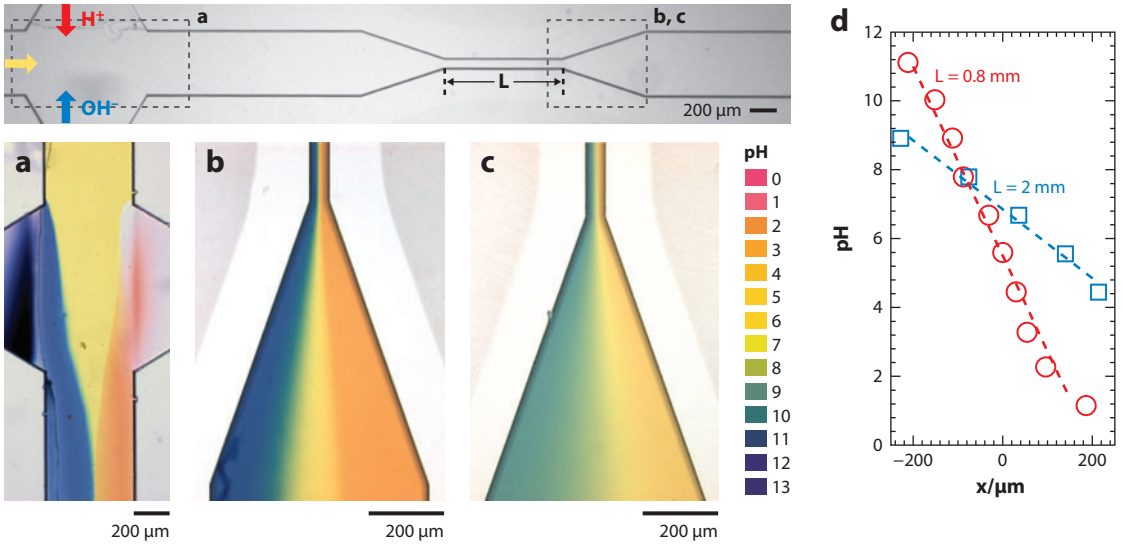

Figure 10

(*a*) Abrupt pH profile builds up near the pH actuators upstream. Different pH gradients were generated across a 500-μm-wide channel downstream after passing through a (*b*) 0.8-mm-long or (*c*) 2-mm-long, 50-μm-wide narrowed channel. (*d*) pH profiles across the downstream of channel in panels *b* and *c*.

dynamic range detection of DNA molecules on a 1-mm^2 sensing area. The simple fabrication and low cost make this detection platform very useful in point-of-care diagnostics.

4.3. Membrane Molecular Separation Techniques

We have also developed a pH actuation unit based on the water-splitting reaction occurring in the bipolar junction by a pair of ion exchange membranes when reverse bias is connected to the system (36). By using two bipolar junctions integrated into a single microchannel, we created a system where the production of H^+ and OH^- ions is controlled independently by applying different voltages on the junction. Mixing these two ions generated at the bipolar junctions downstream of the main channel creates either a gradient in pH across the channel or a solution of a given pH (**Figure 10*a***). This technology thus provides an easy pH tuning tool in a microfluidic channel that can be employed, e.g., for isoelectric focusing separation of proteins (**Figure 10*b***).

5. CONCLUSION

Ion-selective membranes offer several unique functionalities for microfluidic systems that cannot be easily introduced by mechanical, electrochemical, and other techniques in microfluidics. They allow on-chip pumping, mixing, pH actuation, analyte concentration/separation, and target sensing—just about all the functionalities one needs for point-of-care diagnostics or even mass spectrometry interfaces. Moreover, they can be integrated into biochips with minimal effort, thus allowing disposable biochips, and can be easily controlled with a supervising electronic instrument detached from the disposable biochips. The biochips also lend themselves to easy rapid prototyping so that different designs can be optimized and tested. We see membrane microfluidics as a promising direction for field-used portable diagnostic devices.

DISCLOSURE STATEMENT

The authors are not aware of any affiliations, memberships, funding, or financial holdings that might be perceived as affecting the objectivity of this review.

ACKNOWLEDGMENTS

This work is supported by Army Corps of Engineers W9132T, Walther Cancer Fund 0120, USDA 2012-67005-19589, and NSF-CBET 1065652.

LITERATURE CITED

1. Strathmann H, Grabowski A, Eigenberger G. 2013. Ion-exchange membranes in the chemical process industry. *Ind. Eng. Chem. Res.* 52:10364–79
2. Park S, Chung T, Kim H. 2009. Ion bridges in microfluidic systems. *Microfluid Nanofluid* 6:315–31
3. Mortensen NA, Olesen LH, Okkels F, Bruus H. 2007. Mass and charge transport in micro and nanofluidic channels. *Nanoscale Microscale Thermophys. Eng.* 11:57–69
4. Yuan Z, Garcia AL, Lopez GP, Petsev DN. 2007. Electrokinetic transport and separations in fluidic nanochannels. *Electrophoresis* 28:595–610
5. Sparreboom W, van den Berg A, Eijkel JCT. 2010. Transport in nanofluidic systems: a review of theory and applications. *New J. Phys.* 12:015004
6. Piruska A, Gong M, Sweedler JV, Bohn PW. 2010. Nanofluidics in chemical analysis. *Chem. Soc. Rev.* 39:1060–72

7. Napoli M, Eijkel JCT, Pennathur S. 2010. Nanofluidic technology for biomolecule applications: a critical review. *Lab Chip* 10:957–85
8. Sollner K. 1950. Recent advances in the electrochemistry of membranes of high ionic selectivity. *J. Electrochem. Soc.* 97:C139–51
9. Meyer KH. 1937. Artificial membranes: their structure and permeability. *Trans. Faraday Soc.* 33:1073–80
10. Teorell T. 1935. Studies on the "diffusion effect" upon ionic distribution I. Some theoretical considerations. *Proc. Natl. Acad. Sci. USA* 21:152–61
11. Teorell T. 1935. An attempt to formulate a quantitative theory of membrane permeability. *Proc. Soc. Exp. Biol. Med.* 33:282–85
12. Donnan FG. 1911. Theory of the balances of membranes and potential of membranes at the existence of non dialysing electrolytes—a contribution to physical chemical physiology. *Z. Elektrochem. Angew. Phys. Chem.* 17:572–81
13. Chang HC, Yeo LY. 2010. *Electrokinetically Driven Microfluidics and Nanofluidics*. Cambridge/New York: Cambridge Univ. Press.
14. Daiguji H. 2010. Ion transport in nanofluidic channels. *Chem. Soc. Rev.* 39:901–11
15. Postler T, Slouka Z, Svoboda M, Pribyl M, Snita D. 2008. Parametrical studies of electroosmotic transport characteristics in submicrometer channels. *J. Colloid Interface Sci.* 320:321–32
16. Yan Y, Wang L, Xue JM, Chang HC. 2013. Ion current rectification inversion in conic nanopores: nonequilibrium ion transport biased by ion selectivity and spatial asymmetry. *J. Chem. Phys.* 138:044706
17. Plecis A, Pallandre A, Haghiri-Gosnet AM. 2011. Ionic and mass transport in micro-nanofluidic devices: a matter of volumic surface charge. *Lab Chip* 11:795–804
18. Tanaka Y. 2007. Chapter 1: Preparation of ion exchange membranes. In *Membrane Science and Technology*, ed. T Yoshinobu, pp. 3–16. Amsterdam: Elsevier
19. Prakash P, Hoskins D, SenGupta AK. 2004. Application of homogeneous and heterogeneous cation-exchange membranes in coagulant recovery from water treatment plant residuals using Donnan membrane process. *J. Membr. Sci.* 237:131–44
20. Fornasiero F, Bin In J, Kim S, Park HG, Wang Y, et al. 2010. pH-Tunable ion selectivity in carbon nanotube pores. *Langmuir* 26:14848–53
21. Siwy ZS. 2006. Ion-current rectification in nanopores and nanotubes with broken symmetry. *Adv. Funct. Mater.* 16:735–46
22. Chang CC, Yeh CP, Yang RJ. 2012. Ion concentration polarization near microchannel-nanochannel interfaces: effect of pH value. *Electrophoresis* 33:758–64
23. Kang MS, Choi YJ, Moon SH. 2004. Effects of charge density on water splitting at cation-exchange membrane surface in the over-limiting current region. *Korean J. Chem. Eng.* 21:221–29
24. Cheng LJ, Guo LJ. 2009. Ionic current rectification, breakdown, and switching in heterogeneous oxide nanofluidic devices. *ACS Nano* 3:575–84
25. Choi JH, Moon SH. 2001. Pore size characterization of cation-exchange membranes by chronopotentiometry using homologous amine ions. *J. Membr. Sci.* 191:225–36
26. Vlassiouk I, Smirnov S, Siwy Z. 2008. Ionic selectivity of single nanochannels. *Nano Lett.* 8:1978–85
27. Vlassiouk I, Apel PY, Dmitriev SN, Healy K, Siwy ZS. 2009. Versatile ultrathin nanoporous silicon nitride membranes. *Proc. Natl. Acad. Sci. USA* 106:21039–44
28. Yossifon G, Chang HC. 2008. Selection of nonequilibrium overlimiting currents: universal depletion layer formation dynamics and vortex instability. *Phys. Rev. Lett.* 101:254501
29. Yossifon G, Mushenheim P, Chang YC, Chang HC. 2009. Nonlinear current-voltage characteristics of nanochannels. *Phys. Rev. E* 79:046305
30. Duan CH, Majumdar A. 2010. Anomalous ion transport in 2-nm hydrophilic nanochannels. *Nat. Nanotechnol.* 5:848–52
31. Bottenus D, Oh YJ, Han SM, Ivory CF. 2009. Experimentally and theoretically observed native pH shifts in a nanochannel array. *Lab Chip* 9:219–31
32. Svoboda M, Slouka Z, Schrott W, Snita D. 2009. Cation exchange membrane integrated into a microfluidic device. *Microelectron. Eng.* 86:1371–74
33. Slouka Z, Senapati S, Yan Y, Chang HC. 2013. Charge inversion, water splitting, and vortex suppression due to DNA sorption on ion-selective membranes and their ion-current signatures. *Langmuir* 29:8275–83

34. Svoboda M, Kratochvila J, Lindner J, Pribyl M, Snita D. 2011. Dynamic behaviour of a diffusion layer around a cation-exchange membrane in an external electric field. *Microelectron. Eng.* 88:1789–91
35. Kwak R, Guan GF, Peng WK, Han JY. 2013. Microscale electrodialysis: concentration profiling and vortex visualization. *Desalination* 308:138–46
36. Cheng LJ, Chang HC. 2011. Microscale pH regulation by splitting water. *Biomicrofluidics* 5:046502
37. Ko SH, Song YA, Kim SJ, Kim M, Han J, Kang KH. 2012. Nanofluidic preconcentration device in a straight microchannel using ion concentration polarization. *Lab Chip* 12:4472–82
38. Frilette VJ. 1957. Electrogravitational transport at synthetic ion exchange membrane surfaces. *J. Phys. Chem. B* 61:168–74
39. Krol JJ, Wessling M, Strathmann H. 1999. Concentration polarization with monopolar ion exchange membranes: current-voltage curves and water dissociation. *J. Membr. Sci.* 162:145–54
40. Belova E, Lopatkova G, Pismenskaya N, Nikonenko V, Larchet C. 2006. Role of water splitting in development in ion-exchange membrane of electroconvection systems. *Desalination* 199:59–61
41. Belova EI, Lopatkova GY, Pismenskaya ND, Nikonenko VV, Larchet C, Pourcelly G. 2006. Effect of anion-exchange membrane surface properties on mechanisms of overlimiting mass transfer. *J. Phys. Chem. B* 110:13458–69
42. Choi JH, Kim SH, Moon SH. 2001. Heterogeneity of ion-exchange membranes: the effects of membrane heterogeneity on transport properties. *J. Colloid Interface Sci.* 241:120–26
43. Rubinstein I, Staude E, Kedem O. 1988. Role of the membrane-surface in concentration polarization at ion-exchange membrane. *Desalination* 69:101–14
44. Andersen MB, van Soestbergen M, Mani A, Bruus H, Biesheuvel PM, Bazant MZ. 2012. Current-induced membrane discharge. *Phys. Rev. Lett.* 109:108301
45. Maletzki F, Rosler HW, Staude E. 1992. Ion transfer across electrodialysis membranes in the overlimiting current range: stationary voltage current characteristics and current noise power spectra under different conditions of free convection. *J. Membr. Sci.* 71:105–15
46. Rubinstein I, Maletzki F. 1991. Electroconvection at an electrically inhomogeneous permselective membrane surface. *J. Chem. Soc.-Faraday Trans.* 87:2079–87
47. Rubinstein I, Zaltzman B. 2000. Electro-osmotically induced convection at a permselective membrane. *Phys. Rev. E* 62:2238–51
48. Druzgalski CL, Andersen MB, Mani A. 2013. Direct numerical simulation of electroconvective instability and hydrodynamic chaos near an ion-selective surface. *Phys. Fluids* 25:110804–17
49. Pham VS, Li ZR, Lim KM, White JK, Han JY. 2012. Direct numerical simulation of electroconvective instability and hysteretic current-voltage response of a permselective membrane. *Phys. Rev. E* 86:046310
50. Nandigana VVR, Aluru NR. 2012. Understanding anomalous current-voltage characteristics in microchannel-nanochannel interconnect devices. *J. Colloid Interface Sci.* 384:162–71
51. Yossifon G, Mushenheim P, Chang HC. 2010. Controlling nanoslot overlimiting current with the depth of a connecting microchamber. *EPL* 90:64004
52. Yossifon G, Chang HC. 2010. Changing nanoslot ion flux with a dynamic nanocolloid ion-selective filter: secondary overlimiting currents due to nanocolloid-nanoslot interaction. *Phys. Rev. E* 81:066317
53. Yossifon G, Mushenheim P, Chang YC, Chang HC. 2010. Eliminating the limiting-current phenomenon by geometric field focusing into nanopores and nanoslots. *Phys. Rev. E* 81:046301
54. Cheng LJ, Guo LJ. 2010. Entrance effect on ion transport in nanochannels. *Microfluid Nanofluid* 9:1033–39
55. Wang YC, Stevens AL, Han JY. 2005. Million-fold preconcentration of proteins and peptides by nanofluidic filter. *Anal. Chem.* 77:4293–99
56. Li GB, Wang SL, Byun CK, Wang XY, Liu SR. 2009. A quantitative model to evaluate the ion-enrichment and ion-depletion effect at microchannel-nanochannel junctions. *Anal. Chim. Acta* 650:214–20
57. Wang Y, Pant K, Chen ZJ, Wang GR, Diffey WF, et al. 2009. Numerical analysis of electrokinetic transport in micro-nanofluidic interconnect preconcentrator in hydrodynamic flow. *Microfluid Nanofluid* 7:683–96
58. Kim SJ, Ko SH, Kwak R, Posner JD, Kang KH, Han J. 2012. Multi-vortical flow inducing electrokinetic instability in ion concentration polarization layer. *Nanoscale* 4:7406–10

59. Ehlert S, Hlushkou D, Tallarek U. 2008. Electrohydrodynamics around single ion-permselective glass beads fixed in a microfluidic device. *Microfluid Nanofluid* 4:471–87
60. Ben Y, Chang HC. 2002. Nonlinear Smoluchowski slip velocity and micro-vortex generation. *J. Fluid Mech.* 461:229–38
61. Chang HC, Yossifon G, Demekhin EA. 2012. Nanoscale electrokinetics and microvortices: how microhydrodynamics affects nanofluidic ion flux. *Annu. Rev. Fluid Mech.* 44:401–26
62. Harnisch F, Schroder U, Scholz F. 2008. The suitability of monopolar and bipolar ion exchange membranes as separators for biological fuel cells. *Environ. Sci. Technol.* 42:1740–46
63. Aritomi T, van den Boomgaard T, Strathmann H. 1996. Current-voltage curve of a bipolar membrane at high current density. *Desalination* 104:13–18
64. Conroy DT, Craster RV, Matar OK, Cheng LJ, Chang HC. 2012. Nonequilibrium hysteresis and Wien effect water dissociation at a bipolar membrane. *Phys. Rev. E* 86:056104
65. Desharnais BM, Lewis BAG. 2002. Electrochemical water splitting at bipolar interfaces of ion exchange membranes and soils. *Soil Sci. Soc. Am. J.* 66:1518–25
66. Wang XY, Cheng C, Wang SL, Liu SR. 2009. Electroosmotic pumps and their applications in microfluidic systems. *Microfluid Nanofluid* 6:145–62
67. Paul PH, Arnold DW, Rakestraw DJ. 2000. Electrokinetic generation of high pressures using porous microstructures. *Micro Total Anal. Syst.* 1998:49–52
68. Zeng SL, Chen CH, Mikkelsen JC, Santiago JG. 2001. Fabrication and characterization of electroosmotic micropumps. *Sens. Actuators B* 79:107–14
69. Zeng SL, Chen CH, Santiago JG, Chen JR, Zare RN, et al. 2002. Electroosmotic flow pumps with polymer frits. *Sens. Actuators B* 82:209–12
70. Tripp JA, Svec F, Frechet JMJ, Zeng SL, Mikkelsen JC, Santiago JG. 2004. High-pressure electroosmotic pumps based on porous polymer monoliths. *Sens. Actuators B* 99:66–73
71. Wang P, Chen ZL, Chang HC. 2006. A new electro-osmotic pump based on silica monoliths. *Sens. Actuators B* 113:500–9
72. Berrouche Y, Avenas Y, Schaeffer C, Chang HC, Wang P. 2009. Design of a porous electroosmotic pump used in power electronic cooling. *IEEE Trans. Ind. Appl.* 45:2073–79
73. Chen Z, Wang P, Chang HC. 2005. An electro-osmotic micro-pump based on monolithic silica for micro-flow analyses and electro-sprays. *Anal. Bioanal. Chem.* 382:817–24
74. Wang SC, Wei HH, Chen HP, Tsai MH, Yu CC, Chang HC. 2008. Dynamic superconcentration at critical-point double-layer gates of conducting nanoporous granules due to asymmetric tangential fluxes. *Biomicrofluidics* 2:014102
75. Cheng LJ, Guo LJ. 2010. Nanofluidic diodes. *Chem. Soc. Rev.* 39:923–38
76. Nguyen G, Vlassiouk I, Siwy ZS. 2010. Comparison of bipolar and unipolar ionic diodes. *Nanotechnology* 21:265301
77. Yossifon G, Chang YC, Chang HC. 2009. Rectification, gating voltage, and interchannel communication of nanoslot arrays due to asymmetric entrance space charge polarization. *Phys. Rev. Lett.* 103:154502
78. Jung JY, Joshi P, Petrossian L, Thornton TJ, Posner JD. 2009. Electromigration current rectification in a cylindrical nanopore due to asymmetric concentration polarization. *Anal. Chem.* 81:3128–33
79. Cheng LJ, Guo LJ. 2007. Rectified ion transport through concentration gradient in homogeneous silica nanochannels. *Nano Lett.* 7:3165–71
80. García-Giménez E, Alcaraz A, Aguilella VM, Ramírez P. 2009. Directional ion selectivity in a biological nanopore with bipolar structure. *J. Membr. Sci.* 331:137–42
81. Apel PY, Blonskaya IV, Levkovich NV, Orelovich OL. 2011. Asymmetric track membranes: relationship between nanopore geometry and ionic conductivity. *Pet. Chem.* 51:555–67
82. Hlushkou D, Perry JM, Jacobson SC, Tallarek U. 2012. Propagating concentration polarization and ionic current rectification in a nanochannel-nanofunnel device. *Anal. Chem.* 84:267–74
83. Perry JM, Zhou KM, Harms ZD, Jacobson SC. 2010. Ion transport in nanofluidic funnels. *ACS Nano* 4:3897–902
84. Yan RX, Liang WJ, Fan R, Yang PD. 2009. Nanofluidic diodes based on nanotube heterojunctions. *Nano Lett.* 9:3820–25

85. Karnik R, Duan CH, Castelino K, Daiguji H, Majumdar A. 2007. Rectification of ionic current in a nanofluidic diode. *Nano Lett.* 7:547–51
86. Constantin D, Siwy ZS. 2007. Poisson-Nernst-Planck model of ion current rectification through a nanofluidic diode. *Phys. Rev. E* 76:041202
87. Vlassiouk I, Siwy ZS. 2007. Nanofluidic diode. *Nano Lett.* 7:552–56
88. Miedema H, Vrouenraets M, Wierenga J, Meijberg W, Robillard G, Eisenberg B. 2007. A biological porin engineered into a molecular, nanofluidic diode. *Nano Lett.* 7:2886–91
89. Venkatesan BM, Bashir R. 2011. Nanopore sensors for nucleic acid analysis. *Nat. Nanotechnol.* 6:615–24
90. Liu AH, Zhao QT, Guan XY. 2010. Stochastic nanopore sensors for the detection of terrorist agents: current status and challenges. *Anal. Chim. Acta* 675:106–15
91. Jayawardhana DA, Crank JA, Zhao Q, Armstrong DW, Guan XY. 2009. Nanopore stochastic detection of a liquid explosive component and sensitizers using boromycin and an ionic liquid supporting electrolyte. *Anal. Chem.* 81:460–64
92. Krishantha DMM, Breitbach ZS, Padivitage NLT, Armstrong DW, Guan XY. 2011. Rapid determination of sample purity and composition by nanopore stochastic sensing. *Nanoscale* 3:4593–96
93. Lee JH, Song YA, Han JY. 2008. Multiplexed proteomic sample preconcentration device using surface-patterned ion-selective membrane. *Lab Chip* 8:596–601
94. Liu V, Song YA, Han JY. 2010. Capillary-valve-based fabrication of ion-selective membrane junction for electrokinetic sample preconcentration in PDMS chip. *Lab Chip* 10:1485–90

Annual Review of
Analytical Chemistry

Volume 7, 2014

Contents

A Life in Electrochemistry
Allen J. Bard 1

Biologically Inspired Nanofibers for Use in Translational Bioanalytical Systems
Lauren Matlock-Colangelo and Antje J. Baeumner 23

Analytical Approaches for Size and Mass Analysis of Large Protein Assemblies
Joost Snijder and Albert J.R. Heck 43

Nano/Micro and Spectroscopic Approaches to Food Pathogen Detection
Il-Hoon Cho, Adarsh D. Radadia, Khashayar Farrokhzad, Eduardo Ximenes, Euiwon Bae, Atul K. Singh, Haley Oliver, Michael Ladisch, Arun Bhunia, Bruce Applegate, Lisa Mauer, Rashid Bashir, and Joseph Irudayaraj 65

Optical Imaging of Individual Plasmonic Nanoparticles in Biological Samples
Lehui Xiao and Edward S. Yeung 89

Mass Spectrometric Analysis of Histone Proteoforms
Zuo-Fei Yuan, Anna M. Arnaudo, and Benjamin A. Garcia 113

Ultrafast 2D NMR: An Emerging Tool in Analytical Spectroscopy
Patrick Giraudeau and Lucio Frydman 129

Electroanalysis at the Nanoscale
Karen Dawson and Alan O'Riordan 163

Light-Emitting Diodes for Analytical Chemistry
Mirek Macka, Tomasz Piasecki, and Purnendu K. Dasgupta 183

Energetics-Based Methods for Protein Folding and Stability Measurements
M. Ariel Geer and Michael C. Fitzgerald 209

Ambient Femtosecond Laser Vaporization and Nanosecond Laser Desorption Electrospray Ionization Mass Spectrometry
Paul Flanigan and Robert Levis 229

Engineered Proteins for Bioelectrochemistry
Muhammad Safwan Akram, Jawad Ur Rehman, and Elizabeth A.H. Hall 257

Microfluidics-Based Single-Cell Functional Proteomics for Fundamental and Applied Biomedical Applications
Jing Yu, Jing Zhou, Alex Sutherland, Wei Wei, Young Shik Shin, Min Xue, and James R. Heath 275

Point-of-Care Platforms
Günter Gauglitz 297

Microfluidic Systems with Ion-Selective Membranes
Zdenek Slouka, Satyajyoti Senapati, and Hsueh-Chia Chang 317

Solid-Phase Biological Assays for Drug Discovery
Erica M. Forsberg, Clémence Sicard, and John D. Brennan 337

Resonance-Enhanced Multiphoton Ionization Mass Spectrometry (REMPI-MS): Applications for Process Analysis
Thorsten Streibel and Ralf Zimmermann 361

Nanoscale Methods for Single-Molecule Electrochemistry
Klaus Mathwig, Thijs J. Aartsma, Gerard W. Canters, and Serge G. Lemay 383

Nucleic Acid Aptamers for Living Cell Analysis
Xiangling Xiong, Yifan Lv, Tao Chen, Xiaobing Zhang, Kemin Wang, and Weihong Tan 405

High-Throughput Proteomics
Zhaorui Zhang, Si Wu, David L. Stenoien, and Ljiljana Paša-Tolić 427

Analysis of Exhaled Breath for Disease Detection
Anton Amann, Wolfram Miekisch, Jochen Schubert, Bogusław Buszewski, Tomasz Ligor, Tadeusz Jezierski, Joachim Pleil, and Terence Risby 455

Ionophore-Based Optical Sensors
Günter Mistlberger, Gastón A. Crespo, and Eric Bakker 483

Resistive-Pulse Analysis of Nanoparticles
Long Luo, Sean R. German, Wen-Jie Lan, Deric A. Holden, Tony L. Mega, and Henry S. White 513

Concerted Proton-Electron Transfers: Fundamentals and Recent Developments
Jean-Michel Savéant 537

Available online at www.sciencedirect.com
ScienceDirect
Journal of Colloid and Interface Science 320 (2008) 321–332
JOURNAL OF Colloid and Interface Science
www.elsevier.com/locate/jcis

Parametrical studies of electroosmotic transport characteristics in submicrometer channels

T. Postler, Z. Slouka, M. Svoboda, M. Přibyl *, D. Šnita

Center for Nonlinear Dynamics of Chemical and Biological Systems, Department of Chemical Engineering, Institute of Chemical Technology, Technická 5, 166 28 Prague 6, Czech Republic

Received 14 September 2007; accepted 31 October 2007

Available online 16 January 2008

Abstract

Spatially two-dimensional nonequilibrium mathematical model describing electroosmotic flow through a submicrometer channel with an electric charge fixed on the channel walls is presented. This system is governed by the hydrodynamic, electrostatic, and mass transport phenomena. The model is based on the coupled mass balances, Poisson, Navier–Stokes, and Nernst–Planck equations. Nonslip boundary conditions are employed. The effect of an imposed electric field on the system behavior is studied by means of a numerical analysis of the model equations. We have obtained the following findings. If the channel width is comparable to the thickness of the electric double layer, the system behaves as an ion-exchange membrane and the dependence of the electric current passing through the channel on the applied voltage is strongly nonlinear. In the case of negatively (positively) charged walls, a narrow region of very low conductivity (so-called *ionic gate*) is formed in the free electrolyte near the channel entry facing the anode (cathode) side. For a wide channel, the electric current is proportional to the applied voltage and the velocity of electrokinetic flow is linearly proportional to the electric field strength. Complex hydrodynamics (eddy formation and existence of ionic gates) is the most interesting characteristics of the studied system. Hence, current–voltage and velocity–voltage curves and the corresponding spatial distributions of the model variables at selected points are studied and described in detail.

Keywords: DC electroosmosis; Submicrometer channel; Mathematical modeling; Nonequilibrium model; Complex hydrodynamics

1. Introduction

Microfluidic and more recently nanofluidic devices are rapidly emerging tools with a broad range of applications [1,2]. The familiar techniques used in macroscale applications for fluid manipulation do not work on the microscale because of the presence of viscous damping. The microscale mixing of miscible fluids occurs without the contribution of turbulence and thus relies on molecular diffusion alone. The pressure-driven flow has poor scaling on the microscale and does not offer any simple local flow control. Innovative ideas are being considered for pumping [3,4], mixing [5], manipulation [6], and separation [7] on the microscale. Due to the rapid development of microfabrication technologies over the past decade, the electroosmotic flow (EOF) became one of the most popular nonmechanical techniques for the fluid manipulation. EOF is the motion of the bulk liquid caused by the action of an electric field on a mobile electric charge at the solid–liquid interface [8,9]. The origin of the electric charge at the phase interface comes from the dissociation of surface groups or the adsorption of electrically charged molecules from the solution. For example, silica surfaces usually acquire a negative electric charge when immersed into an aqueous solution due to the dissociation of surface silanol groups. Applications of EOF are found in many fields of science as diverse as biotechnology (e.g., DNA analysis [10], DNA amplification [11], proteomics [12]), bioanalytical chemistry [13], electrokinetic remediation [14], pharmaceutical [15], and environmental [16] monitoring.

The EOF transport of fluids and dissolved analytes in channels of nanometer size presents not only theoretical but also practical interest. In contrast to channels of micrometer size, nanochannels are more affected by the proximity of the wall surface. The dimensions of the electric double layer (EDL) at

* Corresponding author.
E-mail address: michal.pribyl@vscht.cz (M. Přibyl).

0021-9797/$ – see front matter
doi:10.1016/j.jcis.2007.10.056

the charged solid–liquid interfaces become comparable to the channel width. The transported electrolytes can be influenced by EDL in the entire nanochannel and this fact has a significant impact on the flow characteristics, electric current, and transport of analytes. Detailed knowledge of the transport processes in the channels thus allows better optimization and performance of various practical applications.

At least two very fast processes occur in nanofluidic systems: (i) electromigration of the ionic species to attain local electro-neutrality, (ii) irreversible chemical reactions, e.g., water dissociation. There are two extreme ways to model nanofluidic systems using the continuum approximation (the mean field theory): (a) the quasi-equilibrium approach (assumptions of local electroneutrality and local chemical equilibria, the electroosmotic slip approximation, Donnan equilibrium at interfaces, etc.), and (b) the nonequilibrium approach based on the first principles of physics (the mass, heat, and momentum balances, Gauss's law of electrostatics, finite rates of chemical reactions, the possible existence of a local electric charge, the coulombic volume force in the Navier–Stokes equation, zero velocity of the flow at solid–liquid interface, etc.). The use of the former approach is often limited, for example, if large gradients of electric potential are present [17] or the characteristic dimension of a studied system is comparable with the Debye length [18]. Such systems are usually far from equilibrium, which means that the quasi-equilibrium approach can be disqualified. Then the latter approach should be employed. Recently, several spatially multidimensional studies of the electrokinetic phenomena in nonequilibrium submicrometer porous systems have been reported [18–20]. However, the nonequilibrium modeling is usually accompanied by huge demands on computer performance. Thus, many hybrid models were developed to analyze electrokinetic processes in spatially two- or three-dimensional fluidic systems. One of the models assumes that the microscopic velocity is low so that equilibrium distribution of electric charge (the Boltzmann distribution) is satisfied at the solid surfaces. This approach was used, e.g., in modeling electrokinetic flow within microchannels and complex porous structures [3,21–23].

In the standard picture of EOF, which involves a uniform DC electric field, surfaces with a constant concentration of the fixed electric charge, i.e., constant zeta potential, and a constant channel cross section, the fluid moves through the channel with a plug-flow profile. Interesting and useful phenomena can arise in systems with a nonhomogeneous zeta potential. For example, surface charge variations can give rise to recirculating flow [24–26]. In practice, the nonhomogeneous zeta potential can be established by patterned adsorption of molecules with different electric charge [27] or induced on polarizable electrode surfaces by applying an external electric field [28]. Recently, Ajdari [29] presented theoretical investigation of transverse electrokinetic effects in micropatterned microchannels. Other work has shown that recirculating flow can be generated by an AC electric field imposed on a microelectrode array [30]. The controlled generation of hydrodynamic eddies rising in micro- and nanochannels due to the transversal EOF has been studied. Lin et al. [31] presented a study on the electrokinetic flow in a long and thin channel with transverse conductivity gradients. Squires and Bazant [32] reviewed the aspects of the induced-charge electroosmosis (ICEO) around polarizable surfaces under DC or AC fields. The same authors studied ICEO in the context of selected microfluidic operations such as mixing and pumping [28]. Thamida and Chang [33] numerically investigated the DC electrokinetic flow around a sharp corner. They found that the ejecting flow entrains tangential flow on the front side of the corner and produces a vortex on the downstream side. Takhistov et al. [34] modeled and experimentally verified electrokinetically driven vortices at channel junctions. It is shown that the influence of a finite permittivity of the channel boundaries on the surrounding electrolyte, which gives rise to a small normal component of the electric field at the channel wall, produces a pressure gradient that leads to eddies.

This work follows two recent reports on EOF modeling in microchannels [35,38]. In contrast to previous simulations [36,37], where the pressure gradient along the microchannel was equal to zero, the authors [35] focus their analysis on pressure drops at the channel inlet and the outlet. The authors point out that such pressure drops at the ends of channels, where the flow contracts and expands, are the key to understand the leakage flow. The other work focuses on the EOF through a constricted cylinder. Park et al. [38] predicted the existence of eddies for certain constricted geometries. They proposed to exploit the eddies for electrokinetic trapping of particles. The authors also introduced a leading-order criterion that predicts the central eddies in very narrow constrictions at the scale of the Debye length. They concluded that eddies can be found both in the center of the channel and along the perimeter. The presence of the eddies is a consequence of the induced pressure gradients that accompany the electrically driven flow in a narrow constriction. In papers [35,38], the authors used the quasi-equilibrium approach to develop and analyze their mathematical models. In this work we consider the nonequilibrium approach. The size (width) of the modeled system is comparable to the thickness of EDL. Hence, the Poisson equation has to be solved in the entire channel in order to get the distribution of electric potential.

In the following section, we introduce the mathematical model of EOF in a submicron channels and describe the methods of the numerical analysis. The results of simulations are presented and discussed in the next section. Our findings are summarized in the last section.

2. Mathematical model

We consider an array of charged submicrometer channels separating cathode and the anode compartments that contain the same electrolyte. The electrolyte is in contact with the solid channel surface. As the surface is electrically charged, an EDL is established. EOF occurs under the influence of an external electric field. Due to the symmetry of the system, only one-half of a channel, including walls and adjacent electrolyte, is modeled. A schematic view of the modeled geometry is shown in Fig. 1. We describe the boundaries at x_1 and x_4 as interfaces between the well-mixed electrode compartments and the stagnant layers. The Dirichlet boundary conditions are considered at x_1

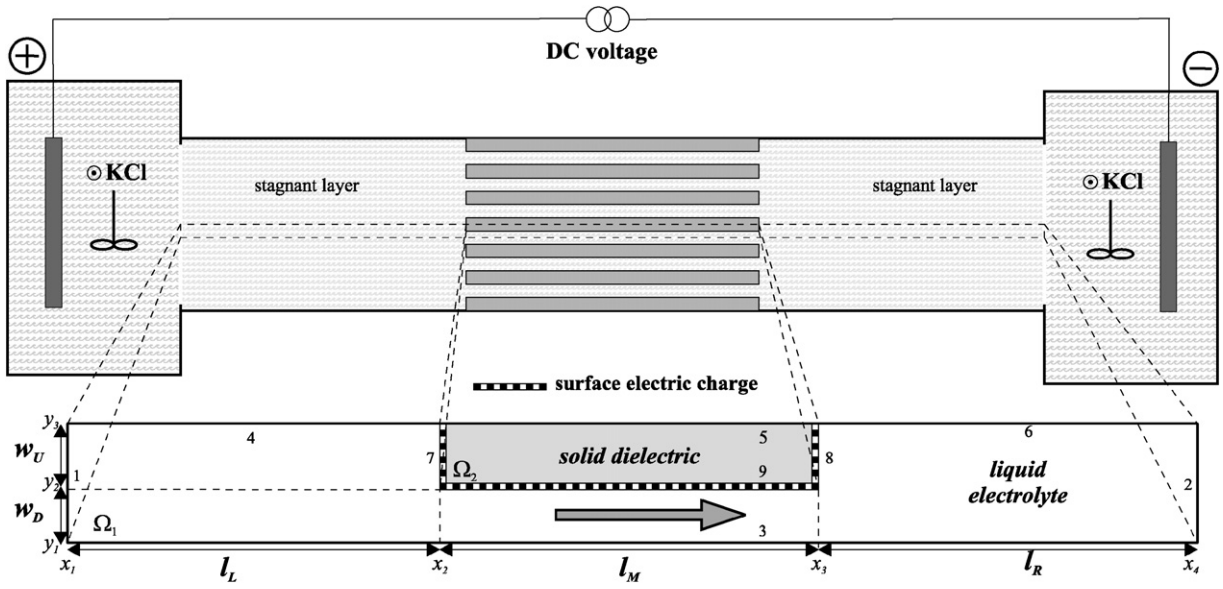

Fig. 1. Schematic view of the array of parallel submicrometer channels and the detail of the modeled geometry with depicted boundary indices.

and x_4. The electrode processes are not included in the model because the model domain is located far from the electrodes. The planes y_1, y_2, and y_3 correspond to the bottom plane of symmetry, the plane attached to the horizontal electrolyte–solid interface, and the top plane of symmetry, respectively.

The following assumptions are made in our model: (i) the system is isothermal, (ii) physical properties of the electrolyte, namely permittivity, dynamic viscosity, fluid density, and molecular diffusivity, are constant, (iii) a symmetrical uni–univalent electrolyte is assumed, and (iv) no chemical reaction takes place.

2.1. Problem formulation

The geometry consists of two spatial domains: the electrolyte Ω_1 and the solid dielectrics Ω_2. The mathematical model is based on Gauss's law of electrostatics applied on the electrolyte,

$$\nabla \cdot \mathbf{D}_1 = q, \quad \mathbf{x} \in \Omega_1, \tag{1}$$

on solid dielectrics without any free electric charge,

$$\nabla \cdot \mathbf{D}_2 = 0, \quad \mathbf{x} \in \Omega_2, \tag{2}$$

and on the interface Γ_{12} between the electrolyte and the dielectrics [39],

$$(\mathbf{D}_2 - \mathbf{D}_1) \cdot \mathbf{n}_{12} = \sigma, \quad \mathbf{x} \in \Gamma_{12}. \tag{3}$$

Other basic equations are (i) the local mass balances of the ionic components in the electrolyte,

$$\frac{\partial c_i}{\partial t} + \mathbf{v} \cdot \nabla c_i = -\nabla \cdot \mathbf{j}_i, \quad \mathbf{x} \in \Omega_1, \tag{4}$$

(ii) the local momentum balance (Navier–Stokes equation including the electrostatic force),

$$\rho\left(\frac{\partial \mathbf{v}}{\partial t} + \mathbf{v}\nabla \cdot \mathbf{v}\right) = \eta \nabla^2 \mathbf{v} - \nabla p + q\mathbf{E}, \quad \mathbf{x} \in \Omega_1, \tag{5}$$

and (iii) the local mass balance (continuity equation) [40],

$$\nabla \cdot \mathbf{v} = 0, \quad \mathbf{x} \in \Omega_1. \tag{6}$$

Equations (1)–(6) are used for the computation of the spatiotemporal fields of the physical quantities

$$c_i(t, \mathbf{x}), \qquad \varphi(t, \mathbf{x}), \qquad \mathbf{v}(t, \mathbf{x}), \qquad p(t, \mathbf{x}). \tag{7}$$

Here

$$c_i(t, \mathbf{x}), \quad \mathbf{x} \in \Omega_1, \tag{8}$$

is the molar concentration of the ith component,

$$\varphi(t, \mathbf{x}) = \begin{cases} \varphi_1(t, \mathbf{x}), & \mathbf{x} \in \Omega_1, \\ \varphi_2(t, \mathbf{x}), & \mathbf{x} \in \Omega_2 \end{cases} \tag{9}$$

is the electric potential,

$$\mathbf{v}(t, \mathbf{x}) = \big(u(t, \mathbf{x}), v(t, \mathbf{x})\big), \quad \mathbf{x} \in \Omega_1, \tag{10}$$

is the vector of the fluid velocity, and

$$p(t, \mathbf{x}), \quad \mathbf{x} \in \Omega_1, \tag{11}$$

is the pressure. Other quantities used in the model are listed below:

$$\mathbf{D}(t, \mathbf{x}) = \varepsilon \mathbf{E} = \begin{cases} \mathbf{D}_1 = \varepsilon_1 \mathbf{E}, & \mathbf{x} \in \Omega_1, \\ \mathbf{D}_2 = \varepsilon_2 \mathbf{E}, & \mathbf{x} \in \Omega_2 \end{cases} \tag{12}$$

is the electric displacement field, $\varepsilon_1 = \varepsilon_0 \tilde{\varepsilon}_1$ is the permittivity of the electrolyte, ε_0 is the vacuum permittivity, $\tilde{\varepsilon}_1 = 78.5 \doteq \tilde{\varepsilon}_{\mathrm{H_2O}}$ (25 °C) is the relative permittivity of the electrolyte, $\varepsilon_2 = \varepsilon_0 \tilde{\varepsilon}_2$ is the permittivity of the dielectrics, and $\tilde{\varepsilon_2} = 7.85$ is the relative permittivity of the dielectrics (e.g., glass) [41]. The vector of electric field strength $\mathbf{E}$ is defined as

$$\mathbf{E} = -\nabla \varphi. \tag{13}$$

The symbol $\mathbf{n}_{12}$ depicts the normal unit vector at the boundary Γ_{12} oriented from the electrolyte (Ω_1) to the dielectrics (Ω_2), ρ and η are the density and the dynamic viscosity of the electrolyte, respectively, and z_i and D_i are the ionic charge number

and the ionic diffusivity of the ith electrolyte component, respectively. The molar flux intensity $\mathbf{j}_i$ of the ith component is described by the Nernst–Planck equation,

$$\mathbf{j}_i = -D_i \nabla c_i + c_i \frac{z_i D_i F}{RT}\mathbf{E}, \quad \mathbf{x} \in \Omega_1. \tag{14}$$

The volume density of the electric charge q in the electrolyte is computed as

$$q = F \sum_i z_i c_i, \quad \mathbf{x} \in \Omega_1. \tag{15}$$

$\sigma(\mathbf{x})$, $\mathbf{x} \in \Gamma_{12}$, is the surface density of the electric charge on the dielectric side of the electrolyte–dielectrics interface, F is the Faraday constant, and R is the molar gas constant. Linear combination of the component balances (Eq. (4)) gives the local balance of the free electric charge [40],

$$\frac{\partial q}{\partial t} + \mathbf{v} \cdot \nabla q = -\nabla \cdot \mathbf{i}, \quad \mathbf{x} \in \Omega_1, \tag{16}$$

where

$$\mathbf{i} = F \sum_i z_i \mathbf{j}_i = \overbrace{-g \nabla \varphi}^{\mathbf{i}^{\text{migr}}} \overbrace{-F \sum_i z_i D_i \nabla c_i}^{\mathbf{i}^{\text{diff}}}, \quad \mathbf{x} \in \Omega_1, \tag{17}$$

is the intensity of the electric current expressed as the sum of the migration i^{migr} and the diffusion i^{diff} currents. The electrolyte conductivity g is written as

$$g = \frac{F^2}{RT} \sum_i z_i^2 c_i D_i. \tag{18}$$

Let us define a set of characteristic values of quantities (the numeric values are given as one possible example): $T_0 = 298.15$ K is the characteristic temperature, $c_0 = 1\ \text{mol}\,\text{m}^{-3}$ is the characteristic concentration, $\rho_0 = 1000\ \text{kg}\,\text{m}^{-3}$ is the characteristic density, $\eta_0 = 0.001$ Pa s is the characteristic dynamic viscosity, $D_0 = 2 \times 10^{-9}\ \text{m}^2\,\text{s}^{-1} \doteq D_+(T_0) \doteq D_-(T_0)$ is the characteristic diffusivity [42] (we consider a symmetric uni–univalent electrolyte, e.g., KCl; subscripts $_+$ and $_-$ denote the cation and anion properties, respectively),

$$q_0 = 2Fc_0 = 1.93 \times 10^5\ \text{C}\,\text{m}^{-3} \tag{19}$$

is the characteristic charge density,

$$g_0 = \frac{2D_0 c_0 F^2}{RT_0} = 1.50 \times 10^{-2}\ \text{S}\,\text{m}^{-1} \tag{20}$$

is the characteristic conductivity,

$$l_0 = \lambda_D = \sqrt{\frac{\varepsilon_1 D_0}{g_0}} = \sqrt{\frac{\varepsilon_1 RT_0}{2c_0 F^2}} = 9.63 \times 10^{-9}\ \text{m} \tag{21}$$

is the characteristic length (Debye length),

$$t_0 = \frac{l_0^2}{D_0} = 4.64 \times 10^{-8}\ \text{s} \tag{22}$$

is the characteristic time,

$$v_0 = \frac{D_0}{l_0} = 2.08 \times 10^{-1}\ \text{m}\,\text{s}^{-1} \tag{23}$$

is the characteristic velocity,

$$\varphi_0 = \frac{RT_0}{F} = 2.57 \times 10^{-2}\ \text{V} \tag{24}$$

is the characteristic electric potential,

$$E_0 = \frac{\varphi_0}{l_0} = 2.67 \times 10^6\ \text{V}\,\text{m}^{-1} \tag{25}$$

is the characteristic electric field strength,

$$\mathcal{D}_0 = \varepsilon_1 E_0 = 1.86 \times 10^{-3}\ \text{C}\,\text{m}^{-2} \tag{26}$$

is the characteristic electric displacement,

$$j_0 = 2v_0 c_0 = 2D_0 \frac{c_0}{l_0} = 4.16 \times 10^{-1}\ \text{mol}\,\text{m}^{-2}\,\text{s}^{-1} \tag{27}$$

is the characteristic molar flux intensity,

$$i_0 = 2v_0 c_0 F = g_0 \frac{\varphi_0}{l_0} = 4.01 \times 10^4\ \text{A}\,\text{m}^{-2} \tag{28}$$

is the characteristic electric current intensity,

$$p_0 = \frac{\eta_0 D_0}{l_0^2} = 2.16 \times 10^4\ \text{Pa} \tag{29}$$

is the characteristic pressure, and

$$\sigma_0 = q_0 l_0 = 9.28 \times 10^{-4}\ \text{C}\,\text{m}^{-2} \tag{30}$$

is the characteristic value of the surface charge density. The dimensionless quantities denoted by $\sim$ are then introduced as [32]

$$\tilde{\mathbf{x}} = \frac{\mathbf{x}}{l_0}, \qquad \tilde{\nabla} = l_0 \nabla, \qquad \tilde{t} = \frac{t}{t_0}, \qquad \tilde{\mathbf{v}} = \frac{\mathbf{v}}{v_0}, \tag{31}$$

$$\tilde{\varepsilon}_1 = \frac{\varepsilon_1}{\varepsilon_0}, \qquad \tilde{\varepsilon}_2 = \frac{\varepsilon_2}{\varepsilon_0}, \qquad \tilde{\eta} = \frac{\eta}{\eta_0}, \tag{32}$$

$$\tilde{\varphi} = \frac{\varphi}{\varphi_0}, \qquad \tilde{\mathbf{E}} = \frac{\mathbf{E}}{E_0} = -\tilde{\nabla}\tilde{\varphi}, \tag{33}$$

$$\tilde{\mathbf{D}}_1 = \frac{\mathbf{D}_1}{\mathcal{D}_0} = \tilde{\mathbf{E}}, \qquad \tilde{\mathbf{D}}_2 = \frac{\mathbf{D}_2}{\mathcal{D}_0} = \frac{\tilde{\varepsilon}_2}{\tilde{\varepsilon}_1}\tilde{\mathbf{E}}, \tag{34}$$

$$\tilde{\sigma} = \frac{\sigma}{\sigma_0}, \tag{35}$$

$$\tilde{c} = \frac{c_+ + c_-}{2c_0} = \frac{g}{g_0}, \tag{36}$$

$$\tilde{q} = \frac{c_+ - c_-}{2c_0} = \frac{q}{q_0}, \tag{37}$$

$$\tilde{\mathbf{j}} = \frac{\mathbf{j}_+ + \mathbf{j}_-}{j_0} = -\tilde{\nabla}\tilde{c} + \tilde{q}\tilde{\mathbf{E}}, \tag{38}$$

$$\tilde{\mathbf{i}} = \frac{\mathbf{j}_+ - \mathbf{j}_-}{j_0} = \frac{\mathbf{i}}{i_0} = -\tilde{\nabla}\tilde{q} + \tilde{c}\tilde{\mathbf{E}}, \tag{39}$$

where $\tilde{c}$ and $\tilde{q}$ represent the dimensionless electrical conductivity and charge density, respectively, and $c_+(\mathbf{j}_+)$ and $c_-(\mathbf{j}_-)$ are the molar concentrations (the flux intensities) of the cation and the anion, respectively.

The dimensionless form of the model equations is written as

$$\tilde{\nabla} \cdot \tilde{\mathbf{D}}_1 = \tilde{q}, \tag{40}$$

$$\tilde{\nabla} \cdot \tilde{\mathbf{D}}_2 = 0, \tag{41}$$

$$\frac{\partial \tilde{c}}{\partial \tilde{t}} + \tilde{\mathbf{v}} \cdot \tilde{\nabla}\tilde{c} = -\tilde{\nabla} \cdot \tilde{\mathbf{j}}, \tag{42}$$

$$\frac{\partial \tilde{q}}{\partial \tilde{t}} + \tilde{\mathbf{v}} \cdot \tilde{\nabla} \tilde{q} = -\tilde{\nabla} \cdot \tilde{\mathbf{i}}, \tag{43}$$

$$\frac{1}{\tilde{\eta} \mathrm{Sc}} \left(\frac{\partial \tilde{\mathbf{v}}}{\partial \tilde{t}} + \tilde{\mathbf{v}} \tilde{\nabla} \cdot \tilde{\mathbf{v}} \right) = \tilde{\nabla}^2 \tilde{\mathbf{v}} - \tilde{\nabla} \tilde{p} + \frac{\mathrm{Ra}}{\tilde{\eta}} \tilde{q} \tilde{\mathbf{E}}, \tag{44}$$

$$\tilde{\nabla} \cdot \tilde{\mathbf{v}} = 0, \tag{45}$$

where

$$\mathrm{Sc} = \frac{\eta_0}{\rho_0 D_0} = 500 \tag{46}$$

and

$$\mathrm{Ra} = \frac{\varepsilon_1}{\eta_0 D_0} \frac{R^2 T_0^2}{F^2} = 0.229 \tag{47}$$

are the Schmidt and the Rayleigh numbers, respectively [2]. Equations (42) and (43) originated from the addition and subtraction of the local mass balances of the cation and the anion, respectively.

The boundary conditions at the solid–liquid interfaces (boundaries 7, 8, and 9 in Fig. 1) are

$$\tilde{\varphi}_1 = \tilde{\varphi}_2, \qquad (\tilde{\mathbf{D}}_2 - \tilde{\mathbf{D}}_1) \cdot \mathbf{n}_{12} = \tilde{\sigma}, \tag{48}$$

$$\tilde{\mathbf{j}} \cdot \mathbf{n}_{12} = 0, \qquad \tilde{\mathbf{i}} \cdot \mathbf{n}_{12} = 0, \qquad \tilde{\mathbf{v}} = \mathbf{0}. \tag{49}$$

The boundary conditions for the left open boundary (boundary 1 in Fig. 1) are

$$\tilde{c} = 1, \qquad \tilde{q} = 0, \qquad \tilde{p} = \Delta \tilde{p}, \qquad \tilde{\varphi} = \Delta \tilde{\varphi}. \tag{50}$$

The boundary conditions for the the right open boundary (boundary 2 in Fig. 1) are

$$\tilde{c} = 1, \qquad \tilde{q} = 0, \qquad \tilde{p} = 0, \qquad \tilde{\varphi} = 0, \tag{51}$$

where $\Delta \tilde{p}$ and $\Delta \tilde{\varphi}$ are the dimensionless differences of pressure and voltage applied to the system, respectively. The boundary conditions on the planes of the symmetry in the electrolyte (boundaries 3, 4, and 6 in Fig. 1) are

$$\tilde{\mathbf{D}}_1 \cdot \mathbf{n} = \tilde{\mathbf{j}} \cdot \mathbf{n} = \tilde{\mathbf{i}} \cdot \mathbf{n} = \tilde{\mathbf{v}} \cdot \mathbf{n} = 0, \tag{52}$$

and in the dielectrics (boundary 5 in Fig. 1)

$$\tilde{\mathbf{D}}_2 \cdot \mathbf{n} = 0. \tag{53}$$

The trivial solution for $\Delta \tilde{p} = \Delta \tilde{\varphi} = \tilde{\sigma} = 0$, i.e.,

$$\tilde{c} = 1, \qquad \tilde{q} = 0, \qquad \tilde{p} = 0, \qquad \tilde{\phi} = 0, \qquad \tilde{\mathbf{v}} = 0, \tag{54}$$

was used as the initial conditions for dynamic simulations (first approximations for a steady-state solution).

2.2. Numerical analysis

The numerical algorithm was implemented in the software COMSOL Multiphysics 3.3a (Femlab). The Femlab procedures use the finite element method for space discretization. The mesh contained about 50,000 finite elements. Triangular and quadrilateral elements were used. The smallest discretization step, i.e., the characteristic dimension of the smallest finite element, was equal to 0.03 of Debye length (λ_D). The smallest elements were used in the proximity of the liquid–solid interface, where the presence of large gradients of the model variables can be observed or expected. The elements larger than the Debye length were used in regions far from the EDL where the variable profiles are relatively flat. As improper spatial discretization can result in an unacceptable error of the numerical approximation, meshes of various densities were tested. We used two numerical solvers implemented in Femlab to analyze the model equations (40)–(45) with the appropriate boundary and initial conditions: (i) the nonlinear stationary solver *femnlin* (the applied voltage chosen as a parameter) and (ii) the time-dependent solver *femtime* (the applied voltage was increased very slowly during time stepping; i.e., the evolution integration was carried out). The time-dependent solver uses the *daspk* algorithm [43], which is based on the backward differentiation formulae. The results obtained by both solvers were analyzed. Their agreement indicates the stability of the solutions obtained by the steady state solver.

3. Results and discussion

We restrict the studied geometry (dimension of the parametric space) by setting that $l = l_L = l_M = l_R$ and $w = w_U = w_D$ (see Fig. 1). As the reference system, we consider the following set of values of dimensionless parameters: the channel length $\tilde{l} = 1000$, the channel width $\tilde{w} = 3$, the surface charge density $\tilde{\sigma} = -1$, the electrolyte viscosity $\tilde{\eta} = 1$, and the pressure difference $\Delta \tilde{p} = 0$. The effects of these parameters on the system behavior are studied. The results associated with the reference state are represented in the figures by the mark [a]. We note that the dimensionless length is defined as $\tilde{l} = l/l_0$ and the dimensionless width as $\tilde{w} = w/l_0$. The divergenceless vector fields $\tilde{\mathbf{i}}$ and $\tilde{\mathbf{v}}$ are in the parametric plots represented by the scalars $\bar{i}$ and $\bar{u}$, respectively, which are computed as the mean values of the x-component of the vectors over the vertical cross-section of the electrolyte in the channel. The applied voltage $\Delta \tilde{\varphi}$ is presented in the parametric plots by the mean value ($\bar{E}$) of the x-component of the electric field strength within the channel and is computed for a hypothetical system fully governed by the Ohm's law ($\bar{E} = \Delta \tilde{\varphi}/2\tilde{l}$ in our geometry). The dependencies of $\bar{i}$ and $\bar{u}$ on $\bar{E}$ for an idealized system governed by Ohm's law and the Helmholtz–Smoluchowski equation and satisfying local electroneutrality are then the identities (the diagonals) in the plots.

3.1. Effect of channel width

The channel width was varied in the range from 1 to 10 of Debye length units. Fig. 2 shows the dependencies of the mean electric current density $\bar{i}$ (a) and the mean fluid velocity $\bar{u}$ (b) on the mean electric field strength $\bar{E}$ for various channel widths. In the case of a wide channel ($\tilde{w} \geqslant 5$, curve [c]), there can be observed almost constant electric conductivity in the current–voltage characteristics over the whole interval of the applied voltage. The system obeys Ohm's law and behaves like a pure electroosmotic pump. The situation is quite different for the thinner channels, curves [a] and [b], where the system behaves like a cation-exchange membrane with the typical nonlinear

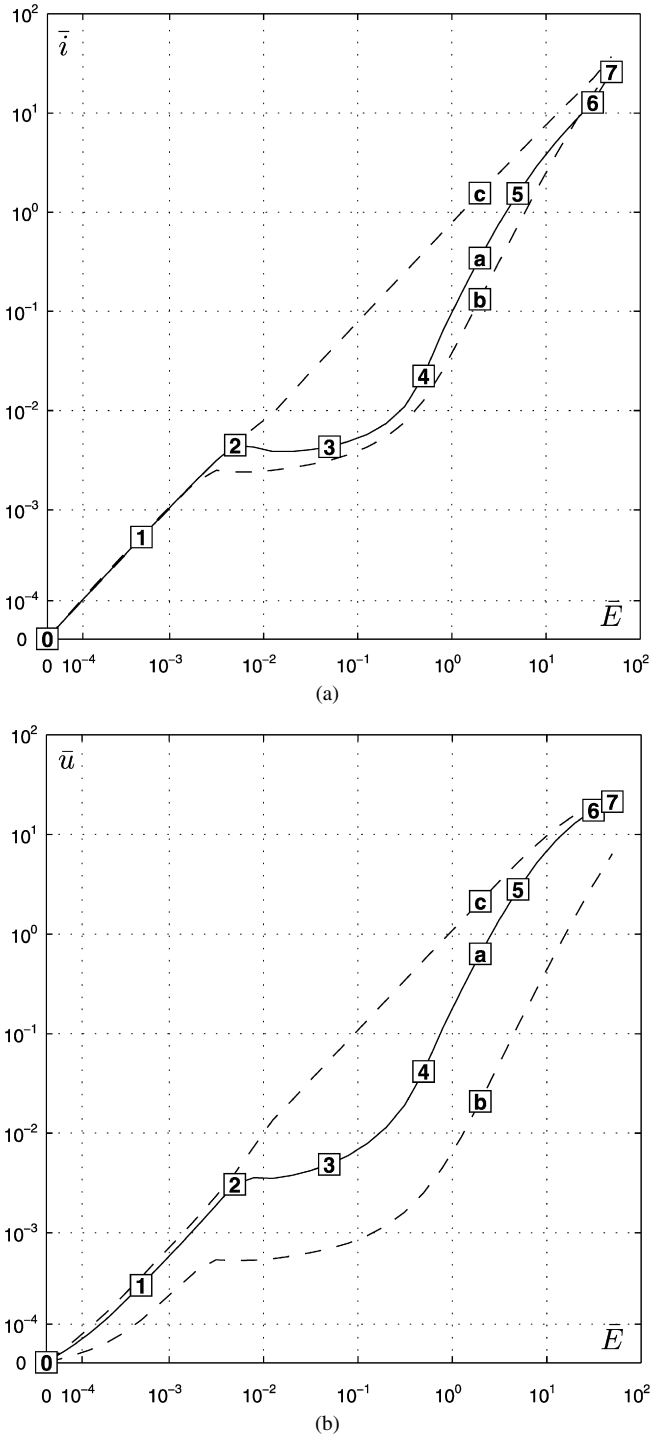

(a)

(b)

Fig. 2. The dependencies of (a) the mean electric current intensity $\bar{i}$ and (b) the mean fluid velocity $\bar{u}$ on the mean electric field strength $\bar{E}$ for various channel widths; a: $\tilde{w} = 3$, b: $\tilde{w} = 1$, c: $\tilde{w} = 5$. Values of other parameters: $\tilde{l} = 1000$, $\tilde{\sigma} = -1$, $\tilde{\eta} = 1$.

shape of the current–voltage characteristics [44]. For a low electric field strength ($\bar{E} < 10^{-2}$), an ohmic (linear) region occurs followed by a plateau, where the limiting current is reached. If the imposed electric field is further increased, the slope again becomes higher; i.e., an over-limiting current is observed. According to the classical theory, the plateau is a result of concentration gradient (concentration polarization) at the electrolyte–membrane interface. Fig. 2b presents the fluid velocity–voltage characteristics for various widths of the channel. The fluid velocity in the wider channel, curve c, is linearly proportional to the applied voltage; i.e., the Helmholtz–Smoluchowski approximation remains valid, while for the thinner channels, curves a and b, the fluid velocity–voltage curves show nonlinearities. When the system approaches the limiting current, the driving force (the applied potential difference) mainly acts outside the channel in the free electrolyte, which results in a significant drop of the fluid velocity with respect to a wider channel. This fall is caused by the development of a narrow layer of a very low conductivity in the anolyte compartment. This layer acts like a conductivity plug for the transport of the electrically charged species.

A more illustrative view (Fig. 3) of the system behavior is presented in the form of the spatial distributions of the studied quantities: the electrical conductivity $\tilde{c}$, the electric charge density $\tilde{q}$, the electric potential $\tilde{\phi}$, and the pressure $\tilde{p}$. Here we consider the system in the reference state, i.e., curve a in Fig. 2. The spatial distributions characterize the system at four qualitatively different steady states: (i) the trivial case, where no voltage is applied 0, (ii) the system in the ohmic region 1, (iii) the system in the limiting current region 3, and (iv) the system in the overlimiting current region 5–7. In Figs. 3a–3f are plotted spatial fields of the computed quantities at the horizontal positions y_1 and y_2 corresponding to the bottom plane of symmetry and the plane attached to horizontal electrolyte–solid interface, respectively (see Fig. 1). The arrangement of Figs. 3a–3f is as follows: the first column shows the distributions in the anolyte compartment ($\tilde{x} \in 0$–1000), the third one in the main channel ($\tilde{x} \in 1000$–2000), and the last one in the catholyte compartment ($\tilde{x} \in 2000$–3000). Columns 2 and 4 display detailed (zoomed) views at the channel inlet and outlet, respectively. The spatial distributions of the quantities for the equilibrium case (no applied voltage) are shown in Fig. 3a. The fixed electric charge at the channel walls attracts the counterions to the charged surface. This situation results in a nonzero net charge density in the vicinity of the channel walls. The nonzero net charge density is observed also in the channel center (solid line) because of the channel thickness is comparable to the Debye length. The profile of the electric potential reflects the distribution of the electric charge. The electric potential both at the interface and in the center is negative due to the fixed negative charge on the solid surface. The pressure increases in the direction of the solid–liquid interface to equilibrate the electrostatic and pressure forces at the interface (to satisfy the continuity equation).

Fig. 3b presents the spatial distributions of the studied quantities in the ohmic region (see 1 in Fig. 2). The low value of the applied potential difference, $\Delta\tilde{\varphi} = 2$, causes only small qualitative changes in the distributions with respect to the case with no applied potential 0. However, the electric potential distribution illustrates the significant potential drop across the channel (driving force). Hence, the electrolyte flow is now driven in the direction from cathode to anode and satisfies the Helmholtz–Smoluchowski concept of electroosmosis.

The situation is quite different when the system approaches the limiting current (see 3 in Fig. 2). This case is presented

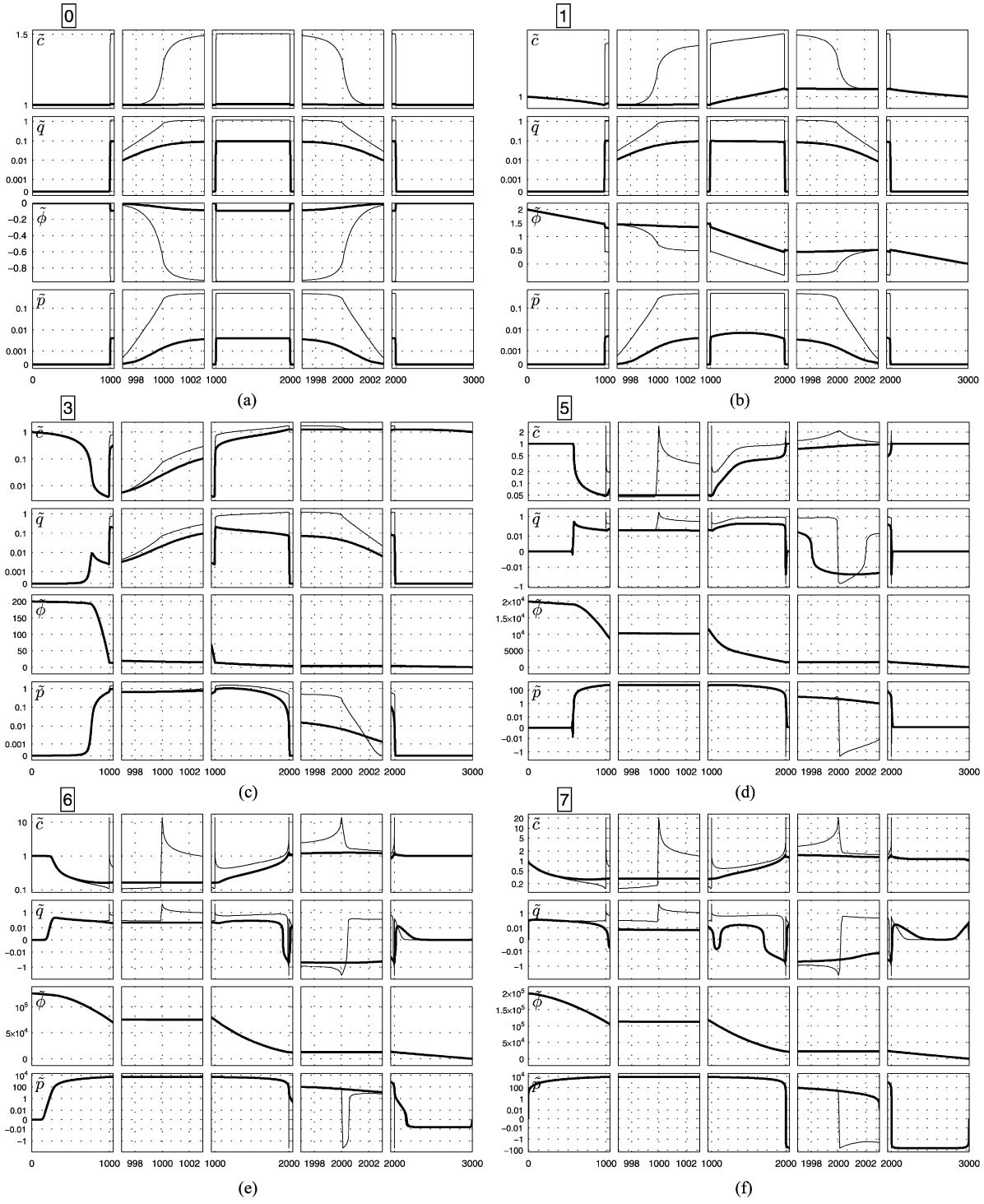

Fig. 3. The spatial profiles (from top to bottom) of the electrical conductivity $\tilde{c}$, the electric charge density $\tilde{q}$, the electric potential $\tilde{\phi}$, and the pressure $\tilde{p}$ for the applied voltage corresponding to the points in Fig. 2 marked by 0, 1, 3, and 5–7; the thick and thin solid lines correspond to the cross sections of the system at y_1 and y_2, respectively. Values of parameters: $\tilde{l} = 1000$, $\tilde{w} = 3$, $\tilde{\sigma} = -1$, $\tilde{\eta} = 1$.

in Fig. 3c ($\Delta\tilde{\varphi} = 200$). In the limiting current region, a very narrow depletion layer (from the nanometer to the micrometer scale) of low electrical conductivity is formed at the channel end facing the anode (the channel inlet). This narrow layer is so-called *ionic gate* [45]. Until the system persists in the limiting current region, the ionic gate deepens in the range of several orders of magnitude and extends over the anolyte. The gate is closed. This steady state is accompanied by a significant potential loss just across the ionic gate. The net charge density distribution shows that there is a significant deviation from the electroneutrality condition. The nonzero electric charge density can be observed not only in the vicinity of the charged channel walls but also in the anolyte far from the charged surface. This behavior is in a qualitative agreement with the results of the an-

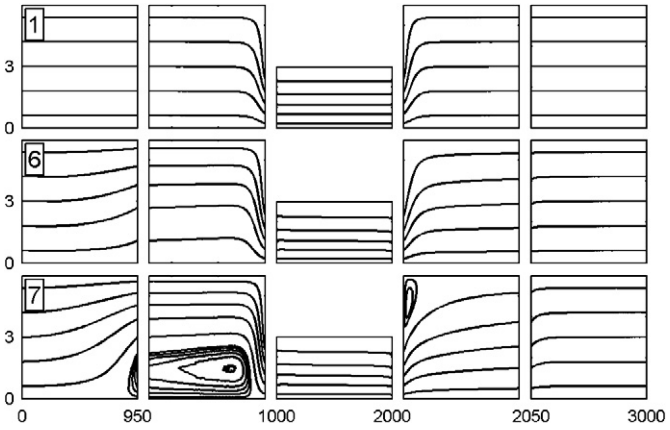

Fig. 4. The streamlines of fluid flow for various potential differences (rows denoted 1, 6, and 7 correspond to the positions on the characteristic plotted in Fig. 2). Values of parameters: $\tilde{l} = 1000$, $\tilde{w} = 3$, $\tilde{\sigma} = -1$, $\tilde{\eta} = 1$.

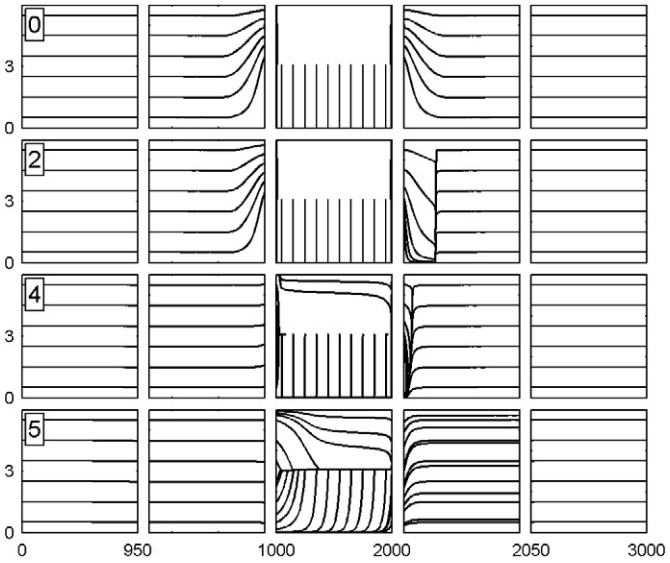

Fig. 5. The flowlines of electric field strength for various potential differences (rows denoted 0, 2, 4, and 5, correspond with the position on the characteristic plotted in Fig. 2). Values of parameters: $\tilde{l} = 1000$, $\tilde{w} = 3$, $\tilde{\sigma} = -1$, $\tilde{\eta} = 1$.

alytical work by Rubinstein et al. [44]. In the limiting current region, the velocity of the fluid flow is approximately constant due to the dissipation of the driving force (potential difference) in the ionic gate. If the applied voltage is further increased, the system shifts in the overlimiting current region. This is documented in Fig. 3d for $\Delta\tilde{\varphi} = 2 \times 10^4$. Here, the ionic gate is reduced in depth, expands across the anolyte, and begins to open. When the ionic gate starts to disappear due to the increase of the applied voltage, the ratio of the electric potential difference observed across the channel and across the ionic gate, respectively, increases. The nonzero charge density (negative value) is also observed in the catholyte compartment very close to the channel outlet. The applied potential difference causes a depletion of positive charge ions from the negative charged surface. Even if the right solid boundary 8 (see Fig. 1) is negatively charged, the applied electric field is so high that the original direction of the electric field (from the right to the left) at the surface is reversed and the negative charged ions are pushed to the surface (overcharging).

As the applied voltage is further increased, the ionic gate in the anolyte disappears (Fig. 3e). However, the positive electric charge density in the anolyte still affects the ionic transport and the negative electric charge density moves into the channel.

Fig. 3f shows the spatial distributions in the case of a very high electric field strength ($\Delta\tilde{\varphi} = 2 \times 10^5$). We are aware of the fact that our formulation of the boundary conditions are not physically relevant for such high applied electric field and these results are given only as a mathematical extrapolation. However, the qualitative change can be expected even for more relevant boundary conditions.

The streamline plots of the velocity field in the selected steady states are shown in Fig. 4. The fluid flow structure remains qualitatively unaffected almost over the whole interval of the applied potential difference, 1, 6. However, it can be seen that a very high difference of electric potential 7 can cause eddy formation at the channel ends. The eddy development can significantly affect the stirring up of the electrolyte. The eddies are probably induced by the acting of the electrostatic field on the formed nonzero charge outside the main channel (far from the electrically charged interfaces in the anolyte, near to the interface in the catholyte).

The electric fields in the selected steady states are plotted in Fig. 5 in the form of *flowlines* (i.e., lines that are tangent to the vector field). At equilibrium, 0, the electric field is generated only by the electric charge fixed on the solid–liquid interfaces. When the external potential difference is applied, the resulting electric field is a consequence of the competition between the applied external field (almost in the longitudinal direction) and the internal field (almost in the transversal direction in the channel and longitudinal direction in the anolyte and the catholyte compartments). For low values of the applied voltage, these two fields have the same direction in the anolyte, while in the catholyte both the components act against each other and a layer where these two fields are balanced (zero value of x-component of the electric field appears) is formed 2. When the voltage is further increased, this layer is reduced 4 and finally disappears 5. The dominance of the external field causes a formation of the negative charge close to the channel (see Fig. 3d).

3.2. *Effect of channel length*

The channel length was varied in the range from 500 to 5000 of Debye length units. The current–voltage and the velocity–voltage characteristics are plotted in Figs. 6a and 6d, respectively. The longest channel, curve c, contains more fixed electric charge than the shorter channels, curves a and b. Higher amount of the fixed electric charge induces more intensive integral electrostatic effects in the anolyte and catholyte compartments. The tendency to create the ionic gate in the anolyte is then more robust. In case c the limiting (overlimiting) current region starts at lower (higher) externally applied electric fields; hence, the limiting current region is wider. In the case of the short channel, curve b, the formation of the ionic gate is not

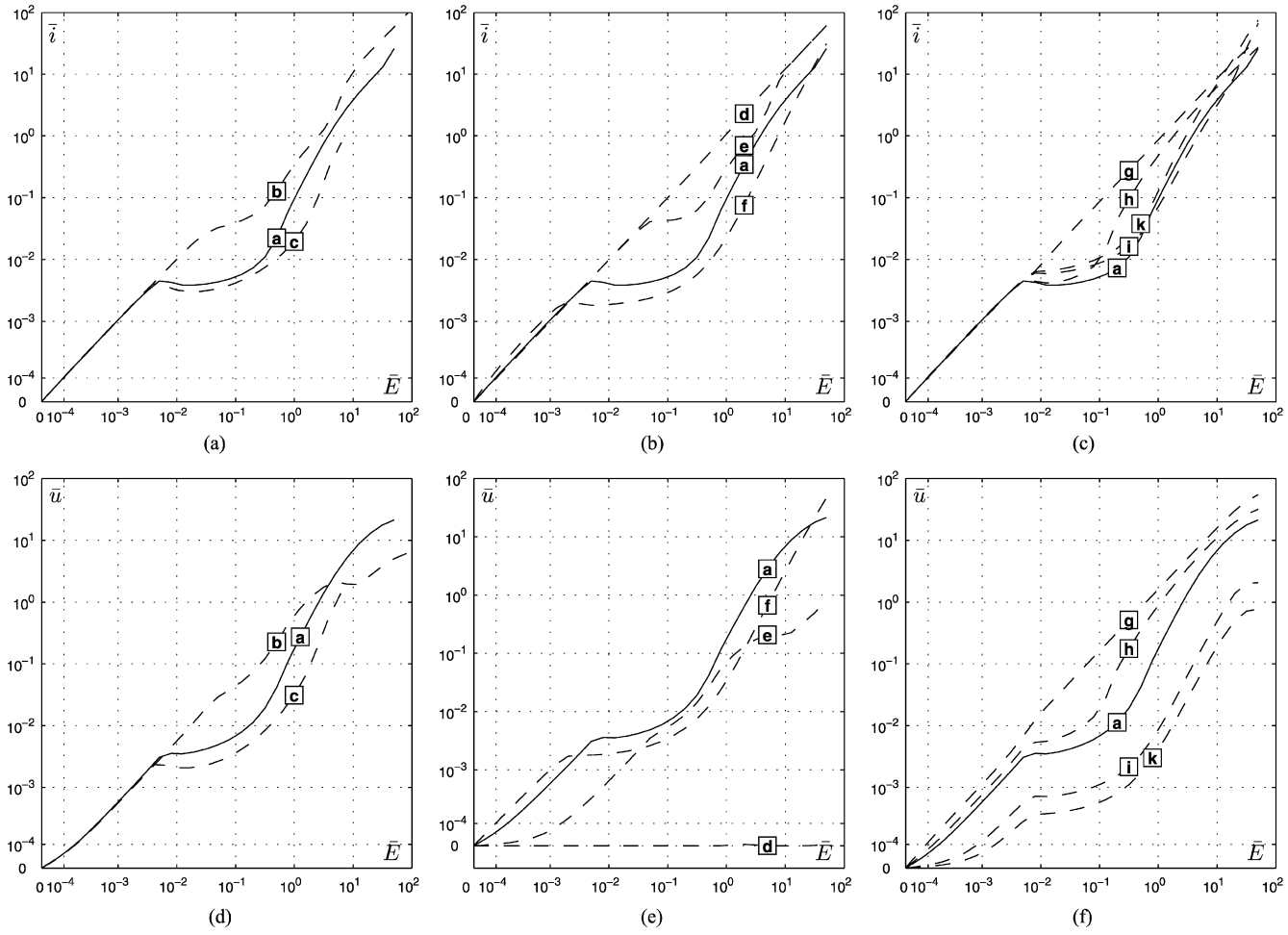

Fig. 6. The dependencies of (top) the mean electric current intensity $\bar{i}$ and (bottom) the mean fluid velocity $\bar{u}$ on the the mean electric field strength $\bar{E}$ for various channel lengths (left column), surface charge densities (middle column), and electrolyte viscosities (right column), respectively; [a]: $\tilde{l} = 1000$, $\tilde{w} = 3$, $\tilde{\sigma} = -1$, $\tilde{\eta} = 1$, [b]: $\tilde{l} = 100$, [c]: $\tilde{l} = 5000$, [d]: $\tilde{\sigma} = 0$, [e]: $\tilde{\sigma} = -0.1$, [f]: $\tilde{\sigma} = -10$, [g]: $\tilde{\eta} = 0.5$, [h]: $\tilde{\eta} = 0.75$, [i]: $\tilde{\eta} = 5$, [k]: $\tilde{\eta} = 10$ (other model parameters in [b]–[k] are the same as for [a]).

so significant. Thus, the system reaches for the limiting current only for short interval of the applied voltage due to the relatively small amount of the fixed electric charge within the channel. The electric current and fluid velocity decrease with growing channel length in the limiting current region. For very high electric fields (overlimiting current), the parametric plots are principally influenced by the hydrodynamics and an explanation of the observed curves should be focused on a detailed analysis of the spatial fields of all model quantities.

3.3. Effect of surface charge density

Figs. 6b and 6e show the current–voltage and the velocity–voltage characteristics for various values of the surface charge density, respectively. In the trivial case of an uncharged channel, curve [d] ($\tilde{\sigma} = 0$), the current–voltage characteristic displays an expected linear dependency (the system obeys Ohm's law) and the velocity of the fluid flow is equal to zero. In the case of a negatively charged channel, nonlinear behavior of the system is observed. It can be seen that a higher density (in absolute value) of the surface electric charge, curves [a] and [f], results in ionic gate formation for a lower voltage applied on the system and a higher voltage has to be applied to reach the overlimiting current. The velocity–voltage dependencies show that for low voltages (ohmic linear region) the fluid velocity grows monotonically with the increasing absolute value of the fixed electric charge. This relation changes in the limiting current region, where we can observe the maximal velocity in the reference system [a] ($\tilde{\sigma} = -1$). For a lower (in absolute value) charge density, curve [e] ($\tilde{\sigma} = -0.1$), the velocity of the fluid flow is lower because the coulombic volume force is proportional to the charge density. It may be surprising that for a higher absolute value of charge density, curve [f] ($\tilde{\sigma} = -10$), the velocity is also lower than in case [a]. The reason is that the coulombic driving force strongly decreases due to the potential loss across the ionic gate. This gate appears for higher surface charge density at lower applied potential difference; i.e., a lower velocity in the limiting current region is observed.

3.4. Effect of viscosity

The current–voltage and velocity–voltage characteristics for various values of electrolyte viscosity are presented in Figs. 6c and 6f, respectively. This example is focused on the study of hy-

pothetical fluids that are either more or less viscous than water. The curve depicted by the mark [a] stands for the water viscosity at room temperature ($\tilde{\eta} = 1$). The velocity–voltage characteristics show the expected inverse proportionality; i.e., a more viscous electrolyte flows more slowly than a less viscous one. The explanation of the current–voltage characteristics is much more difficult. For the middle values of the electric field, when the system is found in the limiting current region, the dependence of the electric current on the electrolyte viscosity is not monotonic. The minimum of electric current is observed for the middle value the electrolyte viscosity, curve [a]. For lower values of electrolyte viscosity, curves [g] and [h], the electric current passing through the system is higher than in case [a]. This is in agreement with the fact that a less viscous fluid flows faster than a more viscous one. It is surprising that the electric current can rise also with increasing electrolyte viscosity, curves [a], [i], and [k]. This phenomenon probably corresponds to the competition between the migration, the diffusion, and the convection within the ionic gate. Until now the exact explanation remains unclear.

3.5. Effect of external pressure gradient

The effects of the coupling between EOF and the pressure-driven flow on the current–voltage and the velocity–voltage characteristics are plotted in Figs. 7a and 7b. We consider two qualitatively different cases: (i) overpressure, where the electrostatic force acts in the same direction as the pressure force so that the applied electric field $\bar{E}$ has positive values, and (ii) underpressure, where the electrostatic force acts in the opposite direction from the pressure force, and thus the applied electric field $\bar{E}$ has negative values. The current–voltage characteristic represented by the solid line in Fig. 7a shows that a nonzero value of electric current (so-called *streaming current*) is observed for the applied potential difference (electric field) equal to zero, and the potential difference (electric field) has nonzero value (so-called *streaming potential*) when the electric current passing through the system is equal to zero.

In the case of overpressure ($\bar{E} > 0$), there is only quantitative change in the shape of the characteristic curve compared to the system with no pressure difference. The resulting driving force is given by the synergetic action of the electrostatic and the pressure force, the limiting current region is thinner, and the velocity is higher. The situation is quite different in the case of underpressure ($\bar{E} < 0$). The competition of the contrary acting pressure force and the electrostatic force causes fluid flow reversal. For a small negative value of the electric field strength, the (positive) pressure force is dominant and the fluid flows toward the cathode (to the right). When the pressure and electrostatic forces are balanced, the mean velocity of fluid flow is equal to zero ($\bar{u} = 0$). A further decrease of the value of the electric field strength leads to flow reversal and the fluid flows toward the anode (to the left). This flow reversal is accompanied by a complicated behavior (Fig. 8). The fixed electric charge on the channel walls causes a higher net charge density in the vicinity of the solid–liquid interface than in the bulk electrolyte. Thus, the coulombic force is highest close to the charged surface. Hence, the fluid flow starts to reverse at the channel wall, while in the center, the fluid flows still in the original direction ([4]). This is the reason for the formation of eddies in the main channel and also in the free electrolyte facing the channel ends. If the imposed negative electric field is further decreased, the fluid flow is reversed also in the center of the channel ([6] and [7]). An additional decrease of the electric field strength leads to complete flow reversal and the eddies disappear ([9]). An extremely low electric field results in eddy formation due to

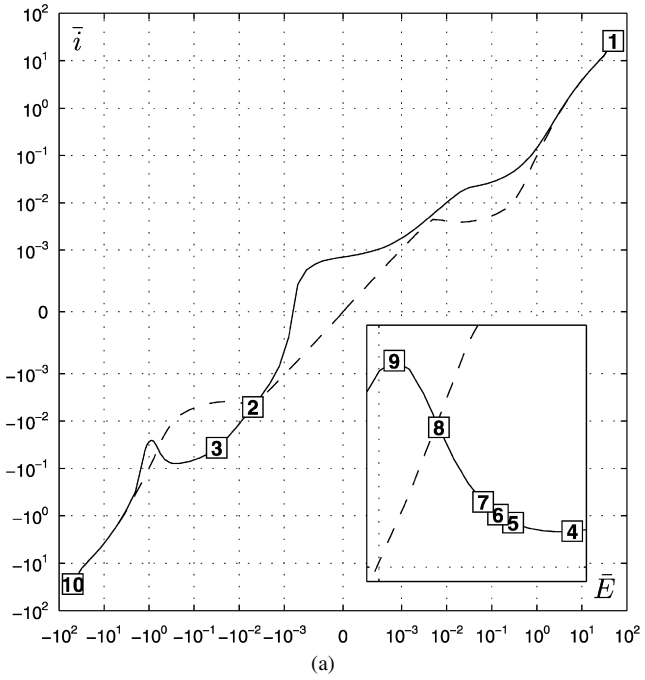

Fig. 7. The dependencies of (a) the mean electric current intensity $\bar{i}$ and (b) the mean fluid velocity $\bar{u}$ on the mean electric field strength $\bar{E}$ for various external pressure gradients; solid and dashed lines correspond to $\Delta\tilde{p} = 10$ and $\Delta\tilde{p} = 0$, respectively. Values of other parameters: $\tilde{l} = 1000$, $\tilde{w} = 3$, $\tilde{\sigma} = -1$, $\tilde{\eta} = 1$.

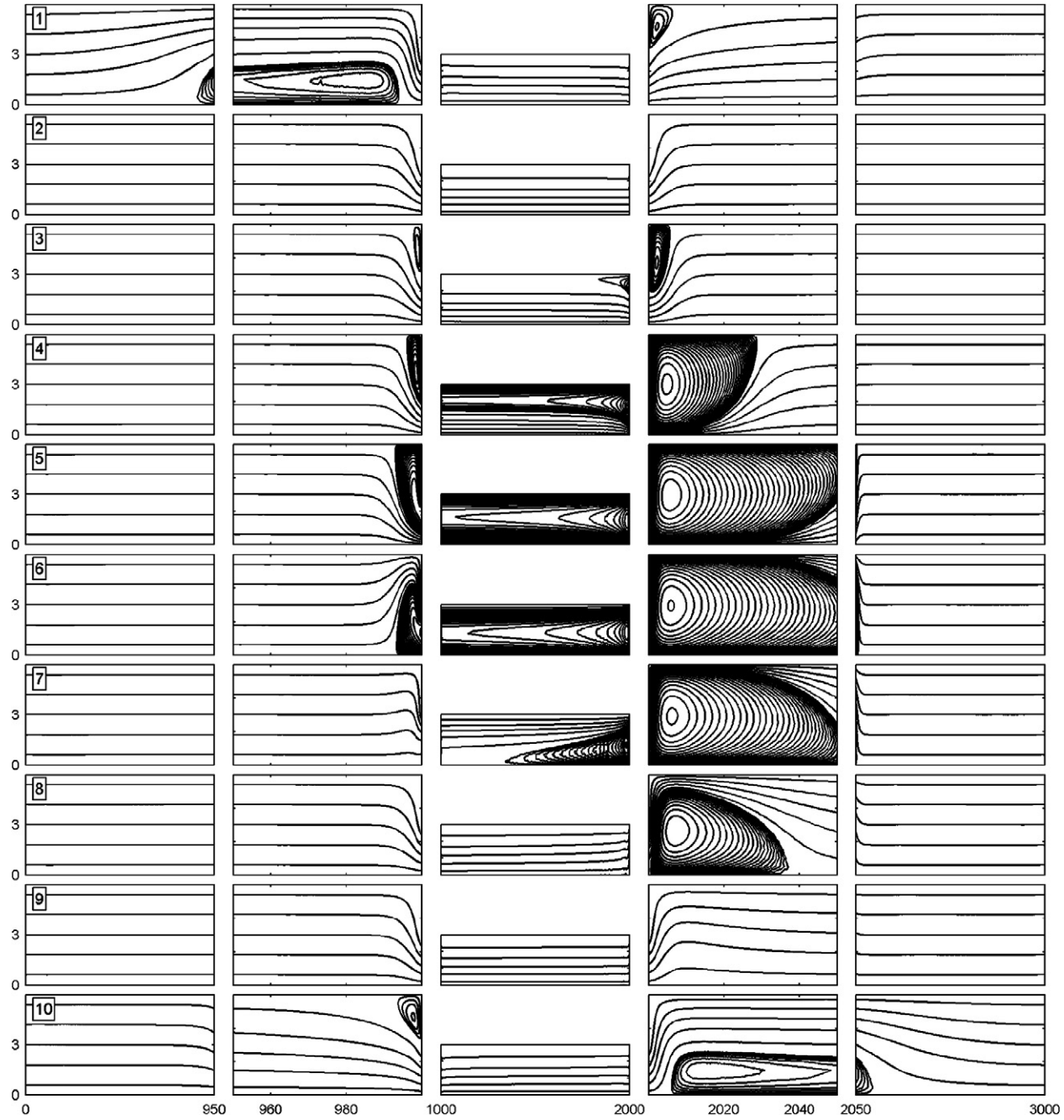

Fig. 8. The flowlines of fluid flow for various potential differences in the case of coupled electroosmotic and pressure-driven flow (rows denoted 1 to 10 correspond to positions on the characteristics plotted in Fig. 7). Values of parameters: $\tilde{l} = 1000$, $\tilde{w} = 3$, $\tilde{\sigma} = -1$, $\tilde{\eta} = 1$, $\Delta\tilde{p} = 10$).

strong electrostatic interactions. The character of these eddies is the same as in case 1 except the flow direction. We note that the notation of rows 1 to 10 corresponds to the points of the solid line in Fig. 7.

4. Conclusions

Numerical analysis of the model equations provides possibilities of studying and understanding electrokinetic phenomena on the submicrometer scale. The spatially two-dimensional model employed in this work makes it possible to study the transport effects not only in the main nanochannel but also in the free electrolyte outside of the channel (the anolyte and the catholyte compartments). High concentration and conductivity gradients, pressure drops, hydrodynamic eddies, and nonzero charge densities far from the charged surfaces were detected in the system. The results indicate that the system behaves like an ion-exchange membrane in the case where the channel width is comparable to the thickness of the EDL, while for wider channels, the classical electroosmotic pumping occurs. These findings are in a qualitative agreement with available experimental data cited below.

The current–voltage characteristics of materials with pores of a larger diameter were reported, e.g., in [46–48]. The au-

thors [46,48] studied electroosmotic flow in silica columns packed with silica particles of micrometer diameters. Linear current–voltage dependencies and electroosmotic velocity linearly proportional to the driving force were observed. Similar results were obtained by Yairi and Richter [47] in a large array of parallel submicrometer channels ($0.7 \times 0.7 \times 30$ μm). Nonlinear current–voltage characteristics are typically exhibited by compact cation-exchange membranes [49]. The reason for the appearance of the overlimiting region is given by mutual interplay of several effects [50]. With high probability, the electroconvection causing hydrodynamic instabilities at the depleted membrane–electrolyte interface plays a significant role (Fig. 4). These instabilities were experimentally observed by means of laser interferometry [51] and by measuring chronopotentiometric curves [52], current noise spectra [53,54], or light-scattering fluctuation spectra [55]. In that work [55], the authors observed hydrodynamic instabilities at the concentrate side of the membrane when very high current densities were applied. The theory of turbulent convection at the membrane–electrolyte interface is further supported by measurement of the electric potential distributions in the electrolyte adjacent to a membrane [56].

Our numerical analysis gives qualitative and also quantitative insight into the complex transport processes in submicroporous materials under the influence of an external DC electric field. As the processes are modeled on the domain that includes the electrolyte in the pores, the surrounding electrolyte, and the solid dielectric with the fixed electric charge, we believe that the obtained results are more realistic than those gained by approximate, analytical, or semianalytical techniques. The main problem of our nonequilibrium model is that the formulation of relevant open boundary conditions is difficult. The use of the Dirichlet conditions is only acceptable when sharp gradients of the model variables are localized sufficiently far from these open boundaries.

Acknowledgments

The authors acknowledge the support of the Ministry of Industry and Trade of the Czech Republic (Grant No. POKROK 1H-PK/24). M.P. acknowledges the partial support of the Grant Agency of the Czech Academy of Science (Project KAN-208240651).

References

[1] J.C.T. Eijkel, A. van den Berg, Microfluid Nanofluid 1 (2005) 249.
[2] T.M. Squires, S.R. Quake, Rev. Mod. Phys. 77 (2005) 977.
[3] M. Wang, J.K. Wang, S.Y. Chen, N. Pan, J. Colloid Interface Sci. 304 (2006) 246.
[4] D.J. Beebe, G.A. Mensing, G.M. Walker, Annu. Rev. Biomed. Eng. 4 (2002) 261.
[5] G.S. Fiorini, D.T. Chiu, Biotechniques 38 (2005) 429.
[6] T. Laurell, F. Petersson, A. Nilsson, Chem. Soc. Rev. 36 (2007) 492.
[7] C.F. Gonzalez, V.T. Remcho, J. Chromatogr. A 1079 (2005) 59.
[8] R.F. Probstein, Physicochemical Hydrodynamics: An Introduction, Wiley, New York, 1994.
[9] D. Li, Electrokinetics in Microfluidics, Elsevier, London, 2004.
[10] Y. Sun, Y.C. Kwok, Anal. Chim. Acta 556 (2006) 80.
[11] C.Y. Lee, G.B. Lee, J.L. Lin, F.C. Huang, C.S. Liao, J. Micromech. Microeng. 15 (2005) 1215.
[12] C.J. Yu, W.L. Tseng, Electrophoresis 27 (2006) 3569.
[13] K. Huikko, R. Kostiainen, T. Kotiaho, Eur. J. Pharm. Sci. 20 (2003) 149.
[14] R.E. Saichek, K.R. Reddy, Crit. Rev. Environ. Sci. Technol. 35 (2005) 115.
[15] B. Weigl, R.L. Bardell, C.R. Cabrera, Adv. Drug Delivery Rev. 55 (2003) 349.
[16] A. Gentili, Anal. Bioanal. Chem. 387 (2007) 1185.
[17] J. Lindner, D. Snita, M. Marek, Phys. Chem. Chem. Phys. 4 (2002) 1348.
[18] D. Hlushkou, A. Seidel-Morgenstern, U. Tallarek, Langmuir 21 (2005) 6097.
[19] R.J. Yang, L.M. Fu, C.C. Hwang, J. Colloid Interface Sci. 244 (2001) 173.
[20] D. Erickson, D.Q. Li, J. Phys. Chem. B 107 (2003) 12212.
[21] M. Wang, S. Chen, J. Colloid Interface Sci. 314 (2007) 264.
[22] J.K. Wang, M. Wang, Z.X. Li, J. Colloid Interface Sci. 296 (2006) 729.
[23] Y.J. Kang, C. Yang, X.Y. Huang, Int. J. Eng. Sci. 42 (2004) 2011.
[24] A.D. Stroock, M. Weck, D.T. Chiu, W.T.S. Huck, P.J.A. Kenis, R.F. Ismagilov, G.M. Whitesides, Phys. Rev. Lett. 84 (2000) 3314.
[25] J.S.H. Lee, C.L. Ren, D. Li, Anal. Chim. Acta 530 (2005) 273.
[26] M. Pribyl, V. Knapkova, D. Snita, M. Marek, Microelectron. Eng. 83 (2006) 1660.
[27] A.E. Herr, J.I. Molho, J.G. Santiago, M.G. Mungal, T.W. Kenny, Anal. Chem. 72 (2000) 1053.
[28] M.Z. Bazant, T.M. Squires, Phys. Rev. Lett. 92 (2004) 0661011.
[29] A. Ajdari, Phys. Rev. E 65 (2001) 016301.
[30] A. Ramos, A. Gonzalez, N.G. Green, A. Castellanos, J. Colloid Interface Sci. 217 (1999) 420.
[31] H. Lin, B.D. Storey, M.H. Oddy, C.-H. Chen, J.G. Santiago, Phys. Fluids 16 (2004) 1922.
[32] T.M. Squires, M.Z. Bazant, J. Fluid Mech. 509 (2004) 217.
[33] S.K. Thamida, H.C. Chang, Phys. Fluids 14 (2002) 4315.
[34] P. Takhistov, K. Duginova, H. Chang, J. Colloid Interface Sci. 263 (2003) 133.
[35] Y. Zhang, X.-J. Gu, R.W. Barber, D.R. Emerson, J. Colloid Interface Sci. 275 (2004) 670.
[36] N.A. Patankar, H.H. Hu, Anal. Chem. 70 (1998) 1870.
[37] A.I. Liapis, B.A. Grimes, J. Chromatogr. A 877 (2000) 181.
[38] S.Y. Park, C.J. Russo, D. Branton, H.A. Stone, J. Colloid Interface Sci. 297 (2006) 832.
[39] L.D. Landau, E.M. Lifshitz, The Classical Theory of Fields Course of Theoretical Physics, vol. 2, Butterworth–Heinemann, Oxford, 1987.
[40] W.M. Deen, Analysis of Transport Phenomena, Oxford Univ. Press, Oxford, 1998.
[41] A. Stogrin, IEEE Trans. Microwave Theory Techniques 19 (1971) 733.
[42] D.H. Li, Geochim. Cosmochim. Acta 38 (1974) 703.
[43] P.N. Brown, A.C. Hindmarsh, L.R. Petzold, SIAM J. Sci. Comput. 15 (1994) 1467.
[44] I. Rubinstein, B. Zaltzman, Phys. Rev. E 62 (2000) 2238.
[45] D. Snita, M. Paces, J. Lindner, J. Kosek, M. Marek, Faraday Discuss. 120 (2001) 53.
[46] S.L. Zeng, C.H. Chen, J.C. Mikkelsen, J.G. Santiago, Sens. Actuat. B Chem. 79 (2001) 107.
[47] M. Yairi, C. Richter, Sens. Actuat. A Phys. 137 (2007) 350.
[48] L.X. Chen, H.L. Wang, J.P. Ma, C.X. Wang, Y.F. Guan, Sens. Actuat. B Chem. 104 (2005) 117.
[49] J.J. Krol, M. Wessling, H. Strathmann, J. Membr. Sci. 162 (1999) 145.
[50] V.I. Zabolotsky, V.V. Nikonenko, N.D. Pismenskaya, E.V. Laktionov, M.K. Urtenov, H. Strathmann, M. Wessling, G.H. Koops, Sep. Purif. Technol. 14 (1998) 255.
[51] V.I. Vasileva, V.A. Shaposhnik, O.V. Grigorchuk, I.P. Petrunya, Desalination 192 (2006) 408.
[52] J.J. Krol, M. Wessling, H. Strathmann, J. Membr. Sci. 162 (1999) 155.
[53] F. Maletzki, H.W. Rosler, E. Staude, J. Membr. Sci. 71 (1992) 105.
[54] Y. Fang, Q. Li, M.E. Green, J. Colloid Interface Sci. 88 (1982) 214.
[55] Q. Li, Y. Fang, M.E. Green, J. Colloid Interface Sci. 91 (1983) 412.
[56] J.H. Choi, J.S. Park, S.H. Moon, J. Colloid Interface Sci. 251 (2002) 311.

Journal of Membrane Science 525 (2017) 195–201

Contents lists available at ScienceDirect

Journal of Membrane Science

journal homepage: www.elsevier.com/locate/memsci

Swelling induced structural changes of a heterogeneous cation-exchange membrane analyzed by micro-computed tomography

Miloš Svoboda[a,b], Jan Beneš[b], Lucie Vobecká[a], Zdeněk Slouka[a,b,*]

[a] University of Chemistry and Technology Prague, Department of Chemical Engineering, Technická 3, Prague 6 16628, Czechia
[b] University of West Bohemia, New Technologies – Research Centre, Univerzitní 8, Plzeň 30614, Czechia

ARTICLE INFO

Keywords:
Heterogeneous ion-exchange membrane
Swelling
Shrinkage
Structure
Micro-computed tomography

ABSTRACT

3D reconstruction of heterogeneous ion-exchange membranes when swollen in an appropriate electrolyte by micro-computed tomography (μ-CT) can provide important information on structural changes caused by their swelling or shrinkage and used this knowledge along with their electrochemical characteristics for optimization of the structure of these industrially important polymeric composites. We developed a methodology that allows scanning of swollen membrane samples while not being immersed in the solution, a condition necessary for μ-CT analysis of polymeric samples. Qualitative description of membrane swelling and shrinkage induced by volume-changing ion-exchange resin particles demonstrates their strong effect on structural changes in the membrane and identifies salt concentration as one of the major factors affecting the extent to which the membrane swells or shrinks. Experimental study focused on investigating the effect of salt concentration reveals that membrane volume decreases with increasing salt concentration. The dependence between the volume of the membrane and the concentration was well fitted with a natural logarithm. This fit can be used as an empirical equation for estimating the volumetric changes of the membrane caused by immersion in salt solutions of different concentrations.

1. Introduction

Heterogeneous ion-exchange membranes (IEMs) are functional composites widely used in industrial electroseparation processes mainly for water purification (e. g. electrodialysis, electrodeionization, etc...) [1]. These membranes consist of three major components: (i) finely ground ion-exchange resin particles (resin powder), (ii) polymeric binder, and (iii) reinforcing polymeric fibers [2,3]. Ion-exchange resin for ion-exchange membranes is usually copolymer of styrene and divinylbenzene which is functionalized with chemical groups providing the required property to exchange either cations or anions. In case of strong ion-exchangers, quaternary ammonium groups bearing positive charge when solvated are used in anion-exchange resin and sulfone groups bearing negative charge when solvated in cation-exchange resin [4]. Ion selectivity [5] of these particles towards ions contained in the surrounding solutions is given by electrostatic repulsion and attraction forces. The polymeric binder is usually polyvinylchloride, polyethylene or polypropylene and its main role is to bind the finely ground resin particles together. The polymeric fibers are mostly made of polyester or polyamide and they improve mechanical stability of the membranes. These membranes are produced as large sheets by lamination when ground ion-exchange resin particles are blended with binder pellets, slightly melted and laminated between two cylindrical rollers along with reinforcing fiber mesh that is placed on both sides of the membrane [1]. The structure of these membranes is thus characterized by (i) random distribution of ground ion-exchange resin particles within the binder, and (ii) wide size distribution of the functional ion-exchange resin. The structure of heterogeneous ion-exchange membranes, which cannot be very well controlled during manufacturing, however, affects both mechanical and electrochemical properties of these functional composites [6] which in turn influence the performance and reliability of large electroseparation industrial units. There is a significant effort devoted to production of optimized heterogeneous ion-exchange membranes [7]. For instance, 3D profiling of ion-exchange membrane by heat pressing against a mold has been used to produce defined structures on the membrane surface. These molded membranes exhibited improved transport characteristics when compared to the original untreated membranes. Enhanced transport across molded membranes was attributed mainly to the increase in active area of these membranes, i. e. the area on the membrane surface occupied by ion-exchange resin particles [8].

The structure of these membranes does not only influence their

Abbreviations: PE, polyethylene; PES, polyester; μ-CT, micro-computed tomography; IEM, ion-exchange membrane; CEM, cation exchange membrane

* Corresponding author at: University of Chemistry and Technology Prague, Department of Chemical Engineering, Technická 3, Prague 6 16628, Czechia.
E-mail addresses: milossvo@ntc.zcu.cz (M. Svoboda), janbenes@ntc.zcu.cz (J. Beneš), lucie.vobecka@vscht.cz (L. Vobecká), sloukaz@vscht.cz (Z. Slouka).

http://dx.doi.org/10.1016/j.memsci.2016.10.046
Received 14 September 2016; Received in revised form 25 October 2016; Accepted 25 October 2016
Available online 02 November 2016

electrochemical characteristics, it also strongly affects the electrokinetic behavior exhibited by these membranes [9,10]. When connected in DC electrical field that is typically applied in electrodialysis, the unequal flux of counter- and co-ions through the membrane caused by the ion selectivity displayed by the membranes results in generation of depletion and concentration regions in the electrolyte adjacent to the membrane [11,12]. When one applies DC voltage that is larger than the critical, electrohydrodynamic vortex appears on the depletion side of the membrane. One of the theories elucidating the occurrence of the vortex builds on the heterogeneous structure of the membrane [13] creating spatial heterogeneity in electrical conductivity of the membrane [14]. Randomly distributed ground ion-exchange particles exhibiting high ionic conductivity are surrounded by nonconductive binder or fibers. The electrical field, which focuses into the conductive regions, distorts from the original direction and drives the electrohydrodynamic vortex [10].

The actual structure of these membranes is commonly studied in a dried state by means of analytical techniques allowing only surface analysis [15]. These studies suffer from two major drawbacks: (i) they do not characterize the volume of the membranes that largely contributes to the overall electrochemical properties, and (ii) they cannot capture the structural changes associated with swelling of the membrane when immersed in a water solution. Interesting data describing the structure of the membranes can be obtained by contact porosimetry. Contact porosimetry evaluates among others distribution of volume of pores as a function their nominal radii ranging from 1 nm to 100 μm [16]. These studies revealed that characteristic radius of pores in ion-exchange material is about 10 nm [17]. However, this technique does not allow spatial reconstruction of the heterogeneous materials.

It is generally known that IEMs have significantly different volumes between a dry and wet state [18]. Ion-exchange resin particles are highly charged macro-porous or gel systems and their exposure to water or electrolytes results in their swelling [19]. The theoretical description of swelling of polyelectrolyte gels (as e. g. ion-exchange resin) is still incomplete and a subject of theoretical and experimental research [20,21]. The major contributing factors are thermodynamic mixing (chemical potentials of the solvent, i. e. water, outside and inside the particle have to be the same), osmotic pressures as a result of different concentrations of solutes inside and outside the particle and electrostatic interactions given by the presence of the fixed charge [22,23].

To be able to (i) analyze the whole volume of the heterogeneous ion-exchange membranes, (ii) evaluate structural changes in the membrane caused by swelling and (iii) describe the structure of the fully swollen membrane, i. e. the membrane that can be used in electrodialysis, we embarked on developing a technique allowing to exploit computed tomography [24,25] for the reconstruction of the membrane 3D structure. Computed tomography exposes the sample under study with X-ray and collects the information about X-ray attenuation in the sample by using a detector. By collecting a set of images capturing the attenuation of X-ray when the sample is exposed from various sides, one can distinguish domains exhibiting different absorption properties towards X-ray, and thus different materials of which the sample consists. One problem that arises in scanning polymeric samples immersed in water is in high absorption of exposing X-ray by water causing undesirable loss in contrast among the scanned polymers. We developed a technique that overcomes this problem by scanning the swollen polymeric samples in saturated water vapor preventing the sample from drying. Using this technique, we performed an experimental study looking at structural changes brought about by swelling the heterogeneous ion-exchange membrane in KCl solutions of various concentrations.

2. Material and methods

2.1. Materials

The studied heterogeneous cation-exchange membrane (CEM) was kindly provided by a Czech company MemBrain a.s. This particular membrane contains polyethylene (PE) as a binder and polyester (PES) as reinforcing fibers. The other materials and chemicals used in this work included: DI water desalted by reverse osmosis (conductivity 3 μS/cm), KCl purchased from Penta a.s. Czech republic, UV curable acrylic glue Acrifix 192 (produced by Evonik), silicone for mold making N1522 purchased from Elchemco a.s. Czech republic.

2.2. Methods

2.2.1. Sample preparation

We cut out a small piece (cca 1×1 mm^2) of the heterogeneous CEM and embed the membrane in the acrylic glue Acrifix 192 by using a specifically developed silicone mold. The embedded membrane has the top and bottom side clear of any glue which allows exposure of the membrane to various KCl solutions. The frame made of acrylic glue allows easy handling with the membrane and attachment to the scanning cell (see Fig. 1a). Before scanning a swollen sample, we soaked the membrane in an appropriate KCl solution for at least 48 h.

2.2.2. Scanning cell

Scanning of the sample swollen in water solutions presents a significant problem due to high absorption of X-rays by water. We developed a scanning cell that allows swelling of the membrane in an appropriate water solution (Fig. 1b) and subsequently removal of the solution from the membrane by centrifugation while keeping the membrane in saturated water vapor (see Fig. 1c). This environment prevents any volumetric changes of the membrane associated with water evaporation. The scanning cell body is made of a thin walled (0.1 mm) polypropylene tube capped with tailor made CNC machined

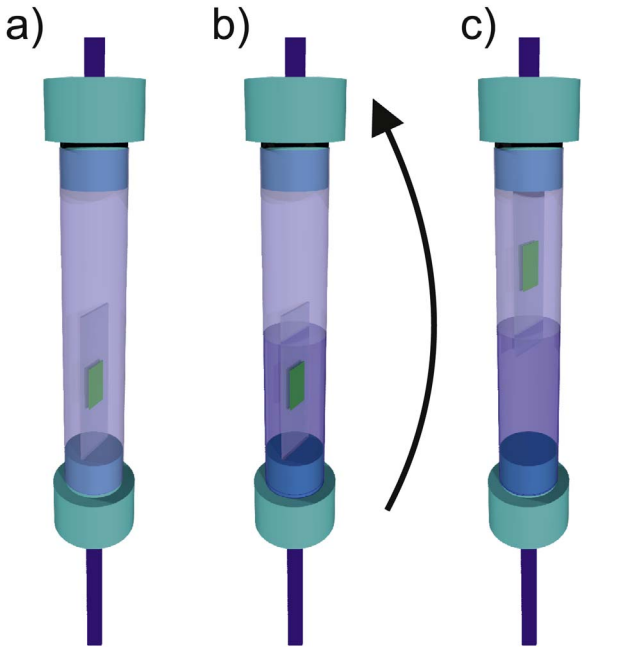

Fig. 1. Scanning cell developed for the analysis of swollen samples by μ-CT. The principle of operation is as follows: a) insertion and attachment of the sample (green rectangle represents a cut-out of the membrane) inside the cell, b) swelling the sample in a given water solution, c) turning the cell upside down (see the arrow) and removal of the remnant solution from the sample by centrifugation followed by scanning. (For interpretation of the references to color in this figure legend, the reader is referred to the web version of this article.)

PMMA plugs at each end. The outer diameter of the tube is 5 mm, so it is possible to move the detector very close to the scanned sample (approximately 6 mm from the center of the sample). This is a crucial parameter to maintain acceptable scanning time when using high resolution. We attach the sample of a CEM embedded in the acrylic resin to one end of the scanning cell with Acrifix 192.

2.2.3. Micro-computed tomography

The sample of the cation-exchange membrane was scanned by Xradia MicroXCT 400 machine. Xradia MicroXCT is a specialized CT machine for scanning of low absorbing materials with high resolution. It utilizes low voltage X-ray source (20–90 kV) and interchangeable high resolution detectors. While the positions of the source and the detector are fixed during scanning, the sample rotates step by step by 360 degrees about its vertical axis. Transmission tomography image of the scanned sample is recorded in every set position. The parameters of the scanning of the membrane sample were: source voltage 25 kV, source power 2.5 W, pixel size 2.1 μm, detector resolution 1024×1024 pixels (binning 2), rotation angle 360°, number of images 1500, overall scanning time 3 h, temperature 28 °C.

2.2.4. Data processing

The results of μ-CT analysis is a grayscale 3D image in which gray color intensity corresponds to the level of X-ray absorption. The brighter the pixel, the higher X-ray absorption and vice versa. This in turn gives information on the absorbing material and eventually composition. Such a grayscale image only provides qualitative information about the structure of the membrane. To gain any quantitative information about the sample, we performed a so called image segmentation. Image segmentation means partitioning of the digital image in a way that each pixel (voxel) is assigned with a colored label corresponding to a single material. Example of image segmentation is shown in Fig. 2. We segment the obtained images by thresholding, i. e. by setting threshold values to the image histogram for each material in the membrane. Automatic thresholding can be easily used when there are sharp divides in the gray color intensity representing different materials. When scanning polymer samples and especially swollen samples, the differences in X-ray absorption, and hence the gray color intensity, can be very small. The processing of such images requires a semi-manual approach. By looking at Fig. 2a, one can see that e. g. PES reinforcing fibers have similar absorption to PE binder and acrylic resin. That is why we first trace PES fibers and acrylic resin along with the contours of the whole sample (to separate the sample from surroundings) manually. After manual labelling of these three phases, we segment the rest of the membrane (macro-pores, PE binder and ion exchange particles) by histogram thresholding. To increase the accuracy of the thresholding we assumed that the volume of the polyethylene binder is constant and does not depend on the concentration of the solution, the membrane is soaked in. This assumption significantly alleviated the setting of the thresholds for the macro-pores and ion-exchange resin particles. When segmentation is applied to the whole stack of slices, the result is a 3D matrix in which each pair of color and corresponding material is represented by a unique number. One can perform all algebraic operations with such a matrix allowing quantitative analysis. The volume of a single voxel in scanning the samples with setting as described in section micro-computed tomography is approximately 9.26 μm^3.

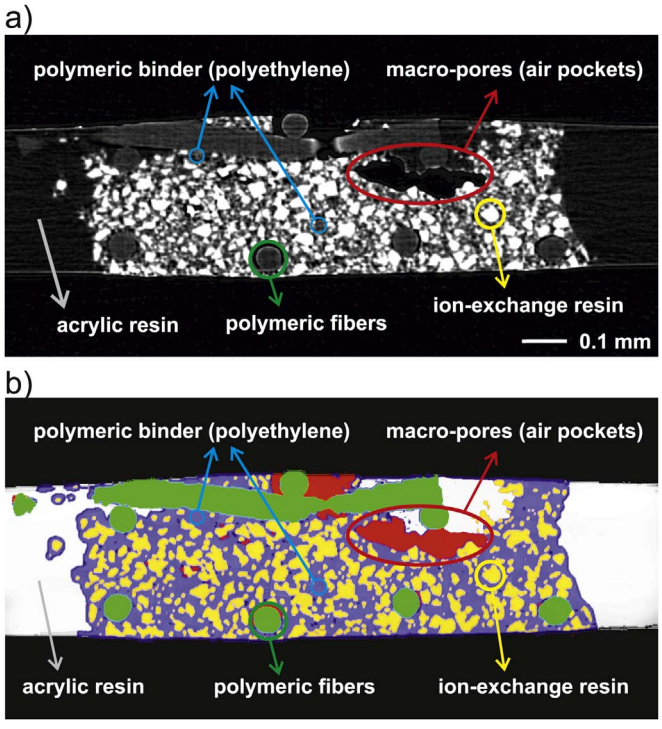

Fig. 2. a) Grayscale image of a single cross-section of a scanned dry membrane with labels for individual materials present in the sample, b) segmented image (assignment of a given color representing one material to each pixel) of the figure above. (For interpretation of the references to color in this figure legend, the reader is referred to the web version of this article.)

3. Results and discussion

This section is organized in the following way. First, we describe qualitatively the cation-exchange membrane structure in a dry state and characterize its main structural features found in the μ-CT image. Next, we focus on the changes in the membrane structure caused by membrane swelling or shrinkage in solutions of various KCl concentrations which are quantified in the last paragraph of this section.

3.1. μ-CT analysis of a dry membrane

We started the μ-CT analysis of the cation-exchange membrane by running the scan of a dry sample. The absence of water as a medium attenuating the X-ray to similar degree as polymers allows one to better distinguish individual polymeric materials in the membrane. By looking at the Fig. 2a that shows a single μ-CT cross-section of the dry membrane, one can easily resolve very bright white objects randomly dispersed throughout the membrane and large black holes present in the membrane. The other structures are of a gray color and do not exhibit significant differences with respect to X-ray attenuation. Knowing the composition of the membrane (of what the membrane consists) and the expected X-ray attenuation exhibited by each material (white – high absorbing, black – low absorbing), we qualitatively assigned each of the grayscale colors and structures to individual materials. The white color represents the ion-exchange resin (cross-linked styrene and divinyl-benzene with sulfone groups). This material is labeled with yellow arrow in Fig. 2a and yellow color in Fig. 2b. The black color represents air pockets that were trapped in the membrane during lamination. In swelling, these air pockets fill with the solution and for this reason we denote them as macro-pores. The macro-pores are labeled with a red arrow and red color in Fig. 2a and b, respectively. As said above, acrylic resin, PES fibers and PE binder display very similar absorption of X-ray and thus show very similar identical gray color. However, PES fiber have symmetrical circular cross-section and one can easily find them in the Fig. 2a and b where they are marked with green color. We can also identify the acrylic resin that is only present on the edges of the membrane. This material is depicted with gray arrow and color in Fig. 2a and b, respectively. We again stress that PES fibers and acrylic resin were traced manually, i. e. by visual inspection of the image. The remaining material is the PE binder that fills the inter ion-exchange particle space and is represented with blue color. Fig. 2b shows the result of the segmentation of the raw CT scan

image as described in the section 2.2.4. Each pixel of the segmented image is now assigned a color that represents one of the phases present in the material. We refer the reader to the movie2.avi to explore the volumetric profile of the original dry membrane (the frame on the left). One surprising result of this analysis is the amount of the macro-pores (air gaps) contained in the membrane. These macro-pores can be considered as defects of the membrane since they cannot contribute to the ion-exchange. The other characteristic feature of this membrane is not only random spatial distribution of ion-exchange resin particles but also their wide size distribution and non-uniformity in shape.

3.2. Qualitative description of swelling

The results obtained for the dry membrane served as a starting point for the analysis of the membrane swollen in KCl solutions. We sequentially let the membrane swell in the following set of solutions: DI water, 1 mM KCl, 10 mM KCl, 100 mM KCl and 1 M KCl. Before immersing the membrane in the next KCl solution, we scanned the membrane according to the procedure described in sections 2.2.2. and 2.2.3. After performing the whole study, we let the membrane dry again on air and obtained the last scan under this condition.

The results of our experimental study are depicted in Fig. 3 as single cross-sections of the dry membrane (a) and swollen in DI water (b), 10 mM (c) and 1 M KCl (d) and summarized in a movie movie1.avi that can be found in the supplemental material. The file movie1.avi contains six roughly synchronized movies capturing the 3D structure of the membrane obtained under various swelling conditions so that one can easily analyze structural changes of the same cross-section of the membrane.

Supplementary material related to this article can be found online at http://dx.doi.org/10.1016/j.memsci.2016.10.046.

By comparing Fig. 3a (dry membrane) and 3b (membrane swollen in water), one can see profound effects of the swelling in water solutions on the membrane structure. Horizontal dashed yellow lines in Fig. 3 aid one to assess the effect of this swelling. The volume of the swollen membrane is much larger than that of the dry one and the transition from dry to swollen state is accompanied by significant structural changes. The swelling of the membrane is caused by swelling of the ion-exchange resin particles that significantly change their volumes. We highlight a few ion-exchange particles in the dry and swollen membrane for comparison (see red, green and blue circles in Fig. 3) and refer the reader to the aforementioned movie movie1.avi capturing 3D projection of the membrane. The swelling of these particles then induces all other structural changes that can be identified in the membrane swollen in water, e. g. the material itself can be significantly displaced from its original position (see the IER particle in red circle in Fig. 3). One of the major effects of membrane exposure to DI water is filling the original air gaps with water. This phenomenon is accompanied by increased absorption of X-ray, which is nicely documented by turning original black air pockets to gray macro-pores in the Fig. 3. Changing the color to gray is one of the reasons for semi-manual segmentation of the obtained results. Some of the air gaps are, however, completely enclosed by water impermeable PE binder and thus remain as air gaps. The PES reinforcing fibers are displaced from the original position by the swelling forces and are still at or close to the surface of the membrane (compare the position of fibers with respect to horizontal dashed yellow lines).

By closely analyzing the cross-sections of the membrane swollen in different KCl concentrations, we can see that the membrane shrinks with increasing concentration. The vertical dashed yellow line that has the same length in all images in Fig. 3 clearly proves this statement. The concentration of KCl (ionic strength) is thus an important factor which contributes to the structural changes of ion-exchange membranes caused by swelling/shrinkage. This effect will be analyzed in the following sections.

At the very end of this parametrical study, we let the membrane dry on air and scanned the dried sample to see consequences of the swelling and shrinkage on the membrane. We present the results of this experiments in a movie movie2.avi in which the frame on the left shows the membrane at the beginning of the experiment and on the right at

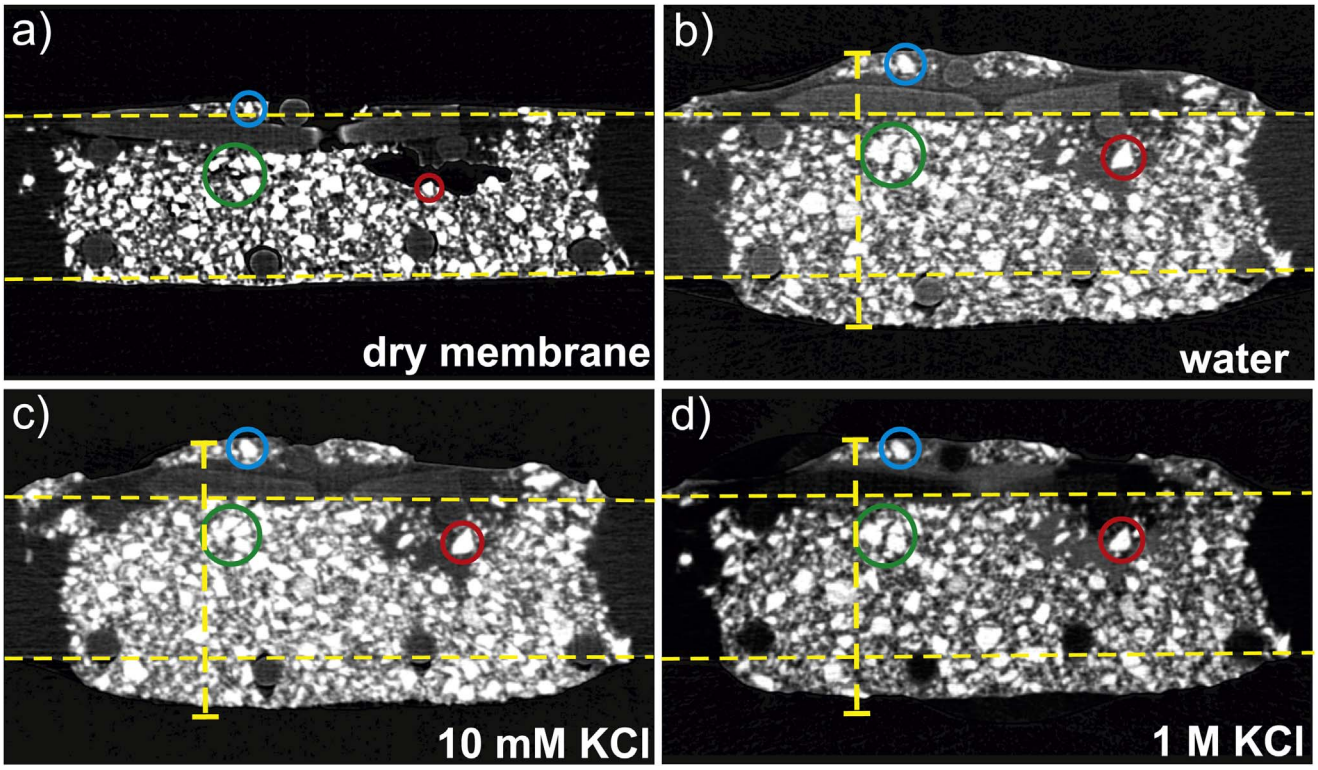

Fig. 3. The same cross-section of the membrane under different swelling conditions: a) dry membrane, b) swollen in water, c) swollen in 10 mM KCl solution, and d) swollen in 1 M KCl solution. (For interpretation of the references to color in this figure, the reader is referred to the web version of this article.)

the end. Again, we roughly synchronized the frames so that the structural changes incurred by swelling and shrinkage are easily observable. One feature which one immediately see in comparing the membrane before and after swelling is associated with increased amount of black spaces (air gaps=macro-pores) that very often contour the white resin particles, especially the larger ones, and polymeric fibers. In general, the dried membrane contains many air pockets reminding one of cracks. This effect is given by shrinkage of ion-exchange particles caused by drying that cannot be fully followed by PE binder and PES fibers. The incapacity of the binder to follow the shrinkage of IER particles then causes the occurrence of void spaces filled with air. This observation will be quantified in the next section.

3.3. Quantitative description of swelling

In the previous paragraph, we described the qualitative changes in the membrane structure caused by swelling and shrinkage in water solutions and the effect of KCl concentration on the overall membrane volume. To quantify the volumetric changes caused by the exposure of the investigated membrane to KCl solutions of various concentrations, we took advantage of segmentation and evaluated the following parameters: volume of the whole membrane, volume of the ion-exchange resin particles, volume of the macro-pores for the membrane swollen under different conditions, volume of PES fibers and volume of the PE. The macro-pores include air gaps enclosed in PE binder that do not fill with a solution on swelling. Because KCl solutions of different concentrations exhibit different X-ray absorptions, the histogram of grayscale intensities of individual scans also differ (see different grayscales in subpanels of Fig. 3). This accompanying effect of CT analysis makes the segmentation more difficult. To increase the accuracy of segmentation, we (i) tracked manually PES fibers (easily recognizable due to their characteristic shape), acrifix resin (located on the edges of the membrane) and the external boundary of the membrane (to exclude surroundings), and (ii) assumed that PE binder does not change volume in different water solutions. We reason this assumption by the following facts: (i) polyethylene does not swell or shrink in water solutions and (ii) the membrane has enough space to swell freely without causing any significant compression of the afore-mentioned material. The volume of the PE binder obtained from the dry and easily segmented membrane was used as a reference and constant value for all other scans and for which the histograms were then adjusted accordingly.

The evaluated volumes as a function of KCl concentrations are plotted in the form of a bar graph in Fig. 4 and summarized in Table 1. Table 1 shows the volume of the whole membrane and volumetric fractions (in %) of individual components which are related to the overall volume of the membrane obtained for a swelling condition. The

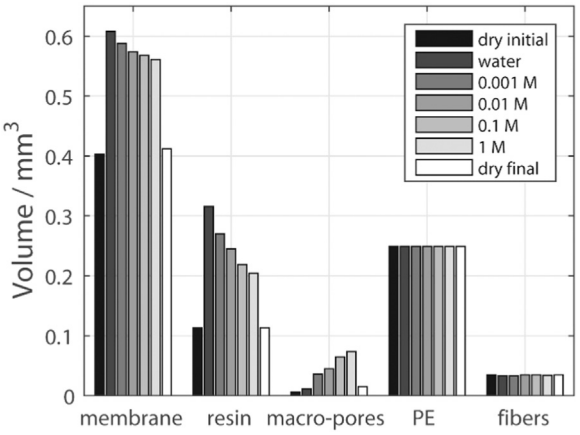

Fig. 4. Volumes of the whole membrane, ion-exchange resin particles, macro-pores, PE binder and PES fibers in the dependence on the concentration of KCl.

Table 1
Volumes of the whole membrane in mm^3, and volume fractions of individual components at different swelling conditions. The volumes of individual components used in calculations of the volume fractions are plotted in the bar graph in Fig. 4.

State of the membrane	$V_{membrane}$/ mm^3	Resin/%	Macropores/%	PE/%	Fibers/%
Initial dry	0.403	28.0%	1.5%	61.8%	8.7%
DI water	0.608	51.8%	1.8%	41%	5.4%
10^{-3} M KCl	0.588	45.9%	6.1%	42.4%	5.6%
10^{-2} M KCl	0.574	42.7%	7.8%	43.4%	6.1%
10^{-1} M KCl	0.568	38.6%	11.4%	43.8%	6.2%
1 M KCl	0.561	36.4%	13.2%	44.4%	6.1%
Final dry	0.412	27.4%	3.6%	60.4%	8.5%

overall volume of the membrane changes from 0.403 mm^3 in the dry state to 0.608 mm^3 after swelling in water. The volumetric change is about 50% which is a number corresponding well to the number provided by the manufacturer of these membranes. The overall volume of the membrane reaches its maximum in DI water and then decreases monotonously with increasing KCl concentration and is 0.561 mm^3 for KCl concentration of 1 M. On drying the membrane on air, the overall volume of the membrane regains value almost corresponding to that of the dry membrane at the beginning of the experiment (compare black bar – dry initial and white bar – dry final for the membrane). The volume of the dry membrane at the end is only 0.01 mm^3 larger than the volume of the dry membrane at the beginning (before any swelling). The data for the resin particles show the same trend as those for the overall volume of the membrane. The transition from dry to swollen state causes their volumetric change from 0.113 to 0.315 mm^3 which corresponds to a change of about 280%. In the context of the overall membrane composition, the ion exchange resin particles occupy 28% of the membrane volume in the dry state and almost 52% when the membrane is exposed to DI water (see Table 1). The volume of the resin particles also decreases monotonously with increasing KCl concentration and is 0.20 mm^3 for 1 M KCl. This monotonous decrease is also observed for the volume fraction of ion-exchange resin particles. Larger degree of swelling/shrinkage of the resin particles just confirms known fact that they control the volumetric changes of the whole membrane. One important effect to notice is the volume of the resin particles at the beginning and at the end of the experiment when the membrane is dry. These two volumes are identical (see the corresponding bars in Fig. 4), which indicates that swelling followed by drying is reversible for the resin particles. Interestingly, the macro-pores (air gaps in the dry membrane) do not change their volume significantly after being immersed in DI water, however, they increase their volume on immersing the membrane in solutions with higher KCl concentration. This trend is documented both by both the bar plot in Fig. 4 and the volume fractions for the macro-pores given in Table 1. This behavior is probably given by the order of solutions to which the membrane was exposed. First, the membrane was swollen to its maximum volume by immersion in water at the very beginning of this experimental study and subsequently shrank on immersion in KCl solutions with increasing concentration causing membrane shrinkage. This effect of shrinkage was attributed to ion-exchange resin particles. However, PES fibers and PE binder are not reversibly forced to follow the decrease in the volume of ion-exchange particles which leaves a space among ion-exchange particles and the surrounding material. On comparing the volume of macro-pores in the dry membrane at the beginning and at the end, one can see that the there is more macro-pores. This result is in a good agreement with qualitative description of the movie movie2.avi where appearance of black stripes around shrunk white resin particles was characteristic for the membrane dried on air.

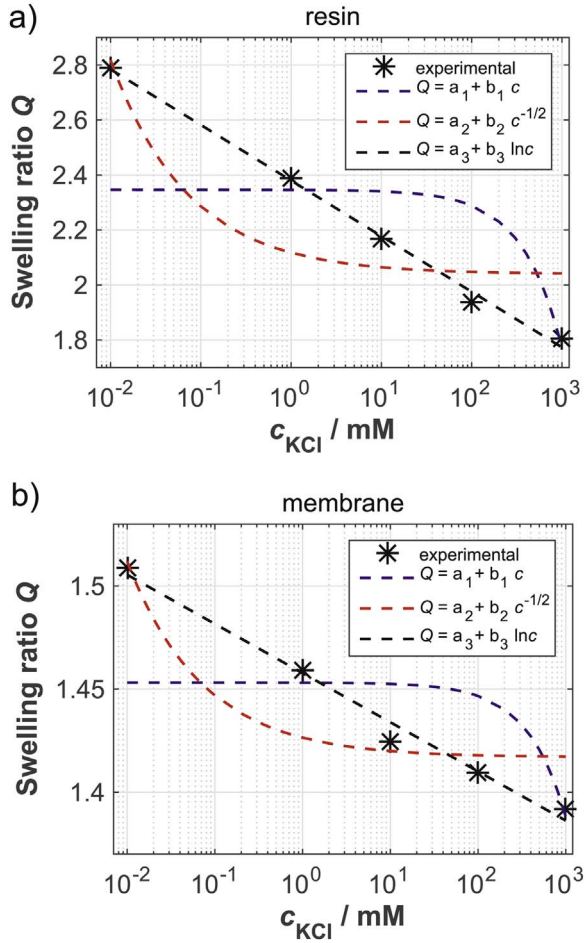

Fig. 5. Dependence of the swelling ratio Q on the concentration of KCl for a) the resin and for b) the whole membrane. The black asterisks represent experimental data, the dashed lines appropriate fits as described in the legend. (For interpretation of the references to color in this figure, the reader is referred to the web version of this article.)

3.4. Swelling/shrinkage of the membrane

The swelling of crosslinked polymers occurs as a result of uptake of a solution in which the crosslinked polymers are soaked. Ion-exchange resin particles are highly crosslinked polymers functionalized with chemical groups that when in water solution dissociate and create a so called fixed charge (part of the functional group covalently linked to the polymer network) and mobile counter-ion easily exchangeable with ions of the like charge contained in the surrounding solutions. The description of the equilibrium swelling behavior of polymeric gels is complex and not yet fully understood. The swelling depends on the type of polymeric network and its structure, and on the solvent and its composition. In case of polyelectrolyte polymeric networks, the balance between elastic forces (opposing swelling) of crosslinked polymers and osmotic pressure (causing swelling) brought about by differences in ion concentration inside and outside particles is considered. Sometimes these two forces are completed with the effect of electrostatic interactions of the charges fixed on the polymeric network.

To see if our results showing the swelling of the particle as a function of KCl concentration scales as one of the two forces causing swelling (osmotic pressure, electrostatic interactions), we evaluated swelling ratio Q defined as a ratio of volume of swollen material V to its volume V_0 when completely dry and fitted its dependence on concentration with two following functions: $Q=a_1+b_1 \cdot c$ and $Q=a_2+b_2 \cdot c^{(-1/2)}$. The first equation captures the linear dependence of osmotic pressure on concentration and the later dependence of Debye screening length (characteristic length scale of electrostatic interactions) on concentration. We evaluated the parameter Q for the ion-exchange resin particles and the whole membrane and plotted the results in Fig. 5a and b, respectively. In these fits, we also included the result for DI water where the concentration of KCl was determined as a theoretical concentration of KCl which would correspond to the electrolytic conductivity of used DI water. In both figures, the black asterisks represent the experimental data, the red dashed curves fit with the first equation and blue dashed curve with the second equation. One can clearly see, that none of these functions fits the data well. On analyzing the experimental data, we fitted them with a logarithm in the form $Q=a_3+b_3 \cdot \ln(c)$. These fits are represented with black dashed lines in Fig. 5. In both cases, the logarithm provides optimal fit of the experimental data and can be used to predict the volume changes of the membrane. The evaluated dependencies are $Q=1.5273-0.0121 \cdot \ln(c)$ and $Q=2.3799-0.0878 \cdot \ln(c)$ for the membrane and resin, respectively where the concentration is substituted in mM. The reason why logarithm fits our data is subject of ongoing investigation.

4. Conclusions

We described a methodology of using μ-CT for the analysis of heterogeneous ion-exchange membranes as functional polymeric composites swollen in water solutions. Our technical solution overcomes the problem of high X-ray absorption by water comparable to polymers and allows long-term scanning of swollen membranes that prevents evaporation of water and accompanying structural changes.

The main results of our micro CT analysis of the heterogeneous ion-exchange membrane can be summarized into the following points:

1. Dry membrane provided by the manufacturer contains ion-exchange resin particles with large size distribution randomly distributed in the polyethylene binder and surprisingly a great many large air gaps.
2. Exposure of the membrane to water solution causes its swelling that is driven by ion-exchange resin particles. The swelling results in significant structural changes in the membrane.
3. We observed a dependence of the membrane volume on the concentration of the potassium chloride. The volume of the membrane and mainly ion-exchange resin particles decreased with increasing concentration. Interestingly, macro-pores showed an opposite trend and their volume increased with increasing concentration. This effect was attributed to the lack of restoring forces that would act on PE binder and PES fibers during shrinkage of the membrane.
4. The drying of the membrane after performing the swelling concentration study revealed more macro-pores when compared to the original dry membrane that often contoured larger ion-exchange resin particles.
5. Neither linear nor inverse-square fit of the experimental data between swelling ratio and the KCl concentration interpolated the experimental data well. The experimental data were nicely fitted with a logarithm that can be used as an empirical equation to predict volumetric changes of the membrane.

Acknowledgement

This work was supported by the Czech Science Foundation (Grant Number 15-10907Y). The result was developed within the CENTEM project, reg. no. CZ.1.05/2.1.00/03.0088, cofunded by the ERDF as part of the Ministry of Education, Youth and Sports OP RDI programme and, in the follow-up sustainability stage, supported through CENTEM PLUS (LO1402) by financial means from the Ministry of Education, Youth and Sports (Grant no. LO1402) under the "National Sustainability Programme I." The authors would also like to thank Zdenek Ruzek for technical help with scanning cell construction.

References

[1] H. Strathmann, Electrodialysis, a mature technology with a multitude of new applications, Desalination 264 (3) (2010) 268–288.
[2] Y. Tanaka, Membrane Science and Technology Series, 12 Ion Exchange Membranes: Fundamentals and Applications Preface, vol. 12, 2007, pp. V–Vii.
[3] M.Y. Kariduraganavar, et al., Ion-exchange membranes: preparative methods for electrodialysis and fuel cell applications, Desalination 197 (1–3) (2006) 225–246.
[4] T.W. Xu, Ion exchange membranes: state of their development and perspective, J. Membr. Sci. 263 (1–2) (2005) 1–29.
[5] Z. Slouka, S. Senapati, H.C. Chang, Microfluidic systems with ion-selective membranes, Annu. Rev. Anal. Chem. 7 (7) (2014) 317–335.
[6] J.H. Choi, S.H. Kim, S.H. Moon, Heterogeneity of ion-exchange membranes: the effects of membrane heterogeneity on transport properties, J. Colloid Interface Sci. 241 (1) (2001) 120–126.
[7] R. Ibanez, D.F. Stamatialis, M. Wessling, Role of membrane surface in concentration polarization at cation exchange membranes, J. Membr. Sci. 239 (1) (2004) 119–128.
[8] S. Melnikov, et al., Electrodialysis treatment of secondary steam condensate obtained during production of ammonium nitrate. Technical and economic analysis, Sep. Purif. Technol. 157 (2016) 179–191.
[9] V.V. Nikonenko, et al., Desalination at overlimiting currents: state-of-the-art and perspectives, Desalination 342 (2014) 85–106.
[10] J. Balster, et al., Morphology and microtopology of cation-exchange polymers and the origin of the overlimiting current, J. Phys. Chem. B 111 (9) (2007) 2152–2165.
[11] Y. Tanaka, Concentration polarization in ion-exchange membrane electrodialysis - The events arising in an unforced flowing solution in a desalting cell, J. Membr. Sci. 244 (1–2) (2004) 1–16.
[12] Z. Slouka, et al., Charge inversion, water splitting, and vortex suppression due to DNA sorption on ion-selective membranes and their ion-current signatures, Langmuir 29 (26) (2013) 8275–8283.
[13] V.I. Zabolotskii, et al., Electroconvection in systems with heterogeneous ion-exchange membranes, Russ. J. Electrochem. 48 (7) (2012) 692–703.
[14] M. Svoboda, et al., Cation exchange membrane integrated into a microfluidic device, Microelectron. Eng. 86 (4–6) (2009) 1371–1374.
[15] S. Mikhaylin, et al., How physico-chemical and surface properties of cation-exchange membrane affect membrane scaling and electroconvective vortices: influence on performance of electrodialysis with pulsed electric field, Desalination 393 (2016) 102–114.
[16] N.A. Kononenko, M.A. Fomenko, Y.M. Volfkovich, Structure of perfluorinated membranes investigated by method of standard contact porosimetry, Adv. Colloid Interface Sci. 222 (2015) 425–435.
[17] N.P. Berezina, et al., Characterization of ion-exchange membrane materials: properties vs structure, Adv. Colloid Interface Sci. 139 (1–2) (2008) 3–28.
[18] Q.J. Duan, S.H. Ge, C.Y. Wang, Water uptake, ionic conductivity and swelling properties of anion-exchange membrane, J. Power Sources 243 (2013) 773–778.
[19] E. Lafond, et al., Investigation of the swelling behavior of cationic exchange resins saturated with Na+ ions in a C3S paste, Cem. Concr. Res. 69 (2015) 61–71.
[20] A.V. Dobrynin, Theory and simulations of charged polymers: from solution properties to polymeric nanomaterials, Curr. Opin. Colloid Interface Sci. 13 (6) (2008) 376–388.
[21] F. Ganji, S. Vasheghani-Farahani, E. Vasheghani-Farahani, Theoretical description of hydrogel swelling: a review, Iran. Polym. J. 19 (5) (2010) 375–398.
[22] E. Vasheghanifarahani, et al., Swelling of ionic gels in electrolyte-solutions, Ind. Eng. Chem. Res. 29 (4) (1990) 554–560.
[23] R. Skouri, et al., Swelling and elastic properties of polyelectrolyte gels, Macromolecules 28 (1) (1995) 197–210.
[24] J. Hsieh, Computed Tomography Principles, Design, Artifacts, and Recent Advances. (2009), 2009, p. 510.
[25] S.R. Stock, MicroComputed Tomography: methodology and Applications, first ed., CRC Press Taylor & Francis Group, Boca Raton (FL), USA, 2008, p. 336.

Langmuir

Article

pubs.acs.org/Langmuir

Charge Inversion, Water Splitting, and Vortex Suppression Due to DNA Sorption on Ion-Selective Membranes and Their Ion-Current Signatures

Zdenek Slouka, Satyajyoti Senapati, Yu Yan, and Hsueh-Chia Chang*

Department of Chemical and Biomolecular Engineering, University of Notre Dame, Notre Dame, Indiana 46556, United States

Supporting Information

ABSTRACT: The physisorption of negatively charged single-stranded DNA (ssDNA) of different lengths onto the surface of anion-exchange membranes is sensitively shown to alter the anion flux through the membrane. At low surface concentrations, the physisorbed DNAs act to suppress an electroconvection vortex instability that drives the anion flux into the membrane and hence reduce the overlimiting current through the membrane. Beyond a critical surface concentration, determined by the total number of phosphate charges on the DNA, the DNA layer becomes a cation-selective membrane, and the combined bipolar membrane has a lower net ion flux, at low voltages, than the original membrane as a result of ion depletion at the junction between the cation- (DNA) and anion-selective membranes. However, beyond a critical voltage that is dependent on the ssDNA coverage, water splitting occurs at the junction to produce a larger overlimiting current than that of the original membrane. These two large opposite effects of polyelectrolyte counterion sorption onto membrane surfaces may be used to eliminate limiting current constraints of ion-selective membranes for liquid fuel cells, dialysis, and desalination as well as to suggest a new low-cost membrane surface assay that can detect and quantify the number of large biomolecules captured by probes functionalized on the membrane surface.

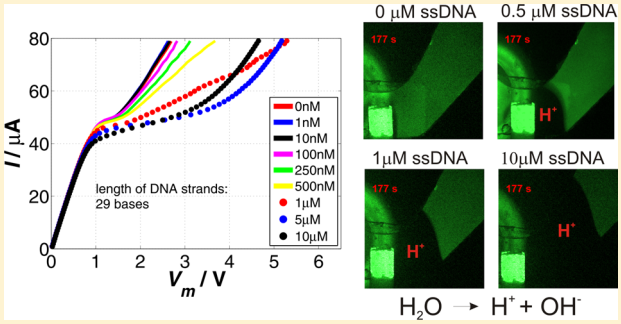

INTRODUCTION

Ion-exchange membranes (IEMs) are extensively used in separation processes, mostly in electrodialysis and electrodeionization.[1] These membranes show a unique property of selective ion transport through the nanopores of IEMs embedded with a fixed charge that allows only counterions (ions with opposite charge to that of the fixed one) to pass through as co-ions experience electrostatic repulsion. The ion-exchange membranes are classified as cation- or anion-exchange membranes on the basis of their ability to exchange cations or anions, respectively. Both anion- and cation-exchange membranes display nonlinear current−voltage characteristics (CVC) with three distinguishable regions (Figure 1, left).[2,3] The first region referred to as the under-limiting region occurs at low voltages where the electrical current is directly proportional to the voltage applied across the membrane, as in the case of an ohmic resistor. The electrical current, however, starts to saturate at a limiting current beyond a critical cross-membrane voltage drop as a result of the ion-transport limitation introduced by ion depletion on one side of the membrane[4,5]. Ben and Chang[6] and Yossifon et al.[7] have shown that the current does not really saturate this limiting region (LR) but is rather a linear function of voltage with a large local differential resistance due to an extended polarized region with space charge at the membrane surface whose existence was first suggested by Rubinstein and Shtilman.[2] However, an inflection point appears on the CVC curve at a critical voltage, corresponding to the end of the LR, and the electrical current rises abruptly, giving rise to a second linear region called the overlimiting region (OR).

Although the nonlinear behavior of IEMs was described more than six decades ago,[8,9] the overlimiting region has been a puzzle and a subject of intensive debate for the last couple of decades. Several mechanisms have been suggested, and the most recent one involves the deionization of the membrane due to an acid−base reaction triggered by the low-pH condition during concentration polarization.[10] However, for most commercial membranes, including the ones used here, chemical stability is essential, so the functional groups are carefully designed to prevent such deionization. The permselectivity of a membrane (Neosepta AMX, Japan) similar to the one used in our work was shown to remain constant after prolonged use,[11] and the loss of selectivity cannot explain the occurrence of the OR. The overlimiting current has also been attributed to the following effects:[12,13] (i) a water-splitting reaction taking place at the interface between the membrane and the depletion zone, (ii) electroconvection (electro-driven vortices) mixing the depletion zone with the conductive bulk of the electrolyte,

Received: February 25, 2013
Revised: April 23, 2013
Published: June 6, 2013

   dx.doi.org/10.1021/la4007179 | Langmuir 2013, 29, 8275−8283

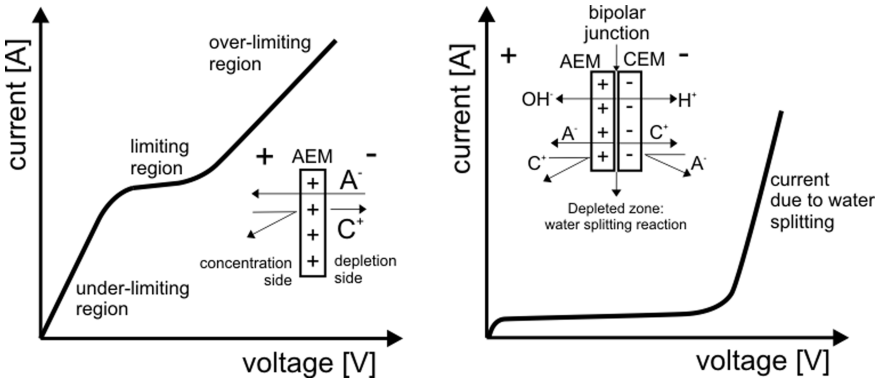

Figure 1. Current–voltage characteristics of an anion-exchange membrane (left) and a bipolar membrane under reverse bias (right) with the schematics showing the transport of cations (C^+) and anions (A^-).

(iii) density gradients developing near the membrane resulting in the transport of the electrolyte due to natural convection, (iv) the exaltation effect associated with water splitting when the H^+ and OH^- ions generated in the depletion region cause an increase in concentration of the other salt ions, and (v) surface conductance and electro-osmotic flow due to a like-charge channel,[14,15] The true picture may be given by the mutual interplay of these effects[16] or by the dominance of one effect over the other, although surface conductance and electro-osmotic mechanisms can be ruled out in our system with large microchannels with a small surface charge that is opposite from that of the membrane charge. The dominance of one effect could be due to the geometry of the experimental setup and the experimental conditions.[17] However, electroconvection is still considered to be the main mechanism contributing to this overlimiting current[18−20] and was shown to be affected by the properties of the membranes, such as the membrane charge density,[21] hydrophobicity,[22] conductive heterogeneity,[23,24] surface heterogeneity of the membrane,[12] or Stokes' radius of the counterions in the electrolyte.[25] The mechanism behind the electroconvection has been intensively investigated in the last couple of decades. Rubinstein et al.[26] first suggested that a microvortex instability of the extended polarized region is responsible for the electroconvection. Theoretical[27−29] and numerical[30,31] studies showed that a strong electric field acting on an extended space charge region adjacent to the membrane can indeed destabilize the extended region and produce electroconvection. A nanochannel having ion-selective properties is often used to study processes associated with ion transport through ion-selective environments.[7,30,32,33] Ion-selective nanochannels allowed the direct observation of electroconvection in the overlimiting region by fluorescence microscopy. These studies revealed the formation of a vortex array in front of a 1-mm-wide, 200-nm-high nanochannel and a pair of symmetrical vortices for a nanochannel with approximately the same width and height.[30] The mechanisms responsible for the occurrence of electroconvection due to the vortex instability were summarized in a review by Chang et al.[34]

The membrane CVC dramatically changes when a second ion-exchange membrane having an opposite fixed charge is stacked onto the first one.[35,36] Such a system can be compared to a semiconductor p-n-type junction, where one side of the junction is formed by a cation-exchange membrane enhancing the transport of cations and the other side is formed by an anion-exchange membrane with the anions as the major electrical current carriers. This system is known as a bipolar membrane. Bipolar membranes, unlike monopolar ion-exchange membranes, behave like an ion diode with a strong rectification effect—the ion current is very different for forward and reverse biases.

The forward bias causes the formation of an ion-enriched region at the bipolar junction and exhibits a linear CVC ohmic curve. With reverse bias, the ions are depleted from the bipolar junction and the local electric field increases with decreasing ionic strength.[37] At a sufficiently high voltage, the electric field at the bipolar junction becomes sufficiently high to split water and the junction becomes an ionic reactor that continuously generates hydrogen cations and hydroxide anions (Figure 1, right).[38−40] The resulting water-splitting current produces an overlimiting current that is higher than any other mechanism, including that due to electroconvection by the microvortex instability.

There has been interest in creating a bipolar membrane by adsorbing and functionalizing large polyelectrolytes with opposite charges onto the surface of an ion-selective membrane. It would be a simple means of synthesizing bipolar membranes with large ion currents, and the enhanced current could also be a sensitive reporter for the presence of surface fouling by biomolecules. Interestingly, the formation of a cationic layer either by adsorbed micelles containing monovalent benzalkonium chloride[41,42] or by chemically introduced quaternary ammonium groups[43] on the surface of a cation -exchange membrane did not result in a water-splitting reaction when connected under reverse bias. In ref 43, the authors hypothesize that the absence of water splitting is caused by an absorbed micelle layer that can form a bipolar interface on the cation -exchange membrane without an intermediate layer of water. Conversely, Loza et al.[44] observed a decrease in the voltage corresponding to the onset of the overlimiting region for increasing coverage of a cation-exchange membrane with TBA^+ (tetrabutyl ammonium cations). The authors hypothesized without further investigation that this effect can be caused either by an enhanced water-splitting reaction due to the creation of local bipolar junctions or by enhanced electroconvection due to increased surface charge variation and heterogeneity. Because water splitting can corrupt the deionization efficiency of the membrane, considerable work has been devoted to removing it by immobilizing a thin layer having the same charge as the original membrane. These modifications have led to the almost complete elimination of the water-splitting reaction for both cation-[45] and anion-exchange membranes.[46]

dx.doi.org/10.1021/la4007179 | Langmuir 2013, 29, 8275−8283

In this work, as a part of the development of new-generation DNA/RNA sensors, we conducted an in-depth study to explain and quantify the charge inversion required to form a bipolar membrane when large multivalent counterions are physisorbed onto a membrane surface. Specifically, we study the charge-inversion phenomenon on a heterogeneous anion-exchange membrane integrated into a microfluidic system in such a way that also allows us to perform pH fluorescence microscopy of the membrane surface. The heterogeneous anion-exchange membrane (Mega a. s., Czech republic) contains strongly basic and chemically stable quaternary ammonium groups bound to polystyrene/divinylbenzene particles that are embedded within a polyethylene matrix reinforced by polyamide or polyester fibers. Samples of single-stranded DNA (ssDNA) are used as large counterions. ssDNA molecules bear a negative charge at neutral pH because of the dissociation of hydrogen from phosphate groups that form the nucleic acid backbone. Phosphate groups on the DNA molecules are fully dissociated for the pH range of 4−8, with a pK_a of 2.0 for the conjugate acid of the DNA phosphate group.[47] We prepare four single-stranded ssDNA samples with different base lengths (29, 50, 75, and 100) to study the effects of the presence and ssDNA length on the experimentally obtained current−voltage characteristics. For simplicity, these four samples are denoted as DNA29, DNA50, DNA75, and DNA100. We then analyze the results and explain the behavior of the system with the use of real-time fluorescence microscopy of the membrane.

EXPERIMENTAL DETAILS

Reagents. PBS (Fisher Scientific, 10×) contained 1.37 M sodium chloride, 27 mM potassium chloride, 100 mM disodium hydrogen phosphate, and 18 mM potassium dihydrogen phosphate. PBS 0.1× used in the experiments was prepared by dilution from the PBS 10× solution. ssDNA (29, 50, 75, 100 bases, Invitrogen), fluorescein, rhodamine (Sigma-Aldrich), and a heterogeneous anion-exchange membrane containing strongly basic quaternary ammonium groups were provided by Mega a.s. (Czech Republic).

Microchip Fabrication. All experiments with the anion-exchange membrane were carried out in a microfluidic chip depicted in Figure 2a. The chip was designed as a two-channel system with four openings for electrolyte and sample loading and a small piece of an anion-exchange membrane bridging the two channels. The asymmetric channels are purposefully designed to measure CVCs as explained later. The basic dimensions of the chip are the following: size of the membrane, 1 × 4 mm^2; size of the membrane exposed to the electrolyte in each channel, 1 × 1 mm^2; height of the channel, 700 μm; width of the channel, 2 to 4 mm; and total length of the channel, 14 mm. The fabrication of the microfluidic chip is based on PDMS cast against a glass/epoxy master containing fluidic structures on which a small piece of anion-exchange membrane was fixed with double-sided tape. The PDMS cast is then bonded to a glass slide by treatment with a hand-held corona discharge. Fluidic structures were designed in Adobe Illustrator and cut into a 700-μm-thick silicon sheet (having one sticky side) by using cutting plotter Graphtec Pro FC 7000MK2-60. A structured silicone sheet was fixed on a microscope slide, and the cut structures were filled with UV-curable glue (Loctite 3492).

After UV glue curing, we removed the silicon sheet, leaving the epoxy glue structures on the glass slide. A small piece of an anion-exchange membrane (1 × 4 mm^2) was then fixed at the designed locations on the master by using double-sided tape. PDMS prepolymer was prepared by mixing polymer base and curing agent in a weight ratio of 10:1 and degassing in vacuum. Four small pieces of silicon tubing serving as fluidic inlets and outlets were fixed on the master by using a small amount of PDMS prepolymer and curing it. PDMS prepolymer was then poured onto the whole master and degassed again. PDMS curing was done in an oven set at 70 °C for 40 min. The cured PDMS cast was peeled off of the master, and the double-sided tape was removed to expose the membrane in the cast channels. Any PDMS blocking inlet and outlet tubing was also removed. The PDMS cast was bonded to a precleaned glass slide using corona discharge followed by heating in an oven at 70 °C for 1 h. After bonding, we filled the channels with PBS 0.1× and allowed the membrane to swell for at least 48 h.

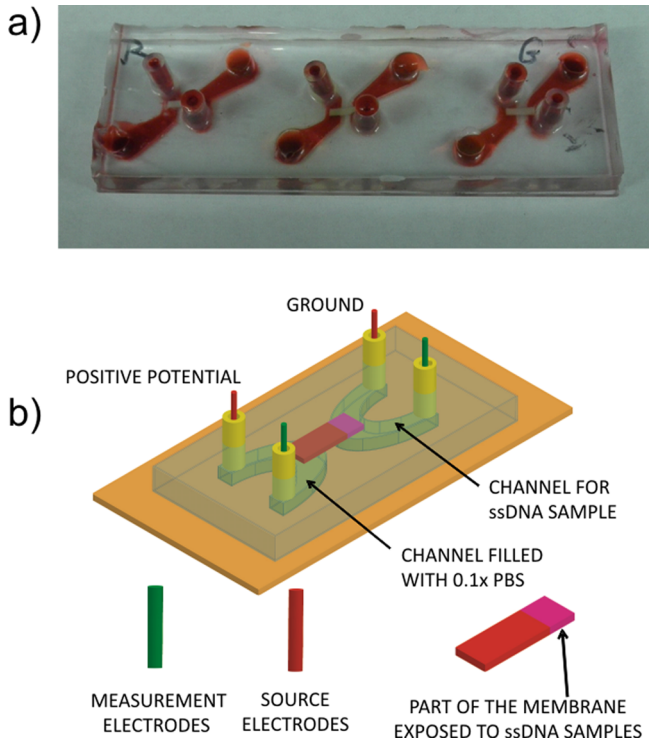

Figure 2. (a) Real chip with channels filled with rhodamine dye and (b) experimental connection of electrodes.

Measurement. All electrical measurements were made using a Gamry 500 potentiostat in a four-electrode setup. Two pseudosilver−silver chloride electrodes were used for the measurement of the actual voltage across the membranes, and two platinum electrodes were used to apply a current load. The whole experimental setup along with the position of the source and measurement electrodes is depicted in Figure 2b. The two measurement electrodes were placed in the channel openings close to the membrane, and the source electrodes were placed in the other two openings far from the membrane. This arrangement of electrodes provided accurate measurements of CVCs and allowed microscopic observation of the membrane surface with a minimum intervention of electrochemical reactions taking place on the source electrodes. One channel of the system was filled with PBS 0.1× solution, and the other one was used to inject DNA samples. The channel with the DNA sample was always connected to the ground whereas a positive potential was applied in the other channel. This connection ensured the formation of the depletion region in the channel with the DNA sample, making it very sensitive to the presence of DNA. To understand the exact mechanisms, we designed a few sets of experiments. In the first set, we measured the current−voltage characteristics of the anion-exchange membrane in the presence of four DNA samples with different concentrations. Different concentrations of each DNA sample were prepared by first dissolving the stock DNA powder in 1 mL of PBS 0.1× with subsequent dilution to the following concentrations: 0 nM, 1 nM, 10 nM, 100 nM, 250 nM, 500 nM, 1 μM, 5 μM, and 10 μM. The microfluidic chip was rinsed with PBS 0.1×, and then the channel on the sensing side of the membrane was filled with the DNA sample of a specific concentration and the CVC was measured immediately for each concentration. The current−voltage characteristics were measured by applying a current load from 0 to 80 μA at a rate of 1 μA/s. Voltage was measured with

dx.doi.org/10.1021/la4007179 | Langmuir 2013, 29, 8275−8283

measuring electrodes and recorded for each value of the applied current. The result of this measurement is plotted as the dependence of the electrical current on the measured voltage. Chronoamperometric curves were obtained by measuring the electrical current response of the system when the voltage on the measuring electrodes was kept constant and equal to 3 V for 180 s. We imaged the membrane surface with an inverted epifluorescence microscope (Olympus 1X71) equipped with a mercury lamp from Olympus. Video was captured using a high-speed camera (Q-Imaging Retiga-EX) and with Streampix microscope software. The obtained videos were processed in a Matlab-based image-processing toolbox.

RESULTS

CVCs of the System with DNA. The qualitative effect of a DNA29 (29-base-long ssDNA in PBS 0.1×) sample with different concentrations on CVCs is shown in Figure 3a. The results for the other three samples (DNA50, DNA75, and DNA100) are qualitatively similar and quantitatively evaluated in the next section.

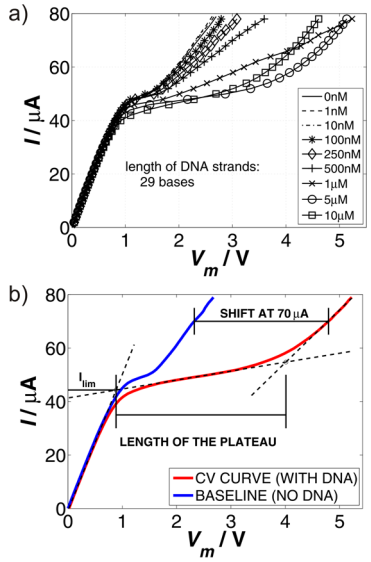

Figure 3. (a) CVCs of the system in the presence of different concentrations of DNA 29 sample in PBS 0.1×. (b) Parameters used for the quantitative description of CVCs for all DNA samples.

The CVCs for all concentrations of the DNA29 sample clearly bear the typical three-region characteristics where two linear regions (underlimiting and overlimiting) are connected to a limiting region. The underlimiting region of the measured CVCs in Figure 3a is same for all of the concentrations we tested. The main differences in the CVCs are seen for the limiting and overlimiting regions, which are strongly dependent on the DNA concentration. The CVCs for DNA concentrations of 1 and 10 nM are almost identical to the baseline, which is the CVC of our system with no DNA (PBS 0.1× only). The first detectable change occurs for the concentration of 100 nM, where the overlimiting region of the CVC slightly shifts away from the baseline. For concentrations larger than 100 nM (250 nM, 500 nM, and 1 μM), we observe that the overlimiting part of the CVC assumes smaller slopes with increasing DNA concentration causing this region to deviate significantly from the baseline. The same values of electrical currents are reached at larger voltages measured across the membrane, and we refer to this behavior as a shift of the CVC to the right. The CVC shift to the right, however, ceases at DNA concentrations between 1 and 5 μM, when two effects happen at the same time: (i) the slope (differential conductance) of the overlimiting region starts to increase again and (ii) the limiting region extends significantly. For any higher DNA concentration (5 and 10 μM), the CVC changes character again by reducing the size of the LR and reducing the electrical current at which it starts to appear. This flip-flopping of CVCs with respect to increasing concentration of the DNA29 sample was surprising, but similar behavior is also observed for the other three DNA samples (DNA50, DNA75, and DNA100). To get a better quantitative picture and a more coherent description of all of the DNA samples (DNA29, DNA50, DNA75, and DNA100), we evaluated five parameters describing the CVCs for each DNA sample and concentration: (1) limiting electrical current, (2) length of the limiting region, (3) slope (differential conductance) of the limiting region, (4) shift in the voltage occurring at 70 μA with respect to the baseline, and (5) slope (differential conductance) of the overlimiting region. These parameters were evaluated in the following way (Figure 3b). First, linear regression was used to fit the three regions (underlimiting, limiting, and overlimiting) with their corresponding lines by analyzing the first 25 measured points (0–25 μA) for the underlimiting region and the last 15 points (65 − 80 μA) for the overlimiting region. The linear regression in the limiting region was done in a two-step process. We first found four consecutive points on the CVC that when fitted gave the smallest slope. We then used these four points for the linear regression of this region. All five parameters for the description of the CVCs can be easily extracted from these linear fits. The length of the limiting region was determined to be the distance between the intersection of the fit for the underlimiting and limiting regions and the intersection of the limiting and overlimiting regions.

Quantitative Description of CVCs. Figure 4a–e depicts the dependence of the five parameters on the concentration and length of the DNA strands. Qualitatively, the results show the same trend for all DNA samples; however, the highest or lowest values of a given parameter are reached at higher or lower DNA concentrations depending upon the length of the DNA strands. Samples containing shorter ssDNA reaches the maximum or minimum of the given parmeter at higher concentration. The slope (differential conductance) of the CVC in the overlimiting region gives the information on the integral conductivity of the system, and thus it indirectly provides information on the effect of the negatively charged DNA molecules on the mechanisms responsible for the occurrence of the overlimiting current. As can be seen in Figure 4a, the addition of DNA to the sample results in a decrease in the slope in OR (overlimiting region), which suggests that the negatively charged DNA molecules suppresses the mechanism initially responsible for the overlimiting current. For all DNA samples, a minimum in the slope is observed; however, this minimum is reached for different concentrations in each sample: 1 μM for DNA29, 500 nM for DNA50, 500 nM for DNA75, and 250 nM for DNA100. This observation clearly shows that longer DNA requires a smaller concentration to reach this minimum and shorter DNA requires a higher concentration. On further increases in the DNA concentration, the slope in the OR again starts to increase, which suggests that a new phenomenon is responsible for the increase in the conductance of the system. We denote the concentration at which a minimum slope in OR occurs as a critical concentration (C_c). The parameter characterizing the slope of CVC in the

dx.doi.org/10.1021/la4007179 | Langmuir 2013, 29, 8275–8283

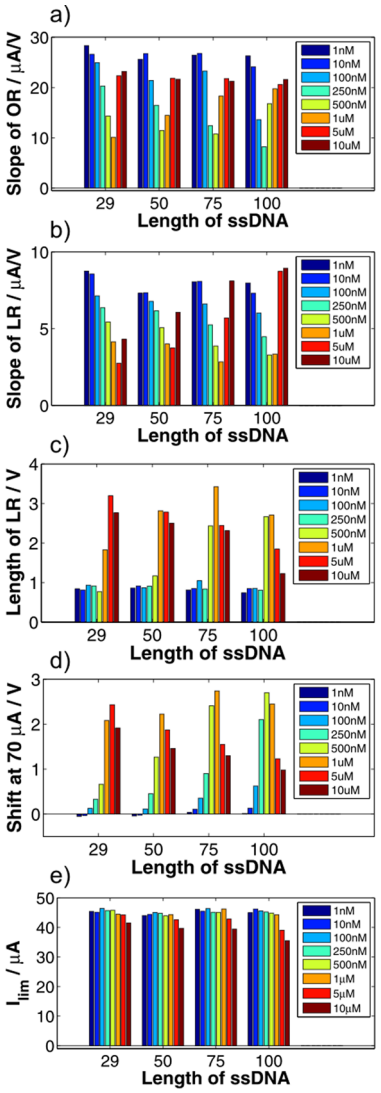

Figure 4. Bar graphs characterizing the CVCs quantitatively. The parameters plotted are (a) the slope of the OR, (b) the slope of the LR, (c) the length of the LR, (d) the shift at 70 μA, and (e) the limiting current.

limiting region (Figure 4b) follows the same trend as the slope in OR (Figure 4a) (i.e., we can find a concentration for each DNA sample at which a minimum in the slope occurs). These concentrations are 5 μM for DNA29, between 1 and 5 μM for DNA50, 1 μM for DNA75, and between 500 nM and 1 μM for DNA100 and are larger than those obtained for the slope in the OR. This observation suggests that the process responsible for the overlimiting current has its origin in the limiting region. The length of the limiting region is another interesting input in understanding the effects of DNA on the CVC (Figure 4c). Although the length of the limiting region is almost constant for DNA concentrations below the C_c, a sudden increase in the length of the limiting region around C_c is observed. This parameter reaches a maximum and then decreases again. This effect is especially profound for the DNA100 sample. A sudden increase in the length of the limiting region around C_c again indicates a change in the mechanisms driving the overlimiting current. The shift in the voltage occurring at 70 μA (Figure 4d) has the opposite trend from the slope of the overlimiting region. First, it grows with increasing DNA concentration, reaches a maximum, and starts to decrease gradually. The concentrations at which the shift is maximal roughly coincide with the critical concentrations (C_c). This parameter is not assumed to be very important with respect to the understanding of the system behavior because its value is indirectly given by the length of the limiting region and the slope in the overlimiting region. The last parameter plotted in Figure 4e is the limiting current, which indicates at what current the limiting region starts. Because the limiting region is associated with the formation of the depletion region on the cathodic side of the membrane, it also provides information on how much current is needed to reach the depletion. Our results show that the limiting current is almost constant for concentrations smaller than C_c and decreases above C_c for all DNA samples.

These results again indicate that after reaching the critical concentration a mechanistic switch happens in our system and a new phenomenon starts to dominate in the OR.

Concentration of the Charge Bound to DNA Molecules Is the Determining Factor. The results in Figure 4a–e show that the DNA length has a profound effect on the CVCs. This is quite apparent in terms of the total negative charge borne by ssDNA molecules with different lengths. The longer the DNA molecule, the more phosphate groups available and the more negative the charge present in the sample. To understand our experimental results in terms of this negative charge (i.e., with respect to the total concentration of the phosphate groups or the charge concentration (assuming the full dissociation of all phosphate groups)), we plotted three of the five parameters evaluated above as a function of the concentration of phosphate groups (charge) for each DNA sample. These parameters are the slope of the LR (Figure 5a), the slope of the OR (Figure 5b), and the shift at 70 μA (Figure 5c). As can be seen from these plots, the curves for the four DNA samples nicely collapse onto each other for all three parameters, showing a nice dependence of the system behavior on the concentration of the charge borne by DNA molecules independent of the DNA sample. We can also define the critical

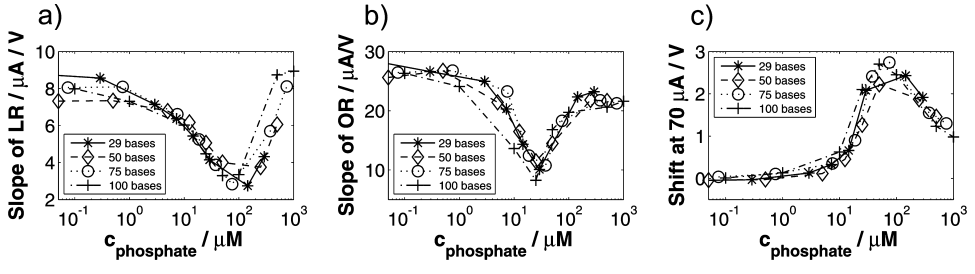

Figure 5. (a) slope of the LR, (b) slope of the OR, and (c) shift at 70 μA plotted against the concentration of the phosphate groups bound to each DNA sample.

dx.doi.org/10.1021/la4007179 | Langmuir 2013, 29, 8275–8283

concentration of phosphate groups (charge concentration) as the concentration at which the conductivity in the overlimiting region drops to its lowest value, in other words, that at which the CVC slope in the overlimiting region reaches the smallest value. From Figure 5b, the value of the critical phosphate concentration is about 25 μM. The plots in Figure 5 give clear evidence that the determining factor affecting the shape of the CVC is the concentration of the charge borne by the DNA molecules.

Direct Observation of Processes Occurring at the Membrane in the Overlimiting Region. In previous sections, we suggested two main competing mechanisms that control the overlimiting current for the concentrations above and below the critical concentration of the negative charge. We propose that the major mechanism that controls the overlimiting current for concentrations smaller than the C_c is electroconvection. By analyzing the experimental results of DNA concentration larger than C_c, we speculate that the negatively charged DNA molecules adsorb onto the positively charged membrane and create a bipolar junction that at sufficiently large voltages splits water. The overlimiting current is then given by the formation of new charge carriers, namely, H^+ and OH^- ions, in the water-splitting reaction. To prove that our hypothesis is correct, we perform real-time fluorescence microscopy measurements on the cathodic side of the membrane in the presence of DNA29 samples of different concentrations when an overlimiting voltage is applied to the system. We choose two fluorescent markers for our purposes: (i) fluorescein as a pH marker and (ii) rhodamine to capture any electroconvection. The fluorescence intensity of fluorescein is strongly affected by the pH of its environment.[48] It gives intensive fluorescent signal in neutral and alkaline solutions, but its fluorescence is completely lost in acidic solutions. Unlike fluorescein, the rhodamine fluorescence intensity does not show any significant dependence on the pH. In these experiments, the cathodic side of the membrane is observed during potentiometric measurements when 3 V is applied to the systems for 3 min. Five different concentrations of the DNA29 sample are tested: 0, 0.5, 1, 5, and 10 μM.

pH Changes Occurring in the Presence of DNA. The results with fluorescein as the pH marker are plotted in Figure 6 and summarized in a movie (Movie1, Supporting Information). The frames capture the cathodic side of the membrane along with the channel leading to the platinum electrode connected as a cathode. Each column in Figure 6 shows the time evolution of a low-pH front in the cathodic channel for each DNA concentration tested. The first column shows the situation when no DNA is present in the sample. In all frames captured, there is a large amount of green fluorescence coming from the whole channel on the cathodic side of the membrane. This observation confirms that when there are no large counterions the extent of water splitting (if any) is very low. The other four columns show the situation when a nonzero concentration of DNA is added to the sample. From the second to the fifth column, these concentrations are 0.5, 1, 5, and 10 μM, respectively. For all DNA concentrations tested, we can see the formation of a zone with low fluorescence intensity. This low-fluorescence-intensity zone shows the change in the pH toward lower values, confirming the appearance of H^+ ions in the channel and their migration toward the cathode. The appearance of H^+ ions in the channel is very strong proof of the water-splitting reaction taking place on the membrane. The low-intensity zone appears at the membrane and extends farther into the channel with time. The extension of this low-intensity zone depends on the concentration of DNA. The higher the DNA concentration, the faster the generation of H^+ ions and hence the rapid broadening of that zone. In other words, the more DNA, the greater the number of H^+ ions generated at the membrane at the same external voltage applied in the range of DNA concentrations tested.

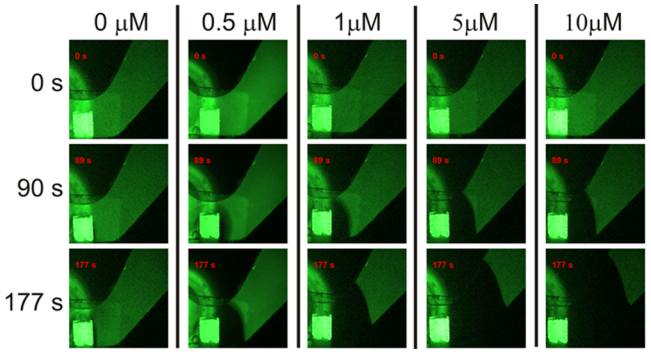

Figure 6. Evolution of the low-pH zone at different concentrations of the DNA29 sample. From left to right, the concentrations in the columns are 0, 0.5, 1, 5, and 10 μM, respectively.

Electroconvection at the Membrane. The experiments with the rhodamine dye are carried out under experimental conditions similar to those for fluorescein (i.e., 3 V is applied to the system for 3 min, and five samples with different DNA concentrations (0, 0.5, 1, 5, and 10 μM) are tested). The experimental results with rhodamine dye are summarized in Movie2 (Supporting Information) consisting of five frames showing the results for different DNA concentrations. The frames in the movie capture the situation occurring directly on the cathodic side of the membrane. When no DNA is present in the sample (the first frame), very intense vortices develop on the membrane surface shortly after the external voltage is applied. The intensity of the vortices does not change with time. This observation shows that the electroconvection can be responsible for the control of the overlimiting current by mixing the depletion region with a fresh electrolyte. The other four frames show the experimental results for DNA samples of different concentrations. From the second to the fifth column, these concentrations are 0.5, 1, 5, and 10 μM, respectively. At 0.5 μM DNA, the vortices generated at the beginning of the movie are much less intense as compared to those for a system without any DNA. The vortices seem to disappear in the course of time, which might be given by the fact that more and more DNA molecules adsorb onto the membrane as a result of the action of the electrical field resulting in the suppression of vortices. For 1 μM DNA concentration, very low intensive whirring on the membrane is observed at the beginning of the experiment; however, after a short time, the vortices completely disappear again probably because of the increase in DNA concentration on the membrane surface. No detectable vortices are observed for 5 and 10 μM DNA concentrations. Overall, these movies show that there is very intensive mixing on the membrane surface for low DNA concentrations and no vortices are detected for high DNA concentrations. The change in intensity of the vortices is dependent on the DNA concentration.

The experimental results obtained for fluorescein and rhodamine dyes can be summarized as the following: (i) the vortices appear very quickly on the membrane when there is no

dx.doi.org/10.1021/la4007179 | Langmuir 2013, 29, 8275−8283

DNA present in the solution, (ii) the intensity of the vortices decreases with increasing concentration of DNA and become undetectable for high concentrations of DNA, (iii) the extent of pH change in the channel on the cathodic side of the membrane caused by the water-splitting reaction depends on the concentration of DNA, and (iv) there is almost no pH change detectable when no DNA is present in the sample. Another interesting conclusion can be made with respect to our critical concentration of DNA. We determine this concentration to be about 25 μM for phosphate groups, which gives a roughly 1 μM concentration for the DNA29 sample. At this concentration, we can detect vortices of a very low intensity whereas the extent of the water-splitting reaction starts to dominate. Therefore, we consider this concentration to separate the regions of vortice-controlled and water-splitting-controlled overlimiting currents in our system.

Chronoamperometry Curves in the Presence of DNA. Figure 7 shows the chronoamperometric curves obtained for

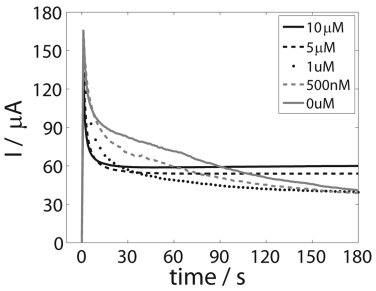

Figure 7. Chronoamperometric curves obtained for different concentrations of the DNA29 sample.

the experiments to explore the overlimiting current mechanism further. The presence of ssDNA has a profound effect on chronoamperometric curves at the beginning of the experiment when the depletion zone is created and at steady state when the overlimiting current fully sets in. At all DNA concentrations, the current reaches a maximum value, right after the voltage is activated, followed by a sharp decrease (0−10 s) and then some slower evolution. The sharp decrease is associated with the formation of the depletion region and is faster for higher DNA concentrations. Beyond the sharp decrease, the current at low DNA concentrations (0 μM, solid gray line; 500 nM, dashed gray line) does not reach a steady value and slowly decreases for the entire experiment. In contrast, the ionic current reaches a steady-state value at around 60 μA for high DNA concentrations (5 μM, dashed black line; 10 μM, solid black line). The curve for 1 μM DNA (dotted black line) creates a transition between low and high DNA concentrations. This observation again confirms our hypothesis for the switch in mechanism for the OR current. At low DNA concentrations (below 1 μM) when vortices are suggested to be the major mechanism for OR, the current slowly but steadily decreases, which reflects a slow decrease in the ion concentration in the bulk. This is in agreement with the fact that the ion concentration slowly decreases (ionic conductivity decreases) on the depletion side of the membrane and some of the ions are even consumed in electrochemical reactions on the electrodes (e.g., Cl^- forms chlorine). In contrast, at high DNA concentration the ionic current reaches a steady value that is slightly higher for the 10 μM DNA solution. The ability of the system to keep the ionic current constant strongly suggests that a new constant source of ions sets in to suppress further ion concentration decreases. Along with the low-pH zone that is observed in the videos in Figure 6 at high DNA concentration, this proves that the water-splitting reaction controls the OR current with large DNA coverage. Again, the concentration of 1 μM separates the vortice-controlled and water-splitting-controlled OR.

Principal Component Analysis of Vortices. To quantify the correlation between electroconvection and the ion current better, we carried out principal component analysis (PCA) of the movies capturing the vortices developed on the membrane surface using the procedure described by Chang et al.[49] By using PCA analysis, we examine the short-time ensemble average of the correlation between the fluorescence intensity of any two pixels in the image, which has been reduced with respect to the mean over the same time interval. The PCA analysis offers a set of statistically uncorrelated eigenimages from the cross-correlation study, with the first one representing the most dominant and correlated intensity fluctuation in time as a result of coherent vortices. The first principal component of this leading eigenimage can hence measure the intensity of the vortex motion. We calculate the dependence of the first principal component coefficient (a_1) on time (on a time scale longer than that used for the ensemble average) and use its power spectrum to examine the frequency signature of the vortices. At the same time, we calculate power spectra of the current signal that was recorded during the measurement subtracted from the current mean and compare these power spectra to those produced for a_1 (Figure 8) for four different ssDNA concentrations (crosses:, 5 μM; circles, 1 μM; diamonds, 0.5 μM; and squares, 0 μM).

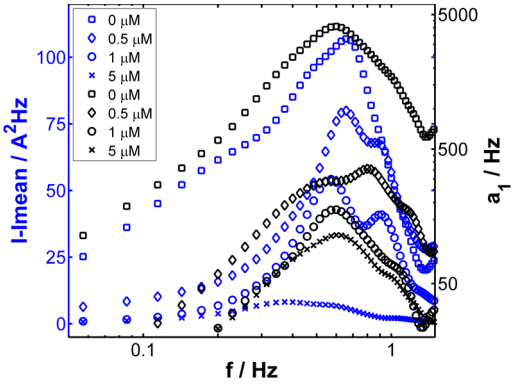

Figure 8. Power spectra of the current (blue curves) and the first principal coefficient (black curves) for different DNA concentrations: squares, 0 μM; diamonds, 0.5 μM; circle, 1 μM, and crosses, 5 μM).

We can see that for a bare membrane we get a maximum in the power spectra of both a_1 and the current for frequencies of around 0.6 to 0.7 Hz. With increasing concentrations of DNA (0.5 and 1 μM), the maximum in the spectra decreases but the position of the maximum remains essentially constant. The decrease in the maxima clearly shows that the DNA molecules, even at rather small concentrations, have a profound damping effect on both the current and fluorescence intensity fluctuations. For the highest DNA concentration (5 μM), the peak is almost completely lost, indicating very small fluctuations in the current and fluorescence intensity. These results are in very good agreement with the visual analysis of Movie2 described earlier. Vortices can hence be correlated with the

dx.doi.org/10.1021/la4007179 | Langmuir 2013, 29, 8275−8283

passage of an electrical current through the membrane with respect to both their mean values and their fluctuation intensities.

DISCUSSION

By performing the experiments above, we have shown two main mechanisms that govern the overlimiting current at an anion-exchange membrane in the presence of large counterions. These two mechanisms are electroconvection and the water-splitting reaction. We found that the importance of each of the mechanisms is dependent on the concentration of DNA molecules, which was further shown to be primarily given by the concentration of the negative charge borne by these molecules. Because electroconvection has been suggested to result from the instability of a surface-extended polarized region with a space charge whose dimension is no larger than 100 nm,[27,29,50] the presence of ssDNA on the surface is expected to reduce the slip length or increase the viscous dissipation in the polarized layer significantly such that the intensities of the vortices and electroconvection are reduced. This effective viscous effect seems to exist at low ssDNA coverage. The scenario changes when ssDNA forms a cation-selective membrane on the original membrane beyond a critical concentration of negative charges borne by the DNA molecules. Our pH-sensitive fluorescence imaging suggests the formation of a proton front sustained by protons generated by water splitting at the DNA/membrane junction. The large pH and ion-current signatures of the water-splitting reaction at large DNA coverage suggests that it can be used to detect and quantify large counterion polyelectrolytes on the membrane surface. Currently, ssDNA adsorbs on the surface, but we expect the same vortex-suppression and water-splitting phenomena to exist when specific ssDNA or ssRNA hybridizes onto short probes functionalized on the membrane surface. Nonspecific binding will be an issue, but as shown earlier,[51] hydrodynamic shear and alkaline shocking[52] can be used to remove nonspecifically bound molecules on the membrane surface. Although the current signatures resemble those for electrochemical conductivity sensors, the current and voltage signals and changes are much larger, thus allowing more sensitive measurement with simpler instrumentation and much lower material cost. The new membrane sensor also does not require redox reporters to enhance the signal and is not sensitive to spurious electrochemical reactions; therefore, there is no electron-transfer reaction involved.

ASSOCIATED CONTENT

Supporting Information

Movies capturing pH changes (Movie1) and electroconvection (Movie2). This material is available free of charge via the Internet at http://pubs.acs.org.

AUTHOR INFORMATION

Corresponding Author

*E-mail: hchang@nd.edu.

Author Contributions

Z.S. designed and carried out the experiments, analyzed the data, and wrote the manuscript. S.S. analyzed the data wrote the manuscript. Y.Y. performed PCA analysis and power spectra analysis. H.-C.C. analyzed the data and wrote the manuscript.

Notes

The authors declare no competing financial interest.

ACKNOWLEDGMENTS

This work is supported by NSF CBET 1065652 and USDA grant 2012-67005-19589.

ABBREVIATIONS

CVC, current−voltage characteristics; LR, limiting region; OR, overlimiting region; DNA, DNA; ssDNA, single stranded DNA

REFERENCES

(1) Xu, T. Ion Exchange Membranes: State of Their Development and Perspective. *J. Membr. Sci.* **2005**, *263*, 1−29.
(2) Rubinstein, I.; Shtilman, L. Voltage against Current Curves of Cation-Exchange Membranes. *J. Chem. Soc., Faraday Trans. 2* **1979**, *75*, 231−246.
(3) Barragan, V. M.; Ruiz-Bauza, C. Current-Voltage Curves for Ion-Exchange Membranes: A Method for Determining the Limiting Current Density. *J. Colloid Interface Sci.* **1998**, *205*, 365−373.
(4) Levich, V. G. *Physicochemical Hydrodynamics*; Prentice-Hall: Englewood Cliffs, NJ, 1962; p 700.
(5) Tanaka, Y. Concentration Polarization in Ion-Exchange Membrane Electrodialysis. The Events Arising in an Unforced Flowing Solution in a Desalting Cell. *J. Membr. Sci.* **2004**, *244*, 1−16.
(6) Ben, Y.; Chang, H. C. Nonlinear Smoluchowski Slip Velocity and Micro-Vortex Generation. *J. Fluid Mech.* **2002**, *461*, 229−238.
(7) Yossifon, G.; Mushenheim, P.; Chang, Y. C.; Chang, H. C. Nonlinear Current-Voltage Characteristics of Nanochannels. *Phys. Rev. E* **2009**, *79*, 4.
(8) Kooistra, W. Characterization of Ion Exchange Membranes by Polarization Curves. *Desalination* **1967**, *2*, 139−147.
(9) Frilette, V. J. Electrogravitational Transport at Synthetic Ion Exchange Membrane Surfaces. *J. Phys. Chem.* **1957**, *61*, 168−174.
(10) Andersen, M. B.; van Soestbergen, M.; Mani, A.; Bruus, H.; Biesheuvel, P. M.; Bazant, M. Z. Current-Induced Membrane Discharge. *Phys. Rev. Lett.* **2012**, *109*, 10.
(11) Krol, J. J.; Wessling, M.; Strathmann, H. Concentration Polarization with Monopolar Ion Exchange Membranes: Current-Voltage Curves and Water Dissociation. *J. Membr. Sci.* **1999**, *162*, 145−154.
(12) Belova, E. I.; Lopatkova, G. Y.; Pismenskaya, N. D.; Nikonenko, V. V.; Larchet, C.; Pourcelly, G. Effect of Anion-Exchange Membrane Surface Properties on Mechanisms of Overlimiting Mass Transfer. *J. Phys. Chem. B* **2006**, *110*, 13458−13469.
(13) Zabolotsky, V. I.; Nikonenko, V. V.; Pismenskaya, N. D. On the Role of Gravitational Convection in the Transfer Enhancement of Salt Ions in the Course of Dilute Solution Electrodialysis. *J. Membr. Sci.* **1996**, *119*, 171−181.
(14) Dydek, E. V.; Zaltzman, B.; Rubinstein, I.; Deng, D. S.; Mani, A.; Bazant, M. Z. Overlimiting Current in a Microchannel. *Phys. Rev. Lett.* **2011**, *107*, 11.
(15) Mani, A.; Bazant, M. Z. Deionization Shocks in Microstructures. *Phys. Rev. E* **2011**, *84*, 6.
(16) Belova, E.; Lopatkova, G.; Pismenskaya, N.; Nikonenko, V.; Larchet, C. Role of Water Splitting in Development in Ion-Exchange Membrane of Electroconvection Systems. *Desalination* **2006**, *199*, 59−61.
(17) Pismenskaya, N. D.; Nikonenko, V. V.; Belova, E. I.; Lopatkova, G. Y.; Sistat, P.; Pourcelly, G.; Larshe, K. Coupled Convection of Solution near the Surface of Ion-Exchange Membranes in Intensive Current Regimes. *Russ. J. Electrochem.* **2007**, *43*, 307−327.
(18) Rosler, H. W.; Maletzki, F.; Staude, E. Ion Transfer across Electrodialysis Membranes in the Overlimiting Current Range - Chronopotentiometric Studies. *J. Membr. Sci.* **1992**, *72*, 171−179.
(19) Maletzki, F.; Rosler, H. W.; Staude, E. Ion Transfer across Electrodialysis Membranes in the Overlimiting Current Range - Stationary Voltage Current Characteristics and Current Noise Power Spectra under Different Conditions of Free-Convection. *J. Membr. Sci.* **1992**, *71*, 105−115.

(20) Krol, J. J.; Wessling, M.; Strathmann, H. Chronopotentiometry and Overlimiting Ion Transport through Monopolar Ion Exchange Membranes. *J. Membr. Sci.* **1999**, *162*, 155−164.
(21) Kang, M. S.; Choi, Y. J.; Moon, S. H. Effects of Charge Density on Water Splitting at Cation-Exchange Membrane Surface in the Over-Limiting Current Region. *Korean J. Chem. Eng.* **2004**, *21*, 221−229.
(22) Belashova, E. D.; Melnik, N. A.; Pismenskaya, N. D.; Shevtsova, K. A.; Nebavsky, A. V.; Lebedev, K. A.; Nikonenko, V. V. Overlimiting Mass Transfer through Cation-Exchange Membranes Modified by Nafion Film and Carbon Nanotubes. *Electrochim. Acta* **2012**, *59*, 412−423.
(23) Volodina, E.; Pismenskaya, N.; Nikonenko, V.; Larchet, C.; Pourcelly, G. Ion Transfer Across Ion-Exchange Membranes with Homogeneous and Heterogeneous Surfaces. *J. Colloid Interface Sci.* **2005**, *285*, 247−258.
(24) Choi, J. H.; Kim, S. H.; Moon, S. H. Heterogeneity of Ion-Exchange Membranes: The Effects of Membrane Heterogeneity on Transport Properties. *J. Colloid Interface Sci.* **2001**, *241*, 120−126.
(25) Choi, J.-H.; Lee, H.-J.; Moon, S.-H. Effects of Electrolytes on the Transport Phenomena in a Cation-Exchange Membrane. *J. Colloid Interface Sci.* **2001**, *238*, 188−195.
(26) Rubinstein, I.; Staude, E.; Kedem, O. Role of the Membrane-Surface in Concentration Polarization at Ion-Exchange Membrane. *Desalination* **1988**, *69*, 101−114.
(27) Rubinstein, I.; Zaltzman, B. Extended Space Charge in Concentration Polarization. *Adv. Colloid Interface Sci.* **2010**, *159*, 117−129.
(28) Zaltzman, B.; Rubinstein, I. Electro-Osmotic Slip and Electroconvective Instability. *J. Fluid Mech.* **2007**, *579*, 173−226.
(29) Kim, Y.; Lawler, D. F. Overlimiting Current by Interactive Ionic Transport between Space Charge Region and Electric Double Layer near Ion-Exchange Membranes. *Desalination* **2012**, *285*, 245−252.
(30) Yossifon, G.; Mushenheim, P.; Chang, Y. C.; Chang, H. C. Eliminating the Limiting-Current Phenomenon by Geometric Field Focusing into Nanopores and Nanoslots. *Phys. Rev. E* **2010**, *81*, 4.
(31) Postler, T.; Slouka, Z.; Svoboda, M.; Pribyl, M.; Snita, D. Parametrical Studies of Electroosmotic Transport Characteristics in Submicrometer Channels. *J. Colloid Interface Sci.* **2008**, *320*, 321−332.
(32) Kim, S. J.; Wang, Y. C.; Lee, J. H.; Jang, H.; Han, J. Concentration Polarization and Nonlinear Electrokinetic Flow near a Nanofluidic Channel. *Phys. Rev. Lett.* **2007**, *99*, 4.
(33) Yossifon, G.; Mushenheim, P.; Chang, H. C. Controlling Nanoslot Overlimiting Current with the Depth of a Connecting Microchamber. *Euro. Phys. Lett.* **2010**, *90*, 6.
(34) Chang, H. C.; Yossifon, G.; Demekhin, E. A. Nanoscale Electrokinetics and Microvortices: How Microhydrodynamics Affects Nanofluidic Ion Flux. *Annu. Rev. Fluid Mechanics* **2012**, *44*, 401−.
(35) Strathmann, H.; Krol, J. J.; Rapp, H. J.; Eigenberger, G. Limiting Current Density and Water Dissociation in Bipolar Membranes. *J. Membr. Sci.* **1997**, *125*, 123−.
(36) Ramirez, P.; Rapp, H. J.; Mafe, S.; Bauer, B. Bipolar Membranes under Forward and Reverse Bias Conditions - Theory vs Experiment. *J. Electroanal. Chem.* **1994**, *375*, 101−.
(37) Conroy, D. T.; Craster, R. V.; Matar, O. K.; Cheng, L. J.; Chang, H. C. Nonequilibrium Hysteresis and Wien Effect Water Dissociation at a Bipolar Membrane. *Phys. Rev. E* **2012**, *86*, 5.
(38) Desharnais, B. M.; Lewis, B. A. G. Electrochemical Water Splitting at Bipolar Interfaces of Ion Exchange Membranes and soils. *Soil Sci. Soc. Am. J.* **2002**, *66*, 1518.
(39) Aritomi, T.; van den Boomgaard, T.; Strathmann, H. Current-Voltage Curve of a Bipolar Membrane at High Current Density. *Desalination* **1996**, *104*, 13−.
(40) Cheng, L. J.; Chang, H. C. Microscale pH Regulation by Splitting Water. *Biomicrofluidics* **2011**, *5*, 46502.
(41) Suendo, V.; Eto, R.; Tanioka, A. Ionic Rectification Properties of a Bipolar Interface Consisting of a Cationic Surfactant and Cation-Exchange Membrane. *J. Colloid Interface Sci.* **2002**, *250*, 507−.
(42) Suendo, V.; Minagawa, M.; Tanioka, A. Bipolar Interface Formation of Cationic Surfactant on the Surface of a Cation-Exchange Membrane: Current-Voltage Characteristics in Aqueous Electrolyte Solution. *Langmuir* **2002**, *18*, 6266−.
(43) Chamoulaud, G.; Belanger, D. Modification of Ion-Exchange Membrane Used for Separation of Protons and Metallic Cations and Characterization of the Membrane by Current-Voltage Curves. *J. Colloid Interface Sci.* **2005**, *281*, 179−.
(44) Loza, N. V.; Kononenko, N. A.; Shkirskaya, S. A.; Berezina, N. P. Effect of Modification of Ion-Exchange Membrane MF-4SK on Its Polarization Characteristics. *Russ. J. Electrochem.* **2006**, *42*, 815−.
(45) Sharafan, M. V.; Zabolotskii, V. I.; Bugakov, V. V. Electric mass transport through homogeneous and surface-modified heterogeneous ion-exchange membranes at a rotating membrane disk. *Russ. J. Electrochem.* **2009**, *45*, 1162.
(46) Lopatkova, G. Y.; Volodina, E. I.; Pis'menskaya, N. D.; Fedotov, Y. A.; Cot, D.; Nikonenko, V. V. Effect of Chemical Modification of Ion-Exchange Membrane MA-40 on Its Electrochemical Characteristics. *Russ. J. Electrochem.* **2006**, *42*, 847−.
(47) Inoshita, S.; Tsukahara, S.; Fujiwara, T. In Situ Fluorescence Microscopic Investigation into the Dependence of Conformation and Electrophoretic Velocity of Single DNA Molecules on Acid or Spermidine Concentration. *Anal. Sci.* **2009**, *25*, 293−.
(48) Doughty, M. J. pH Dependent Spectral Properties of Sodium Fluorescein Ophthalmic Solutions Revisited. *Ophthalmic Physiol. Opt.* **2010**, *30*, 167−.
(49) Chen, C. C.; Wolf, E. E.; Chang, H. C. Low-Dimensional Spatiotemporal Thermal Dynamics on Nonuniform Catalytic Surfaces. *J. Phys. Chem.* **1993**, *97*, 1055−.
(50) Rubinstein, I.; Maletzki, F. Electroconvection at an Electrically Inhomogeneous Permselective Membrane-Surface. *J. Chem. Soc., Faraday Trans.* **1991**, *87*, 2079−.
(51) Cheng, I. F.; Froude, V. E.; Zhu, Y. X.; Chang, H. C.; Chang, H. C. A Continuous High-Throughput Bioparticle Sorter Based on 3D Traveling-Wave Dielectrophoresis. *Lab Chip* **2009**, *9*, 3193−.
(52) Basuray, S.; Senapati, S.; Aijian, A.; Mahon, A. R.; Chang, H. C. Shear and AC Field Enhanced Carbon Nanotube Impedance Assay for Rapid, Sensitive, and Mismatch-Discriminating DNA Hybridization. *ACS Nano* **2009**, *3*, 1823.

Microelectronic Engineering 86 (2009) 1371–1374

Contents lists available at ScienceDirect

Microelectronic Engineering

journal homepage: www.elsevier.com/locate/mee

Cation exchange membrane integrated into a microfluidic device

Miloš Svoboda *, Zdeněk Slouka, Walter Schrott, Dalimil Šnita

Institute of Chemical Technology, Department of Chemical Engineering, Technická 5, 166 28 Prague 6, Czech Republic

ARTICLE INFO

Article history:
Received 30 September 2008
Received in revised form 9 January 2009
Accepted 13 January 2009
Available online 20 January 2009

Keywords:
Micro-fluidics
Cation exchange membrane
Micro-electrodes
Chronopotentiometry
Lab-on-a-chip

ABSTRACT

We have developed an electrochemical micro-system with embedded Ralex® CM PES membrane which separates two electrolytes of the same composition and concentration. Gold sensing micro-electrodes were integrated into the micro-system. The precise control of the hydrodynamic conditions – uniform flow of the solutions, uniform electric current distribution in micro-channels, spatial resolution of the measurement (small dimensions of the electrodes) and the precise positioning of the measuring elements represent the main advantages of the micro-scale arrangement. Polarization curves of the fabricated micro-system were measured to verify the functionality of the system. Dependencies of the key parameter, limiting current density, on several parameters as hydrodynamic conditions and electrolyte concentration have been also studied. Chronopotentiometric curves of the constructed micro-system were measured and evaluated.

1. Introduction

Ionic-exchange membranes are industrially used in separation processes [1–3], e.g. electrodialysis. Their principle is based on repulsive and attracting electrical forces between the fixed charge in the membrane and ionic species in the solutions.

When measuring polarization characteristics of a cation exchange membrane (CEM), typical S-shape curve is obtained on which three regions of different behavior are distinguishable (see Fig. 2). The first region is characterized by linear dependency of current on the voltage imposed on the membrane, the second region follows the tendency of electric current to saturation, i.e., electric current approaches to a certain limiting value (plateau). This behavior is explained by the theory of concentration polarization (CP) [4], which predicts formation of a narrow zone with low electrolytic conductivity (depleted layer) at the anodic side of the membrane.

The limiting current density i_{lim}, based on CP theory, can be calculated according to [4]

$$i_{\mathrm{lim}} = \frac{FD}{(t_+^m - t_+^s)} \frac{c_0}{\delta} \tag{1}$$

where F is the Faraday constant, D is the diffusion coefficient of the electrolyte, c_0 is the bulk concentration of the electrolyte, t_+^m is the cation transference number in the membrane, t_+^s is the cation transference number in the solution and δ is the thickness of the boundary layer at the membrane. It is seen that the limiting current density increases with an increasing electrolyte diffusion coefficient, increasing bulk concentration, decreasing cation transference number in the membrane and decreasing boundary layer thickness. The boundary layer thickness is mainly determined by hydrodynamic conditions [5].

However, the third region on polarization curve occurs when voltage is further increased. We call it "over-limiting current region" in which electric current is linearly proportional to the voltage applied where the slope is less than that in the first region. Moreover, in this region an electric current noise occurs [6]. The explanation of over-limiting current is based on the presence of electro-hydrodynamic instabilities originating from membrane heterogeneity [7]. These instabilities result in formation of eddies at the membrane surface. Balster et al. [8] studied the influence of CEM heterogeneity on plateau length and verified the existence of electroconvection as an ionic transport mechanism in over-limiting current density region.

Several measurements on macroscale were performed to characterize the polarization phenomena [9–12], but no measurements with micro-electrodes in miniaturized systems have been performed yet. Therefore we have developed an electrochemical micro-system with embedded CEM and integrated gold sensing micro-electrodes. Polarization and chronopotentiometric curves of the constructed micro-system were measured together with dependencies of the limiting current density on several parameters.

2. Microchip fabrication

The micro-system consists of tree main parts: (i) PMMA plate with microfluidic structures, (ii) PMMA plate with gold micro-electrodes and (iii) the CEM. The microfluidic part and chambers for membrane embedding are made by mechanical milling. Gold

* Corresponding author. Tel.: +420 2 2044 3239; fax: +420 2 2044 4320.
E-mail address: Milos.Svoboda@vscht.cz (M. Svoboda).

0167-9317/$ - see front matter © 2009 Elsevier B.V. All rights reserved.
doi:10.1016/j.mee.2009.01.019

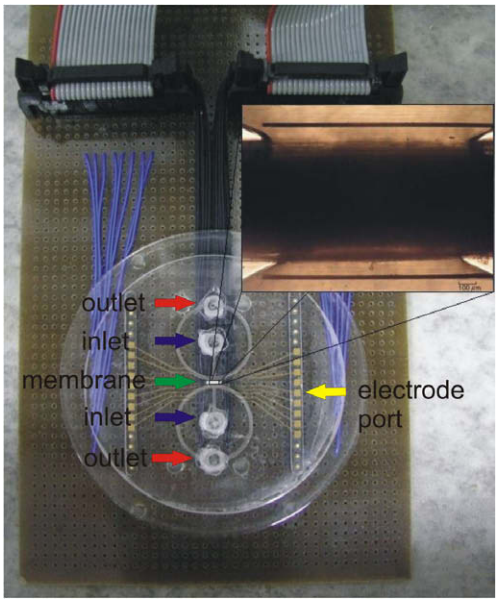

Fig. 1. Fabricated micro device with embedded CEM + detail of the CEM and gold measuring electrodes (25 μm wide).

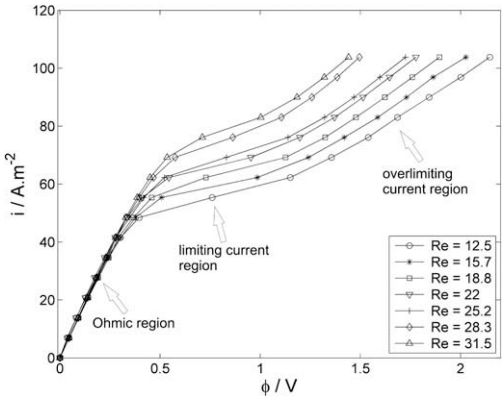

Fig. 2. Polarization curves for various hydrodynamic conditions, c_0 = 0.025 M NaCl.

electrodes are made by our novel technique based on sacrificed substrate.

The individual steps of the technique are as follows: (i) UV lithography on a metallic substrate, (ii) filling the structures in the photoresist with gold (galvanic deposition), (iii) photoresist stripping, (iv) embedding gold structures in UV curable resin Acrifix® 192 (Degussa) and (v) metallic substrate removal. The width of each electrode is 25 μm.

A small piece of cation exchange membrane Ralex® CM PES (MEGA, Czech Republic) is then embedded into micro-chambers. The final active area of the membrane is 1.5 mm^2 (see Fig. 1).

The step of temperature bonding follows. The individually structured PMMA plates are pressed together and subjected to the temperature of 126 °C in an electrically heated vacuum oven for 12 min.

Tubing and electrical connection is then fixed on the plates with a UV curable polymer resin.

3. Experimental setup

Two measuring electrodes are contacted and connected to Keithley 2700 multimeter via our universal multichannel measurement platform (see Fig. 1). Only two electrodes, each placed on one side in the close vicinity of the membrane, are active during measurement (see Fig. 1 – detail). Other electrodes shown on Fig. 1 are inactive during the measurement. Two source platinum tube electrodes are inserted into the outlet channels. The source electrodes are connected to Keithley 2400 sourcemeter. Both the sourcemeter and the multimeter are connected to PC. The measurement is controlled via Matlab environment. The electrolytes are continuously introduced by a pump into the micro-system. All measurements were carried out in a galvanostatic mode and voltage response of measuring electrodes was recorded.

4. Results

4.1. The influence of hydrodynamic conditions on polarization curve of the CEM

Polarization curves for various hydrodynamic conditions were measured to verify the relation between the boundary layer thickness and the limiting current density (Eq. (1)). Fig. 2 shows polarization curves for various Reynolds numbers. Individual Reynolds numbers were evaluated for the equivalent diameter of the solution delivery channel (800 μm) and for used fluid velocities at 25 °C (1.4–3.5 cm s^{-1}). Polarization curves show the tendency of an increasing limiting current density with increasing Reynolds number. Higher Reynolds number represents higher fluid velocity. Higher fluid velocity causes the thinning of the boundary layer, hence an increase in limiting current density occurs. Fig. 3 shows the measured limiting current density values vs. corresponding Reynolds numbers.

4.2. The influence of an electrolyte concentration on polarization curve of the CEM

Fig. 4 shows the polarization curves measured for the following concentrations of NaCl: 0.025, 0.05 and 0.1 M. Reynolds number was kept constant at the value 15.7. The measured polarization curves show the tendency of an increasing limiting current density with an increasing electrolyte concentration. The linear dependency of limiting current density on electrolyte concentration (see Fig. 5) is in agreement with theoretical predictions (see Eq. (1)).

4.3. Chronopotentiometry

Constant current in the over-limiting region is applied and the voltage-drop dependence on time is measured (see Fig. 6). An instantaneous increase in voltage-drop (part A of the curve) is

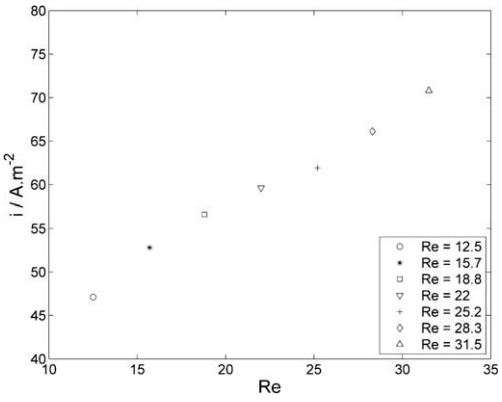

Fig. 3. Dependency of limiting current density on Re, c_0 = 0.025 M NaCl.

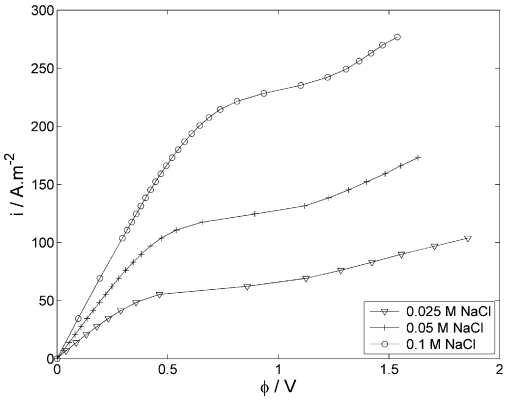

Fig. 4. Polarization curves for various electrolyte concentrations, *Re* = 15.7.

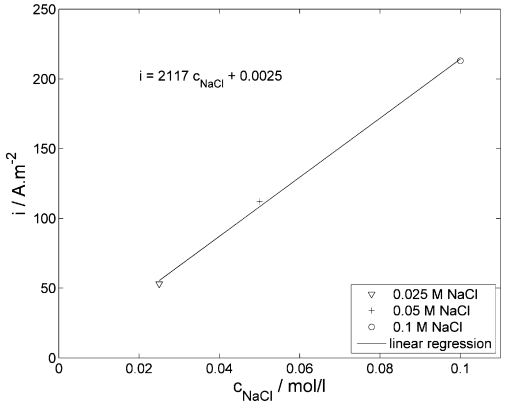

Fig. 5. Dependency of limiting current density on electrolyte concentration, *Re* = 15.7.

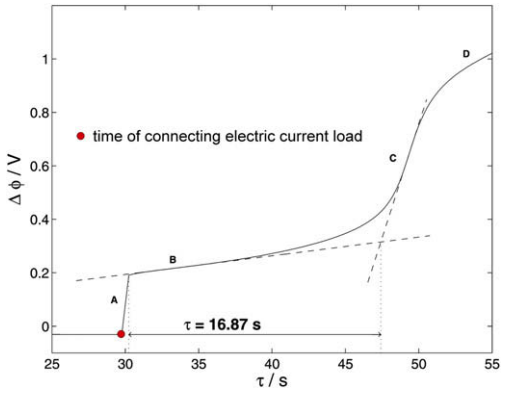

Fig. 6. Transition curve of CEM, c_0 = 0.1 M NaCl, i = 96 A m^{-2}.

due to the initial ohmic resistance of the solution and membrane. In part B, slow increase in voltage-drop follows. At certain time, steep increase in voltage occurs (part C). So called transition time – time when the diffusion layer on the anode side is depleted of cations can be evaluated from the measured curve. It is evaluated as the intersections of the tangent to part B with tangents to part A and C. Part D corresponds to further broadening of the depleted layer.

Mathematical description of the transition time comes out of Fick's second law for unsteady semi-infinite diffusion problem [13]

$$\tau = \frac{\pi D}{4}\left(\frac{c_0 zF}{t_+^m - t_+^s}\right)^2 \frac{1}{i^2} \tag{2}$$

Transition characteristics for various applied current densities were measured (see Fig. 7) and the transition times were evaluated. It can be seen that the curve for current density 76 A m^{-2} is in under-limiting region. Other curves are in over-limiting region. The value of the transition time increases with the inverse square of electric current density, which corresponds to the theory. Transition times τ_{meas} as a function of inverse square of applied current density are compared to calculated (Eq. (2)) transition times τ_{calc1} for 100% (t_+^m = 1) and τ_{calc2} for 95% (t_+^m = 0.95) permselective membrane (see Fig. 8). For the calculation, the diffusion coefficient of NaCl $D = 1.48 \times 10^{-9}$ m^2 s^{-1} and transference number $t_+^s = 0.39$ were used [10]. It is obvious that even a small decrease in permselectivity causes an increase in transition time. It can be seen, that measured transition times are much lower than the calculated. This cannot be explained by permselectivity reduction or by consumption of current for charging the double layers at membrane-solution interface, because that would lead to increase of transition time [14]. Krol et al. [10] explains the decrease of transition time by reduction of active area of membrane available for ion conductance because of membrane heterogeneity. This heterogeneity of CEMs is given by their composition, which usually includes non-conductive supporting fibers, non-conductive gluing polymer and conductive ion exchange resin granules. Rösler [14] studied several membranes and compared the slope of measured transition times to slope of transition times calculated for an ideally permselective membrane. The ratio in slopes varied between 0.64 and 0.87 and

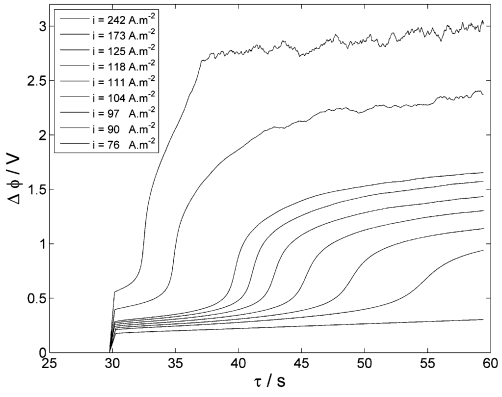

Fig. 7. Transition curves for various applied current densities, c_0 = 0.1 M NaCl.

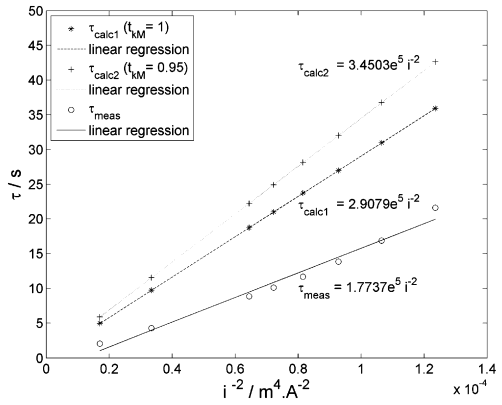

Fig. 8. Measured transition times compared to calculated ones for 100 % and 95 % CEM permselectivity, c_0 = 0.1 M NaCl.

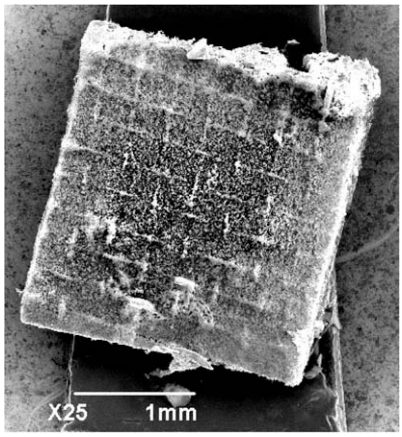

Fig. 9. SEM picture of the CEM sample (25× mag.).

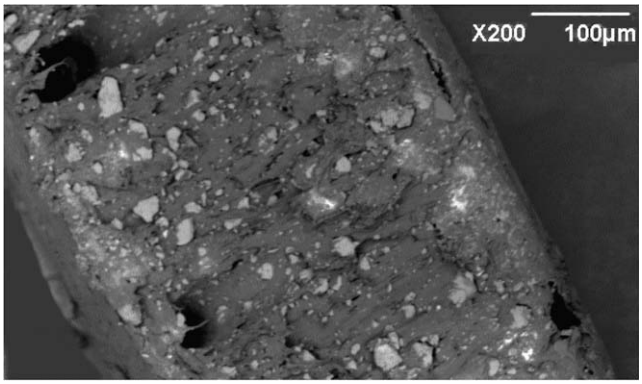

Fig. 10. SEM image of the the cross section of Ralex® CM PES membrane (200× mag.).

was in a direct correlation with membrane conductive heterogeneity. The ratio in slopes of measured to calculated transition time in our experiment was evaluated to 0.6, which indicates high conductive heterogeneity of the membrane sample. SEM picture analysis of the membrane sample has shown that the domain size of conductive polymer granules varies in range from units to tens of microns (see Fig. 10). The thickness of non-conductive supporting fibers is approx. 50 µm (see Fig. 9). Typical dimensions of the membrane embedded in the microdevice are hundreds of microns. Concerning the heterogeneity domain size to membrane dimensions ratio it can be deduced, that the conductive heterogeneity of the membrane may assume greater importance in micro-scale measurement. Also relatively low ratio in slopes of measured to calculated transition time supports this presumption.

5. Conclusions

We have integrated CEM into a microfluidic device with embedded gold measuring micro-electrodes. We have verified the functionality of the fabricated device by comparing of measured polarization curve to those, typically exhibited by CEM. We have also verified theoretical predictions of dependency of limiting current density on both hydrodynamic conditions and electrolyte concentration. Chronopotentiometric measurements have proven the linear dependency of transition time on inverse square of electric current density. The comparison of slopes of the measured transition times to the calculated ones along with the SEM image analysis has shown high conductive heterogeneity of the membrane.

Acknowledgements

The authors would like to thank for support by the Czech Science Foundation; Grant no. 104/08/H055, by the grant of Ministry of Education, Youth and Sport of the Czech republic; Grant no. MSM 6046137306 and D.S. acknowledges the project POKROK 1H-PK/24 of the Ministry of Industry and Trade of the Czech Republic.

References

[1] H. Strathmann, J. Membrane Sci. 9 (1981) 121–189.
[2] R. Audinos, Chem. Eng. Technol. 20 (1997) 247–258.
[3] R.K. Nagarale, G.S. Gohil, V.K. Shahi, Adv. Colloid Interf. Sci. 119 (2006) 97–130.
[4] K.S. Spiegler, Desalination 9 (1971) 367–385.
[5] D.A. Cowan, J.H. Brown, Ind. Eng. Chem. 51 (1959) 1445–1448.
[6] F. Maletzki, H.-W. Rösler, E. Staude, J. Mem. Sci. 71 (1992) 105–116.
[7] I. Rubinstein, Phys. Fluids A3 (1991) 2301–2309.
[8] J. Balster, M.H. Yildirim, D.F. Stamatialis, R. Ibanez, R.G.H. Lammertink, V. Jordan, M. Wessling, J. Phys. Chem. B 111 (2007) 2152–2165.
[9] J.J. Krol, M. Wessling, H. Strathmann, J. Mem. Sci. 162 (1999) 145–154.
[10] J.J. Krol, M. Wessling, H. Strathmann, J. Mem. Sci. 162 (1999) 155–164.
[11] C. Larchet, S. Nouri, B. Auclair, L. Dammak, V. Nikonenko, Adv. Colloid Interf. Sci. 139 (2008) 45–61.
[12] E. Volodina, N. Pismenskaya, V. Nikonenko, C. Larchet, G. Pourcelly, J. Coll. Interf. Sci. 285 (2005) 247–258.
[13] J.O'M. Bockris, A.K.N. Ready, Modern Electrochemistry, vol. 2, Plenum Press, New York, 1970.
[14] H.-W. Rösler, F. Maletzki, E. Staude, J. Mem. Sci. 72 (1992) 171–179.

Volume 15 | Number 7 | 7 April 2015 | Pages 1621–1784

Lab on a Chip

Miniaturisation for chemistry, physics, biology, materials science and bioengineering

www.rsc.org/loc

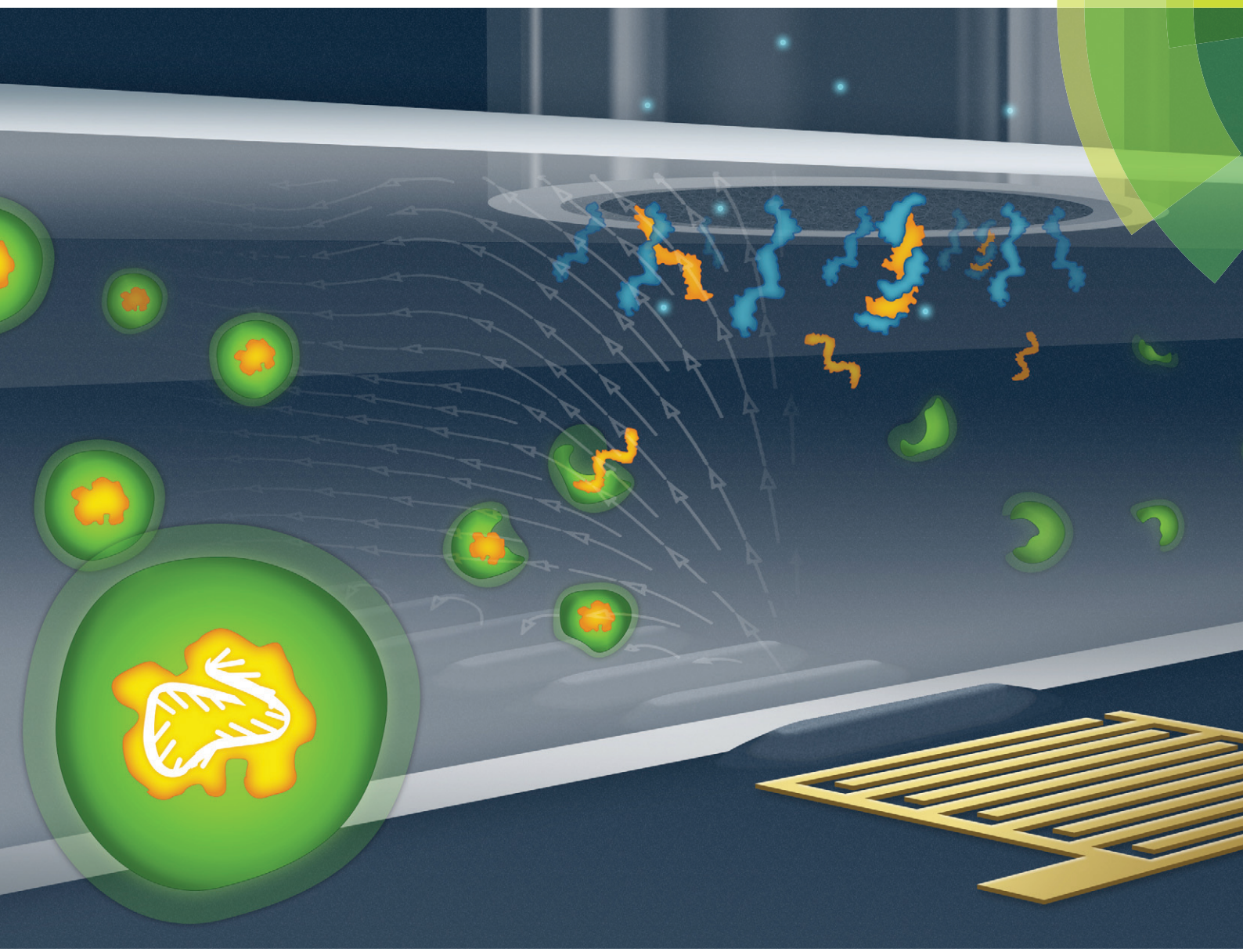

ISSN 1473-0197

ROYAL SOCIETY OF CHEMISTRY

PAPER

David B. Go, Hsueh-Chia Chang *et al.*

On-chip surface acoustic wave lysis and ion-exchange nanomembrane detection of exosomal RNA for pancreatic cancer study and diagnosis

Lab on a Chip

PAPER

View Article Online
View Journal | View Issue

Cite this: *Lab Chip*, 2015, **15**, 1656

On-chip surface acoustic wave lysis and ion-exchange nanomembrane detection of exosomal RNA for pancreatic cancer study and diagnosis†

Daniel Taller,[ab] Katherine Richards,[c] Zdenek Slouka,[bd] Satyajyoti Senapati,[bd] Reginald Hill,[c] David B. Go*[ad] and Hsueh-Chia Chang*[bd]

Received 9th January 2015,
Accepted 11th February 2015

DOI: 10.1039/c5lc00036j

www.rsc.org/loc

There has been increasing evidence that micro and messenger RNA derived from exosomes play important roles in pancreatic and other cancers. In this work, a microfluidics-based approach to the analysis of exosomal RNA is presented based on surface acoustic wave (SAW) exosome lysis and ion-exchange nanomembrane RNA sensing performed in conjunction on two separate chips. Using microRNA hsa-miR-550 as a model target and raw cell media from pancreatic cancer cell lines as a biological sample, SAW-based exosome lysis is shown to have a lysis rate of 38%, and an ion-exchange nanomembrane sensor is shown to have a limit of detection of 2 pM, with two decades of linear dynamic range. A universal calibration curve was derived for the membrane sensor and used to detect the target at a concentration of 13 pM in a SAW-lysed sample, which translates to 14 target miRNA per exosome from the raw cell media. At a total analysis time of ~1.5 h, this approach is a significant improvement over existing methods that require two overnight steps and 13 h of processing time. The platform also requires much smaller sample volumes than existing technology (~100 μL as opposed to ~mL) and operates with minimal sample loss, a distinct advantage for studies involving mouse models or other situations where the working fluid is scarce.

1. Introduction

Early detection of pancreatic cancer is critical to improving long term survival rates, which are currently less than 6% within 5 years of diagnosis.[1] Traditionally, the presence of a malignant tumor is confirmed upon biopsy procurement—an invasive procedure, which in itself is not useful for early detection since most patients develop symptoms only with late stage/metastatic disease. A minimally invasive method, which could be done on routinely collected biological samples, would be ideal for the diagnosis of pancreatic cancer and the subsequent tailoring of molecularly targeted therapies for patients.

MicroRNA (miRNA), in particular, have begun to receive significant attention as important indicators of cancer state and progression. MiRNAs are small strands (~22 nucleotides) of RNA that can be upregulated or downregulated in cancer cells and function as posttranscriptional gene regulators by binding to their target messenger RNAs (mRNAs). A number of recent findings have suggested that understanding miRNA regulation and expression is essential to understanding cancer development and could give an indication of disease presence before the onset of recognizable symptoms in the patient.[2–4] Furthermore, miRNAs are ideal biomarkers for early diagnosis of cancer due to their importance in disease development, their presence in biological fluids, and their short sequence length, which leads to increased stability. The miRNA transfer between cells in a tumor is mediated by exosomes, secreted membrane vesicles ~30–200 nm in diameter that are present in blood, saliva, urine, and other bodily fluids.[5–7] Therefore, the detection of miRNAs enclosed in exosomes is of great promise to the study and the non-invasive diagnosis of many cancers. Pancreatic cancer, as a particularly important but difficult to diagnose cancer, serves as a prime candidate for advances in exosome miRNA biomarker detection.

Extracting RNA from exosomes derived from extracellular biological matrices in sufficient concentration for conventional RNA detection methods such as reverse transcription polymerase chain reaction (RT-PCR) is not trivial, typically requiring multiple stages of ultra-centrifugation or field-flow fractionation.[8–10] In total, the typical standard process

[a] *Department of Aerospace and Mechanical Engineering, University of Notre Dame, Notre Dame, Indiana 46556, USA. E-mail: dgo@nd.edu*
[b] *Center for Microfluidics and Medical Diagnostics, University of Notre Dame, Notre Dame, Indiana 46556, USA. E-mail: hchang@nd.edu*
[c] *Department of Biological Sciences, University of Notre Dame, Notre Dame, Indiana 46556, USA*
[d] *Department of Chemical and Biomolecular Engineering, University of Notre Dame, Notre Dame, Indiana 46556, USA*

† Electronic supplementary information (ESI) available. See DOI: 10.1039/c5lc00036j

requires two overnight steps and approximately 13 h of processing time, demanding the use of multiple instruments and a wide variety of chemical kits and washes, with training times and other common inefficiencies frequently leading to several days in processing time. Additionally, these methods typically require large starting volumes of biomaterial, *e.g.*, 5–10 mL of cell culture, to collect a sufficient number of exosomes required for RT-PCR analyses due to exosome loss during the isolation process. Therefore, an on-chip device with low losses and reduced processing times would expedite cancer cell culture and animal studies and human cancer diagnostics.

In order to overcome the aforementioned obstacles, a new on-chip analysis strategy has been developed for the rapid lysis of exosomes and the detection of the miRNA released from these exosomes. Two microfluidic platforms are developed here, a lysis device and a separate detection device. The two devices reduce the total analysis time to ~1.5 h, which includes ~30 min for lysing and ~1 h for detection. The smaller sample volume required in the present study, ~100 μL, makes this platform more attractive for studies where only small amounts of biological fluid, *e.g.*, blood, can be safely extracted as would be the case in mouse models. This would also be ideal for use with fine needle aspiration (FNA) samples from clinical patients; a technique routinely conducted to confirm cancer diagnosis by pathological verification of neoplastic cells. The scientific community could gain much more insight about the tumor from fluid collected during this procedure, but the total sample volume is very limited, with only 250–500 μL of fluid typically being collected with each FNA.[11,12] Although the study presented herein was conducted with cancer cell media, a recent study conducted by Schageman *et al.*[6] shows that both the total exosome count and the concentration of exosomal RNA are greater in blood serum derived from human donors than in cell media samples, implying that studies involving human-derived samples should be feasible using the given approach.

1.1 Overview of lysis and detection devices

Lysis is achieved *via* surface acoustic waves (SAWs), which are Rayleigh waves generated on the surface of a piezoelectric crystal by alternating current applied through an interdigitated electrode transducer.[13,14] When the SAW waves interact with a bulk liquid droplet or film, as depicted in Fig. 1a, scattered sound waves produce an acoustic pressure in the liquid bulk while the electric component of the wave produces an electric Maxwell pressure at the solid liquid interface.[15,16] Historically, SAWs have been used in the electronics industry as filters, oscillators, convolvers, and transformers.[13,17] More recently, SAW devices have found new life in the microfluidics discipline as a tool to overcome the traditional microscale challenges of constrained geometries, surface tension, and viscous effects in order to provide high Reynolds number flows. In particular, it has been shown that SAWs on the surface of the piezoelectric crystal will scatter into a liquid bulk, inducing an acoustic radiation force which allows Reynolds numbers as high as 7000 and effective turbulent mixing.[18] In addition, the electromechanical coupling inherent in SAWs produces an electric field as high as ~10^6 V m^{-1} at the surface of the substrate.[15,19] The application of both the electric and acoustic pressures applied by SAWs have proven useful for focusing and sorting particles and cells,[20,21] for producing charged aerosols for mass spectrometry,[15,22] and for cell lysis.[23,24] In this work, we utilize SAWs to lyse exosomes, which are an order of magnitude smaller than most cells. The lysis of particles as small as exosomes is likely made possible due to the effects of the acoustic radiation

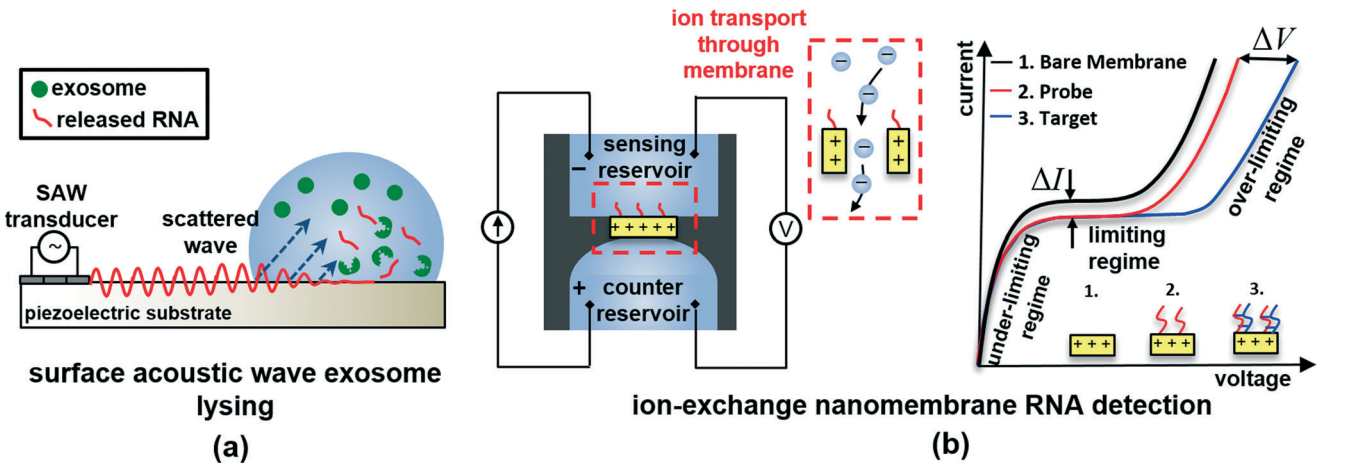

Fig. 1 (a) Schematic of surface acoustic wave (SAW) device (side view) and SAW-induced lysing of exosomes to release RNA for detection. SAWs generated at the transducer refract into the liquid bulk, inducing fluid motion, and electromechanical coupling also generates a complimentary electric wave at the surface of the substrate. (b) Schematic of ion-exchange nanomembrane sensor consisting of two reservoirs separated by the membrane. RNA in the sensing reservoir hybridize to complimentary oligos immobilized on the surface of the membrane. The inset shows the ion transport through the device to generate current and the right image is a characteristic current–voltage curve illustrating the under-limiting, limiting, and over-limiting regimes.

force and the dielectrophoretic force acting on small particles, as detailed in previous studies on SAW-induced particle manipulation.[25–28] The well-known dielectrophoretic force arises due to an induced particle dipole occurring in an inhomogeneous electric field. The acoustic radiation force is analogous, with a gradient in mechanical stress replacing the electric field gradient as the mechanism and factors involving the relative density and compressibility of the particle and the surrounding medium replacing similar factors involving the relative electric permittivity and conductivity. SAW lysis thus proves to be an excellent alternative to traditional chemical or surfactant lysates,[29–31] which can interfere with RNA detection downstream by changing the buffer pH and ionic strength or forming/disrupting self-assembled layers for surface assays.

Label-free, specific on-chip detection of RNA is achieved by using a separate device, an ion-exchange nanomembrane sensor developed by the authors' group.[32–34] The sensor consists of an anion-exchange nanoporous membrane sandwiched between two reservoirs of fluid, as shown in Fig. 1b. When an electric current is applied across the membrane, anions are driven through the membrane pores, producing a corresponding voltage drop measured across the membrane. Measuring the current–voltage characteristic (CVC), which has been the subject of extensive study,[34–36] thus becomes the basis for RNA detection. Briefly, the CVC of the nanomembrane consists of three regimes as illustrated in Fig. 1b: an ohmic under-limiting regime at low voltages, a limiting regime where current saturates at intermediate voltages, and an over-limiting regime at high voltages where current once again increases abruptly. It has been shown that the CVC dramatically changes when large, negatively charged molecules such as RNA are adsorbed to the surface of the positively charged membrane.[34] In particular, the over-limiting regime shifts rightward to higher voltages as more molecules adsorb to the surface, as shown by the voltage shift ΔV in Fig. 1b. The sensor works on the principle that after oligonucleotide probes are functionalized on the surface of the membrane, target RNA bind to the surface selectively while non-target molecules do not, allowing the target RNA concentration to be accurately determined through CVC measurements. Building on previous work that has demonstrated this detection method for solutions of pure DNA and RNA dissolved in phosphate buffer saline (PBS),[34] in this work we perform membrane sensor detection of RNA suspended in cell media for the first time. Together, these two separate devices provide a complete platform for the detection of exosomal RNA for pancreatic cancer study and diagnosis.

2. Materials and methods

2.1 Target miRNA and oligonucleotide probe

As our initial target, we focused on the miRNA hsa-miR-550-002410 (miR-550, base sequence given by AGUGCCUGAGGGAGUAAGAGCCC), which is known to be present in pancreatic exosomes and which early reports suggest may be an indicator for cancer development.[37] Target miRNA were extracted from exosomes in cell media from the PANC1 cell line. PANC1 cells were grown in the initially exosome-free Dulbecco's Modified Eagle's Medium (Sigma Aldrich), with the exosome-containing media being collected once 70–90% confluent. In addition, artificial target miRNA were purchased (Life Technologies) to serve as a baseline during calibration, diluted to known concentrations with UltraPure™ DNase/RNase-Free distilled water (Invitrogen). PBS 10× solution with pH 7.4 was purchased from Hoefer and diluted to 0.1× for current–voltage measurements with the membrane sensor and to 4× concentration to wash the membrane to prevent non-specific binding. For RNA detection, an amine-coupled ssDNA oligionucleotide probe of the same length as the miR-550 target and with a complementary sequence of TCACGGACTCCCTCATTCTCGGG was also purchased (Life Technologies).

2.2 Surface acoustic wave (SAW) device integrated into microfluidic channel

The SAW device was fabricated using standard UV photolithographic methods. Twenty pairs of titanium/aluminum interdigitated electrodes (Ti/Al 20 nm/200 nm) were patterned on a 127.68° *yx*-cut piezoelectric lithium niobate ($LiNbO_3$) substrate (Precision Micro-Optics PWLN-431232) to form an electrode-width controlled (EWC) single phase unidirectional SAW transducer (SPUDT), which generates plane SAWs propagating in one direction only.[38,39] Each SAW device consisted of a rectangular piece of $LiNbO_3$ 16 mm × 40 mm and 0.5 mm in thickness. The fingers of the interdigitated electrodes spanned 4 mm in length and were designed to produce a SAW wavelength of 136 μm, with finger width and spacing based on multiples of 1/8 of the wavelength as determined according to standard EWC SPUDT design.[38,40–42] The operating frequency was 28.3 MHz. The SAW was activated by a function generator (Agilent 33250A) in series with an amplifier (E&I 325LA RF Power Amplifier).

A channel for fluid flow was fabricated using three layers of polycarbonate thermosoftening plastic. The channel and holes for the inlet and outlet were cut and sealed together *via* heat curing in a manner similar to Slouka *et al.*,[32] yielding a channel with height of 300 μm and width of 2000 μm. The channel was constructed with an opening in the bottom and the front side, so that it conformed to the size of the $LiNbO_3$ substrate on which the SAW electrodes were fabricated. The channel was then attached to the substrate with UV curing glue (Loctite 3492) and cured (Electro-Cure 500 UV Flood Curing Chamber). The open channel facing the SAW device is sealed with UV curable glue (Acrifix 1R 0192) so that no fluid leaked out of the channel. The outlet was made out of Tygon tubing, while a port fitting cast out of polyurethane was attached to the inlet hole. The combined microfluidic channel and SAW lysis unit is shown in Fig. 2a and b.

Sample was pumped through the device at a rate of 250 μL h^{-1} and the SAW device operated at 1 W of power. The device was operated for 25 min. and the residence time in

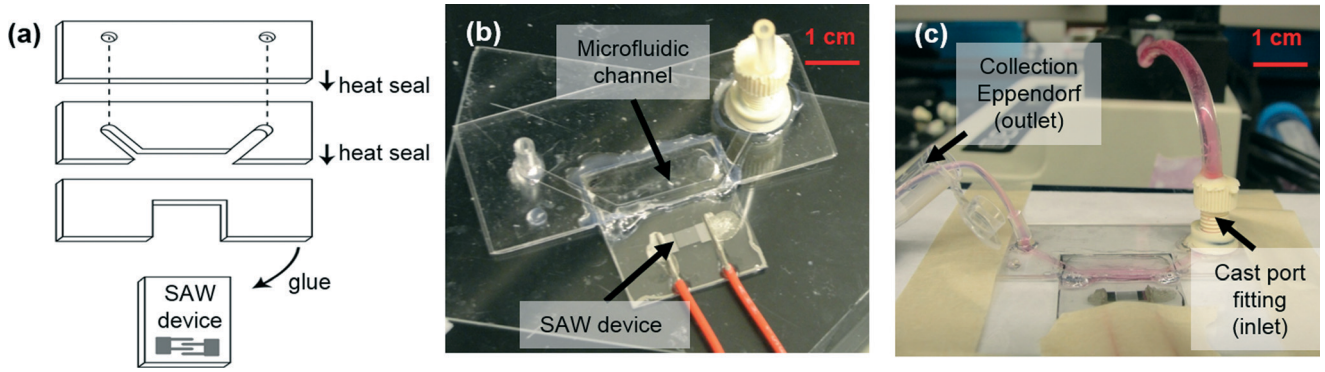

Fig. 2 (a) Schematic of SAW lysis device. (b)–(c) Images of the as-fabricated SAW device and liquid channel used to lyse exosomes.

the portion of the channel exposed to the SAW device was approximately 30 s. Sample was collected at the outlet of the microfluidic channel into an Eppendorf tube, as shown in Fig. 2c, before transfer to the nanomembrane sensor device *via* pipette.

Visualization and measurement of the particle distribution in the suspension before and after SAW exposure was conducted using light scattering-based particle tracking (Nanosight LM10). Unlike traditional dynamic light scattering (DLS) technology, a video is taken with the Nanosight so that particles may be counted individually and their Brownian motion can be recorded over time, yielding more accurate measurements of both particle size and concentration for the exosome sizes anticipated here (~100 nm). All samples measured with the Nanosight were diluted in 0.1× PBS to between 1×10^8 and 4×10^8 particles mL^{-1} to obtain maximum accuracy in the results, as prescribed in previous studies.[5,43] The Nanosight exosome concentration and size distribution statistics reported by the Nanosight, have been proven to yield accurate results for exosomes and thus the Nanosight is among the most widely-used and most reliable methods for *in vivo* exosome quantification available to researchers to date.[5,7,43–50]

2.3 Ion-exchange nanomembrane sensor

The ion-exchange nanomembrane device consisted of two reservoirs made of hard polyurethane resin bridged together by a heterogenous ion-exchange membrane (type AMH5E-HD RALEX® membrane, Mega a.s.) as illustrated in Fig. 1b. Two silicone reservoirs were cast from a two-component silicone RTV resin (TAP Plastic Inc.) in a silicone mold. The ion-exchange nanomembrane was sandwiched between the two silicone molds, and the system was filled with polyurethane resin (TAP Quik-Cast Polyurethane Resin, 1 : 1 ratio) and allowed to set for 30 minutes. Release of the silicone mold produced the membrane sensor chip. The membrane was cut with a razor blade to be just large enough to cover the exposed sensing area of 0.25 mm^2, with the probes attached to membrane surface as described in previous work.[34] The bottom reservoir was sealed with a plexiglass (Poly(methyl methacrylate) or PMMA) sheet with two holes for electrodes. The biological fluid sample was transferred to the membrane sensor after SAW lysis as described in the previous section.

For RNA detection, an amine-coupled oligionucleotide probe of the same length as the miR-550 target and with a complementary sequence was purchased from Life Technologies as previously noted. The process to attach the probe to the membrane using ethyl-3-(3-dimethylaminopropyl)-carbodiimide (EDC) and benzophenone-3,3′,4,4′-tetracarboxylic acid powders (Sigma Aldrich) has been detailed elsewhere.[34] To summarize, the surface was first treated with photo-reactive benzophenone-3,3′,4,4′-tetracarboxylic acid and exposed to UV light (Electro-Cure 500, Electro-Lite Corp.) in order to create COOH groups on the surface of the membrane, followed by treatment with 0.4 M EDC for 30 min. Lastly, an overnight incubation with the probe in 0.1× PBS solution was performed to covalently bind the probe to the membrane surface.

In order to perform detection of multiple samples on the same membrane sensor, a pH 13 solution of NaOH and 0.1× PBS was used to dehybridize the target RNA from the probes between runs. A wash with 4× PBS was used to wash away contaminants and to eliminate non-specific binding prior to each measurement. After application of the NaOH solution or the 4× PBS solution, repeated measurements were taken using a 0.1× PBS solution buffer until the CVC stabilized, a process which takes 5 to 15 min per measurement.

3. Results and discussion

3.1 Raw sample analysis

Prior to any processing of the cell media sample with our microfluidic devices, the cell media was spun down at 1500 rpm for 5 min and then analysed to confirm the presence of exosomes and the presence of the target miR-550. The presence of exosomes was confirmed using transmission electron microscopy (TEM) imaging, where Fig. 3a shows a representative TEM image of particles size ~20–50 nm, consistent with TEM analyses by other researchers.[51]

We also used RT-PCR to confirm that the target RNA was present in the sample. In brief, exosomes were collected from

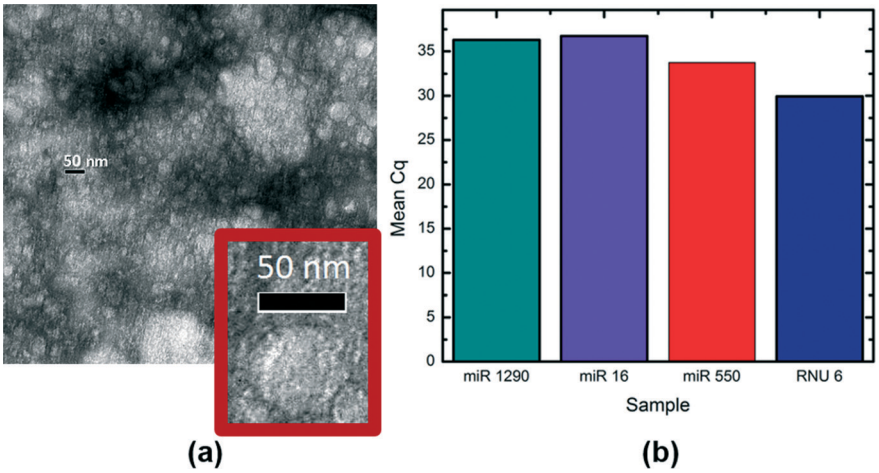

Fig. 3 (a) Representative transmission electron microscope (TEM) image, confirming the presence of exosomes in the ~30–50 nm size range in the sample. A zoomed-in view of a single exosome is shown in the inset. (b) Mean quantification cycle (Cq) for different RNA targets from RT-PCR analysis after chemical lysing.

an initial sample 10 mL cell media sample *via* the ExoQuick TC™ exosome precipitation solution and incubated at 4 °C overnight. The exosome pellet was then collected and chemically lysed (lysate Triton X-100 added to the solution at 2% by volume and incubated at 70 °C for 10 minutes) prior to RNA collection using the SV Total RNA Isolation System (Promega Corporation). RT-PCR analysis was performed using the miScript SYBR® Green PCR Kit (Qiagen), following the manufacturer's guidelines. For the present study, the mean quantification cycle (Cq) represents the number of cycles needed to reach a computer-determined fluorescence amplification threshold of approximately 75 times the background (negative control) fluorescence level. Cq values correlate with the relative amount of starting sample, with a lower Cq correlating with a higher amount of starting sample and *vice versa*. Fig. 3b summarizes the RT-PCR results, displaying the mean quantification cycle (Cq) for the target miR-550, in addition to two additional potential targets (miR 1290 and miR 16) as well as the bookkeeping strand RNU 6, confirming the presence of the target miR-550 in the sample, as expected. However, we found that RT-PCR could not be used to quantify SAW lysis because the SAW lysis unit produces ~100 μL of lysed cell media, whereas RT-PCR requires 5–10 mL of sample in order to isolate a sufficient number of exosomes as previously noted.

3.2 SAW-induced exosome lysis characterization

SAW-induced lysing was achieved by exposing raw cell media to ~30 s of SAW at 1 W of power, and the results were quantified using NanoSight nanoparticle tracking measurements. Fig. 4a shows particle size distributions averaged across multiple trials for three sets of experiments: (1) raw cell media, (2) cell media pumped through the channel with the SAW

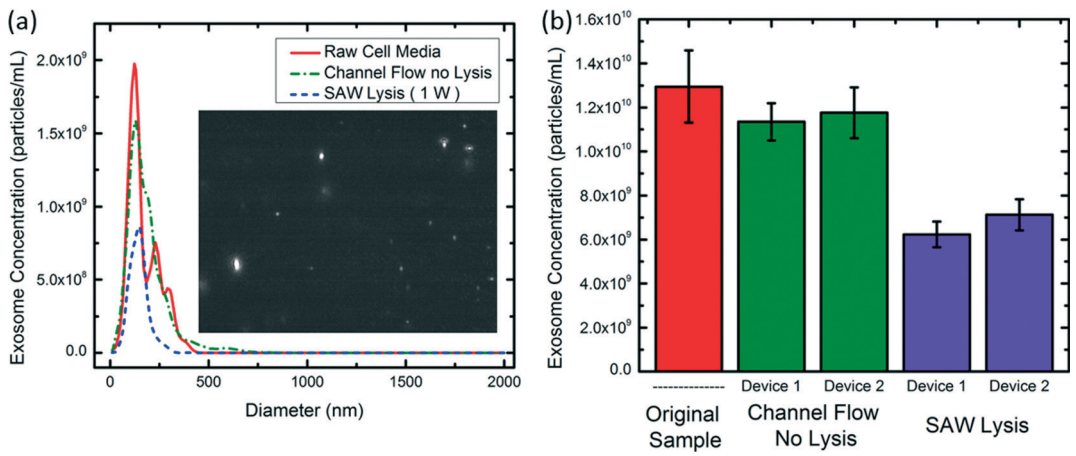

Fig. 4 (a) Average Nanosight LM10 size distributions for exosomes in the cell media sample. While there is a 10.8% loss due to flow in the channel alone (difference between red and green curves), turning on the SAW device decreases the exosome count substantially. The inset shows visual confirmation of exosomes in the cell media obtained from the Nanosight. (b) Quantified exosome concentrations from the size distributions using two separate SAW lysis units, with four samples processed by each. Error bars: 1 standard deviation.

device turned off as a negative control, and (3) cell media pumped through the microfluidic channel while exposed to action of the SAW device. For these experiments, two separate SAW-channel devices were fabricated and four sets of experiments with steps (1) to (3) were conducted on each so that there were 8 measurements of the SAW lysed sample in all. In each experiment, an identical sample volume of 100 μL was collected. Fig. 4b shows the quantified exosome concentration statistics based on the reported Nanosight values. These experiments indicate that 10% of the exosomes are lost when flowing through the microchannel, likely because they stick to the channel walls. Of the remainder, 42% are lysed, for an overall lysis rate of 38 ± 10% (all data are expressed as the mean ± standard deviation). It should be noted that the exosome size distributions shown in TEM images (*e.g.*, Fig. 3a) are generally not comparable to those produced by the Nanosight in part because the TEM analysis particles are dehydrated and observed in vacuum rather than counted *in vivo* as for the Nanosight, which causes shrinkage.[52–54]

While this lysis rate is satisfactory for the present study, it should be noted that significant improvements may be possible. To date, no comprehensive study has been undertaken to study lysis rate as a function of channel height, SAW wavelength, applied power, cell membrane elasticity, fluid properties, or any number of other possible variables. A more thorough understanding of the lysis mechanisms (whether mechanical or electric in nature) should yield improvement. Additional steps may also be taken to prevent loss of exosomes due to the adhesion to the walls of the device. In particular, a number of researchers have had success in preventing the cell and protein adhesion to surfaces *via* chemical treatment of the device walls,[55–57] which suggests a similar approach may prove fruitful for exosome analysis. This approach would not require substantial changes to the fabrication process.

3.3 Nanomembrane sensor calibration

3.3.1 Description of model. Before using our nanomembrane sensor to quantify miR-550 in our raw cell media samples, it was necessary to calibrate it. Fig. 5 shows representative CVC data for one of our nanomembrane sensors before attachment of the complementary probe (baseline), after functionalizing the membrane with the probe (probe) and after hybridizing with the target miR-550 of a various concentrations for 15 min, where the sensor was regenerated after each measurement. The CVCs are acquired by ramping the current at a rate of 0.5 μA s^{-1}. The voltage shift in the over-limiting region is indicative of hybridization and has been associated with vortex suppression by the hybridized probe-target,[35] and progressively higher concentrations of the target on the sensor results in larger voltage shift ΔV until the sensor saturates. Calibration is determined by measuring the ΔV at a pre-defined current in the overlimiting regime and correlating ΔV to the concentration C. The current where these shifts are measured was chosen separately for each

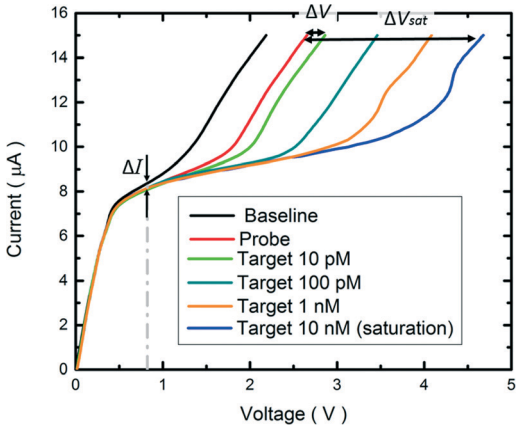

Fig. 5 Representative current voltage characteristic (CVC) for nanomembrance sensor. The black, red, and blue curves indicate a CVC taken with the bare membrane, a CVC taken with the probe attached to the membrane, and a CVC taken with the probes on the membrane surface fully saturated with target RNA, respectively. ΔV measurements were taken at 15 μA, while the limiting current I_o and current shift ΔI were measured at 0.822 V (dotted grey line). Additional CVCs are given in the ESI.†

chip to be as high as possible without damaging the membrane.

In previous work, as many as eight calibration points were needed to detail the full dynamic range of the sensor.[33] However a universal calibration curve valid over the entire range of the sensor significantly expedites the calibration process. To determine a universal calibration curve, we derive a formula that requires only two calibration points to determine two unknown parameters – the saturation voltage shift ΔV_{sat} and the Langmuir equilibrium constant K related to the maximum capacity of the sensor in the linear dynamic range.

The voltage shift we observe in the response of the nanomembrane sensor results from target RNAs binding to complimentary probes on the surface of the membrane. This process may be described using the Langmuir adsorption model,[58,59] which relates the adsorption of molecules on a solid surface to the concentration C of the molecules in the fluid above the solid surface, by using coverage dependent absorption (k_r) and desorption (k_f) rates:

$$k_r\theta = k_f C(1 - \theta), \quad (1)$$

where θ is the fractional coverage of the target on the surface. Rearranging,

$$\theta = \frac{KC}{1 + KC}, \quad (2)$$

where $K = k_f/k_r$ is the affinity or Langmuir equilibrium constant. This parameter describes how strongly the target molecule is attracted to the surface for binding. We see that K has units of inverse concentration, and according to eqn (2) it is related to the critical concentration when exactly half of the target has bound to probes on the membrane (so when $\theta = 1/2$, $K = 1/C_{critical}$). Thus K can also be interpreted as a

measure of the target capacity of the sensor within the linear dynamic range.

We may relate θ to the measured voltage ΔV shift by noting that each time a target miRNA reaches a probe and binds, the impedance of the system increases. For ΔV measurements taken at constant current as in Fig. 5, this implies that the voltage will increase proportionally. We thus assume $\theta = \Delta V/\Delta V_{sat}$ so that coverage by the target reduces the ion flux cross-section area and increases the ion-current resistance proportionally until all the probes have hybridized at saturation ΔV_{sat}. Therefore, we have the calibration equation,

$$\frac{\Delta V}{\Delta V_{sat}} = \frac{KC}{1+KC}. \quad (3)$$

While the parameter K is not necessarily known *a priori* and may vary between different membrane sensors, we shall see that it can be extracted from the initial slope of the calibration curve at low concentrations. Expanding eqn (3) in a Taylor series at the low concentration limit, we find that

$$\frac{\Delta V}{\Delta V_{sat}} \approx KC. \quad (4)$$

Taking a derivative of voltage shift with respect to concentration and evaluating at low concentration yields

$$K = \frac{1}{\Delta V_{sat}} \frac{\partial \Delta V}{\partial C}\bigg|_{C=0}. \quad (5)$$

We see that although each membrane sensor device varies in sensitivity due to differences in fabrication and variations in the membrane surface topology, it is possible to construct a universal calibration curve by normalizing voltage and current measurements with the saturation voltage shift ΔV_{sat} and using a critical concentration inversely proportional to K. As previously noted, this reduces the number of calibration points required to two. Experimentally, a calibration curve may be constructed in full by using the zero-shift voltage at zero target concentration and taking a measurement at a relatively low concentration (5 pM) and another measurement at high concentration (100 nM) so that K and ΔV_{sat} may be extracted from the initial slope and the saturation voltage shift.

The theoretical relationship between concentration of target miRNA and voltage shift derived above was verified with data taken from 7 different membrane sensors, normalized using the parameters K and ΔV_{sat} determined separately for each sensor. Data for all 7 sensors are shown in the ESI,† including the currents chosen for each chip where these shifts are measured. The parameter ΔV_{sat} was obtained from one saturation voltage measurement for each sensor at high concentration (10 nM) as previously described. The constant K was obtained by finding the slope between the zero-shift voltage with no target molecules and the voltage shift from one low-concentration (5 pM) measurement to obtain an approximate slope for use in eqn (5). Fig. 6a shows the raw data prior to normalization alongside the Langmuir adsorption calibration curves given by eqn (3) with parameters extracted from two data points as described above. The collapsed normalized data is shown in Fig. 6b. The linear dynamic range spans two decades, computed by fitting a line to the linear and saturation regions of the calibration and measuring the concentration at which they intersect relative to the limit of detection. We observe excellent agreement between theory and experimental data, even though the voltage shifts are measured at different currents, apart from one anomalous data set given by closed red markers in Fig. 6a. In the initial linear region only (not including the saturation region since detection occurs in the initial linear region only), we find a coefficient of determination of $R^2 = 0.88$ excluding this anomalous data set and $R^2 = 0.82$ with the anomalous data set included; both being satisfactory given the potential for variation across sensors. The average limit of detection was computed as 2 pM based upon the mean voltage and standard deviation of four blank measurements taken on each of the seven nanomembrane sensors tested. Large variations were observed in the values for the two parameters, however, with $C_{critical} = 209 \pm 73$ pM (=1/K) without the anomalous data set and $C_{critical} = 184 \pm 94$ pM with it. We find that $\Delta V_{sat} = 0.92 \pm 0.59$ V without the anomalous data set and $\Delta V_{sat} = 0.84 \pm 0.58$ V including it.

3.3.2 *A priori* parameter estimation. In order to further simplify the calibration in future studies, we explore the possibility of estimating the two parameters K and ΔV_{sat} using data available from the CVC of the bare nanomembrane and the CVC of the nanomembrane with only the probe attached, before the system is exposed to the target miRNA. The Langmuir equilibrium constant K, which is dependant on the free energy of absorbance when a target miRNA binds to a probe on the membrane surface, should ideally be the same for all chips whenever the same target/probe pair are used, obviating the measurements at low concentration during calibration that would otherwise be required for every chip. However, as previously mentioned, significant variation occurs in practice, perhaps due to inconsistencies in fabrication or due to variations in the surface energy of the membrane itself. Improvements in the fabrication process for the membrane sensor or use of a different brand of nanoporous membrane may yield more consistent values in future studies, but at the present time it is advisable to take a low concentration measurement for every chip to estimate K, since the parameter K is especially important in defining the low-concentration portion of the calibration curve (Fig. 5b) where measurements will be taken during practical use of the device.

In order to estimate the parameter ΔV_{sat}, we consider the limiting current in both the bare membrane and the membrane with the probe attached. (Note that in this section, the anomalous data set, closed red markers in Fig. 6, is excluded from all calculations.) Previous studies have demonstrated

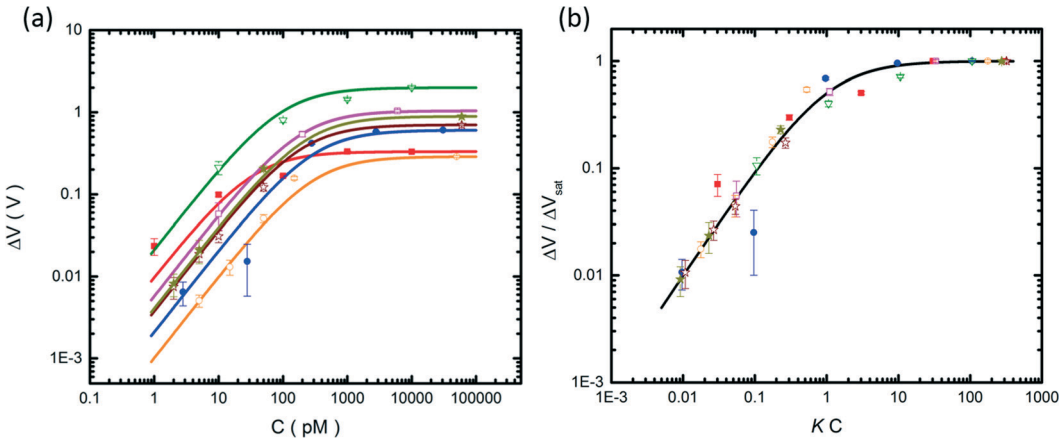

Fig. 6 (a) Voltage shift (ΔV) as a function of the concentration (C) for five separate membrane sensors. Solid lines show the calibration curve eqn (3) with parameters extracted from two data points. (b) Corresponding data normalized by the saturated voltage shift ($\Delta V/\Delta V_{sat}$) as a function of the normalized concentration (KC) for seven separate membrane sensors along with the universal calibration curve from eqn (3). Each data set was normalized by its maximum saturation voltage shift ΔV_{sat} and the affinity constant K determined by the slope of the curve at low concentration, extracted from two data points. Error bars: 1 standard deviation.

that the limiting current is proportional to the area of the membrane.[60] When the probe is attached to the bare membrane, the limiting current is reduced, corresponding to a reduction in the effective area of the membrane due to probes attaching to the surface of the nanoporous membrane and blocking the pore openings. This means that the fractional change in the limiting current, $\Delta I/I_o$, measures the membrane surface area that the probe covers. That is, $\Delta I/I_o = \Delta A/A$, where A is the membrane surface area, I_o is the initial limiting current of the bare membrane, before the probe is applied, and ΔI is measured as the average current shift in the limiting regime as indicated in Fig. 1b, and is hence related to probe density. More specifically, the limiting current region is defined to be the voltage range between the two "knees" of the base-line probe-free bare-membrane CVC curve with maximum curvatures. The average limiting current I_o and current shift ΔI can be accurately estimated by values at the mid-point of this voltage range. The voltage values for each chip where these current shifts are measured as indicated in the ESI.† It is known that probes binding to the surface of the nanoporous membrane also cause the voltage shift ΔV in the overlimiting regime, in this case as a result of the hydrodynamic mechanism of vortex suppression.[33] It is thus unsurprising that $\Delta I/I_o$ correlates with $\Delta V_{sat}/V_o$, where V_o is the voltage in the overlimiting regime before the target is added, with only the probe attached. This relationship is shown in Fig. 7a, along with the linear regression line

$$\Delta V_{sat}/V_o = 15.83(\Delta I/I_o), \quad (6)$$

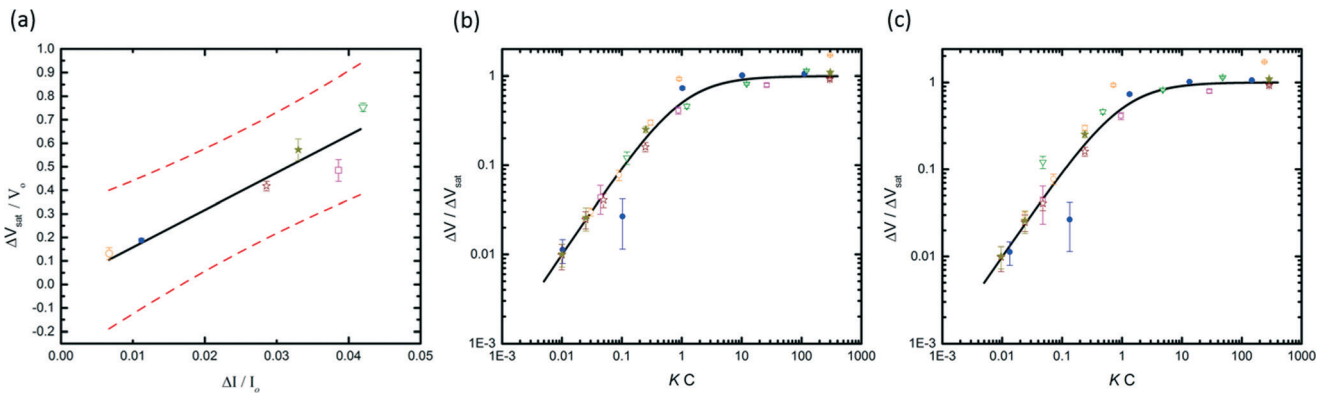

Fig. 7 (a) Correlation between the fractional change in the limiting current ($\Delta I/I_o$) and the fractional change in voltage when the probes on the membrane surface are saturated with target miRNA ($\Delta V_{sat}/V_o$), together with the empirical correlation $\Delta V_{sat}/V_o = 15.83\Delta I/I_o$ marked with a solid black line and 95% confidence interval marked with dotted red lines. (b) Data normalized by the saturated voltage shift ($\Delta V/\Delta V_{sat}$) as a function of the normalized concentration (KC) for five separate membrane sensors along the universal calibration curve from eqn (3). Here, the maximum saturation voltage shift ΔV_{sat} was computed *a priori* from the empirical correlation in (a), while the affinity constant K was determined from one data point using the slope of each calibration at low concentration. (c) Data normalized with ΔV_{sat} computed *a priori* from the empirical correlation in part and K = 1/(209 pM) held constant for all chips. The anomalous data set shown in Fig. 6 in closed red markers is excluded from all parts (a)–(c). Error bars: 1 standard deviation.

for the same sensors shown in Fig. 6a. Using eqn (6) to compute ΔV_{sat} (rather than use a measured value of ΔV_{sat}) yields the collapsed normalized data of Fig. 7b with a value of R^2 = 0.78 in the initial linear region only. Collapsing the data using both the voltage correlation and a constant K value for all data sets of $K = 1/C_{critical}$ = 1/209 pM (using $C_{critical}$ = 209 pM for the case where the anomalous data set is excluded) yields the result shown in Fig. 7c with a value of R^2 = 0.72 in the initial linear region. This indicates that reducing the number of calibration points may still yield results accurate enough for some applications, with room for improvement in future work.

3.4 RNA quantification

Detection of the target miRNA contained both in the cell media sample (free floating) and after lysis was performed using the universal calibration curve. We performed detection on two different membrane sensors, using two calibration points on each to obtain K and ΔV_{sat} in combination with the universal calibration curve shown in Fig. 6b. Each cell media sample was placed on the sensor prior to measurement, washed off, and then repeated twice more for a total of three measurements per sample per sensor. Fig. 8 shows that the raw cell media has a concentration of 6 ± 1 pM of free-floating miRNA, while the SAW lysed sample has 13 ± 2 pM. We estimate that this sample of cell media sample contained $8.2 \pm 0.5 \times 10^8$ exosomes mL^{-1}, computed as the average and standard deviation of four subsamples with concentrations reported from the Nanosight according to the protocol described in Section 2.2. Taking into account exosome loss and lysis, we estimate that there are 14 ± 6 copies of the target miRNA 550 per exosome. Use of the *a priori* estimate for ΔV_{sat} (calibration curve Fig. 7b), and the *a priori* estimates for both ΔV_{sat} and K (calibration curve Fig. 7c) yields estimates of 15 ± 6 and 10 ± 9 copies of target RNA per exosome, respectively, which are comparable to the estimate of 14 copies per exosome produced without *a priori* parameter estimation.

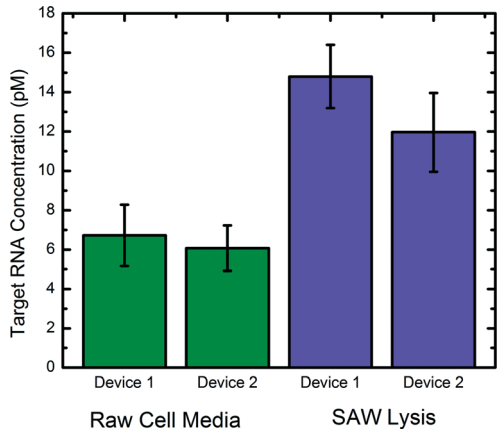

Fig. 8 Target RNA concentration as detected by the nanomembrane sensor and determined using the universal calibration curve before and after SAW lysis for two different nanomembrane devices. Error bars: 1 standard deviation.

These findings are consistent with the findings of others. It is well known that free floating miRNA are stable in cell media independent of exosomes, likely the by-product of dead cells.[61] Furthermore, it has previously been reported that tumour cells have the same concentration of the target miR-550 as the exosomes themselves,[62] so it is unsurprising that this target is found free floating in extracellular space in comparable quantity as within the exosomes themselves. Based on our studies involving cancerous pancreatic cell lines and prior findings by others, we have independent confirmation[63] that there are ~10^3–10^4 highly expressed RNA per exosome and ~10^2–10^3 different genes or miRNA, which implies than an estimate of ~10 target miRNA per exosome is reasonable.[63,64]

Although in the current study the target miR-550 is present within the exosomes as well as free-floating in approximately equal amounts, this will likely not be true for most targets of interest in future studies. For instance, Valadi *et al.* conducted a study on exosomes from the mouse cell line MC/9 and the human cell line HMC-1 that demonstrated that of the 1300 genes present, many were not found in the cytoplasm of the donor cell.[65] A review by Vlassov *et al.* emphasizes that RNA degrades rapidly when in peripheral circulation in blood, and that exosomes provide the necessary protective packaging in this biological fluid.[7] The biological significance of RNA contained within exosomes (as opposed to cellular or free-floating RNA) is underscored by Chen *et al.*, who suggests that the selective enrichment of a group of miRNAs in an exosome sample reveals a "nonrandom but orchestrated network before their release", making it "essential" from a biological perspective to study exosomes and the mechanism by which particular miRNAs are directed to these exosomes.[66] The upshot of these studies is that although the particular target used for the present study was present in appreciable quantities in both free floating media and in the exosomes, a device which lyses exosomes with minimal sample loss or contamination will prove crucial to future studies due to the biological significance of exosomal miRNA in particular and due to the degradation of free floating miRNA free floating in the blood. This will be important in future work on mice models or human-based samples.

4. Conclusions

We have demonstrated SAW-driven exosome lysis coupled with nanomembrane sensor-based microRNA detection as a promising vehicle for the study and early diagnosis of pancreatic cancer. SAW lysis of exosomes was demonstrated for the first time as an on-chip alternative to chemical lysates, which chemically interfere with detection using the nanomembrane sensor. A universal calibration curve was developed for the nanomembrane sensor for miRNA detection and was used to analyse unlysed and lysed samples. These rapid, sensitive, and non-invasive tools provide a new approach to the

diagnosis and prognosis of cancer *via* detection of miRNAs. Taken together, the devices presented here push forward the state of the art in exosome detection and identification.

This study demonstrates the feasibility of microfluidic miRNA profiling for cancer study and diagnosis, paving the way for full integration of the different components onto a single device in the near future. An integrated configuration will eliminate losses of exosomes occurring in sample transfer and allow for automated processing, with both devices both be operated and controlled by the same portable electrical instrument. The integrated device can likely be achieved by attaching an ion-exchange membrane and electrodes to disposable port fittings integrated downstream of the SAW lysis unit, without requiring new advances in microfluidic fabrication techniques. Membrane probes for several different target miRNAs could then be integrated on a single chip with measurements taken in series, so that multiple target miRNAs can be analysed without increasing the duration of the experiment, putting early diagnosis of pancreatic cancer within reach. Blood or other biological samples with greater debris content may be incorporated into the device after additional centrifugation steps or a filter incorporated into the device. Future work should also be conducted to more fully explore SAW lysis with an eye towards optimizing lysis rate as a function of SAW frequency, channel height, and other parameters. Although the current lysis rate is only 38%, significant improvement may be possible without increasing the residence time.

Acknowledgements

The authors wish to acknowledge Professor Jeffrey S. Schorey at the University of Notre Dame for permission to use his Nanosight LM10 and Professor Robert Stahelin at the Indiana University School of Medicine at South Bend for use of his Dynamic Light Scattering (DLS) equipment. In addition, the authors would like to thank Mayra Alejandra Duarte Ow for help in producing the figures. DT is supported by the Harper Cancer Research Institute and the Walther Cancer Foundation.

Notes and references

1 H. Brenner, *Lancet*, 2002, **360**, 1131–1135.
2 A. Osman, *Clin. Lab.*, 2012, **58**, 393–402.
3 A. Ventura and T. Jacks, *Cell*, 2009, **136**, 586–591.
4 W. Stoorvogel, *Blood*, 2012, **119**, 646–648.
5 R. A. Dragovic, C. Gardiner, A. S. Brooks, D. S. Tannetta, D. J. P. Ferguson, P. Hole, B. Carr, C. W. G. Redman, A. L. Harris, P. J. Dobson, P. Harrison and I. L. Sargent, *Nanomed.: Nanotechnol., Biol. Med.*, 2011, 7, 780–788.
6 J. Schageman, E. Zeringer, M. Li, T. Barta, K. Lea, J. Gu, S. Magdaleno, R. Setterquist and A. V. Vlassov, *BioMed Res. Int.*, 2013, **2013**, 253957.
7 A. V. Vlassov, S. Magdaleno, R. Setterquist and R. Conrad, *Biochim. Biophys. Acta, Gen. Subj.*, 2012, **1820**, 940–948.
8 X. Li and M. Donowitz, in *Exocytosis and Endocytosis*, ed. A. Ivanov, Humana Press, 2008, ch. 8, vol. 440, pp. 97–110.
9 B. J. Tauro, D. W. Greening, R. A. Mathias, H. Ji, S. Mathivanan, A. M. Scott and R. J. Simpson, *Methods*, 2012, **56**, 293–304.
10 C. Sser, M. Eldh and J. Tvall, *Isolation and Characterization of RNA-Containing Exosomes*, 2012, p. e3037.
11 G. Lami, M. R. Biagini and A. Galli, *World J. Gastroenterol.*, 2014, **6**, 272.
12 A. Garuti, I. Rocco, G. Cirmena, M. Chiaramondia, P. Baccini, M. Calabrese, C. Palermo, D. Friedman, G. Zoppoli and A. Ballestrero, *Gynecol. Oncol.*, 2014, **132**, 389–396.
13 D. Morgan, *Surface Acoustic Wave Filters, With Applications to Electronic Communications and Signal Processing*, Academic Press, Waltham, Massachusetts, 2nd edn, 2007.
14 B. A. Auld, *Acoustic Fields and Waves in Solids*, Krieger Publishing Company, Malabar, Florida, 1990.
15 J. Ho, M. K. Tan, D. B. Go, L. Y. Yeo, J. R. Friend and H.-C. Chang, *Anal. Chem.*, 2011, **83**, 3260–3266.
16 M. K. Tan, J. R. Friend and L. Y. Yeo, *Lab Chip*, 2007, 7, 618–625.
17 D. P. Morgan, *Int. J. High Speed Electron. Syst.*, 2000, **10**, 553–602.
18 W.-K. Tseng, J.-L. Lin, W.-C. Sung, S.-H. Chen and G.-B. Lee, *J. Micromech. Microeng.*, 2006, **16**, 539.
19 D. Taller, D. B. Go and H.-C. Chang, *Phys. Rev. Lett.*, 2012, **109**, 224301.
20 H. Li, J. Friend and L. Yeo, *Biomed. Microdevices*, 2007, **9**, 647–656.
21 P. R. Rogers, J. R. Friend and L. Y. Yeo, *Lab Chip*, 2010, **10**, 2979–2985.
22 S. R. Heron, R. Wilson, S. A. Shaffer, D. R. Goodlett and J. M. Cooper, *Anal. Chem.*, 2010, **82**, 3985–3989.
23 J. Reboud, Y. Bourquin, R. Wilson, G. S. Pall, M. Jiwaji, A. R. Pitt, A. Graham, A. P. Waters and J. M. Cooper, *Proc. Natl. Acad. Sci. U. S. A.*, 2012, **109**, 15162–15167.
24 T. J. Lyford, P. J. Millard and M. P. da Cunha, *Cell lysisa using surface acoustic wave devices for sensor applications*, 2012.
25 X. Ding, P. Li, S.-C. S. Lin, Z. S. Stratton, N. Nama, F. Guo, D. Slotcavage, X. Mao, J. Shi, F. Costanzo and T. J. Huang, *Lab Chip*, 2013, **13**, 3626–3649.
26 Y. Chen, X. Ding, S.-C. Steven Lin, S. Yang, P.-H. Huang, N. Nama, Y. Zhao, A. A. Nawaz, F. Guo and W. Wang, *ACS Nano*, 2013, **7**, 3306–3314.
27 F. Guo, P. Li, J. B. French, Z. Mao, H. Zhao, S. Li, N. Nama, J. R. Fick, S. J. Benkovic and T. J. Huang, *Proc. Natl. Acad. Sci. U. S. A.*, 2015, **112**, 43–48.
28 X. Ding, S.-C. S. Lin, B. Kiraly, H. Yue, S. Li, I.-K. Chiang, J. Shi, S. J. Benkovic and T. J. Huang, *Proc. Natl. Acad. Sci. U. S. A.*, 2012, **109**, 11105–11109.
29 A. de Gassart, C. Géminard, B. Février, G. Raposo and M. Vidal, *Blood*, 2003, **102**, 4336–4344.
30 I. Feliciello and G. Chinali, *Anal. Biochem.*, 1993, **212**, 394–401.
31 J. P. Banáth, A. Kim and P. L. Olive, *Radiat. Res.*, 2001, **155**, 564–571.
32 Z. Slouka, S. Senapati and H.-C. Chang, *Annu. Rev. Anal. Chem.*, 2013, 317–335.

33 Z. Slouka, S. Senapati, Y. Yan and H.-C. Chang, *Langmuir*, 2013, **29**, 8275–8283.
34 S. Senapati, Z. Slouka, S. S. Shah, S. K. Behura, Z. Shi, M. S. Stack, D. W. Severson and H.-C. Chang, *Biosens. Bioelectron.*, 2014, **60**, 92–100.
35 G. Yossifon, P. Mushenheim, Y.-C. Chang and H.-C. Chang, *Phys. Rev. E: Stat., Nonlinear, Soft Matter Phys.*, 2009, **79**, 046305.
36 I. Rubinstein and L. Shtilman, *J. Chem. Soc., Faraday Trans. 2*, 1979, **75**, 231–246.
37 A. Li, J. Yu, H. Kim, C. L. Wolfgang, M. I. Canto, R. H. Hruban and M. Goggins, *Clin. Cancer Res.*, 2013, **19**, 3600–3610.
38 C. S. Hartmann and B. P. Abbott, *Overview of design challenges for single phase unidirectional SAW filters*, 1989.
39 T. Kodama, H. Kawabata, H. Sato and Y. Yasuhara, *Electronics and Communications in Japan (Part II: Electronics)*, 1987, **70**, 32–44.
40 H. Nakamura, T. Yamada, T. Ishizaki and K. Nishimura, *IEEE Trans. Microwave Theory Tech.*, 2001, **49**, 761–768.
41 R. Shilton, M. K. Tan, L. Y. Yeo and J. R. Friend, *J. Appl. Phys.*, 2008, **104**, 014910.
42 A. Qi, L. Yeo, J. Friend and J. Ho, *Lab Chip*, 2010, **10**, 470–476.
43 V. Filipe, A. Hawe and W. Jiskoot, *Pharm. Res.*, 2010, **27**, 796–810.
44 A. Malloy, *Mater. Today*, 2011, **14**, 170–173.
45 L. Alvarez-Erviti, Y. Seow, H. Yin, C. Betts, S. Lakhal and M. J. Wood, *Nat. Biotechnol.*, 2011, **29**, 341–345.
46 A.-K. Ludwig and B. Giebel, *Int. J. Biochem. Cell Biol.*, 2012, **44**, 11–15.
47 P. P. Singh, V. L. Smith, P. C. Karakousis and J. S. Schorey, *J. Immunol.*, 2012, **189**, 777–785.
48 J. Caradec, G. Kharmate, E. Hosseini-Beheshti, H. Adomat, M. Gleave and E. Guns, *Clin. Biochem.*, 2014, **47**, 1286–1292.
49 C. Redman, D. Tannetta, R. Dragovic, C. Gardiner, J. Southcombe, G. Collett and I. Sargent, *Placenta*, 2012, **33**, S48–S54.
50 Y. Ouyang, J.-F. Mouillet, C. Coyne and Y. Sadovsky, *Placenta*, 2014, **35**, S69–S73.
51 M. Kesimer, M. Scull, B. Brighton, G. DeMaria, K. Burns, W. O'Neal, R. J. Pickles and J. K. Sheehan, *FASEB J.*, 2009, **23**, 1858–1868.
52 O. Jensen, J. Prause and H. Laursen, *Albrecht von Graefes Arch. Klin. Exp. Ophthalmol.*, 1981, **215**, 233–242.
53 C. Théry, S. Amigorena, G. Raposo and A. Clayton, *Current Protocols in Cell Biology*, 2006, pp. 3.22. 21–23.22. 29.
54 Y. Yuana, R. M. Bertina and S. Osanto, *Thromb. Haemostasis*, 2011, **105**, 396.
55 D. W. Inglis, R. Riehn, R. Austin and J. Sturm, *Appl. Phys. Lett.*, 2004, **85**, 5093–5095.
56 N. F. Owens, D. Gingell and P. R. Rutter, *J. Cell Sci.*, 1987, **87**, 667–675.
57 T. McPherson, A. Kidane, I. Szleifer and K. Park, *Langmuir*, 1998, **14**, 176–186.
58 D. D. Do, *Adsorption analysis*, World Scientific, 1998.
59 F. L. Slejko, *Adsorption technology. A step-by-step approach to process evaluation and application*, Dekker, New York, Basel, 1985.
60 H.-C. Chang and L. Y. Yeo, *Electrokinetically driven microfluidics and nanofluidics*, Cambridge University Press, Cambridge, UK, 2010.
61 A. Turchinovich, L. Weiz, A. Langheinz and B. Burwinkel, *Nucleic Acids Res.*, 2011, **39**(16), 7223–7233.
62 D. D. Taylor and C. Gercel-Taylor, *Gynecol. Oncol.*, 2008, **110**, 13–21.
63 W. W. Chen, L. Balaj, L. M. Liau, M. L. Samuels, S. K. Kotsopoulos, C. A. Maguire, L. LoGuidice, H. Soto, M. Garrett and L. D. Zhu, *Mol. Ther.–Nucleic Acids*, 2013, **2**, e109.
64 S. Keller, J. Ridinger, A.-K. Rupp, J. Janssen and P. Altevogt, *J. Transl. Med.*, 2011, **9**, 86.
65 H. Valadi, K. Ekström, A. Bossios, M. Sjöstrand, J. J. Lee and J. O. Lötvall, *Nat. Cell Biol.*, 2007, **9**, 654–659.
66 W.-X. Chen, Y.-Q. Cai, M.-M. Lv, L. Chen, S.-L. Zhong, T.-F. Ma, J.-H. Zhao and J.-H. Tang, *Tumor Biol.*, 2014, 1–11.

Biosensors and Bioelectronics 60 (2014) 92–100

Contents lists available at ScienceDirect

Biosensors and Bioelectronics

journal homepage: www.elsevier.com/locate/bios

An ion-exchange nanomembrane sensor for detection of nucleic acids using a surface charge inversion phenomenon

Satyajyoti Senapati [a,b], Zdenek Slouka [a], Sunny S. Shah [b], Susanta K. Behura [c], Zonggao Shi [d,e], M. Sharon Stack [b,d,e], David W. Severson [b,c], Hsueh-Chia Chang [a,b,e,*]

[a] Department of Chemical and Biomolecular Engineering, University of Notre Dame, Notre Dame, IN 46556, USA
[b] Advanced Diagnostics & Therapeutics, University of Notre Dame, Notre Dame, IN 46556, USA
[c] Department of Biological Sciences and Eck Institute for Global Health, University of Notre Dame, Notre Dame, IN 46556, USA
[d] Department of Chemistry and Biochemistry, University of Notre Dame, Notre Dame, IN 46556, USA
[e] Harper Cancer Research Institute, University of Notre Dame, Notre Dame, IN 46556, USA

ARTICLE INFO

Article history:
Received 21 January 2014
Received in revised form
1 April 2014
Accepted 2 April 2014
Available online 13 April 2014

Keywords:
Biosensing
DNA/RNA
Electrokinetics
Charge inversion
Nanoporous membrane

ABSTRACT

We present a novel low-cost biosensor for rapid, sensitive and selective detection of nucleic acids based on an ionic diode feature of an anion exchange nanoporous membrane under DC bias. The ionic diode feature is associated with external surface charge inversion on the positively charged anion exchange nanomembrane upon hybridization of negatively charged nucleic acid molecules to single-stranded oligoprobes functionalized on the membrane surface resulting in the formation of a cation selective monolayer. The resulting bipolar membrane causes a transition from electroconvection-controlled to water-splitting controlled ion conductance, with a large ion current signature that can be used to accurately quantify the hybridized nucleic acids. The platform is capable of distinguishing two base-pair mismatches in a 22-base pairing segment of microRNAs associated with oral cancer, as well as serotype-specific detection of dengue virus. We also show the sensor's capability to selectively capture target nucleic acids from a heterogeneous mixture. The limit of detection is 1 pM for short 27 base target molecules in a 15-min assay. Similar hybridization results are shown for short DNA molecules as well as RNAs from Brucella and *Escherichia coli*. The versatility and simplicity of this low-cost biosensor should enable point-of-care diagnostics in food, medical and environmental safety markets.

1. Introduction

DNA and RNA-based pathogen diagnostics remain as one of the most active fields of nucleic acid research (Gingeras et al., 2005; Wei et al., 2010). PCR amplification remains a gold standard in nucleic acid-based diagnosis, but it requires expensive labels and trained personnel – and is time consuming because of multiple steps involved. In recent years, there has been interest in developing probe-based non-optical sensors that can obviate the use of PCR and fluorophore labeling to improve the detection time and lower the cost of diagnostic tests. A large number of papers have been published on amplification-free nucleic acid biosensors employing different transduction sensing mechanisms (Drummond et al., 2003; O'Connor and Glynn, 2010; Palchetti and Mascini, 2008; Peng and Miller, 2011) of which label-free technologies are of special interest (Kataoka-Hamai and Miyahara, 2011; Ricci and Plaxco, 2008).

Nucleotides in DNA/RNA molecules are linked together through a sugar-phosphate backbone. The presence of the phosphate groups in this backbone renders both DNA and RNA molecules negatively charged making them suitable for manipulation (e.g. gel electrophoresis) as well as detection under electrical field. This intrinsic negative charge of DNA/RNA molecules can have a profound effect on both electronic and ionic conductivity of a system and has been explored to develop label-free nucleic acid sensors by measuring the electrical signal of the system. One such example is the field-effect-transistor (FET) that uses the electronic conductivity of the system for the detection of DNA molecules. In this system, the current passing between a source and a drain is controlled by the potential connected to a gate. This potential is sensitive to the negative charge of nucleic acid molecules present within the Debye length of the gate (Fritz et al., 2002). This changes the capacitance of the gate–electrolyte interface resulting in a change in the total current passing through the transistor (Kim et al., 2004; Pandana et al., 2008). Further, Li et al. (2004)

* Corresponding author at: 182 Fitzpatrick Hall, Notre Dame, IN 46556, USA. Tel.: +1 574 631 5697; fax: +1 574 631 8366.
E-mail address: hchang@nd.edu (H.-C. Chang).

http://dx.doi.org/10.1016/j.bios.2014.04.008
0956-5663/

demonstrated the detection of DNA by monitoring the change in conductivity of silicon nanowires.

Researchers have also demonstrated nucleic acid detection by directly monitoring the influence of DNA/RNA molecules on the ionic conductivity of nanochannels. These nanochannels are often single nanopores or an array of nanopores, where the charge and conductance of the nucleic acids within the nanochannels affects the intra-channel ion conductance. The immobilized DNA can render the nanochannel, or part of it, ion selective (Hou et al., 2013). Jagerszki et al. (2007) measured flux of easily traceable anionic dye in a nanochannel functionalized with neutral peptide nucleic acid (PNA) probe and its hybridization to target DNA. While the PNA probe did not hinder the flux of anionic dye, the hybridized target DNA molecules efficiently decreased the flux through the channel. Further, Ali et al. (2010) observed a significant change in current voltage characteristics (CVC) upon hybridization of target DNA to uncharged peptide nucleic acid probes functionalized to a conical nanopore. Wang and Smirnov (2009) employed an ion selective alumina nanochannel for the detection of DNA molecules and used the change in conductivity of nanochannel upon DNA hybridization as a detection signal. Other groups have demonstrated sensors involving biological nanopores where DNA hybridization causes opening or closing of the nanopore which can be tracked by measuring the ionic current going through the nanopore (Krishnamurthy et al., 2010a, 2010b; Steller et al., 2012). This switch mechanism can essentially be used to detect any biomolecules including proteins and nucleic acids (Lucas and Harding, 2000). A similar but simpler approach was presented by WeissWichert et al. (1997) where the binding of the target molecules blocked the entrance to the gramidicin pore resulting in diminished flux of ions.

Both FET and nanochannel sensors remain expensive to fabricate – and hence have not been commercialized for field-use diagnostics. Their small current (nA) and voltage (mV) signals also render both platforms sensitive to noise and contamination. While translocation time for single molecule through a nanochannel is short (ms), the total time to interrogate every molecule in the sample is still prohibitively long. Herein we report a novel, low cost and label-free biosensing platform for the detection of negatively charged nucleic acids using a positively-charged, heterogeneous anion exchange nanoporous membrane (Fig. 1A). The sensor is based on a charge inversion phenomenon (Slouka et al., 2013) that occurs on the surface of a positively charged nanomembrane (not within the nanopores of the membrane) when negatively charged nucleic acid molecules bind to its surface. It operates at a much higher voltage than the nanochannel sensors because ion conductance is controlled by the surface charge of the membrane surface and two unique non-equilibrium ion transport phenomena described later. Anion exchange membranes are known to exhibit interesting non-linear current–voltage characteristics (Fig. 1B – black curve) that arise due to the differences in fluxes of ions in the solution and the membrane. Small counter-ions (anions) are the main carriers of ionic current in the positively charged membrane (Fig. 1C), while large anions and cations do not contribute to this ionic current due to size exclusion and electrostatic repulsion effects respectively. At low voltages, the current increases linearly with voltage showing an Ohmic behavior which is also known as the underlimiting region on the CVC (Fig. 1B black curve). Nanochannel sensors operate in this low-voltage Ohmic region. With increasing voltage, the concentration of the electrolyte on one side of the nanomembrane decreases (depletion side) while the concentration of the electrolyte on the other side

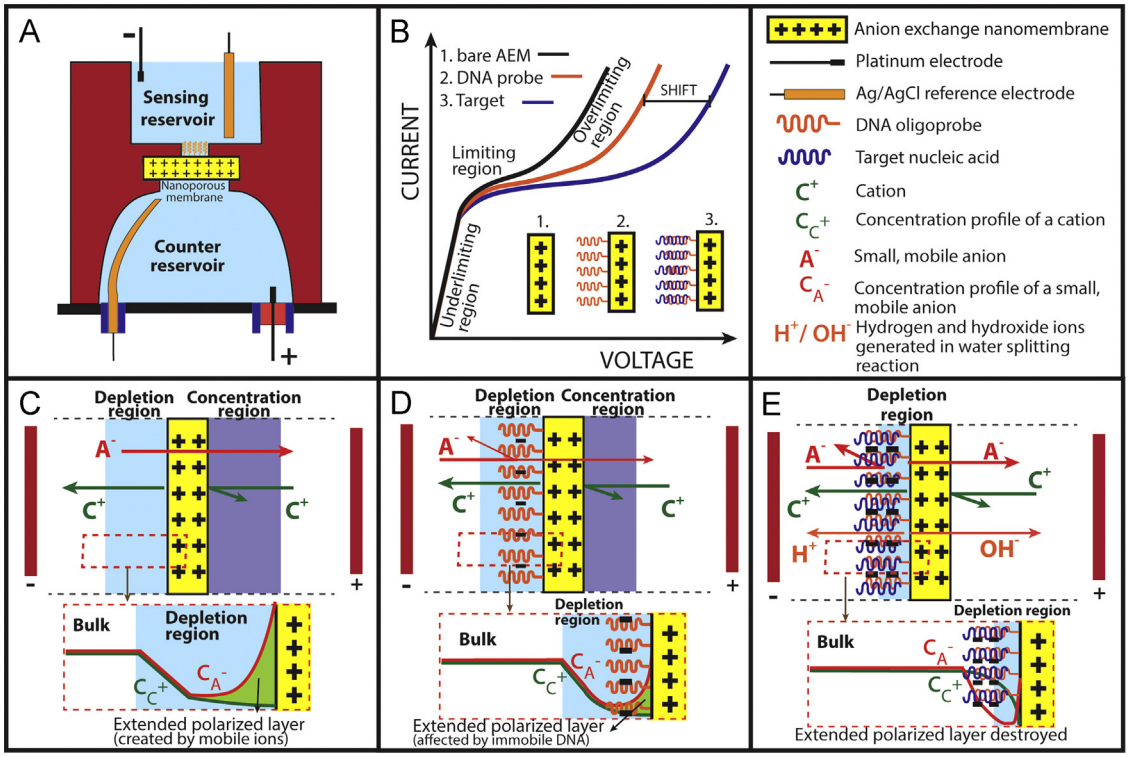

Fig. 1. Schematics and working principle of the nanomembrane sensor. (A) Diagrammatic representation of a nanomembrane electrokinetic sensor consisting of the top sensing reservoir and bottom counter reservoir bridged together by a positively charged nanomembrane. (B) Current–voltage characteristics (CVC) showing changes in Ohmic, limiting and overlimiting regions for bare anion-exchange membrane (black), membrane functionalized with oligoprobe (red) and hybridization of DNA/RNA with oligoprobe (blue). We utilize these changes in CVC for detection of nucleic acids. (C) Mechanism for the Ohmic relationship at low voltages known as the underlimiting regions. (D) Changes in CVC as a result of DNA adsorption on the membrane surface leading to changes in the limiting regions. (E) Mechanism for the overlimiting region at high DNA concentrations causing electroconvection and water splitting phenomenon. (For interpretation of the references to color in this figure legend, the reader is referred to the web version of this article.)

increases (concentration side). This establishes a concentration gradient, known as concentration polarization, across the membrane (Krol et al., 1999; Tanaka, 2004). The depletion side of the nanomembrane starts controlling the behavior of the system. At a certain current, the electrolyte concentration within the depletion region approaches zero, resulting in an increase in current resistance, which is reflected by a sudden decrease in the slope of the CVC. This region is denoted as the limiting region on the CVC (Fig. 1B – black curve). The system gradually develops a very large differential resistance causing the electrical current to almost saturate out. In an ideal case, further increase in the voltage would result in broadening of the depletion region far into the electrolyte. However, experimental results show that the current does not saturate completely but instead starts to increase abruptly giving rise to a region known as overlimiting region. The explanation for this behavior is quite complex (Belova et al., 2006) as it usually involves a mechanism that destroys the depletion region. Recently, we reviewed possible mechanisms involving the overlimiting current and experimentally demonstrated that the electroconvection phenomenon (Chang et al., 2012; Slouka et al., 2013; Yossifon et al., 2009) developed at the depletion side was the major contributing factor for the appearance of sudden increase in current in the overlimiting region (Fig. 1B – black curve). This electroconvection mechanism results from an action of a very strong electrical field developed in the depletion region on an extended polarized layer where an excess of anions creates a space charge (see inset of Fig. 1C for concentration profiles of anions and cations) (Chang et al., 2012; Rubinstein and Zaltzman, 2010). This extended polarized layer is only a few times larger than the Debye layer and is no more than 100 nm in thickness, even though the electroconvection microvortices can reach 100 μm in dimension. This suggests that the overlimiting current and to a lesser extent, the limiting current are both sensitive to surface charge changes on the membrane surface making it ideal for rapid surface assays, as the molecules do not need to enter the nanopores of the membrane. Its non-equilibrium features also endow them with large voltage/current signatures with correspondingly high dynamic range and noise insensitivity.

We recently demonstrated significant CVC changes when large, negatively charged molecules (e.g. DNA) are added to the surface of a positively charged membrane (Slouka et al., 2013). The size of these molecules prevents them from passing through the membrane (size exclusion); however they can easily adsorb to the membrane surface. The adsorption is facilitated by strong electrostatic interactions between positively charged membrane and negatively charged molecules. By running real time fluorescence imaging on membrane surface, we observed a gradual suppression of electroconvection of the system for DNA concentrations lower than 1 μM (for 29 nucleotide long DNA). This behavior is related to the effect of DNA on extended polarized layer, where the adsorbed, immobile DNA replaces small, mobile anions (Fig. 1D). The corresponding CVC of such a system is plotted in Fig. 1B (red curve) and is characterized with a shift of the overlimiting region to the right. At high DNA concentrations (over 1 μM) the layer of DNA becomes ion selective and creates a bipolar junction which at sufficiently large voltages splits water (Fig. 1E), a phenomenon observed in bipolar membranes (Cheng and Chang, 2011; Desharnais and Lewis, 2002). We note that the transition from electroconvection-controlled to water splitting-controlled regime is gradual and water splitting reaction was detected even for concentrations below 1 μM (Slouka et al., 2013).

Fig. 1B represents our strategy of using the behavior described above for detection of nucleic acids. Our strategy involves covalent immobilization of negatively charged DNA oligoprobes onto the membrane surface which results in a shift in the overlimiting region to the right (black to red curve in Fig. 1B). Upon hybridization with specific DNA/RNA target molecules, the amount of negative charge increases corresponding to a further shift in the overlimiting region as depicted by the blue curve in Fig. 1B. Such a change in the overlimiting region of CVC was used to record the signature of the hybridization event for the detection of short DNA molecules, microRNA molecules associated with oral cancer as well as RNA from dengue virus, Brucella bacteria and *Escherichia coli* (*E. coli*). The proposed sensor is novel because, for the first time, the signal from the surface charge change is significantly amplified with charge inversion and with the large "overlimiting currents" that arise from microvortices and water splitting phenomena that accompany the surface charge inversion. In terms of voltage signals, typical Field-Effect-Transistor sensors record up to 100 mV signals with surface charge changes compared to ~2 V shifts with our unique nanoporous membrane sensor. Additionally, novel mechanisms like water splitting reactions at the junction of a bipolar membrane (Cheng and Chang, 2011) and also vortices at the external boundary of a bipolar membrane (Senapati et al., 2011) are designed to enhance the signal. We demonstrate the unique performance of the sensor with high stability (8 days) and reproducibility, current limit of detection of 1 pM, selectively of 2 base pair mismatch as well as capability of identifying targets from a heterogeneous sample and a current time of detection of 20 min/sample. As the sensing principle is based on hybridization of negatively-charged nucleic acid molecules, the versatility of this platform makes it amenable for detection of other pathogenic targets in food, medical and environmental safety.

2. Experimental procedure

2.1. Reagents and chemicals

Commercially-available heterogeneous anion exchange nanomembrane composed of polystyrene–divinylbenzene fine particles with strong basic quaternary ammonium groups ($R\text{-}(CH_3)_3N^+$) supported by polyethylene as a binder and polyamide/polyester textile fiber was obtained from Mega a.s., Czech Republic (http://www.mega.cz/heterogenous-ion-exchange-membranes-ralex.html). The thickness of the membrane was ~450 μm when dry and ~700 μm after swelling in water with an exchange capacity of 1.8 mval/g and a pore size of around 1 nm. Two component silicon RTV system and Quick cast polyurethane resin were purchased from TAP Plastic Inc. (San Leandro, CA, USA). Phosphate Buffer Saline (PBS) 10× solution containing 1.37 M sodium chloride, 27 mM potassium chloride, 100 mM disodium hydrogen phosphate, and 18 mM potassium dihydrogen phosphate was purchased from Fisher Scientific (Waltham, MA, USA). 1-Ethyl-3-(3-dimethylaminopropyl)carbodiimide (EDC), benzophenone-3,3′,4,4′-tetracarboxylic acid, and sodium hydroxide were purchased from Sigma Aldrich (St. Louis, MO, USA). Maintenance media including supplements, fetal bovine serum, streptomycin, penicillin, TRIzol®, amine-coupled oligoprobes and complementary single stranded DNA targets were obtained from Life Technologies (Grand Island, NY, USA). RNeasy Mini Kit was obtained from Qiagen (Valencia, CA, USA).

2.2. Fabrication of biochip

A polyurethane-based microfluidic device with top and bottom reservoirs bridged together by an anion exchange nanomembrane was used as the sensing biochip. To fabricate the biochip, two separate silicone molds representing the two reservoirs were cast from a primary mold created using CAD designs and 3D printing. A circular anion exchange membrane was sandwiched between the two silicone molds creating the reservoirs. A two-component polyurethane resin (1:1 ratio) was poured inside the mold and allowed to cure for 30 min. Release of the silicone mold yielded

the polyurethane-based microfluidic biochip with an exposed membrane sensing area of either 3.5 or 1 mm^2 depending on the initial CAD designs. The biochip was then mounted onto a glass slide with inlet and outlet. The schematic of the biochip is depicted in Fig. 1A.

2.3. Attachment of oligoprobe on the sensing surface

The nanomembranes are made of divinylbenzene/polystyrene particles functionalized with quaternary ammonium groups that are embedded inside a polyethylene–polyamide/polyester matrix, where polyethylene acts as a binder and polyester/polyamide fibers provide mechanical stability. We used the inherent C–H bonds present on the membrane surface to covalently attach target specific oligoprobes using EDC chemistry (Sigal et al., 1996) and a carboxyl-terminated photo-crosslinker (Lin et al., 1988). First, COOH groups were created on the surface of the anion exchange nanomembrane by adsorbing 10 µl of photo-reactive benzophenone-3,3′,4,4′-tetracarboxylic acid (1 mg in 10 µl water at pH 6–7) and exposing it to UV light for 20 min. This allowed selective functionalization of carboxyl-benzophenone through radical polymerization to the C–H bonds on the membrane surface forming a carboxyl-terminated membrane surface. ElectroCure 500 UV Flood Curing Chamber with UV output of 30 mW/cm^2 at 356 nm wavelength was used to perform the photo-curing reaction (Electro-Lite Corp., Bethel, CT, USA). Next, the membrane was incubated with 0.4 M EDC in MES buffer for 30 min followed by an overnight incubation with 10 µM of the amine-coupled oligoprobe in 0.1 × PBS solution to covalently attach the probe to the sensing surface by amide linkage. The successful functionalization of the probe on the membrane surface was characterized using IR spectroscopy (Bruker FTIR) and by measuring the CVC of nanomembrane before and after functionalization.

2.4. Isolation of target RNA

Aedes albopictus C6/36 were grown in 75 cm^3 tissue culture flasks at 28 °C to ~80% confluency and infected with dengue serotype 2 (DENV-2 strain JAM1409) at a multiplicity of infection of 0.1. Maintenance media consisting of L-15 (Leibovitz) media supplemented with 10% tryptose phosphate broth and 2% FBS was added to the flasks after virus inoculation. Media was renewed 7 days post-infection. Cells were harvested day 14 post-infection by scraping them from the flask. To isolate the DENV-2 RNA, TRIzol® lysing solution was added to the infected cells, followed by spin column purification using the Qiagen RNeasy kit. For isolation of microRNA associated with oral cancer, oral squamous cell carcinoma cell line USCC-1 was engineered to overexpress miR-146a with viral vectors. The cells were cultured with MEM medium containing 10% fetal bovine serum, penicillin (100 U/ml) and streptomycin (100 µg/ml). Total RNA extraction was performed with TRIzol® reagent per instructions from the manufacturer. Purified Brucella RNA was obtained from the Purdue University and *E. coli* RNA was obtained from the Construction Engineering Research Laboratory at the US Army Engineer Research and Development Center.

2.5. Measurement of current–voltage characteristics

All electrical measurements were made using the Gamry 500 potentiostat in a four-electrode setup (Gamry Instruments, Warminster, PA, USA). Two reference Ag–AgCl electrodes were used for the measurement of the voltage across the membrane whereas two platinum electrodes were used to apply the current load. The reference electrodes were positioned close to the membrane surface in both reservoirs of the biochip, whereas the source electrodes were placed farther away to prevent any interference. Both reservoirs of the biochip were filled with 0.1 × PBS solution prior to the measurement of the CVC. Two sensing areas of 3.5 mm^2 and 1 mm^2 were used to study the characteristics of the sensor. The CVC was obtained by applying current load from 0 to 75 µA for 3.5 mm^2 sensing area and from 0 to 40 µA for sensing area of 1 mm^2 at the step rate of 1 µA/s and measuring voltage drop across the membrane. The sensing reservoir (side of the anion exchange membrane functionalized with the oligoprobe) was connected to the ground whereas a positive potential was applied in the other reservoir. This connection ensured the formation of the depletion region in the sensing reservoir, making it sensitive to functionalization of the probe as well as its hybridization with the target of interest. In a typical experiment, CVC was measured in 0.1 × PBS solution prior to functionalization of the oligoprobes on the sensing region. To confirm the functionalization, a second CVC was measured to observe changes in the signal. Finally, the DNA/RNA sample of interest was incubated for 15 min in the sensing reservoir to allow hybridization. Non-specifically bound DNA/RNA molecules on membrane surface were washed three times using 4 × PBS solution. A final CVC was measured after equilibrating the reservoirs in 0.1 × PBS solution. Any shift in CVCs in the overlimiting region before and after hybridization indicated the successful detection of the target nucleic acids. To confirm the observed CVC shift was indeed due to hybridization of target nucleic acid molecules, a basic pH 13 solution was used to dehybridize and re-generate the probe resulting in the shift of CVCs back to the probe level.

3. Results and discussions

Our sensor works on the principle that target nucleic acid molecules upon hybridization to molecular probes functionalized to the positively charged nanomembrane alter the ion conductance across the membrane–solution interface resulting in a significant shift in CVC in the overlimiting region (Fig. 1). As stated earlier, an increase in DNA concentration on the anion exchange nanomembrane has two major effects on the system in the overlimiting region as follows: (i) suppression of electroconvection and (ii) enhancement of water splitting reaction (Cheng and Chang, 2011; Slouka et al., 2013). The extent to which electroconvection is suppressed and water splitting enhanced is given by the total amount of DNA present on the membrane surface and the combined effect reflects the amount of shift in the overlimiting region of the CVC. Here, we demonstrate our ability to use this highly sensitive overlimiting region of the CVC for the specific detection of complementary DNA as well as RNA from dengue virus, Brucella bacteria and *E. coli* O157:H7, microRNA associated with oral cancer and heterogeneous nucleic acid samples. We also studied stability, reproducibility, selectivity, limit of detection and dynamic range of the nanomembrane sensor.

3.1. Sensor stability and reproducibility

To validate the sensor stability, a bare sensor with 1 mm^2 sensing area (data not shown for sensing area of 3.5 mm^2) was fabricated and CVC was measured on the same sensor for 8 days at room temperature. For each measurement, the sensor was rinsed and equilibrated with a 0.1 × PBS analyte solution and several CVC measurements were obtained on the same device to measure reproducibility ($n=5$). Fig. 2A shows no significant change in CVC after 8 days of measurement suggesting the sensor was very stable over time. We observed an average voltage of 3.25 V at 40 µA with a standard deviation of 0.06 V for the 20 measurements (five

measurements on each of the four day points) thus demonstrating the sensors stability. Additionally, to study the sensor reproducibility, we again fabricated three different bare chips (without any analyte) with similar sensor area (1 mm^2). As seen from Fig. 2B, all three biochips showed similar CVCs (average of 1.54 V at 40 μA with a standard deviation of 0.03 V), suggesting the nanomembrane sensor is reproducible for biochips with similar sensor area. This is a very unique characteristic of our sensor over electrochemical sensors. Electrochemical sensors have the advantage of signal amplification using redox reporters which is useful for enhancing the detection sensitivity but are often instable in detection signal (Bogomolova et al., 2009). In our case, sensing is based on transport of ions through the membrane and by keeping the source electrodes far away from the membrane surface we do not observe any electrochemical reactions on the sensor surface making the sensor highly stable and reproducible.

3.2. *Characterization of probe functionalization on membrane surface*

The functionalization of oligoprobe was first evaluated by measuring the CVC before and after probe attachment and determining the shift in voltage at 50 μA. We observed a significant shift (0.5 V) in the CVC after performing the functionalization process as compared to the CVC of the bare membrane confirming successful functionalization of probe onto the membrane surface (Fig. 3A). It should be noted that the CVC was measured after washing the membrane with high ionic strength solution (4 × PBS) to remove any non-covalently bound DNA oligos. The high salt buffer (4 ×) nullifies the electrostatic interaction between positively charge nanomembrane surface and negatively charge DNA molecules resulting in the removal of non-specifically adsorbed DNA molecules from the surface. We generally observed a shift of ~0.5 to 0.6 V after probe attachment on a sensing area of 1 mm^2 and a smaller shift (~0.2 V, data not shown) for larger sensing area (3.5 mm^2) since more oligoprobes are required to register the shift due to the charge inversion phenomenon described previously in Fig. 1. The functionalization of oligoprobe on membrane surface was also characterized by IR-spectroscopy. Fig. 3B shows the IR spectra of the oligoprobe in DI water and on a dry nanomembrane surface after functionalization. Upon hydration, DNA undergoes a structural transition (Pevsner and Diem, 2001) resulting in symmetric and antisymmetric stretching vibrations of the phosphate linkage shifts progressively towards lower wavenumber. As seen in Fig. 3B, the dry DNA probe-functionalized nanomembrane shows PO_2^- symmetric and antisymmetric stretching at 1092 cm^{-1} and 1236 cm^{-1} respectively while both the peaks shift for aqueous DNA sample and reaches at 1088 cm^{-1} and 1223 cm^{-1} respectively. Similarly, C–O stretching vibration of the phosphodiester observed at 1062 cm^{-1} is also affected by the presence of water molecules and shifts at 1054 cm^{-1} for the aqueous DNA solution. Further, the presence of the characteristic in-plane vibrations of C═O, C═C and C═N groups of the heterocyclic bases in the 1550–1750 cm^{-1} region clearly confirms the successful attachment of the oligoprobe onto the nanomembrane surface (Fig. 3B).

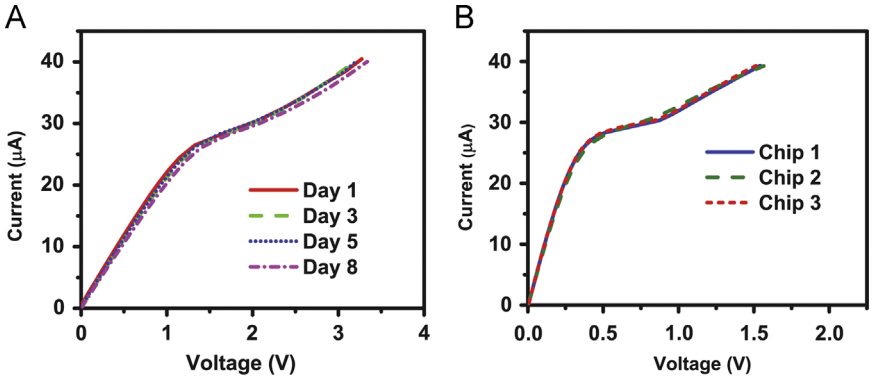

Fig. 2. Stability and reproducibility of the sensor. (A) A bare nanomembrane biosensing chip (1 mm^2) stable for 8 days at room temperature. (B) Three bare biochips with identical surface area (1 mm^2) showing reproducible curves.

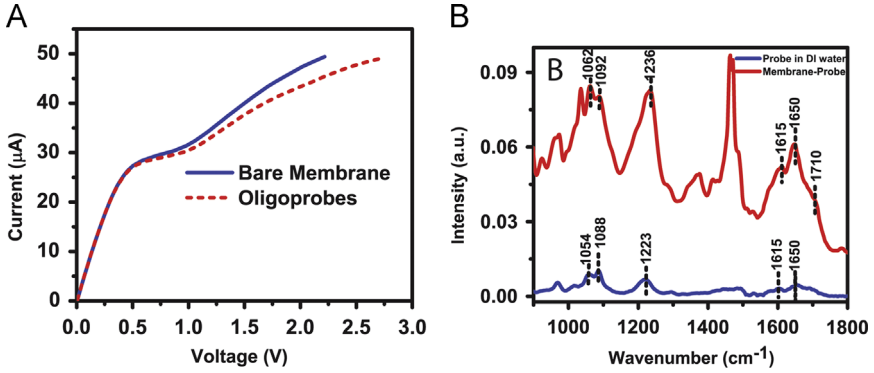

Fig. 3. Characterization of probe on membrane surface. (A) CVC depicting a significant shift in voltage upon functionalization of probe indicating covalent attachment of probe onto the nanomembrane surface. (B) IR spectra confirming the probe immobilization by comparing probe-specific peaks on the nanomembrane surface compared to a probe sample in DI water.

3.3. Detection of pathogenic nucleic acids using nanomembrane technology

To demonstrate proof-of-concept, the nanomembrane sensor was first validated using a 27-base DNA sequence complementary to the probe functionalized on the membrane surface (Fig. 4A). First, an oligoprobe was attached to the nanomembrane surface and CVC was measured and used as the baseline. The sensor was then exposed to 1 μM non-complementary probe sequence for 15 min; no significant shift from probe signal was observed. However, upon incubation of the same biochip with 1 μM complementary probe sequence for 15 min, the CVC showed a large shift of ~0.65 V, suggesting successful hybridization with the complementary probe sequence. To further confirm that the shift was due to hybridization, the biochip was treated with pH 13 solution to dehybridize and re-generate the probe. This resulted in the shifting of CVC back to the probe level. This clearly demonstrated the capability of the sensor to specifically detect short nucleic acid sequences. We would like to point out that since a larger sensing area (3.5 mm^2) was used for all the experiments in Fig. 4, a higher current load (0–75 μA) was applied for all biochip measurements. It should also be noted that changes in CVC for all experiments in Fig. 4 were conducted at 70 μA.

3.4. Specificity of the nanomembrane sensor

Another important criterion for the success of any sensor is the detection specificity and its capability to discriminate closely related sequences. We first demonstrated the capability of the platform to specifically distinguish between two of the four serotypes of RNA-based Dengue virus (DENV-2 and DENV-3). Dengue virus is a rapidly emerging global public health threat with an estimated 390 million people infected annually – three times more than the current estimate by WHO (Bhatt et al., 2013; Mangold and Reynolds, 2013). Early diagnosis of dengue therefore has significant clinical importance, and can help facilitate appropriate supportive therapies to reduce morbidity and mortality. Diagnostic sequences for serotype-specific oligonucleotides have been previously published (Seah et al., 1995a, 1995b; Shu and Huang, 2004) and were used for the experiments described here. First, the specific oligoprobe for DENV-2 was functionalized on membrane surface as described earlier. A CVC was recorded after functionalization and used as the baseline. A non-target complementary sequence corresponding to DENV-3 was incubated for 15 min, followed by a 4× PBS solution wash. A subsequent CVC was measured to observe any changes. A similar protocol was then used with the target RNA obtained from dengue serotype 2. As shown in Fig. 4B, a shift of ~0.6 V was observed in CVC for target RNA sample (DENV-2) incubated at a concentration of 50 pg/μl while no significant shift was observed for non-target sequence (DENV-3), suggesting the capability of the sensor for serotype-specific detection of dengue virus. To further confirm that the shift with DENV-2 RNA was indeed due to hybridization to the functionalized probe, a high pH wash was performed resulting in the regeneration of CVC back to the probe level confirming the specific detection of DENV-2 RNA (Fig. 4B).

We further tested the specificity of the nanomembrane-based sensor by using closely related microRNA sequences that differ by

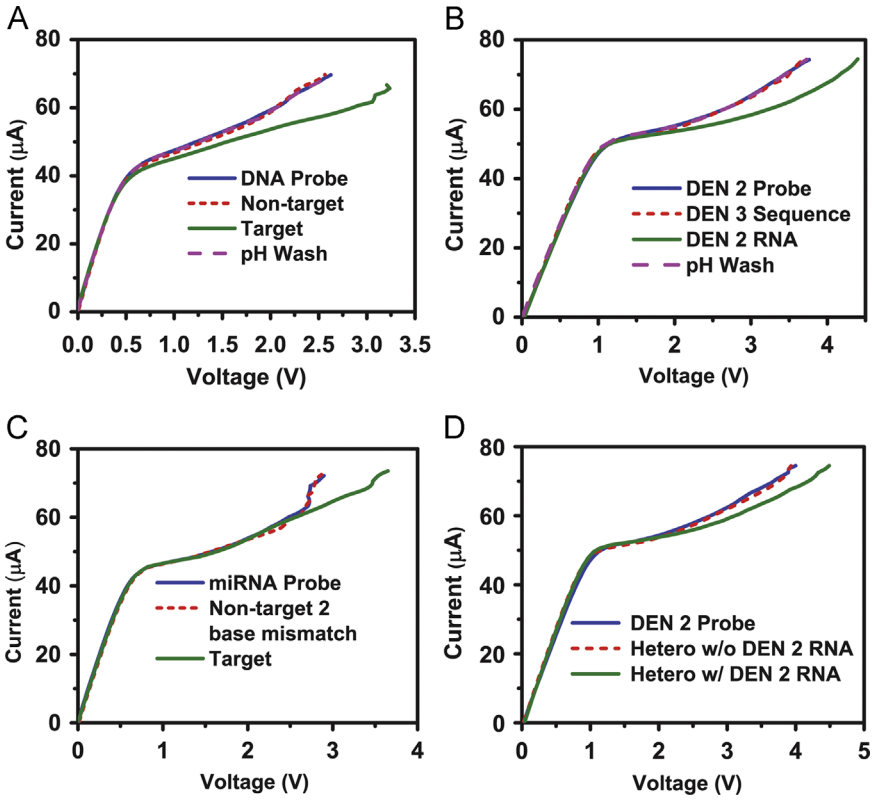

Fig. 4. Specificity of the nanomembrane sensor. (A) A proof-of-concept demonstration of nanomembrane sensor using 27 base DNA sequence complementary to the probe sequence attached on the nanomembrane surface. (B) Serotype-specific detection of dengue virus indicating the sensor's capability to specifically detect RNA from dengue serotype 2 when incubated with a sensor pre-functionalized with a DENV-2 oligoprobe. No shift was observed when the sensor was incubated with a sequence corresponding to DENV-3. In addition, high pH wash resulted in dehybridization of target and probe resulting in a regeneration of CVC corresponding to the probe level. (C) The specificity of the sensor was challenged by using a non-target sequence differing by only two base pairs compared to the target sequence. Change in CVC was only observed for the target microRNA sequence indicating the sensor's capability to distinguish two base pair mismatches. (D) The specificity of the sensor when exposed to a heterogeneous mixture of target sequence along with three non-target sequences. Again, a change in CVC was only observed when the target DENV-2 RNA was present in the heterogeneous sample but no shift was observed for heterogeneous sample without the target RNA.

only 2 bases (miR146a target sequence: UGAGAACUGAAUUCCAU**G**GG**U**U and miR146b non-target sequence: UGAGAACUGAAUUCCAU**A**GG**C**U). Changes in expression level of miR146a plays a significant role in oral cancer detection (Shi et al. 2012). As seen in Fig. 4C, no significant shift was observed for the two-base mismatch non-target sequence whereas a shift of ~0.7 V was observed when the target sequence (50 ng/μl) was incubated in the biochip. This clearly demonstrated our sensor's capability to successfully discriminate microRNA sequences with two base mismatch.

To further test the efficacy of the sensor, we designed an experiment mimicking a practical sample consisting of several nucleic acids. We wanted to test the ability of the nanomembrane sensor to capture and record the hybridization of target nucleic acids from a heterogeneous mixture. To test the selectivity of the sensor in a heterogeneous RNA mixture, we first modified a nanomembrane surface with DENV-2 probe. A lab-constructed heterogeneous sample consisting of equal proportions (10 pg/μl) of DENV-2 target RNA, oligo sequence corresponding to DENV-3, Brucella RNA and *E. coli* RNA was prepared. After incubating this heterogeneous sample in the biochip functionalized with DENV-2 probe, a shift in the CVC (0.45 V) was observed confirming the ability of the sensor to pick up the specific target RNA sequence from a heterogeneous mixture (Fig. 4D). Importantly, the same heterogeneous mixture without the DENV-2 RNA produced no significant shift in voltage showcasing the ability of our sensor to be specific even in the presence of three non-target sequences.

3.5. Limit of detection and dynamic range

In the experiments described earlier, a biochip with sensing area of 3.5 mm^2 was used and we observed a noticeable shift for rather large concentrations of the target molecules on the order of 10–100 nM for a 27 base DNA sequence. Since the sensing principle is dependent on the amount of negatively charged molecules on the membrane surface, we expect to see enhanced sensitivity simply by reducing the sensing area of the nanomembrane sensor. We fabricated biochips with a smaller sensing area of 1 mm^2 and performed a concentration study to see the effect of the sensing area on the limit of detection. We observed an improvement in the limit of detection of the nanomembrane biochip down to 1 pM (10^7 copies/100 μl) after reducing the sensing area from 3.5 mm^2 to 1 mm^2 (inset of Fig. 5A). This limit of detection is comparable to traditional electrochemical nucleic-acid based biosensors (Cagnin et al. 2009). However, it is not clearly understood why 3.5 times reduction in sensing area improves the limit of detection by 4–5 folds and is the subject of current investigation in our laboratory. We also observed a dependence of the voltage shift on the concentration of target molecules, which allows calibration of the nanomembrane sensor. 27 base target ssDNA solutions with concentrations of 1 pM, 100 pM, 10 nM and 1 μM were allowed to hybridize sequentially with the specific probe functionalized on membrane surface for 15 min and the appropriate CVCs were measured. Fig. 5A shows clear evidence that higher concentrations produce larger voltage shifts in the CVC evaluated at 40 μA. It should be noted that the same biochip was used to perform the limit of the detection study after dehybridizing and regenerating the probe using pH 13 solution. The experiment was repeated in triplicates which show the reproducibility of the membrane to consistently detect low concentrations of DNA. Thus we expect a further enhancement in the sensitivity (< pM) for even smaller sensing area as well as for longer RNA sequences (> 1000 bases long) as the detection is based on the amount of negative charge attaching to the membrane surface. Fig. 5B depicts the bar diagram showing changes in CVC from probe level with increasing DNA concentration clearly demonstrating the sensor's dynamic range of six orders of magnitude.

3.6. Versatility of the nanomembrane technology

The versatility of the nanomembrane-based sensor was then demonstrated to detect target nucleic acids of various pathogens provided a target-specific oligoprobe sequence was known. To further extend the scope of our sensor, we tested the sensor against RNA samples of Brucella and *E. coli* O157:H7. Foodborne diseases are one of the most common causes of mortality worldwide, and have significant economic consequences with financial losses accounting to billions of dollars to food industry (Myint et al., 2006; Scharff, 2012). Over the past decade, the noticeable increase in foodborne illnesses due to the bacterial contamination of foods have been reported with increasing illnesses resulting from consumption of fresh fruits and vegetables (Erickson et al., 2010; Heaton and Jones, 2008) and furthermore, there is continued threat of transmission of emerging pathogens including Brucella sp., and *E. coli* O157:H7 through food (Altekruse et al., 1998; Skovgaard, 2007). Similar to the experiment for dengue detection, previously-studied oligoprobes for Brucella were functionalized onto the membrane surface (Nelson et al., 2002; Wellinghausen et al., 2006). After confirming an improvement in sensitivity with smaller sensing area, experiments in Fig. 6 were carried out with a smaller surface area (1 mm^2) and hence the

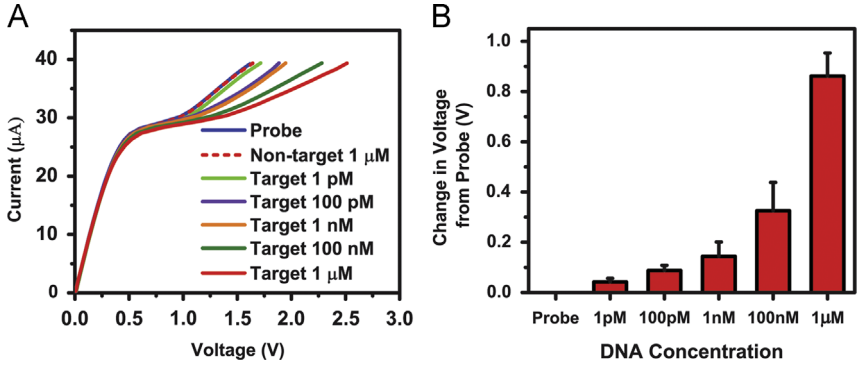

Fig. 5. Sensitivity of the nanomembrane sensor. (A) Changes observed in CVC with gradual increase in the voltage shift upon incubating the same probe-functionalized biochip with increasing DNA concentration (27-base long target). As the sensing principle is based on the charge inversion phenomenon, we observed that by decreasing the exposed sensing area, we were able to achieve sensitivity down to 1 pM concentration. Again, no change in CVC was observed for non-target sequence. (B) Bar diagram showing voltage shift from probe level with increasing DNA concentration ($N=3$ experiments).

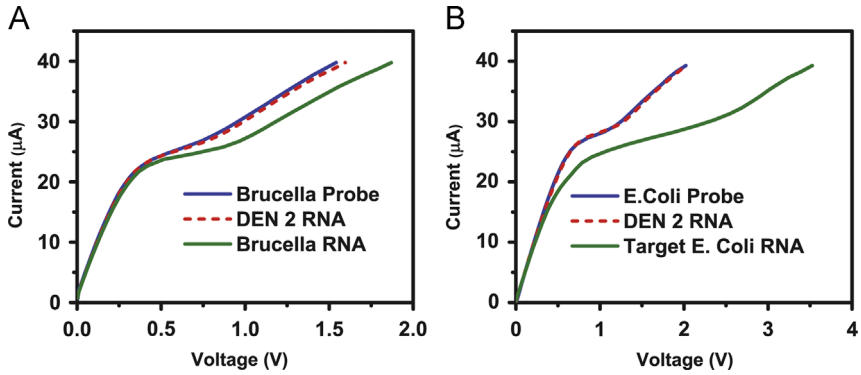

Fig. 6. Versatility of the nanomembrane sensor for detection of pathogenic nucleic acids. Specific shift in voltage observed in CVC upon incubation of a probe with specific target in case of (A) Brucella RNA and (B) *E. coli* RNA whereas no shift was observed for non-specific target (DENV-2 RNA in both cases).

current load applied ranged from 0 to 40 μA. As expected, target Brucella RNA (2 pg/μl) caused a significant shift in voltage (0.3 V) at 40 μA while non-target RNA (DENV-2 RNA in this case) resulted in no shift from the probe level confirming the sensor's ability to detect Brucella RNA (Fig. 6A). Fig. 6B shows similar results for detection of *E. coli* O157:H7. After functionalizing the probe (Sharma, 2006), a significant shift in CVC (~1.5 V) was only observed for 40 pg/μl target RNA whereas no shift was observed when the biochip was incubated with non-specific DENV-2 RNA. It should be noted that for all the detection experiments, identical incubation (15 min) and washing conditions (high ionic strength 4× PBS solution) were used.

4. Conclusions

We have successfully demonstrated a novel biosensor capable of rapid detection of nucleic acids (DNA/RNA) from any pathogen of interest, using the charge inversion phenomenon when negatively charged nucleic acids assemble on the surface of the positively charged membrane. Changes in current–voltage characteristics were used to identify and quantify targets that hybridize with specific complementary probes covalently functionalized on the membrane surface. In our platform, we observed large voltage and current signal changes suggesting better signal-to-noise ratio with more accurate quantification. We have shown that the nanomembrane sensor is stable, reproducible, and can specifically detect RNA of dengue virus, Brucella and *E. coli* as well as microRNA associated with oral cancer. The nanomembrane sensor is specific and able to distinguish two base mismatches in the target sequence as well as capable of capturing and recording the target sequence from a heterogeneous mixture. By reducing the sensing area, we demonstrated a limit of detection of 1 pM and a 6-order dynamic range. The versatility, specificity, sensitivity and its capability of rapid detection without prior amplification provide several future applications of this nanomembrane sensor in environmental, food and medical safety.

Acknowledgment

The authors would like to thank Ramesh Vemulapalli of the Purdue University for providing Brucella RNA. The authors would also like to thank Travis King and Stephen Grimme of the U.S. Army Engineer Research and Development Center for providing *E. coli* RNA samples. Finally, the authors would also like to thank the Center for Environmental Science and Technology at the University of Notre Dame for use of Bruker FT-IR instrument. This work has been supported by the Engineer Research and Development Center, U.S. Army Corps of Engineers W9132T, USDA 2012-67005-19589, and NSF-CBET 1065652 and the Walther Cancer Foundation Grant 0120.

References

Ali, M., Neumann, R., Ensinger, W., 2010. ACS Nano 4 (12), 7267–7274.
Altekruse, S.F., Swerdlow, D.L., Wells, S.J., 1998. Food Anim. Pract. 14 (1), 1–15.
Belova, E.I., Lopatkova, G.Y., Pismenskaya, N.D., Nikonenko, V.V., Larchet, C., Pourcelly, G., 2006. J. Phys. Chem. B 110 (27), 13458–13469.
Bhatt, S., Gething, P.W., Brady, O.J., Messina, J.P., Farlow, A.W., Moyes, C.L., Drake, J.M., Brownstein, J.S., Hoen, A.G., Sankoh, O., Myers, M.F., George, D.B., Jaenisch, T., Wint, G.R.W., Simmons, C.P., Scott, T.W., Farrar, J.J., Hay, S.I., 2013. Nature 496 (7446), 504–507.
Bogomolova, A., Komarova, E., Reber, K., Gerasimov, T., Yavuz, O., Bhatt, S., Aldissi, M., 2009. Anal. Chem. 81 (10), 3944–3949.
Cagnin, S., Caraballo, M., Guiducci, C., Martini, P., Ross, M., SantaAna, M., Danley, D., West, T., Lanfranchi, G., 2009. Sensors 9, 3122–3148.
Chang, H.C., Yossifon, G., Demekhin, E.A., 2012. Annu. Rev. Fluid Mech. 44, 401–426.
Cheng, L.J., Chang, H.C., 2011. Biomicrofluidics 5 (4), 046502–046508.
Desharnais, B.M., Lewis, B.A.G., 2002. Soil Sci. Soc. Am. J. 66 (5), 1518–1525.
Drummond, T.G., Hill, M.G., Barton, J.K., 2003. Nat. Biotechnol. 21 (10), 1192–1199.
Erickson, M.C., Webb, C.C., Diaz-Perez, J.C., Phatak, S.C., Silvoy, J.J., Davey, L., Payton, A.S., Liao, J., Ma, L., Doyle, M.P., 2010. J. Food Prot. 73 (6), 1023–1029.
Fritz, J., Cooper, E.B., Gaudet, S., Sorger, P.K., Manalis, S.R., 2002. Proc. Natl. Acad. Sci. USA 99 (22), 14142–14146.
Gingeras, T.R., Higuchi, R., Kricka, L.J., Lo, Y.M.D., Wittwer, C.T., 2005. Clin. Chem. 51 (3), 661–671.
Heaton, J.C., Jones, K., 2008. J. Appl. Microbiol. 104 (3), 613–626.
Hou, G., Peng, Z., Tian, Y., Zhang, H., Jiang, L., 2013. Chin. Sci. Bull. 58 (13), 1473–1482.
Jagerszki, G., Gyurcsanyi, R.E., Hofler, L., Pretsch, E., 2007. Nano Lett. 7 (6), 1609–1612.
Kataoka-Hamai, C., Miyahara, Y., 2011. IEEE Sens. J. 11 (12), 3153–3160.
Kim, D.S., Jeong, Y.T., Park, H.J., Shin, J.K., Choi, P., Lee, J.H., Lim, G., 2004. Biosens. Bioelectron. 20 (1), 69–74.
Krishnamurthy, V., Monfared, S.M., Cornell, B., 2010a. IEEE Trans. Nanotechnol. 9 (3), 303–312.
Krishnamurthy, V., Monfared, S.M., Cornell, B., 2010b. IEEE Trans. Nanotechnol. 9 (3), 313–321.
Krol, J.J., Wessling, M., Strathmann, H., 1999. J. Membr. Sci. 162 (1–2), 145–154.
Li, Z., Chen, Y., Li, X., Kamins, T.I., Nauka, K., Williams, R.S., 2004. Nano Lett. 4 (2), 245–247.
Lin, A.A., Sastri, V.R., Tesoro, G., Reiser, A., Eachus, R., 1988. Macromolecules 21 (4), 1165–1169.
Lucas, S.W., Harding, M.M., 2000. Anal. Biochem. 282 (1), 70–79.
Mangold, K.A., Reynolds, S.L., 2013. Pediatr. Emerg. Care 29 (5), 665–669.
Myint, M.S., Johnson, Y.J., Tablante, N.L., Heckert, R.A., 2006. Food Microbiol. 23 (6), 599–604.
Nelson, B.P., Liles, M.R., Frederick, K.B., Corn, R.M., Goodman, R.M., 2002. Environ. Microbiol. 4 (11), 735–743.
O'Connor, L., Glynn, B., 2010. Expert Rev. Med. Devices 7 (4), 529–539.
Palchetti, I., Mascini, M., 2008. Analyst 133 (7), 846–854.
Pandana, H., Aschenbach, K.H., Lenski, D.R., Fuhrer, M.S., Khan, J., Gomez, R.D., 2008. IEEE Sens. J. 8 (5-6), 655–660.
Peng, H.I., Miller, B.L., 2011. Analyst 136 (3), 436–447.
Pevsner, A., Diem, M., 2001. Appl. Spectrosc. 55 (11), 1502–1505.
Ricci, F., Plaxco, K.W., 2008. Microchim. Acta 163 (3–4), 149–155.
Rubinstein, I., Zaltzman, B., 2010. Adv. Colloid Interface Sci. 159 (2), 117–129.
Scharff, R.L., 2012. J. Food Prot. 75 (1), 123–131.
Seah, C.L., Chow, V.T., Chan, Y.C., 1995a. Clin. Diagn. Virol. 4 (2), 113–120.

Seah, C.L., Chow, V.T., Tan, H.C., Can, Y.C., 1995b. J. Virol. Methods 51 (2–3), 193–200.
Senapati, S., Basuray, S., Slouka, Z., Cheng, L.J., Chang, H.C., 2011. Top. Curr. Chem. 304, 153–170.
Sharma, V.K., 2006. Mol. Cell. Probes 20 (5), 298–306.
Shi, Z., Johnson, J.J., Stack, M.S., 2012. J. Oncol. 2012, 903581.
Shu, P.Y., Huang, J.H., 2004. Clin. Diagn. Lab. Immunol. 11 (4), 642–650.
Sigal, G.B., Bamdad, C., Barberis, A., Strominger, J., Whitesides, G.M., 1996. Anal. Chem. 68 (3), 490–497.
Skovgaard, N., 2007. Int. J. Food Microbiol. 120 (3), 217–224.
Slouka, Z., Senapati, S., Yan, Y., Chang, H.C., 2013. Langmuir 29 (26), 8275–8283.
Steller, L., Kreir, M., Salzer, R., 2012. Anal. Bioanal. Chem. 402 (1), 209–230.
Tanaka, Y., 2004. J. Membr. Sci. 244 (1–2), 1–16.
Wang, X., Smirnov, S., 2009. ACS Nano 3 (4), 1004–1010.
Wei, F., Lillehoj, P.B., Ho, C.M., 2010. Pediatr. Res. 67 (5), 458–468.
WeissWichert, C., Smetazko, M., ValinaSaba, M., Schalkhammer, T., 1997. J. Biomol. Screen. 2 (1), 11–18.
Wellinghausen, N., Nockler, K., Sigge, A., Bartel, M., Essig, A., Poppert, S., 2006. J. Clin. Microbiol. 44 (5), 1828–1830.
Yossifon, G., Mushenheim, P., Chang, Y.C., Chang, H.C., 2009. Phys. Rev. E 79 (4), 046305–046309.

Talanta 145 (2015) 35–42

Contents lists available at ScienceDirect

Talanta

journal homepage: www.elsevier.com/locate/talanta

Integrated, DC voltage-driven nucleic acid diagnostic platform for real sample analysis: Detection of oral cancer

Zdenek Slouka [a,b], Satyajyoti Senapati [a], Sunny Shah [a], Robin Lawler [a], Zonggao Shi [c], M. Sharon Stack [c], Hsueh-Chia Chang [a,*]

[a] Department of Chemical and Biomolecular Engineering, University of Notre Dame, Notre Dame, IN 46556, USA
[b] Department of Chemical Engineering, University of Chemistry and Technology, Technicka 3, Prague 6 16628, Czech Republic
[c] Department of Chemistry and Biochemistry and Harper Cancer Research Institute, University of Notre Dame, Notre Dame, IN 46556, USA

ARTICLE INFO

Article history:
Received 4 March 2015
Received in revised form
24 April 2015
Accepted 27 April 2015
Available online 6 May 2015

Keywords:
Point-of-care diagnostics
Ion exchange membranes
Oral cancer
Electrokinetics
Integrated platform technology
Sample-to-answer detection

ABSTRACT

We present an integrated and low-cost microfluidic platform capable of extraction of nucleic acids from real biological samples. We demonstrate the application of this platform in pathogen detection and cancer screening. The integrated platform consists of three units including a pretreatment unit for separation of nucleic acids from lysates, a preconcentration unit for concentration of isolated nucleic acids and a sensing unit localized at a designated position on the chip for specific detection of the target nucleic acid. The platform is based on various electrokinetic phenomena exhibited by ion exchange membranes in a DC electrical field that allow them to serve as molecular filters, analyte preconcentrators and sensors. In this manuscript, we describe each unit of the integrated chip separately and show specific detection of a microRNA (miRNA 146a) biomarker associated with oral cancer as a proof-of-concept experiment. This platform technology can easily be extended to other targets of interest by optimizing the properties of the ion exchange membranes and the specific probes functionalized onto the sensors.

1. Introduction

The development of an integrated microfluidic diagnostic platform has been of considerable interest in recent years as it enables molecular detection with miniature devices that are amenable to use in any setting without the need for extensive resources. Such settings may include the patient's bedside at a modern hospital, or a clinic in a low-resource setting. The device may be used by first responders investigating a biological event or a medic at a military base. Eventually, such an integrated platform can reduce the disease-associated morbidity and mortality rate, particularly for infectious or cancer-related diseases [1]. The lack of availability of good diagnostic tests significantly contributes to health problems in developing countries [2]. In low-resource settings, the diagnosis is often based on the physician's experience rather than results from laboratory tests. Thus an integrated platform capable of providing sample-to-answer solution in low-resource settings as well as in a timely fashion could significantly impact disease control and advance the benefits of treatment in the developing world [3,4].

Conventional and standard laboratory techniques for pathogen detection generally use the cell culture method, enzyme-linked immunosorbent assay (ELISA) or polymerase chain reaction (PCR). However, these tests cannot be employed in low-resource settings due to their long assay times, high costs per test and their need for trained personnel and infrastructure resources [5,6]. Compared to current laboratory-based detection techniques, fully automated push-button integrated devices would need to be rapid and low-cost with simple assay protocol to be useful in such settings [7].

In recent years, there have been significant efforts to develop sample-to-answer, low-cost, integrated microfluidic platforms capable of analyzing biological samples like oral rinse [8–10], nasal fluids [11], urine [12], serum [13], and whole blood [14–16]. The use of microfluidic architecture to develop point-of-care (POC) diagnostic devices brings some inherent advantages such as portability, short assay time, lower sample/reagent requirement, lower power consumption, disposability and automation. This significantly reduces the cost, time, complexity and contamination of assay without compromising the sensitivity and specificity of the test [5]. Researchers have developed different promising microfluidic technologies such as droplet-based devices [17,18], centrifugal devices [19,20], capillary devices [1,21], paper-based devices [5,6,22], and lateral flow assays [1,8,23,24] to realize such integrated diagnostic platforms. For instance, Sauer-Budge et al. used silica and polymeric monolith in the lateral flow assay strip to

* Corresponding author.
E-mail address: hchang@nd.edu (H.-C. Chang).

http://dx.doi.org/10.1016/j.talanta.2015.04.083
0039-9140/

detect different types of pathogens from fluid samples [23]. These microfluidic cassettes can perform cell lysis, mixing, target isolation, PCR, and detection of amplified products in the integrated chip [24]. Commercially-available diagnostic devices based on lateral flow include GenoType (Hain Lifescience GmbH) and INNO-LiPA (Innogenetics NV) [25]. Yang et al. used an affinity column and capillary electrophoresis channels in an integrated microdevice to detect multiple biomarkers from human blood serum [26]. Such systems used the solid phase extraction principle to capture the target on the microchip column functionalized with antibody and later elute the target for downstream analysis. Lee et al. developed a portable, fully-automated immunoassay platform to test for infectious disease from whole blood sample using centrifugal microfluidic compact disk technology [14,15]. However, most of these platforms employ a high level of integration and functionality to perform an assay. The use of a multilayer design, different types of materials, and a number of assembly steps for all these platforms renders their mass production expensive. Although some commercially available medical diagnostics products are FDA-approved (e.g. Focus Dx (Quest), Handy Lab (BD), i-Stat Corp (Abbott), IQuum, Idaho Technologies, and Cepheid GeneXpert), they are still not amenable to low-resource settings [1,4,27,28].

As an extension of the current effort, we report a simple, low-cost, label-free, PCR-free, integrated microfluidic biosensing platform capable of analyzing real samples using commercially available heterogeneous ion-selective nanoporous membranes. The integrated design has been conceived in a way to allow for easy automation and would only require the user for sample loading, thus fully exploiting the simplicity of our integrated platform. The device consists of three units: pretreatment, preconcentration and sensing. All units use ion-exchange membranes for various purposes: to isolate nucleic acids from the lysed cell sample (pretreatment unit), to concentrate the isolated nucleic acid molecules at a precise location (pre-concentration unit), and to specifically detect target nucleic acid biomarkers (sensing unit). The three units of the integrated platform utilize the inherent negative charge of the nucleic acid molecules and the ion-selective properties of cation- and anion-exchange membranes to transport, concentrate and detect target nucleic acid biomarkers in the integrated microfluidic platform, whereas electric field is used to extract the nucleic acid molecules from the sample through an agarose gel.

Recently, several sample pretreatment lab-on-a-chip techniques have been developed to process real biological samples including hydrodynamic, mechanical, acoustic, electric, magnetic bead, and ultrasonic approaches [4,25,28,29]. Some of these lysing methods require complicated metal electrode fabrication, expensive instrumentation and multistep protocols [29]. Here, we demonstrate an easy-to-integrate, on-chip sample pretreatment process to extract nucleic acids from real samples by integrating gel electrophoresis into our microfluidic platform. By applying a DC field, we separated and extracted the negatively-charged nucleic acid molecules from cell debris and other positively charged biomolecules like proteins below their isoelectric point, thus reducing contamination for downstream functionalities.

To accomplish rapid detection of target, we used the cation exchange membrane under DC field to create an electrokinetic filter, which does not create any hydrodynamic resistance, to concentrate the target molecules close to the sensor. We used the ion depletion feature of the membrane on one side to exclude all charged molecules, such that subsequent application of flow opposite to the depletion front concentrates all the molecules at a precise location in the microfluidic channel. This simple analyte concentration design reduces diffusion time to the sensor and allows for rapid target detection.

Several sensing technologies exist for molecular targets, such as colorimetric, fluorescence-based, and electrochemical detection [1,4,24]. However, colorimetric assay generally lacks the necessary detection limit. Optical detection methods provide excellent detection limit down to an impressive single-molecule level, but require costly and bulky optical systems. Several low-cost, label-free molecular sensing technologies like electrochemical sensors which amplify signals using redox reporters can enhance detection sensitivity, yet are hampered by instability of the electrochemical signal and calibration difficulties [30,31]. Capacitance, conductance and field-effect transistor (FET) electrode sensors are typically insensitive as the ionic strength within the electrical Debye layer is about 2–3 times higher than the bulk and the presence of the nucleic acid molecules would not significantly affect the change of local conductance. Additionally, the screening effect of the thin Debye layer would allow the detection of only the smallest charged molecules [32,33]. Importantly, they all require an expensive micro-fabricated electrode. The largest drawback of all electrode sensors is their long assay time due to diffusion-based transport of large nucleic acid molecules to the electrode surface [34]. Several techniques have been suggested to enhance the transport rate. One involves the activation of high voltage at the electrode sensor to electrophoretically attract nearby DNAs [35]. However, this electrophoretic concentration technique is non-specific and the elevated voltage can produce undesirable Faradaic reactions for high-ionic strength buffers resulting in false current or voltage signals. Further, all the existing nucleic acid detection technologies require purified samples, rendering them ineffective for field applications. Recently, we demonstrated the detection of target RNA molecules from different pathogens including dengue virus, brucellosis, and *Escherichia coli* using a commercially available anion exchange membrane [36–39]. The membrane sensor is highly stable over time and the sensor signal is reproducible [36]. This is due to the absence of any electron transfer reaction on the membrane surface, unlike the spurious side reactions in unstable electrochemical sensors [40]. We used the probe-functionalized anion exchange membrane sensor in this integrated platform for rapid and sensitive detection of target molecules. To successfully demonstrate the performance of our integrated platform, we have chosen oral cancer as our model target. Head and neck squamous cell carcinoma (HNSCC), which includes tumors of the oral cavity, larynx and oropharynx, is the 6th most prevalent cancer worldwide, representing a major global health problem, with $>400{,}000$ cases/year and $>200{,}000$ deaths annually [41,42]. Thus, development of an integrated platform to detect the upregulated cancer-relevant microRNA is highly desirable. In the future, a fully developed instrument along with the integrated platform described in this manuscript can be used in dental clinics for early diagnosis of oral cancer. As the integrated platform uses the inherent negative charge of the target nucleic acids, this platform can be used for detection of any target nucleic acid provided their sequences are known so that the complementary oligoprobes can be employed.

2. Materials and methods

2.1. Reagents and chemicals

Commercially-available heterogeneous anion and cation exchange nanomembranes were obtained from Mega a.s., Czech Republic (http://www.mega.cz/hetero genous-ion-exchange-membranes-ralex.html). A two-component silicon RTV system and Quick cast polyurethane resin were purchased from TAP Plastic Inc. (San Leandro, CA, USA). Phosphate Buffer Saline (PBS) $10\times$ solution containing 1.37 M sodium chloride, 27 mM potassium chloride,

100 mM disodium hydrogen phosphate, and 18 mM potassium dihydrogen phosphate was purchased from Fisher Scientific (Waltham, MA, USA). 1-Ethyl-3-(3-dimethylaminopropyl)carbodiimide (EDC), benzophenone-3,3,4,4-tetracarboxylic acid, and sodium hydroxide were purchased from Sigma Aldrich (St. Louis, MO, USA). TRIzol, fluorophore FAM and amine-coupled oligoprobes were obtained from Life Technologies (Grand Island, NY, USA). RNeasy Mini Kit was obtained from Qiagen (Valencia, CA, USA). The oral cancer cell line OSCC1 engineered to re-express miR-146a or housekeeping microRNAs were prepared as previously described [36] and obtained from Prof. Stack's laboratory at the Harper Cancer Research Institute, University of Notre Dame.

2.2. Attachment of oligoprobe on the sensing surface

The oligoprobe was covalently attached to the anion exchange nanomembrane as previously described [36,43]. Briefly, COOH groups were created on the surface of the anion exchange nanomembrane by adsorbing 10 µl of photoreactive benzophenone-3,3,4,4-tetracarboxylic acid (1 mg in 10 µl water at pH 6–7) and exposing it to UV light for 20 min. Next, the membrane was incubated with 0.4 M EDC in MES buffer for 30 min followed by an overnight incubation with 10 µM of the amine-coupled oligoprobe in 0.1x PBS solution to covalently attach the probe to the sensing surface.

2.3. Fabrication of integrated chip

The sample pretreatment, preconcentration and sensing units were integrated on to a single chip with dimensions of approximately 25 mmx75 mm. The schematic of the integrated chip with the three units is depicted in Fig. 1d and the actual microfluidic chip is shown in Fig. 1e.

The sample pretreatment unit was fabricated by gluing a plastic cuvette to a perforated tube using a UV curing Acrifix 192. The inner tube acts as a reservoir for target sample whereas cuvette acts as a buffer reservoir. Prior to placing the pretreatment unit into the main integrated platform, the interface between the sample reservoir and the main microfluidic channel is plugged with 2% agarose gel. A diagrammatic representation of the sample pretreatment unit is shown in Fig. 1a.

The preconcentration unit, shown in Fig. 1b, was made by placing two small strips of a cation exchange membrane at designated spots in a silicone mold and embedding in a UV curable Acrifix 192 glue capped with a small PMMA plate. The preconcentration unit was fixed to the main body of the integrated chip with UV curable glues Loctite 3492 and Acrifix 192.

We fabricated the sensor by embedding a small piece of anion exchange membrane in a two-component fast curing polyurethane resin (1:1 ratio) using a specific molding protocol. Release of the silicone mold yielded a polyurethane-based microfluidic biochip disk with an exposed sensing membrane. Later, a PMMA tube was glued to the biochip disk. This PMMA tube served for connecting electrodes needed to measure signals from the sensor. A depiction of the sensing unit is shown in Fig. 1c.

The main body of the integrated chip consisted of three layers of polycarbonate sheets structured by cutting on a plotter Graphtec 7000. The three structured polycarbonate sheets were aligned and thermally laminated together. The top polycarbonate sheet contained openings for the modular designs of the pretreatment and sensing units, the middle sheet for the main microfluidic channel and the bottom sheet cutouts for fixing the preconcentration unit. Tygon tubing as fluidic inlets and outlets and cut pipet tips as buffer reservoirs were glued into their designated places on the integrated chip.

In integrating the units on a single chip, we simplified the system by using one reservoir with a cation exchange membrane for both pretreatment and preconcentration and also placed the cation exchange membranes for preconcentration unit at the bottom of the channel. This allowed us to independently change the position of the sensing and preconcentration unit based on the preliminary experimental results and spatial requirements of each unit. On the other hand, the pretreatment and sensing units were designed in a modular fashion to allow easy replacements of these units in the integrated platform.

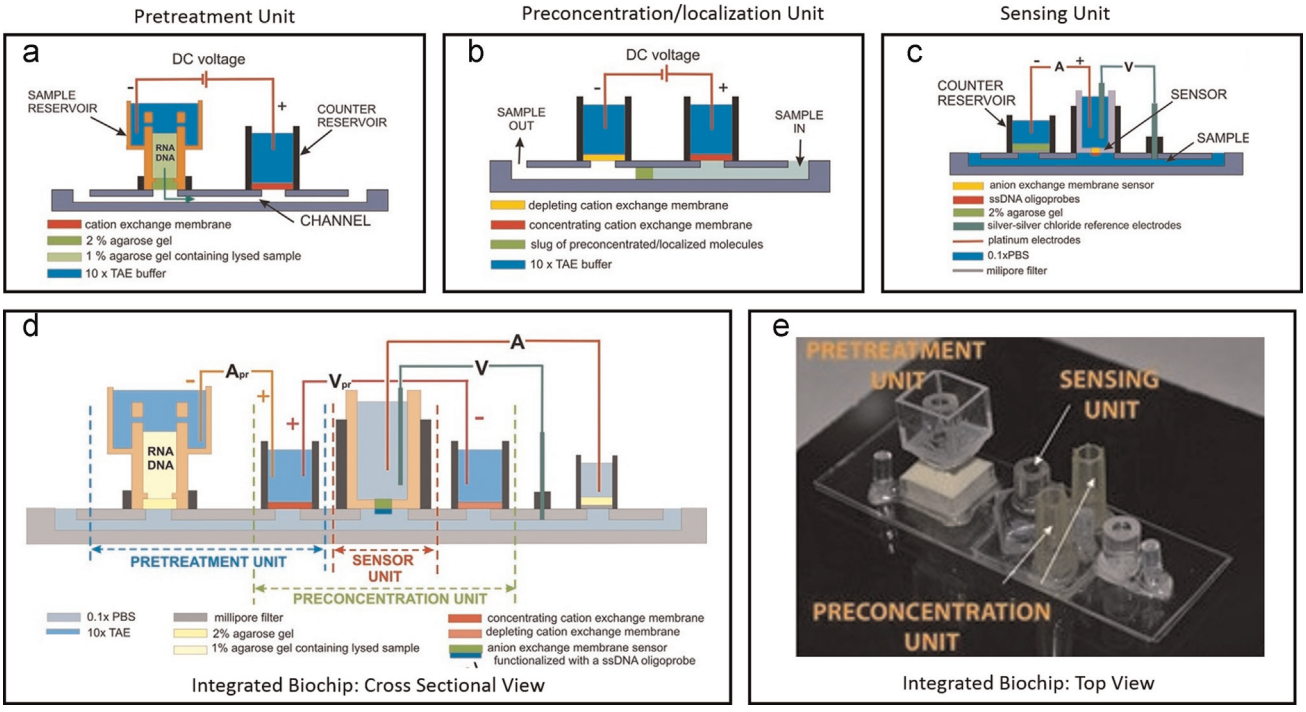

Fig. 1. Schematics of a (a) pretreatment unit, (b) preconcentration unit, (c) flow-through sensing unit, (d) integrated platform with all electrical connections. (e) Top view of an actual integrated device.

2.4. Electrical measurements

The Gamry 500 potentiostat (Gamry Instruments, Warminster, PA, USA) was used to perform the electrical measurement of the nanomembrane sensor in a four-electrode setup. Two reference Ag–AgCl electrodes were used for the measurement of the voltage across the membrane whereas two platinum electrodes were used to apply the current load. The current voltage characteristics (CVC) was obtained by applying current load from 0 to 40 μA at the step rate of 1 μA/s and measuring voltage drop across the membrane. The sensing reservoir (side of the anion exchange membrane functionalized with the oligoprobe) was connected to the ground, whereas a positive potential was applied in the other reservoir. In a typical experiment, a first CVC was measured for the oligoprobe functionalized sensor in a 0.1x PBS solution, which acted as the baseline signal. 10 μl of lysing buffer and 50 μl cancer cell lines were mixed with 50 μl of 1% agarose gel and transferred into the sample loading chamber on top of the 2% agarose gel. 10x TAE buffer (pH 7.4) was used as a sample loading buffer. A constant DC current (800 mV) was applied for 15 min that allowed all the negatively charged molecules including microRNA to move to the microfluidic channel. Extracted nucleic acids were concentrated by applying 150 V to the preconcentration unit. The location of the concentrated slug was adjusted to align with the location of the sensing unit by optimizing the electric DC field and flow rate. The concentrated nucleic acid slug was then incubated for 15 min to allow for hybridization of target molecules with the probes functionalized on the sensing surface. Non-specifically bound DNA/RNA molecules on membrane surface were washed three times using a high-salt 4x PBS solution. A final CVC was measured after equilibrating the reservoirs in 0.1x PBS solution. Any shift in CVCs in the overlimiting region before and after hybridization indicated the successful detection of the target nucleic acids.

3. Results and discussion

The work presented in this paper focuses on the fundamental aspects of developing a standalone platform that can process real biological samples, prepare them for further processing and finally perform specific detection of targeted nucleic acids. The concept of the integrated platform for detection of chosen nucleic acid biomarkers in complex samples has been built on the following requirements: (i) the platform must release the nucleic acid biomarkers from their intracellular environment and separate them from cell debris and other biomolecules that may interfere with the sensing; (ii) the platform must actively preconcentrate and localize the target molecules at the sensor to decrease the time associated with the transport of the molecules to the sensor and increase the limit of detection; and (iii) the platform must realize the actual sensing that is based on hybridization on the ssDNA oligoprobes complementary to the single-stranded targets. The platform is divided into three main functional units (pretreatment, preconcentration and sensing) which provide the three different functions described above. The entire platform is based on the use of commercially available heterogeneous ion exchange membranes. The heterogeneous ion exchange membranes are used for a number of different purposes, namely as molecular filters, molecular preconcentrators and even sensors. These membranes in conjunction with microfluidics and external DC voltage exhibit phenomena stemming from their unique property of ion selectivity that offer unprecedented possibilities in both control of the transport and manipulation of nucleic acids and their specific detection. The other important aspect of the platform is its ability to exploit the omnipresent negative charge of the nucleic acids. This negative charge is used to transport the nucleic acid in the DC electrical field and also to sense the presence of the target nucleic acids after hybridizing to the complementary probes attached on the sensor. In the next section we describe each unit of the platform in detail with the emphasis on the role of ion exchange membranes and eventually show the sensing of a miRNA target from oral cancer cells using the fully integrated platform.

3.1. Pretreatment unit

The operation of the pretreatment unit is based on chemical lysis of biological samples and allows separation of negatively charged nucleic acids while leaving behind large cellular debris, uncharged molecules and positively charged molecules. The separation is based on electrophoretic extraction from the lysate through an agarose gel layer and it significantly purifies the actual sample for downstream processing. The schematics of the pretreatment unit with its major components is depicted in Fig. 1a, and the actual chip in shown in Fig. 2a. The unit consists of three major fluidic components: (i) a sample reservoir for introduction of biological samples mixed with chemical lysis buffers, (ii) a counter reservoir with a cation exchange membrane and (iii) a fluidic channel connecting the two reservoirs. The process of electrophoretic separation of nucleic acids is based on the movement of the molecules towards the positively biased electrode through a layer of agarose gel. The agarose gel separates the sample reservoir from the main channel and thus prevents any convective mixing of the fluids in those spaces. Additionally, the gel blocks any molecules or cell debris larger than the pore size of the gel from entering the main channel. Typically, the pore size of 1% agarose gel used for our study was around 500 nm [44,45]. While all positively charged molecules will migrate towards the cathode (away from the microfluidic channel) and neutral molecules will remain in the sample reservoir this technique offers an easy way to purify and separate nucleic acids from other molecules

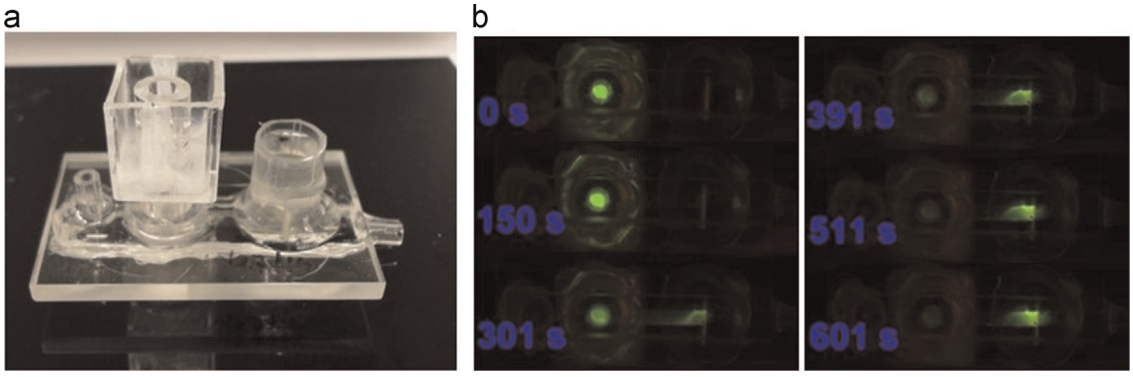

Fig. 2. (a) Picture of the actual pretreatment unit. (b) Separation of a fluorescently labeled ssDNA from an oral cancer cell lysate.

that can interfere with the sensing. The cation exchange membrane in the counter reservoir acts as a nucleic acid filter that prevents the nucleic acid from escaping the main channel and migrating to the positive electrode. This molecular filtering is given by synergistic effects of very strong electrostatic repulsion that occurs between the negatively charged cation exchange membrane and the negative nucleic acids and steric restrictions of the membrane nanopores that simply do not allow these relatively large molecules to penetrate. The separated nucleic acid molecules thus accumulate underneath the cation exchange membrane.

The processing starts with pipetting a thin layer of 2% agarose gel at the bottom of the sample reservoir. Next, the biological sample is lysed with a chemical agent and the lysate is mixed with a warm 2% agarose gel yielding lysate dispersed in the agarose gel at final concentration of 1%. This mixture is quickly pipetted on top of the 2% agarose layer and refrigerated for 5–10 min to solidify the gel. This combination of two gels creates a layer that is mechanically stable enough to withstand the DC electrical field applied during electrophoretic extraction. The reservoirs are then filled with 10x TAE buffer that keeps the pH in the electrode compartments constant. We apply a constant DC electrical current and limit the voltage imposed on the system thus preventing the system from overheating due to Joule heating. This electrophoretic separation is performed in approximately 15 min.

Fig. 2b shows our results from our separation experiment. In this case, the sample of lysed oral cancer cells was spiked with fluorescently labeled short ssDNA mimicking the real miRNA molecules in the sample so that we could observe the separation in real time. At the beginning of the experiment all the fluorescence comes from the sample reservoir. After applying the DC voltage, the fluorescently labeled ssDNA starts moving across the gel layer into the channel where it accumulates at the cation exchange membrane. The fluorescence in the sample reservoir slowly disappears over time whereas it increases at the membrane. The separation is completed in about 15 min and the extracted nucleic acid molecules are ready for further processing. Currently, we are performing studies aimed at analyzing the contents of the extracted nucleic acids using the basic tools of molecular biology.

3.2. Preconcentration/localization unit

The main use of this unit is to concentrate the previously extracted nucleic acid molecules and localize them at a specific location in the channel. The preconcentration unit is based on balancing electrophoretic and convective transport of separated molecules in order to localize and concentrate the nucleic acid molecules at the position of the sensor. While the cation exchange membrane in the pretreatment unit acts as a “mechanical” filter of nucleic acids (the molecules cannot penetrate the membrane), the cation exchange membranes in the preconcentration unit develop a condition in the channel that works as a non-mechanical ionic plug. This ionic plug, depending on the conditions applied, desalts the solution pumped through the channel. The ionic plug is based on the effect of concentration polarization that takes place around the cation exchange membrane when DC voltage is applied. This concentration polarization creates zones in the electrolyte adjacent to the membrane in which the concentration of ions is either lower or higher than that of the electrolyte bulk. These zones are called depletion and enrichment zones. In our unit, we use two cation exchange membranes that are placed on top of the microfluidic channel and separate the electrode compartments from the main channel as shown in Fig. 1b. When a DC voltage is applied on the system, the two membranes connected in series produce localized depletion and enrichment zones in the main channel simultaneously. The formation of the depletion and enrichment zones is reflected in the voltage drops that occur in different parts of the channel and thus in the local electrical field. Fig. 3a depicts experimental voltage profile established between the two membranes at the applied voltage of 100 V and the flow rate of 5 μl/min. The voltage profile clearly shows two regions with different voltage drops, a large one closer to the depleting membrane and a smaller one at the concentrating membrane. This is reflected in the electrical field profile (Fig. 3b) that was numerically calculated from the voltage profile. The electrical field is strongest under the depleting membrane and weakest under the concentrating membrane. The difference between the strongest and the weakest electrical field can be up to two orders of magnitude. The nonlinear profile of the electrical field results in a spatially dependent electrical force that acts upon charged molecules. In case of nucleic acids, this force acts against the direction of the electrical field (towards the positively biased electrode). By applying a convective flow through the channel, we can counterbalance the electrical force acting on the nucleic acids and localize them at a position along the channel where the resultant force on nucleic acids is essentially zero. By tuning the voltage and flow rate we can adjust the final position of the preconcentration slug. While we demonstrate that the flow rate and the voltage are major parameters affecting the position of the slug in the channel, other electrokinetic phenomena, like vortex instabilities, can also contribute to the overall behavior of the system.

Fig. 4a shows dynamics of the development of the preconcentration slug. In this case fluorescently labeled ssDNA diluted in 0.01x PBS is pumped through the channel while a voltage of 150 V is applied simultaneously. The preconcentration slug develops immediately after starting the experiment, settling into its final position which does not change in time. However, the fluorescent intensity of the slug increases over time as more and more nucleic acid molecules accumulate at the region.

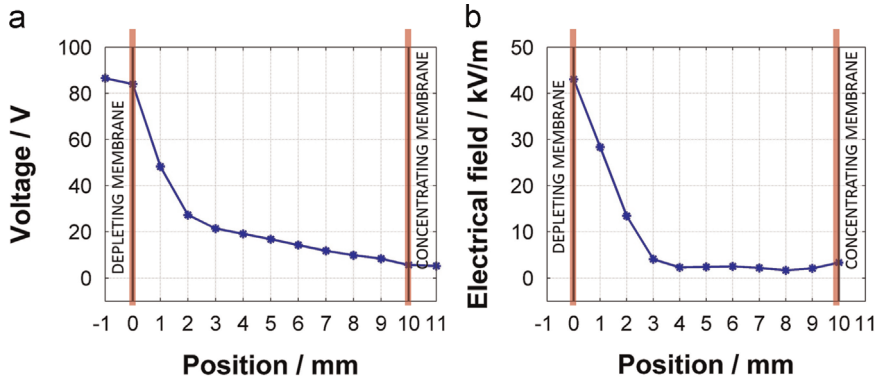

Fig. 3. (a) Experimentally obtained voltage profile that develops between the depleting and concentrating membrane at the applied voltage of 100 V and the flow rate of 5 μl/min and (b) the corresponding electric field profile (absolute values) numerically calculated from the voltage profile.

We studied the effect of the voltage and the flow rate on the position of the preconcentration slug. The results are depicted in Fig. 4b in which a set of images shows the fluorescence of the preconcentration slug obtained under different conditions in experiments that were run for 10 min. Each row shows the position of the slug at constant voltage but varying flow rate and each column at constant flow rate and varying voltage. The set of images clearly shows the effect of both parameters. While increasing voltage pushes the slug further away from the depleting membrane, the increasing flow rate acts in the opposite direction. Fig. 4c shows the positions of the preconcentration slugs that have been evaluated as a distance of the front edge of the slug from the depleting membrane in the center of the channel. The trend of all curves confirms our hypotheses that the flow rate and electric field influence the location of the concentrated slug. This study also revealed the limits of the parameters. In case of low voltages and large flow rates, the electrical field is not strong enough to keep the molecules in the intermembrane region of the channel and the molecules are convected out of the channel (see Fig. 4c for 50 V and flow rate of 5 and 7.5 µl/min).

3.3. Sensing unit

The sensing of nucleic acids using an anion exchange membrane is based on a phenomenon denoted as surface charge inversion as described earlier [35–39]. The anion exchange membrane is comprised of molecules that bear a fixed positive charge at a very high concentration. This fixed charge affects the transport of ions through the membrane that in turn gives rise to peculiar phenomena such as concentration polarization, electroconvection and water splitting. These behaviors are reflected in the non-linear current voltage characteristics of the membrane. When an oppositely charged, large poly-ion (e.g. DNA and RNA) is added on the appropriate side of the membrane, the polyanions tend to adsorb on the membrane by strong electrostatic charge–charge interactions. This process creates a thin layer of immobile opposite charge on the membrane that is reflected in the measurement of current voltage characteristics as a characteristic shift. By functionalizing the membrane with specific ssDNA oligoprobes complementary to the detected targets, the original nonspecific signal coming from any adsorbed polyanions is turned into specific detection of target nucleic acids hybridized on the complementary probes. The specific detection requires use of optimized washing buffers to remove all non-specifically bound molecules. The chip consists of a single channel, a counter reservoir, the actual sensor

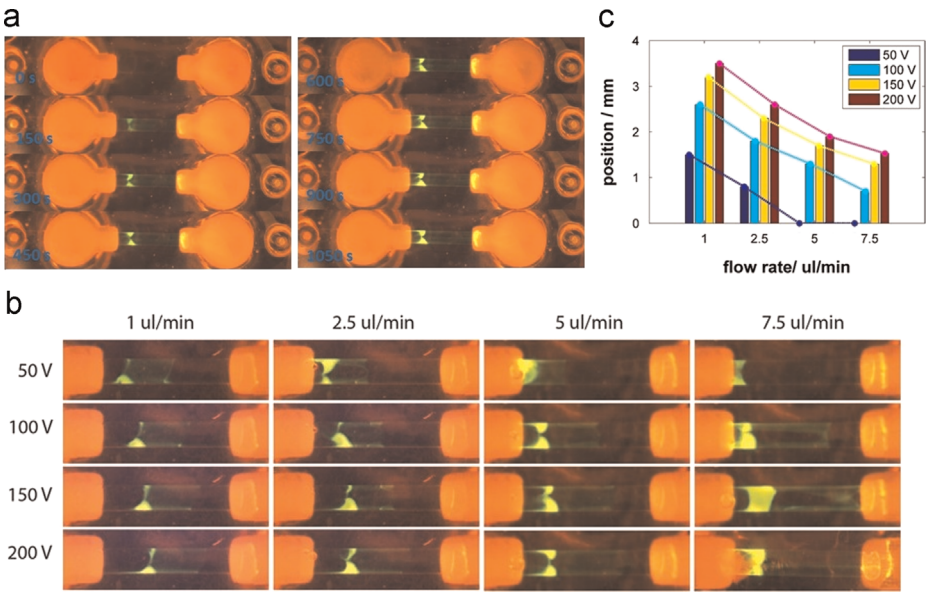

Fig. 4. (a) Dynamics of the preconcentration of a fluorescently labeled ssDNA, (b) experimental study showing the effect of the voltage and the flow rate on the position of the preconcentration slug and (c) graph showing the positions of the preconcentration slug related to the flow rate and voltage applied.

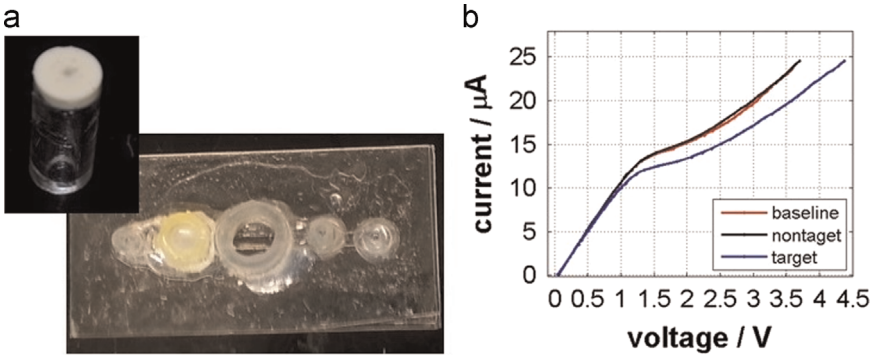

Fig. 5. (a) Picture of an actual flow-through sensing unit and (b) representative experiment showing specific detection of a DNA with a sequence corresponding to miRNA 146a as shown by the shift in the I-V curve.

and a fitting for inserting a reference electrode (Fig. 5a). As described earlier, the sensor is made by embedding a small piece of anion exchange membrane into a polyurethane resin and attaching it to a short piece of a plexiglass tubing. First, the probe is functionalized to the sensor as described earlier. The measurement of the current voltage characteristics is done in a four electrode setup. Two platinum source electrodes connect a given DC electrical signal to the membrane (A in Fig. 1c) and two silver-silver chloride electrodes measure the voltage response of the system (V in Fig. 1c). Fig. 5b shows a representative result of a specific detection obtained in our flow-through sensor, in this case the target is ssDNA sequence corresponding to miRNA 146a. An artificial ssDNA non-specific sequence was used as a negative control. The red curve in the figure represents the signal of the ssDNA oligoprobe covalently linked to the membrane. The black curve represents the signal of the non-target which clearly indicates the sensors specificity, as no shift was detected. Unlike the non-target, the signal for the target represented by the blue curve in Fig. 5b provided a significant deviation from the baseline. The signal can be quantified by evaluating the voltage shift between the baseline and the signal for the target that occurs at the highest current applied to the system. For the results presented in Fig. 5b this shift is approximately 0.8 V (measured at 25 μA). This demonstrates our ability to selectively detect short single-stranded nucleic acids using changes in current–voltage characteristics. Changes in voltage shift can be used to not only gather information about the selectivity of the sensor but also the sensitivity of the sensor by measuring the amount of shift. An extensive study on the selectivity and sensitivity of the sensing unit was demonstrated previously by our group [36].

3.4. Integrated platform

Fig. 6 shows some of the results obtained with the integrated chip. Because the platform aims to perform detection in a PCR-free manner, this limits the use of the platform for single stranded nucleic acids, e.g. microRNA, rRNA and ssDNA (in some viruses). MicroRNAs are a convenient target since they are short (20–24 nucleotides long) and are more stable than mRNAs. At the same time, miRNA profiles are being considered as novel biomarkers carrying a diagnostic value, e.g. for cancer. Here we present our results for detection of miRNA 146a in samples containing oral cancer cells OSCC1 in 30 min. The protocol for all experiments was as follows. Roughly 500,000 cancer cells of OSSC1 cell line were chemically lysed and the lysate was embedded into a 1% agarose gel in the pretreatment unit that was previously capped with a 2% agarose gel plug. This pretreatment unit and a freshly functionalized sensor were inserted in the appropriate fittings on the integrated chip and the chip was filled with 0.1x PBS and 10x TAE in appropriate reservoirs. All tubing and electrode connections were then established. The baseline corresponding to the probe functionalized on the membrane is measured. Then 800 mA are applied on the pretreatment unit (A_{pr} in Fig. 1d) and this current is connected for 15 min to separate targeted miRNA from the lysate. The target is then allowed to hybridize with the probes functionalized on the sensor for 5 min. The channel is then washed with 4x PBS buffer to remove nonspecifically bound molecules from the membrane and the channel is again filled with 0.1x PBS to equilibrate the sensor. The current–voltage curve was measured again and compared to the baseline.

Fig. 6a shows the results for a system where a bare membrane without probe (negative control) was used as a sensor. As expected, no change in CVC was observed after performing the experiment thus clearly indicating no detection of target. This result implies that the nonspecific binding on the membrane can be removed with our washing protocol and that the membrane itself in not affected by the preceding processes done on the chip. Fig. 6b shows the results for a system where the membrane creating the sensor was functionalized with carboxyl groups used for attachment of the ssDNA oligoprobe but no probe was attached. Similar to Fig. 6a, when the target molecules were flowed through this setup followed by a washing step, no signal was detected indicating sensor selectivity. The results in Fig. 6c show the detection of the actual target. We used solution of ssDNA complementary to the probe functionalized on the membrane as a target and a short ssDNA non-complementary as a negative control both at a concentration of 1 μM. In this case, the negative control experiment was run first. The CVCs in this graph show that the sensor specifically detected the target DNA sequence (shift of 0.7 V obtained at 30 μA) while no shift was observed when non-target was run through the system. Finally, the plot in Fig. 6d shows the results for actual cell samples from the oral cancer cell line. We used the parental oral cancer cell line as a negative control and a genetically modified line that overexpresses miRNA 146a as a positive control. Again the experiments with the parental cell line were performed first and we did not detect any signal as demonstrated by no shift in voltage. However, the derived oral cancer cell line overexpressing the microRNA of interest provided a signal amounting to about 0.5 V at 30 μA thus showcasing our ability to selectively extract and detect microRNA biomarkers using our integrated platform. Successful discrimination of two oral cancer cell lines based on the presence of miRNA 146a provides a proof-of-concept data for further development of the detection platform.

4. Conclusion

We have successfully developed an integrated, sample-to-answer diagnostic platform for rapid detection of microRNA biomarkers from cancer cell lines in approximately 30 min. We used

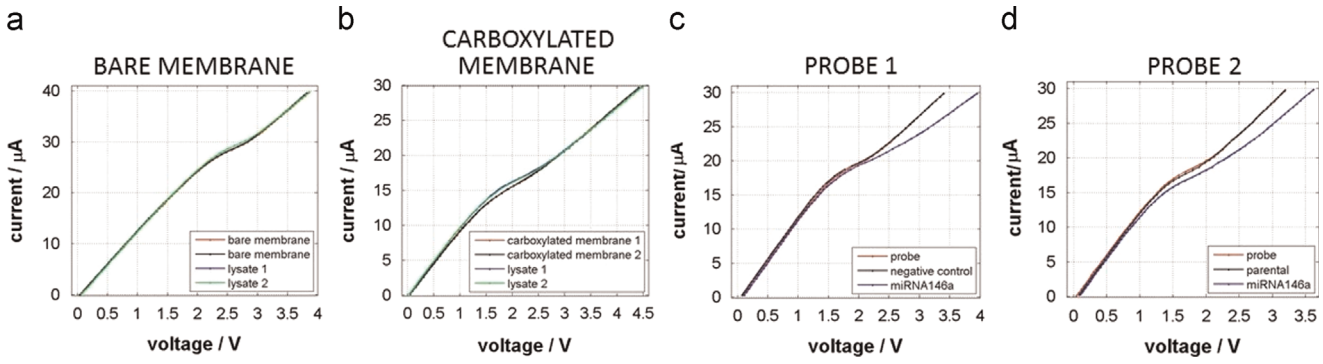

Fig. 6. (a) Control experiment performed with a sensor that was not functionalized with a probe, (b) control experiment performed with a sensor that was carboxylated but not functionalized with a probe, (c) specific detection of ssDNA from clean samples, and (d) detection of miRNA 146a from oral cancer cell lysate.

low cost polymeric materials to design a disposable integrated chip that can be easily manufactured. The integrated platform consisted of three units: a pretreatment unit to isolate nucleic acids from lysed cell sample, a preconcentration unit to concentrate the isolated nucleic acid molecules at a precise location where the sensing unit is placed to detect target nucleic acids. The ion-selective properties of the cation- and anion-exchange membranes and the negative charge of the nucleic acids were used to manipulate, concentrate and detect target nucleic acid biomarkers. The sample pretreatment is designed based on the principle of gel electrophoresis where an electric field is used to extract the nucleic acid molecules from the sample chamber through an agarose gel. The sensing is based on the charge inversion phenomenon when negatively charged target nucleic acids hybridize with oligoprobes attached on the surface of the positively charged membrane. Changes in current–voltage characteristics are used to selectively identify targets microRNA 146a biomarkers. As the sensor uses the inherent negative charge for detection, this platform can be used to detect any pathogen nucleic acids not only in medical diagnostics but also in food and environmental diagnostics provided probes of interest are known. This low-cost, integrated platform has the potential to reach low resource settings and conduct testing at the location of an outbreak, at dental clinics or at the point-of-care application thus significantly improving safety and reducing disease outbreaks.

Acknowledgment

This work has been supported by the Walther Cancer Foundation Grant 0120, NIH 1R21AI105361-01A1, USDA 2012-67005-19589, NSF-CBET 1065652 and NIH RO1CA085870 (M.S.S).

References

[1] P. Yager, G.J. Domingo, J. Gerdes, Annu. Rev. Biomed. Eng. 10 (2008) 107–144.
[2] G. Jones, R.W. Steketee, R.E. Black, Z.A. Bhutta, S.S. Morris, Lancet 362 (2003) 65–71.
[3] L. Bissonnette, M.G. Bergeron, Clin. Microbiol. Infect. 16 (2010) 1044–1053.
[4] W. Su, X. Gao, L. Jiang, J. Qin, J. Chromatogr. A 1377 (2015) 13–26.
[5] J. Hu, S. Wang, L. Wang, F. Li, P.M. Belinda, T.J. Lu, F. Xu, Biosens. Bioelectron. 54 (2014) 585–597.
[6] A.W. Martinez, S.T. Phillips, G.M. Whitesides, E. Carrilho, Anal. Chem. 82 (2010) 3–10.
[7] R.W. Hart, M.G. Mauk, C. Liu, X. Qiu, J.A. Thompson, D. Chen, D. Malamud, W.R. Abrams, H.H. Bau, Oral Dis. 17 (2011) 745–752.
[8] D. Chen, M. Mauk, X. Qiu, C. Liu, J. Kim, S. Ramprasad, S. Ongagna, W. R. Abrams, D. Malamud, P.L. Corstjens, Biomed. Microdevices 12 (2010) 705–719.
[9] B.S. Ferguson, S.F. Buchsbaum, T.-T. Wu, K. Hsieh, Y. Xiao, R. Sun, H.T. Soh, J. Am. Chem. Soc. 133 (2011) 9129–9135.
[10] L. Paul, Lab Chip 9 (2009) 768–776.
[11] C.J. Easley, J.M. Karlinsey, J.M. Bienvenue, L.A. Legendre, M.G. Roper, S.H. Feldman, M.A. Hughes, E.L. Hewlett, T.J. Merkel, J.P. Ferrance, Proc. Natl. Acad. Sci. USA 103 (2006) 19272–19277.
[12] G.V. Kaigala, R.J. Huskins, J. Preiksaitis, X.L. Pang, L.M. Pilarski, C.J. Backhouse, Electrophoresis 27 (2006) 3753–3763.
[13] Y.-F. Lee, K.-Y. Lien, H.-Y. Lei, G.-B. Lee, Biosens. Bioelectron. 25 (2009) 745–752.
[14] B.S. Lee, Y.U. Lee, H.-S. Kim, T.-H. Kim, J. Park, J.-G. Lee, J. Kim, H. Kim, W.G. Lee, Y.-K. Cho, Lab Chip 11 (2011) 70–78.
[15] H. Jiang, X. Weng, D. Li, Microfluid. Nanofluid. 10 (2011) 941–964.
[16] L. Lafleur, D. Stevens, K. McKenzie, S. Ramachandran, P. Spicar-Mihalic, M. Singhal, A. Arjyal, J. Osborn, P. Kauffman, P. Yager, Lab Chip 12 (2012) 1119–1127.
[17] M.T. Guo, A. Rotem, J.A. Heyman, D.A. Weitz, Lab Chip 12 (2012) 2146–2155.
[18] D.K. Harshman, R. Reyes, T.S. Park, D.J. You, J.-Y. Song, J.-Y. Yoon, Biosens. Bioelectron. 53 (2014) 167–174.
[19] Y.-K. Cho, J.-G. Lee, J.-M. Park, B.-S. Lee, Y. Lee, C. Ko, Lab Chip 7 (2007) 565–573.
[20] S. Lutz, P. Weber, M. Focke, B. Faltin, J. Hoffmann, C. Muller, D. Mark, G. Roth, P. Munday, N. Armes, Lab Chip 10 (2010) 887–893.
[21] L. Gervais, E. Delamarche, Lab Chip 9 (2009) 3330–3337.
[22] T.S. Park, W. Li, K.E. McCracken, J.-Y. Yoon, Lab Chip 13 (2013) 4832–4840.
[23] A.F. Sauer-Budge, P. Mirer, A. Chatterjee, C.M. Klapperich, D. Chargina, A. Sharon, Lab Chip 9 (2009) 2803–2810.
[24] D. Mark, S. Haeberle, G. Roth, F.V. Stetten, R. Zengerle, Chem. Soc. Rev. 39 (2010) 1153–1182.
[25] C.D. Chin, S.Y. Chin, T. Laksanasopin, S.K. Sia, Low-Cost Microdevices for Point-of-Care Testing, in: D. Issadore, R.M. Westervelt (Eds.), Point-of-Care Diagnostics on a Chip, Biol. Med. Phys. Biomed., Springer-Verlag, Berlin Heidelberg, 2013, pp. 3–12.
[26] W. Yang, M. Yu, X. Sun, A.T. Woolley, Lab Chip 10 (2010) 2527–2533.
[27] D.J. You, K.J. Geshell, J.-Y. Yoon, Biosens. Bioelectron. 28 (2011) 399–406.
[28] C.D. Chin, V. Linder, S.K. Sia, Lab Chip 12 (2012) 2118–2134.
[29] J.-H. Wang, C.-H. Wang, G.-B. Lee, Ann. Biomed. Eng 40 (2012) 1367–1383.
[30] E. Bakker, Y. Qin, Anal. Chem. 78 (2006) 3965–3984.
[31] Y. Umezawa, H. Aoki, Anal. Chem. 76 (2004) 321–326.
[32] E. Stern, R. Wagner, F.J. Sigworth, R. Breaker, T.M. Fahmy, M.A. Reed, Nano Lett. 7 (2007) 3405–3409.
[33] I.I. Suni, TrAC Trend Anal. Chem. 27 (2008) 604–611.
[34] A.E. Nkodo, J.M. Garnier, B. Tinland, H. Ren, C. Desruisseaux, L.C. McCormick, G. Drouin, G.W. Slater, Electrophoresis 22 (2001) 2424–2432.
[35] R. Sosnowski, E. Tu, W.F. Butler, J.P. O'Conell, M.J. Heller, Proc. Natl. Acad. Sci. USA 94 (1997) 1119–1123.
[36] S. Senapati, Z. Slouka, S. Shah, S. Behura, S. Stack, D. Severson, H.-C. Chang, Biosens. Bioelectron. 60 (2014) 92–100.
[37] Z. Slouka, S. Senapati, H.-C. Chang, Ann. Rev. Anal. Chem. 7 (2014) 317–335.
[38] Z. Slouka, S. Senapati, Y. Yan, H.-C. Chang, Langmuir 29 (2013) 8275–8283.
[39] S. Senapati, S. Basuray, Z. Slouka, L.J. Cheng, H.-C. Chang, Top. Curr. Chem. 304 (2011) 153–169.
[40] A. Bogomolova, E. Komarova, K. Reber, T. Gerasimov, O. Yavuz, S. Bhatt, M. Aldissi, Anal. Chem. 81 (2009) 3944–3949.
[41] D.L. Miller, M.D. Puricelli, M.S. Stack, Biochem. J. 443 (2012) 339–353.
[42] U. Duvvuri, J.N. Myers, Curr. Probl. Surg. 46 (2009) 114–117.
[43] C. Berens, P.J. Courtoy, E. Sonveaux, Bioconjug. Chem. 10 (1999) 56–61.
[44] N. Pernodet, M. Maaloum, B. Tinland, Electrophoresis 18 (1997) 55–58.
[45] J. Narayanan, J.-Y. Xiong, X.-Y. Liu, J. Phys, Conf. Ser. 28 (2006) 83–86.

Biosensors and Bioelectronics 86 (2016) 840–848

Contents lists available at ScienceDirect

Biosensors and Bioelectronics

journal homepage: www.elsevier.com/locate/bios

Induced nanoparticle aggregation for short nucleic acid quantification by depletion isotachophoresis

Steven Marczak, Satyajyoti Senapati, Zdenek Slouka [1], Hsueh-Chia Chang *

Department of Chemical and Biomolecular Engineering, University of Notre Dame, 182 Fitzpatrick Hall, Notre Dame Avenue, Notre Dame, IN, 46556 United States

ARTICLE INFO

Article history:
Received 10 March 2016
Received in revised form
31 May 2016
Accepted 26 July 2016
Available online 27 July 2016

Keywords:
Ion-selective membrane
Isotachophoresis
Nanoparticle aggregation
Nucleic acid

ABSTRACT

A rapid (<20 min) gel-membrane biochip platform for the detection and quantification of short nucleic acids is presented based on a sandwich assay with probe-functionalized gold nanoparticles and their separation into concentrated bands by depletion-generated gel isotachophoresis. The platform sequentially exploits the enrichment and depletion phenomena of an ion-selective cation-exchange membrane created under an applied electric field. Enrichment is used to concentrate the nanoparticles and targets at a localized position at the gel-membrane interface for rapid hybridization. The depletion generates an isotachophoretic zone without the need for different conductivity buffers, and is used to separate linked nanoparticles from isolated ones in the gel medium and then by field-enhanced aggregation of only the linked particles at the depletion front. The selective field-induced aggregation of the linked nanoparticles during the subsequent depletion step produces two lateral-flow like bands within 1 cm for easy visualization and quantification as the aggregates have negligible electrophoretic mobility in the gel and the isolated nanoparticles are isotachophoretically packed against the migrating depletion front. The detection limit for 69-base single-stranded DNA targets is 10 pM (about 10 million copies for our sample volume) with high selectivity against nontargets and a three decade linear range for quantification. The selectivity and signal intensity are maintained in heterogeneous mixtures where the nontargets outnumber the targets 10,000 to 1. The selective field-induced aggregation of DNA-linked nanoparticles at the ion depletion front is attributed to their trailing position at the isotachophoretic front with a large field gradient.

1. Introduction

Recently, genomic diagnosis and prognosis liquid biopsies involving detection of fragmented circulating tumor DNA (ctDNA) and messenger RNA (mRNA) as well as quantification of microRNA (miRNA) expression levels have been proposed for numerous diseases, disorders, and cancers (Calin and Croce, 2006; Lujambio and Lowe, 2012; Vogelstein et al., 2013). These are short nucleic acids with the shortest being single-stranded miRNA which are typically 19–26 nucleotides in length. Current genomic biopsy detection and quantification techniques are microarray and PCR based. Other than sample cost and reliance on lab-bound equipment and trained personnel, both techniques suffer from long assay times due to diffusion to the surface bound probes for the microarrays and extensive pretreatment to eliminate inhibitors in PCR. Thus, there has been a continuous search for new, simple, rapid quantification methods for low-resource settings that do not require extensive pretreatment (Slouka et al., 2014). More importantly, variations in amplification efficiency and nontarget interference significantly compromise the quantification accuracy of PCR and microarray techniques, respectively. A highly selective PCR-free technique, similar to the lateral flow immunoassay but with quantification capability, would be the ideal platform.

Plasmonic nanoparticles, first reported for use as selective DNA sensors by Elghanian et al. (1997), are an essential feature in most lateral flow devices which traditionally detect proteins (Parolo et al., 2013; Fang et al., 2011; Hampl et al., 2001) but increasingly focus on nucleic acids (Mao et al., 2009; He et al., 2011; Chua et al., 2011; Rohrman et al., 2012; Gao et al., 2014; Hou et al., 2012; Hu et al., 2013). Their attractiveness lies in their simplicity, yet their

* Corresponding author.
E-mail addresses: smarczak@nd.edu (S. Marczak), satyajyoti.senapati.1@nd.edu (S. Senapati), sloukaz@vscht.cz (Z. Slouka), hchang@nd.edu (H.-C. Chang).
[1] Present Address: Department of Chemical Engineering, University of Chemistry and Technology, Technicka 3, Prague 6 16628, Czech Republic.

http://dx.doi.org/10.1016/j.bios.2016.07.093
0956-5663/

primary drawbacks include low sensitivities and poor limits of detection. Several strategies attempting to overcome these limitations are use of upconverting nanoparticles (Hampl et al., 2001; Corstjens et al., 2003), amplification by enzymatic reaction (Parolo et al., 2013), or isotachophoretic concentration (Moghadam et al., 2015). However, because the immobilized probes are often insufficiently selective (de Avila et al., 2013) and the isolation of targets based on mobility differences is inadequate, lateral flow assays, which tend to be only semi quantitative, are nearly always limited to detection of a single target at high concentration and lack mechanisms to improve specificity such as shear by hydrodynamic flow or by electric fields.

In contrast, gel electrophoresis is a very common procedure for separating and detecting multiple analytes and is routinely used in the lab to identify PCR products (Traver et al., 2014) and other nucleic acid samples quantitatively through Northern blotting. Gel separations of probe-functionalized nanoparticles, though, have been confined mostly to slab gel electrophoresis wherein various groups purified polydisperse nanoparticle mixtures based on their characteristic size, shape, charge, and functional molecules (Xu et al., 2007; Hanauer et al., 2007; Wu et al., 2013; Hlavacek et al., 2014; Kim et al., 2013). Capillary electrophoresis was also used for separating nanoparticles (Liu and Wei, 2004; Liu et al., 2005; Liu, 2009) but for purposes of characterization rather than detection. Notably lacking from previous research are techniques which take advantage of nanoparticles' size and shape properties to separate and detect small molecules with similar sizes such as short DNAs and RNAs. Although gel electrophoresis lacks the capacity to separate different sequences with identical numbers of base pairs, these sequences can be separated based on the physical and chemical properties of the nanoparticles themselves. In principle, isotachophoresis with two electrolytes of different ionic strength can also achieve nanoparticle concentration and isolation in a gel medium or in a capillary, and there are a few groups who worked on such applications (Pyell et al., 2009; Hlavacek and Skladal, 2012; Praus et al., 2015) but without realizing any diagnostic application.

Towards this goal of nanoparticle assisted separations in gel, which can also be used for isolating the miRNA, mRNA, and ctDNA from a raw sample (Slouka et al., 2014), we report a proof-of-concept platform to detect and quantify short nucleic acids through induced nanoparticle aggregation and separation. Our technique relies on the ion-selective properties of ion-exchange membranes which are nanoporous and possess fixed positive or negative charges. The ion-selectivity of these membranes produces unique ion depletion and enrichment concentration polarization phenomena in their vicinity. Our group previously attached single-stranded DNA probes to anion-exchange membranes and demonstrated significant effects of hybridized targets on the concentration polarization phenomena to produce strong current-voltage signals (Slouka et al., 2013) leading to the detection of miRNA biomarkers for oral and pancreatic cancers (Senapati et al., 2014; Taller et al., 2015). Furthermore, the membrane's analyte enrichment capabilities improve the sensitivities and limits of detection in our microfluidic devices (Slouka et al., 2014). Other groups used the ion depletion front, with different ion conductivity across it, to isotachophoretically concentrate molecules in microfluidic channels (Quist et al., 2011, 2012) and paper media (Gong et al., 2015). Here, we integrate the analyte concentration and isotachophoretic depletion front generation with the molecular isolation and nanoparticle separation capabilities of the gel medium to perform selective field-induced aggregation of linked nanoparticles from a DNA sandwich assay.

Short nucleic acid targets are particular amenable to sandwich assays, wherein two different probe-functionalized gold nanoparticles link together through a common target to form nanoparticle dimers, because long targets and probes tend to collapse and encapsulate the nanoparticles and suppress dimerization (Gagnon et al., 2008). Typical nanoparticle dimerization also suffers from diffusion limitations and hence requires long assay times for low analyte concentrations with a typical assay requiring overnight incubation for a target concentration of 20 nM (Elghanian et al., 1997). We use electrophoresis to pack the target and the particles against a cation-exchange membrane to both concentrate particles and achieve rapid target hybridization. After packing, we reverse the field, drive the nanoparticles in the opposite direction, and simultaneously form the depletion region. When the depletion front reaches the nanoparticles, it induces selective aggregation of the dimer particles while isotachophoretically driving the monomer particles down the channel. We then optically quantify the plasmon resonance band of the dimer particles to measure the DNA target concentration. Our technique quantifies the target within minutes and avoids the many arduous and hours-long steps involved in lab-based techniques such as Southern and Northern blotting. Additionally, the high electric fields formed by the depletion region create high shear forces to prevent nonspecific binding thus shortening the assay time. Here we demonstrate only single target detection but extension to multiple targets using nanoparticles with different plasmonic frequencies should be easily achievable.

2. Materials and methods

2.1. Materials

Fluorescein sodium salt was obtained from Fisher Scientific. Sodium chloride, sodium citrate, and chloroauric acid trihydrate were obtained from Sigma-Aldrich. Buffers were prepared by dilution from 10 X PBS (pH 7.4) and 50 X TAE (pH 8.4) obtained from Boston Bioproducts and 150 mM sodium phosphate buffer (pH 7.2) obtained from Teknova. Agarose gels were prepared at 1 wt% in 1 X TAE using agarose powder from Ominpur and stored as liquids inside an oven maintained at 65 °C. All agarose gels containing fluorescein were prepared in a like manner with the fluorescein concentration equal to 10 μM. QuikCast polyurethane casting resins (side A and side B) were obtained from TAP Plastics Inc. Acrifix 1R 0192 UV reactive cement was obtained from Evonik Industries while Loctite 3492 light cure adhesive was obtained from Loctite Corporation. Custom single stranded DNA probes and target sequences were used as received from Integrated DNA Technologies Inc. The two probe sequences were 5′/TGG TTC TCT CCG AAA TAG CTT TAG GG TA/3′ for probe 1 and 5′/GAA GGG AAG AGG AAG AGG CAG GTG TCC TGT GGT AG/3′ for probe 2. Probe 1 possessed a thiol modification at the 5′ end while probe 2 possessed a thiol modification at the 3′ end. The target sequence was 5′/CT ACC ACA GGA CAC CTG CCT CTT CCT CTT CCC TTC AAAAA TA GCC CTA AAG CTA TTT CGG AGA GAA CCA/3′ while the nontarget sequence was 5′/GCT GGC ACT CTA CAC TAG AAG GGA TAG ATA TGC CAA AAA AAC CAA ATT TCA GGC CCG GAA CTT TCT TGC/3′. The DNA probes and nontarget were dissolved in water to concentrations of 1 mM while the target DNA were dissolved in water to concentrations of 0.1 mM. All DNA samples were stored in a freezer at −4 °C until ready for use. Cation-exchange membranes whose fixed negative charge is supplied by organosulfanate groups were provided by Mega a.s (Czech Republic).

2.2. Synthesis and functionalization of Au nanoparticles

For detailed information on nanoparticle synthesis and probe functionalization, see Supporting Information Section 2.2. Gold nanoparticles were prepared by standard citrate reduction (Brown

Please cite this article as: Marczak, S., et al., Biosensors and Bioelectronics (2016), http://dx.doi.org/10.1016/j.bios.2016.07.093

et al., 2000). They were sized by a Malvern Nano-ZS Zetasizer and found to be approximately 20 – 30 nm in diameter. Their concentration was 2 nM as determined by UV–Vis spectroscopy (Haiss et al., 2007) using a Thermo Scientific NanoDrop 2000 spectrophotometer.

The particles were functionalized with DNA probes 1 and 2, in separate solutions, by gold-thiol bonding as described elsewhere (Demers et al., 2000). The final nanoparticle concentration was approximately 8 nM. DNA target solutions from 1 μM down to 10 pM were prepared by mixing equal amounts of probe 1 and 2 nanoparticles followed by adding DNA targets. A nontarget solution was prepared in a like manner at 10 μM. Heterogeneous mixtures were also prepared with concentrations of 1 nM target/10 μM nontarget and 100 pM target/1 μM nontarget. The solutions were mixed vigorously and incubated for at least twelve hours before use.

2.3. Chip fabrication

For detailed information regarding chip fabrication and design, see supporting information Section 2.3. Microfluidic chips were fabricated from 300 μm polycarbonate sheets in a layer-by-layer fashion forming a single, straight channel with dimensions 2 mm width × 60 mm length × 500 μm height. At either end of the channel were inlet/outlet holes for fluid and liquid gel. A 2 mm × 2 mm square hole for inserting the sample lay 10 mm from the inlet and between the inlet and the membrane. Another 6.9 mm diameter hole whose center was 10 mm away from the sample hole held the membrane cast. The cation-exchange membrane was sealed to the bottom of the cast and remained flush with the top of the microfluidic channel. The chip schematic is shown in Fig. 1c.

2.4. Separation and detection protocol

Chips were filled with agarose gel and used after the gel solidified. The gel occupying the sample reservoir was removed and filled with 2 μL nanoparticle/DNA sample. The fluid reservoirs were all filled with 1 X TAE buffer. Gel electrophoresis was conducted using a Keithley 2400A Sourcemeter with platinum electrodes as the voltage source. The protocol consisted of four steps: enrichment, depletion, expulsion, and repacking. 1) During enrichment, shown in Fig. 1a, the positive electrode was placed inside the membrane reservoir while ground was placed inside the inlet reservoir, and the sample was electrophoretically driven towards the membrane for five minutes by a 150 V potential. The particles required approximately one minute to reach the membrane at which point the sample reservoir was refilled with agarose gel. 2) During depletion, typically eight to nine minutes, the field was reversed by changing the electrode potential in the membrane reservoir to −150 V. As shown in Fig. 1b, this generated a depletion front causing aggregation of one fraction of the nanoparticles while forcing away the remainder back towards the sample loading reservoir. 3) Expulsion was conducted by transferring the electrode in the membrane reservoir to the sample reservoir for one minute and forcing the particles therein into the region between the sample and inlet reservoirs. 4) In the repacking step, the field was reversed again with the positive electrode at 150 V in the membrane reservoir and the ground in the sample reservoir. The aggregated nanoparticles were concentrated and repacked against the membrane. From sample loading to target detection, the total time required was sixteen minutes.

The nanoparticles were imaged using a QImaging Retiga 2000R Fast 1394 camera and custom MATLAB programming. Images were recorded before the enrichment and depletion steps and after the repacking step. The particles near the membrane were quantified using the mean pixel intensity as measured by ImageJ. The fraction of aggregated particles was then calculated by taking the ratio of the intensity after repacking to the intensity after enrichment.

2.5. SEM analysis

In order to confirm the state of aggregation of the nanoparticles, SEM images of the two different bands were collected. To carry out the collection, a special chip was used where clear packaging tape replaced the bottom surface. After the depletion

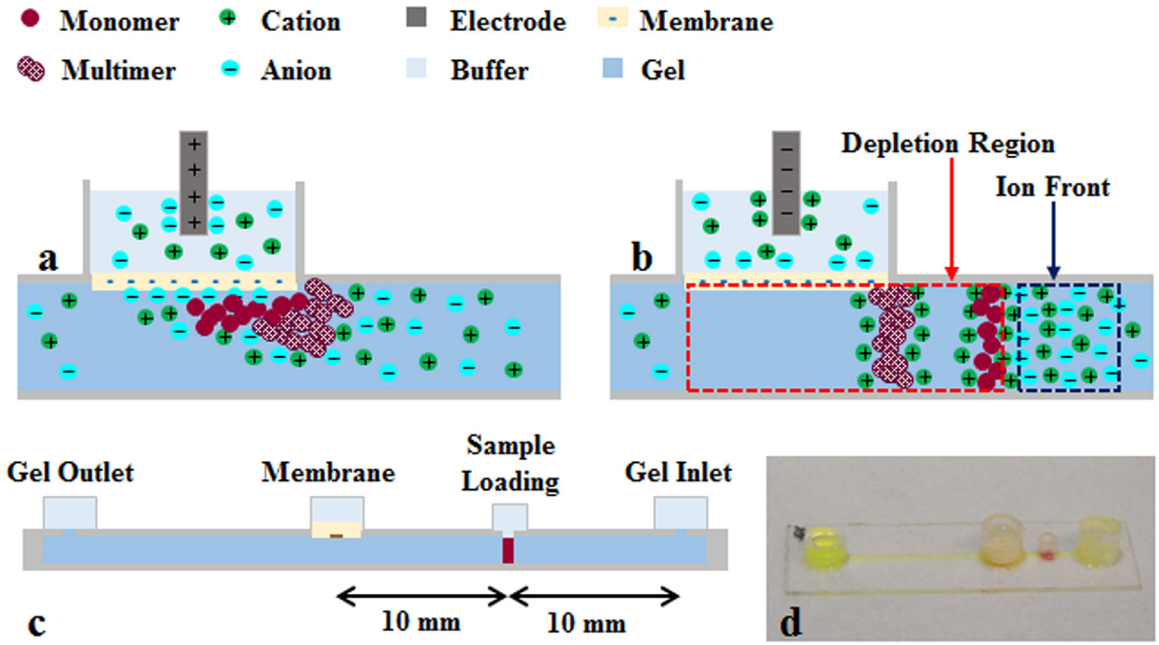

Fig. 1. Mechanism of nanoparticle separation. a) Enrichment: An electric field drives the particles towards the membrane and packs them at its surface. b) Depletion: The field is reversed, a depletion region forms, and the multimer particles aggregate while the monomer particles are driven away. c) Side view schematic of entire microfluidic chip. d) Chip filled with fluorescein-doped agarose gel and nanoparticles in the sample reservoir.

Please cite this article as: Marczak, S., et al., Biosensors and Bioelectronics (2016), http://dx.doi.org/10.1016/j.bios.2016.07.093

step separated the nanoparticles, the tape was peeled off, the two bands were cut from the gel, and then they were placed into separate containers in 20 μL of water. The solutions were heated at 60 °C for twenty minutes to melt the gel. The solutions were then dispensed onto silicon substrates and evaporated. Following evaporation, the substrates were washed with water to remove any residual salt. The dried particles were imaged by a Carl Zeiss EVO-50 SEM. The subsequent images were analyzed in ImageJ using the "Analyze Particles" function to determine the area of the particles from which the diameter was then calculated.

3. Results and discussion

3.1. Hybrid membrane-gel electrophoresis

Ion concentration polarization by the cation-exchange membrane is an essential feature of our new detection strategy. A positive potential applied above the membrane electrophoretically drives anions and negatively charged gold particles to accumulate at the surface because fixed negative charges prevent any negatively charged entity from passing through due to electrostatic repulsion. On the other hand, cations pass through freely leading to an enrichment effect beneath the membrane surface as in Fig. 1a. When the applied potential becomes negative, both cations and anions migrate away from the enriched region leaving behind a zone depleted of ions. Because the system must maintain electroneutrality, cations encounter the anions at the head of the depletion region and form the concentrated ion front illustrated in Fig. 1b. High voltages produce an extended space-charge region which forms a vortex instability that mixes the bulk electrolyte with the depletion zone and increases the current (Chang et al., 2012). In our system however, the gel suppresses vortex formation. Hence, the depletion region migrates down the channel creating a sharp boundary between the depletion region and the ion front as shown by the fluorescein doped gel in supplementary information Fig. S-1. In the figure, the depletion is easily monitored by tracking the movement of the bright green fluorescein ions next to the dark, depleted region. As shown in the inset, the current falls dramatically due to lack of charge carriers in the depletion region. The drop in current places a high-field and a low-field region adjacent to each other and therefore facilitates an isotachophoretic separation front and avoids the tedious task of loading the channel with two different conductivity buffers. As we discuss later in more detail, this isotachophoretic front is responsible for the selective aggregation of DNA-linked nanoparticles.

For this proof-of-concept study, we used a combination of probe-functionalized gold nanoparticles, cation-exchange membranes, and gel electrophoresis to isolate and detect specific DNA sequences. An example separation of 100 nM target is illustrated in Fig. 2. In Fig. 2b, the nanoparticles pack at the membrane surface during enrichment. In Fig. 2c, the depletion causes the linked particles to aggregate whereas the uncaptured particles continue their migration back up the channel. As mentioned above, we also perform expulsion and repacking steps as in Fig. 2d which is necessary at low concentrations to enhance sensitivity and increase signal strength. Fig. 2 demonstrates a clear separation between targets and unlinked particles in less than 5 mm of channel length and less than seventeen minutes between sample loading and detection. We isolate the nanoparticle signal by image subtraction and set a threshold to avoid measurement noise. Our assay detects down to 10 pM which is approximately 10 million copies with our sample volume. Our result is comparable to previous isotachophoretic platforms with gel filters that report detection of 300 million copies of miRNA (Garcia-Schwarz and Santiago, 2012). Electrochemical methods such as differential pulse voltammetry

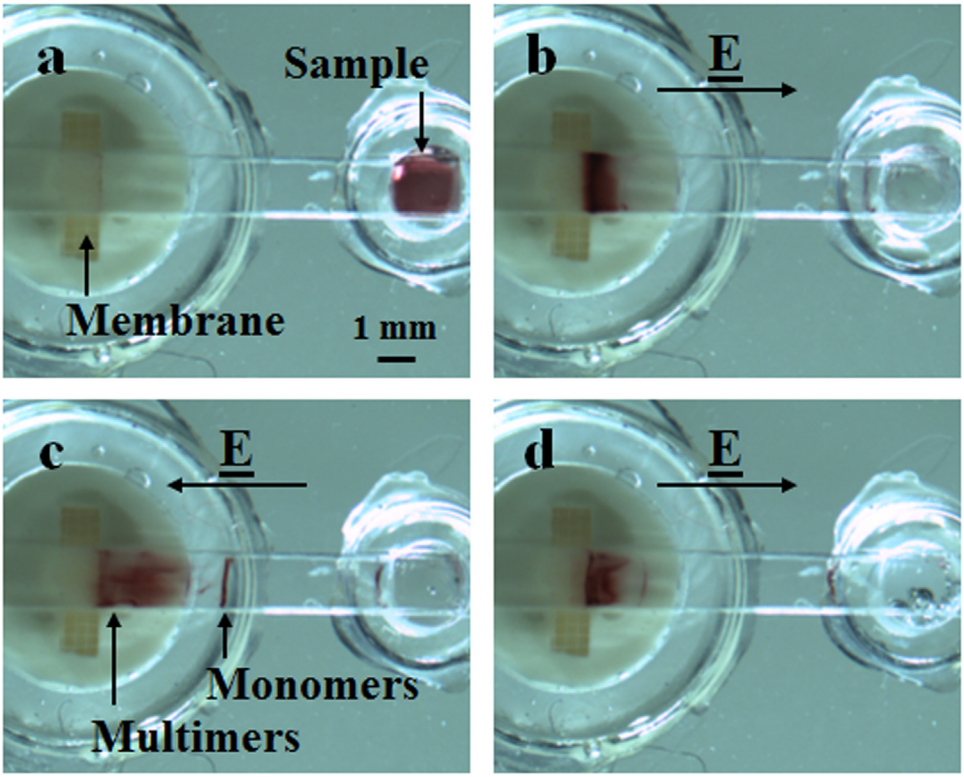

Fig. 2. Example separation of sample with 10 nM target. a) Nanoparticle/DNA mixture is inserted into sample inlet. b) Sample packs tightly against the membrane during the enrichment step. c) Five minutes into the depletion step, the uncaptured monomer particles separate from the now aggregated multimer particles linked by target molecules. The monomer particles continue to migrate up the channel as a thin line at the front of the depletion region. d) The aggregated particles are repacked against the membrane for detection.

Please cite this article as: Marczak, S., et al., Biosensors and Bioelectronics (2016), http://dx.doi.org/10.1016/j.bios.2016.07.093

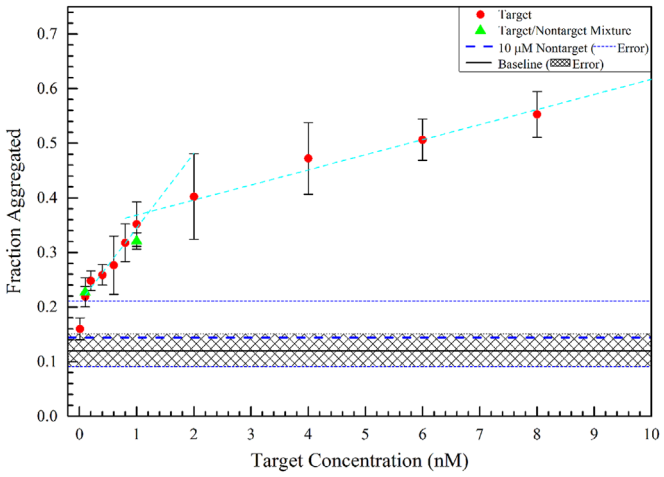

Fig. 3. Calibration curve showing the fraction of aggregation as a function of DNA concentration. The target/nontarget mixture points possess a nontarget-to-target ratio of 10,000:1. The baseline signal corresponds to the nanoparticle mixture without either target or nontarget. Linear fits are shown from 100 pM to 1 nM and 1 nM to 8 nM with correlation coefficients of 0.96 and 0.98, respectively. Error bars represent uncertainties within a 95% confidence interval and n=4.

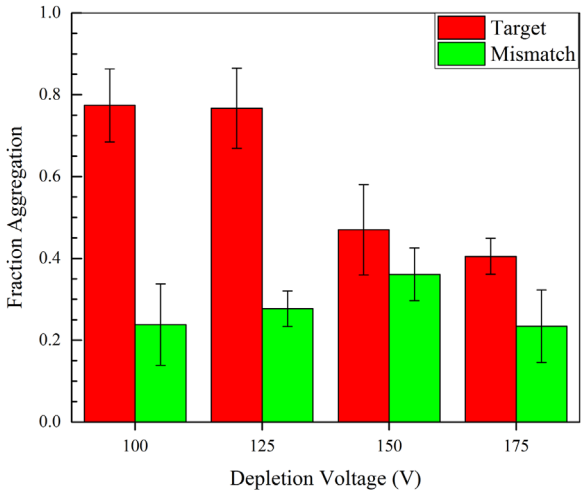

Fig. 4. Selectivity of the sensor for fully complementary target versus two-base pair mismatch target. The depletion voltage was initially applied at −200 V potential for one minute followed by a step to change to different lower voltages. Error bars represent uncertainties within a 95% confidence interval and n=4.

report detection limits that vary from 800 pM (Luo et al., 2013) to 2 pM (Li et al., 2015) down to 0.4 fM (Jia et al., 2016) and 0.2 fM (Pan et al., 2015). Although these biosensors report lower limits of detection, they typically rely on diffusion-based hybridization. Hence, they report assay times from one hour up to five hours, particularly at low concentrations. In contrast, our assay requires less than twenty minutes from sample loading to detection. In addition, electrochemical sensors employ expensive fabrication methods and tedious preparation of electrodes making them unsuitable for point-of-care applications.

Following this procedure, we established the calibration curve in Fig. 3 for the 10 pM to 10 nM range. First, Fig. 3 shows our system is highly selective between targets and nontargets. It should be noted that there is a small amount of aggregation despite the absence of any DNA targets or nontargets, and this is the baseline signal of our platform, yet we detect down to 10 pM target above the baseline. On the other hand, even at 10 μM, the signal from the nontarget is, within error, equivalent to the baseline. Furthermore, we maintain the signal intensity in heterogeneous mixtures where the nontargets outnumber the targets by a factor of 10,000 to 1. At 1 nM and 100 pM, the mixture's signal is identical to the signal from pure target thereby demonstrating the selective nature of our assay and its potential use for complex media. Second, the graph reveals two linear regimes: one from 100 pM to 1 nM and one from 1 nM to 8 nM with correlation coefficients of 0.96 and 0.98, respectively, for the lines of best fit. The ratio of nanoparticles to target molecules explains the presence of these two regimes and the decrease in sensitivity between 1 and 8 nM. In an ideal scenario, each target links a nanoparticle to only one other nanoparticle and forms them into dimers. However, in practice, targets link nanoparticles into trimmers, tetramers, and higher multimers. At low target concentrations, when the ratio of nanoparticles to targets is large, the probability to form dimers is much higher. At a concentration of 8 nM gold nanoparticles, the nanoparticle to target ratio goes from 800:1 to 8:1 in the 100 pM to 1 nM range, respectively, and is significant enough to form mainly dimers. Above 1 nM, the ratio approaches and then falls below 1:1 so that multimer formation becomes more probable. The concentration range where dimers form is more sensitive because each additional target corresponds to an additional two nanoparticles. In contrast, in the multimer regime there is a greater probability that targets will hybridize to particles already linked as dimers. Therefore, there is a smaller increase in the signal and consequently lower sensitivity. The changing sensitivity with the nanoparticle to target ratio demonstrates the scalability of our platform. That is, we can potentially lower the limit of detection by decreasing the concentration of the nanoparticles at low target concentrations to obtain higher order multimers and hence more severe aggregation. It follows that we may also increase the dynamic range by careful adjustment of the nanoparticle concentration depending on the amount of target present in the sample. This could be achieved by testing multiple channels with different nanoparticle concentrations simultaneously and then running subsequent measurements at only one concentration for greater precision. A future publication will more completely study the effects and performance of changing the nanoparticle to target ratio.

In Fig. 4, we provide preliminary results examining the selectivity of the sensor using targets with two base mismatches on each probe, so the target sequence becomes 5′/CTACCGT…GCAACCA/3′. The experiments were carried out using slightly altered conditions where the distance between the channel inlet and membrane reservoirs reduced to 15 mm, the enrichment time increased to six minutes, and the applied potential during depletion underwent a step change. We applied the maximum output of the sourcemeter, −200 V, for one minute, and then we lowered the potential for the remainder of the depletion step (i.e. until the monomer reached the sample reservoir). In Fig. 4, we see the greatest selectivity when the potential is lowered to 100 V and obtain target to mismatch signal ratio greater than 3. Our results are comparable to other assays such as the NanoBioArray chip of Sedighi et al. (2014) based on hybridization of target-conjugated nanoparticles to surface-immobilized probes and the molecular beacon/Ag nanocluster technique of Cao et al. (2015) who report selectivity values of approximately 3 to 6 and 2-3, respectively. It is important to realize the mismatches occur in the middle of the probes rather than at the ends. Mismatches positioned in the middle may significantly reduce the selectivity (Cheng et al., 2010), yet we are still able to discriminate between them and the completely matched target. Although we do not offer a detailed explanation here, we also note the importance of changing the electric field strength on improving the selectivity. We intend to offer a more detailed and exhaustive study concerning the selectivity and the effects of numbers of mismatches as well as mismatch location in a future publication.

Please cite this article as: Marczak, S., et al., Biosensors and Bioelectronics (2016), http://dx.doi.org/10.1016/j.bios.2016.07.093

Our SEM analysis confirms the presence of monomers and multimers in the separated bands. In Fig. 4a, the SEM image of the monomer band demonstrates the dominant presence of monomer particles over dimers and higher multimers. The inset of Fig. 4a shows a histogram analysis of the diameters of over 1000 particles. The average particle diameter is 17 nm which corresponds well with the known diameters from dynamic light scattering. Very few particles possess diameters above 30 nm which would be indicative of the formation of dimers. In Fig. 4b though, large aggregates dominate over the presence of monomers. Although the histogram in the inset still shows some monomer particles, the distributions shifts significantly to higher diameters compared to the inset in Fig. 4a. The diameters of the aggregates may also be underestimated due to the decreasing circularity of the large aggregates. Moreover, during sample preparation, the heating stage which melts the gel may have denatured some of the hybridized pairs causing particle dissociation and thus resulting in more monomers. However, Fig. 4 clearly proves the depletion front aggregates linked particles but removes monomer particles.

3.2. Reducing hybridization time

We performed further experiments to examine the role enrichment plays in our assay by investigating how the enrichment time affects aggregation. For an 8 nM target sample, we carried out the enrichment step for various times beginning at one minute and increasing the time in one minute intervals up to twelve minutes. The subsequent depletion, expulsion, and repacking steps we performed as usual although the time required for the depletion step increased as the enrichment time increased. We show the results in Fig. S-2 in the supporting information. Overall, the fraction of aggregated particles increases linearly with the enrichment time although the data at one and two minutes fall below the baseline signal. Longer than six minutes, the slope decreases and finally begins to saturate at twelve minutes.

Other than reducing the diffusion time for nanoparticle linkages by concentrating the nanoparticles, the enrichment step also favorably affects the hybridization thermodynamics. The increasing aggregation shown in Fig. S-2 indicates increasing numbers of targets hybridize to the nanoparticles while packing near the membrane surface. This effect can be explained by examining the thermodynamic equilibrium surrounding the hybridization reaction. From Gong and Levicky (2008), the hybridization of a DNA target to a surface-bound probe can be written as $T+P+JC \rightarrow D$ where T is the target, P is the probe, and D is the hybridized duplex. The JC term accounts for a number J of cations, C, which are initially free in solution but associate to the duplex to screen the increased charge density on the DNA duplex. The equilibrium expression is then

$$\frac{[D]}{[T][P][C]^J} = \frac{1}{K_D}$$

where K_D is the dissociation constant. Because target molecules and cations are small compared to the size of the nanoparticles, we expect them to concentrate more than the nanoparticles which, by the surface bound nature of the probes, effectively control the probe and duplex concentrations. Therefore, the concentrations of targets and cations increase relative to the concentration of the duplexes and push equilibrium to favor hybridization. When we reverse the field and form the depletion, we expect the reverse reaction rate to increase. That is, we should see the dissociation of duplexes as targets and cations migrate away from the membrane. However, the depletion induces aggregation of the nanoparticles before significant dissociation ensues. So, although dehybridization is thermodynamically more favorable during depletion, it is kinetically limited because of the aggregation. We effectively lower the dissociation constant by the combined effects of enrichment and depletion. This result is particularly encouraging since target hybridization to surface-based probes tends to be less favorable than solution-based probes (Levicky and Horgan, 2005; Ravan et al., 2014).

We see further proof that hybridization takes place during the enrichment step by comparing the aggregation between targets hybridized on-chip and targets hybridized off-chip. For on-chip hybridization, we prepared 100 nM target samples, vortexed them briefly, and then immediately analyzed them using our protocol. For off-chip hybridization, we simply used our normal samples with twelve hour hybridization. We also compared the aggregation to a 10 μM nontarget sample hybridized on-chip and samples with no target. The fractional aggregation for on-chip hybridization is identical to that for off-chip hybridization disposing of the need for the hours-long incubation step. Additionally, there is no significant aggregation from the nontarget DNA sample, so no selectivity is lost. Therefore, we can achieve rapid, selective hybridization on-chip and significantly reduce the total analysis time to less than twenty minutes. The enrichment concentrates the target which increases the reaction rate and thereby overcomes the kinetic limitations and the transport-limited hybridization reaction in the bulk.

3.3. Mechanism for selective field-induced nanoparticle aggregation by the depletion front

It is quite apparent from Figs. 3 and 5 that the depletion front induces nanoparticle aggregation only for linked nanoparticles. Field induced nanoparticle dipoles are known to induce aggregation (Hermanson, 2001; Kloepper et al., 2004), but it is unclear why only linked particles aggregate in our platform. To elucidate the mechanism behind this curious selective aggregation, we conducted another experiment wherein we used fluorescein doped gel to track the movement of the depletion region and simultaneously monitor the aggregation and separation of the nanoparticles. As we expect, the separation does not take place until the depletion region reaches the nanoparticles; after the separation, the monomers remain isotachophoretically packed against the depletion front and carried by the front downstream. This experiment is repeated with a series of pauses during the depletion step. Images simultaneously displaying the fluorescence-tracked depletion and the nanoparticles are shown in Fig. 6 while the nanoparticles' position is confirmed by bright field images (not shown). Fig. 6a shows the nanoparticles' initial position at the beginning of the depletion step while Fig. 6b shows them three minutes later just as the depletion front begins to form. Here, we introduce the first pause before any separation. Each pause lasts fifteen minutes, and during this time, the fluorescein diffuses into the depletion region as in Fig. 6c. We reapply the voltage for one minute and then allow another fifteen minute pause. When we reapply the voltage, the depletion region quickly reforms, and overtakes the nanoparticles in Fig. 6d. The fluorescein again diffuses into the depletion region in Fig. 6e until we apply the voltage for another minute to yield the final image, Fig. 6f, where the gap between the nanoparticles and the depletion front becomes very obvious. We note first that the nanoparticles no longer migrate under the applied field indicating aggregation. Second, no separation exists between hybridized and unhybridized nanoparticles, indicating the aggregation of both monomer (unhybridized) and multimer (hybridized) particles.

Results obtained from Fig. 6 reveal the crucial role of depletion ramping in inducing selective aggregation, and we explain them through depletion induced isotachophoretic separation. Separation by depletion isotachophoresis was actually first reported only

Please cite this article as: Marczak, S., et al., Biosensors and Bioelectronics (2016), http://dx.doi.org/10.1016/j.bios.2016.07.093

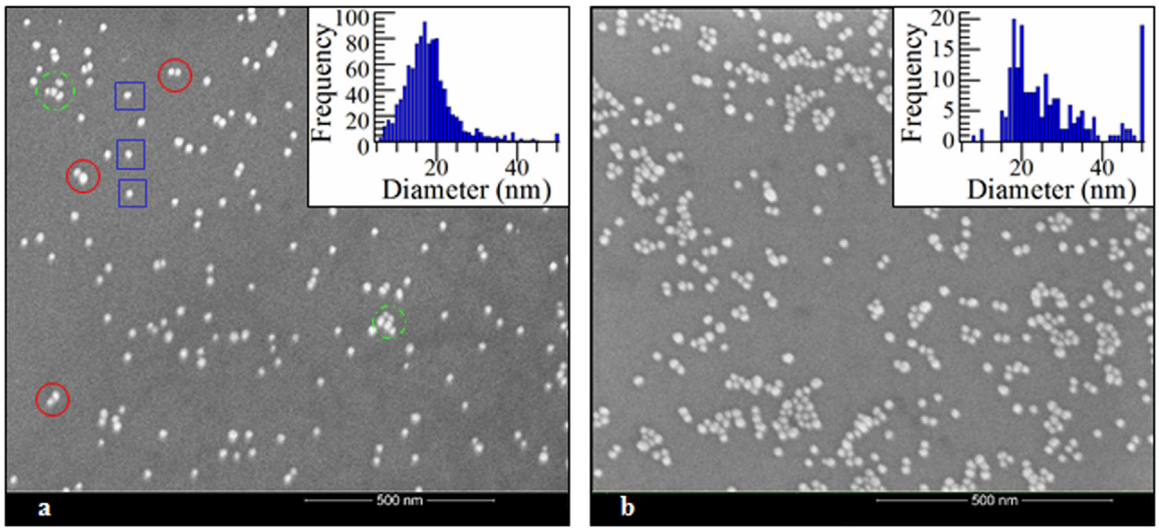

Fig. 5. SEM images of nanoparticles from the a) monomer band and b) aggregated band. Examples of different types of particles in part a are monomers shown by blue squares, dimers by red circles, and larger aggregates by broken green circles. The insets are representative histograms of particle diameters from each respective band. (For interpretation of the references to color in this figure legend, the reader is referred to the web version of this article.)

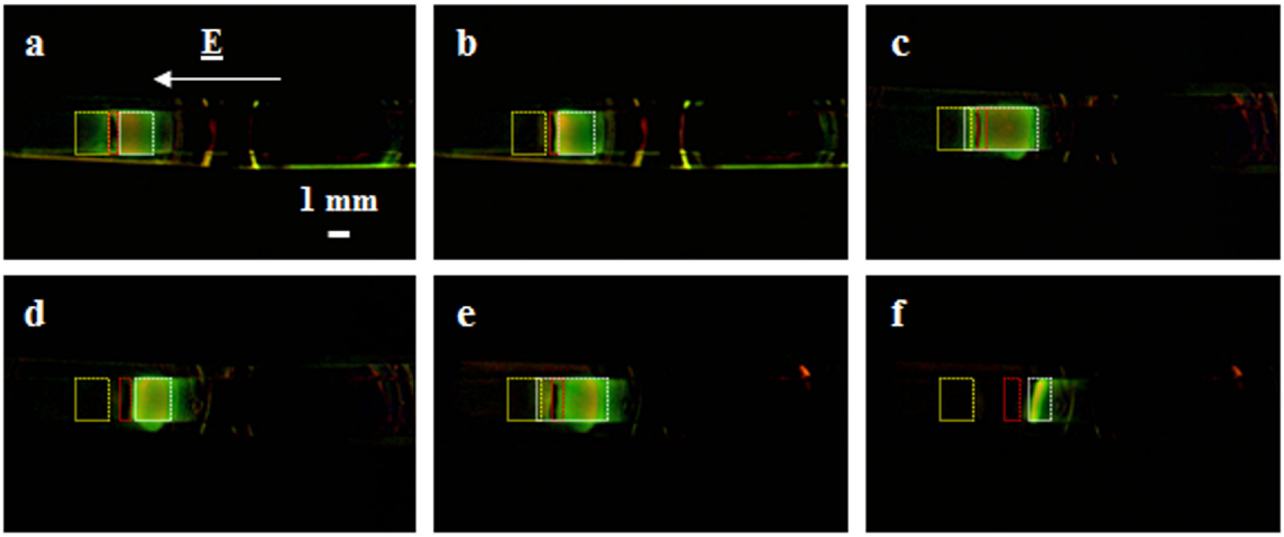

Fig. 6. Depletion step in fluorescein doped gel. Positions of the membrane, nanoparticles, and ion front are indicated by the yellow, red, and white boxes, respectively. The depletion front, indicated by the concentrated fluorescein band, was isolated by image subtraction. Images were taken after a) 0 min, b) 3 min applied voltage, c) 15 min no voltage, d) 1 min applied voltage, e) 15 min no voltage, and f) 1 min applied voltage. (For interpretation of the references to color in this figure legend, the reader is referred to the web version of this article.)

recently by Quist et al. (2011, 2012) for fluorescent analytes. As explained in Fig. S-1, the formation of the depletion region leads to a rapid drop in current which in turn creates a high electric field. At the same time, ions accumulate just ahead of the depletion front. A very sharp electric field gradient develops between the high electric mobility environment in the depletion region and the low electric mobility environment in the concentrated ion front. The adjacent high and low electric mobility environments facilitate the proper conditions for an isotachophoretic separation without using immiscible solvents with different ionic strengths. The linked and unlinked nanoparticles possess enough of a mobility difference to separate within the isotachophoretic region. However, such a separation is feasible only with a continuous depletion front with all the nanoparticles initially packed at the membrane. We determine this from the stop/start experiment illustrated in Fig. 6. The fluorescein ions quite obviously diffuse into the depletion region. Although it is not readily apparent, we can assume the monomer and dimer particles also diffuse and mix with each other. Once we reapply the voltage, however, the particles do not have enough time to separate before the depletion overtakes them. Therefore, when the dimer particles aggregate, the monomer particles become trapped within the aggregated complex as well. When we let the depletion run continuously instead, we see aggregation of only the linked particles. With a continuous depletion front, the band of separated, linked dimers are in the high field region at the isotachophoretic front and the band of unlinked nanoparticles are in the high ionic strength, low field region just ahead. The large field gradient within the isotachophoretic front hence induces selective aggregation of the linked nanoparticles in the back of the front and not the unlinked nanoparticles at the front only if the two sets of particles are separated at the isotachophoretic front with continuous depletion.

We have shown that the dimerization of the particles in the advancing depletion front occurs only if the particles are linked by a single target molecule. We believe this is due to a selective and irreversible aggregation kinetic mechanism in the presence of a

Please cite this article as: Marczak, S., et al., Biosensors and Bioelectronics (2016), http://dx.doi.org/10.1016/j.bios.2016.07.093

decaying electric field. Wijenayaka et al. (2015) recently performed extensive characterization of the interparticle interactions between Au nanoparticles functionalized with negatively charged ligands using an extended DLVO theory. The dominant interactions between the particles are the repulsive electrostatic forces and the attractive van der Waals (vdW) forces. Wijenayaka et al. showed that our smaller particles (<50 nm) have higher Hamaker constants. The result is that for conditions where spontaneous aggregation does not occur, a potential barrier more than 10 k_BT exists at roughly a few nanometers of particle separation due to a balance between these two opposing interactions but both interactions will vanish more than 10 nm away (Wijenayaka et al., 2015). The linking target molecule can reduce this barrier because of the preferred association of free polyvalent cations around the duplex (Gong and Levicky, 2008) that screen the electrostatic repulsion between the negatively charged particles. This aggregation barrier can be lowered significantly or even eliminated entirely by imposing a sufficiently high electric field (Liu et al., 2013) due to an attractive interaction between the two induced nanoparticle dipoles. How much the barrier is lowered by the electric field can be estimated by the voltage drop across the separation where the barrier lies (a few nanometers). Most of the 150 V voltage drop is in the depleted region and hence when the depletion front has only advanced a few millimeters, the voltage drop across the barrier separation of a few nanometers can be as large as 10 k_BT but it decays to below 1 k_BT when the front has advanced more than 1 cm. The barrier for linked particles hence disappears and appears in less than one minute between the time the depletion region hits the particles and the time it passes them. The particles would aggregate spontaneously without the barrier because the linker particles keep them within 10 nm of each other to allow rapid attractive interaction. The unlinked particles either still have a significant barrier during this interval or are too far apart to aggregate within the interval. This is then the role of the linking target molecules— their cations lower the barrier, so it can be removed by the electric field for an interval in time, and they tether the two linked nanoparticles so they are driven irreversibly by the attractive vdW force in that interval.

4. Conclusion

We developed a new detection and quantification protocol for short single-stranded nucleic acids which uses the enrichment and depletion features of a cation-exchange membrane to isolate gold nanoparticle reporters with captured DNA targets during depletion-generated gel isotachophoresis. Our microfluidic chip detects single-stranded DNA targets down to 10 pM within a 2 μL sample volume. One key component, the enrichment, helps achieve rapid hybridization while also effectively lowering the dissociation constant to increase the number of hybridized targets. The crucial features of the other key component, the depletion, are creating a sharp electric field gradient to isotachophoretically separate the linked and unlinked particles and then selectively aggregating the linked particles. The assay is highly selective against nontargets even when such nontargets significantly outnumber targets in heterogeneous mixtures. Unlike lateral flow assays, we retain a method to remove nontarget molecules and increase specificity; that is, the depletion region creates a high electric field which removes nonspecific binding. Our gel platform can also be readily integrated with other gel systems such as those which purify nucleic acids from proteins and large cell debris from lysate. Our group previously developed a gel-based filter which selectively passed short nucleic acids while blocking the passage of proteins and cell debris (Slouka et al., 2013, 2014; Egatz-Gomez et al., 2016). Therefore, nucleic acids purified from blood or serum will not suffer from fouling of nonspecific interactions caused by undesirable components.

As a proof-of-concept study, the microfluidic chip we presented here is largely unoptimized. We expect to improve sensitivity and attain lower limits of detection as well as increase the dynamic range by decreasing the microchannel's dimensions, employing better optical detectors, and scaling the nanoparticle concentration with the target concentration. In addition, there are many variables, such as the buffer concentration, the electric field strength, the nanoparticles' size and concentration, target length, etc, which affect how much aggregation takes place as well as when and where it occurs, so they must be studied systematically to determine the optimal parameters for maximum aggregation. We can also transition to multitarget sensing by incorporating different types of nanoparticles into the assay. These could be other plasmonic nanoparticles such as silver and nickel, or they could be fluorescently doped silica particles. Differences in electrophoretic mobility could result in DNA barcodes, but even mixed aggregation where the particles overlap is still useful with a simple spectrometer. We can hence, in principle, identify and quantify multiple short nucleic acids without the tedious and time-consuming steps of blotting, pretreatment for PCR, or long microarray assay time for genomic liquid biopsies.

Acknowledgments

Thanks are due to Ceming Wang for obtaining SEM images of the nanoparticles. We also express our gratitude for funding to the Naughton Foundation and to NSF-CBET1065652.

Appendix A. Supporting information

Supplementary data associated with this article can be found in the online version at http://dx.doi.org/10.1016/j.bios.2016.07.093.

References

de Avila, B.E.F., Watkins, H.M., Pingarron, J.M., Plaxco, K.W., Palleschi, G., Ricci, F., 2013. Anal. Chem. 85 (14), 6593–6597.
Brown, K.R., Walter, D.G., Natan, M.J., 2000. . J. Chem. Mater. 12, 306–313.
Calin, G.A., Croce, C.M., 2006. Nat. Rev. 6, 857–866.
Cao, Q., Teng, Y., Yang, X., Wang, J., Wang, E., 2015. Biosens. Bioelectron. 74, 318–321.
Chang, H.-C., Yossifon, Y., Demekhin, E.A., 2012. Annu. Rev. Fluid Mech. 44, 401–426.
Cheng, I.F., Senapati, S., Cheng, X., Basuray, S., Chang, H.C., Chang, H.C., 2010. Lab Chip 10, 828–831.
Chua, A., Yean, C.Y., Ravichandran, M., Lim, B., Lalitha, P., 2011. Biosens. Bioelectron. 26, 3825–3831.
Corstjens, P.L.A.M., Zuiderwijk, M., Nilsson, M., Feindt, H., Niedbala, R.S., Tanke, H.J., 2003. Anal. Biochem. 312, 191–200.
Demers, L.M., Mirkin, C.A., Mucic, R.C., Reynolds, R.A., Letsinger, R.L., Elghanian, R., Viswanadham, G., 2000. Anal. Chem. 72, 5535–5541.
Egatz-Gomez, A., Wang, C., Klacsmann, F., Pan, Z., Marczak, S., Wang, Y., Sun, G., Senapati, S., Chang, H.C., 2016. Biomicrofluidics 10, 032902.
Elghanian, R., Storhoff, J.T., Mucic, R.C., Letsinger, R.L., Mirkin, C.A., 1997. Science 277 (5329), 1078–1081.
Fang, Z., Ge, C., Zhang, W., Lie, P., Zeng, L., 2011. Biosens. Bioelectron. 27, 192–196.
Gagnon, Z., Senapati, S., Gordon, J., Chang, H.C., 2008. Electrophoresis 29, 4808–4812.
Gao, X., Xu, H., Baloda, M., Gurung, A.S., Xu, L., Wang, T., Zhang, X., Liu, G., 2014. Biosens. Bioelectron. 54, 578–584.
Garcia-Schwarz, G., Santiago, J.G., 2012. Anal. Chem. 84, 6366–6369.
Gong, P., Levicky, R., 2008. PNAS USA 105 (14), 5301–5306.
Gong, M.M., Nosrati, R., San Gabriel, M.C., Zini, A., Sinton, D., 2015. J. Am. Chem. Soc. 137, 13913–13919.
Haiss, W., Thanh, N.T.K., Aveyard, J., Fernig, D.G., 2007. Anal. Chem. 79, 4215–4221.
Hampl, J., Hall, M., Mufti, N.A., Yao, Y.M., MacQueen, D.B., Wright, W.H., Cooper, D.E., 2001. Anal. Biochem. 288, 176–187.
Hanauer, M., Pierrat, S., Zins, I., Lotz, A., Sonnichsen, C., 2007. Nano Lett. 7 (9), 2881–2885.
He, Y., Zhange, S., Zhang, X., Baloda, M., Gurung, A.S., Xu, H., Zhang, X., Liu, G., 2011.

Biosens. Bioelectron. 26, 2018–2024.
Hermanson, K.D., Lumsdon, S.O., Williams, J.P., Kaler, E.W., Velev, O.D., 2001. Science 294 (5544), 1082–1086.
Hlavacek, A., Skladal, P., 2012. Electrophoresis 33, 1427–1430.
Hlavacek, A., Sedlmeier, A., Skladal, P., Gorris, H.H., 2014. Appl. Mater. Interfaces 6, 6930–6935.
Hou, S.Y., Hsiao, Y.L., Lin, M.S., Yen, C.C., Chang, C.S., 2012. Talanta 99, 375–379.
Hu, J., Wang, L., Li, F., Han, Y.L., Lin, M., Lu, T.J., Xu, F., 2013. Lab Chip 13, 4352–4357.
Jia, L., Shi, S., Ma, R., Jia, W., Wang, H., 2016. Biosens. Bioelectron. 80 (392– 297).
Kim, J.Y., Kim, H.B., Jang, D.J., 2013. Electrophoresis 34, 911–916.
Kloepper, K.D., Onuta, T.D., Amarie, D., Dragnea, B., 2004. J. Phys. Chem. B 108, 2547–2553.
Li, Z., Miao, X., Xing, K., Zhu, A., Ling, L., 2015. Biosens. Bioelectron. 74, 687–690.
Liu, F.K., Wei, G.T., 2004. Anal. Chim. Acta 510, 77–83.
Liu, F.K., Ko, F.H., Huang, P.W., Wu, C.H., Chu, T.C., 2005. J. Chromatogr. A 1062, 139–145.
Liu, F.K., 2009. J. Chromatogr. A 1216, 9034–9047.
Liu, S., Yan, Y., Wang, Y., Senapati, S., Chang, H.C., 2013. Biomicrofluidics 7, 061102.
Levicky, R., Horgan, A., 2005. TRENDS Biotechnol. 23 (3), 143–149.
Lujambio, A., Lowe, S.W., 2012. Nature 482, 347–355.
Luo, X.W., Du, F.J., Wu, Y., Gao, L.J., Li, X.X., 2013. Chin. J. Anal. Chem. 41 (11), 1664–1668.
Mao, X., Ma, Y., Zhang, A., Zhang, L., Zeng, L., Liu, G., 2009. Anal. Chem. 81, 1660–1668.
Moghadam, B.Y., Connelly, K.T., Posner, J.D., 2015. Anal. Chem. 87, 1009–1017.
Pan, H., Yu, H., Wang, N., Zhang, Z., Wan, G., Liu, H., Guan, X., Chang, D., 2015. J. Biotechnol. 214, 133–138.
Parolo, C., Escosura-Muniz, A., Merkoci, A., 2013. Biosens. Bioelectron. 40, 412–416.
Praus, P., Turicova, M., Suchomel, P., Kvitek, L., 2015. RSC Adv. 5, 59131–59136.
Pyell, U., Bucking, W., Huhn, C., Herrmann, B., Merkoulov, A., Mannhardt, J., Jungclas, H., Nann, T., 2009. Anal. Bioanal. Chem. 395, 1681–1691.
Quist, J., Janssen, K.G.H., Vulto, P., Hankemeier, T., van der Linden, H., J., 2011. Anal. Chem. 83, 7910–7915.
Quist, J., Vulto, P., van der Linden, H., Hankemeier, T., 2012. Anal. Chem. 84, 9065–9071.
Ravan, H., Kashanian, S., Sanadgol, N., Badoei-Dalfard, A., Karami, Z., 2014. Anal. Biochem. 444, 41–46.
Rohrman, B.A., Leautaud, V., Molyneux, E., Richards-Kortum, R.R., 2012. PLoS One 7 (9), e45611–e45618.
Sedighi, A., Li, P.C.H., Pekcevik, I.C., Gates, B.D., 2014. ACS Nano 8 (7), 6765–6777.
Senapati, S., Slouka, Z., Shah, S.S., Behura, S.K., Shi, Z., Stack, M.S., Severson, D.W., Chang, H.C., 2014. Biosens. Bioelectron. 60, 92–100.
Slouka, Z., Senapati, S., Yan, Y., Chang, H.C., 2013. Langmuir 29, 8275–8283.
Slouka, Z., Senapati, S., Chang, H.C., 2014. Annu. Rev. Anal. Chem. 7, 317–335.
Taller, D., Richards, K., Slouka, Z., Senapati, S., Hill, R., Go, D.B., Chang, H.C., 2015. Lab. Chip, 1656–1666.
Traver, S., Assou, S., Scalici, E., Haouzi, D., Al-Edani, T., Belloc, S., Hamamah, S., 2014. Hum. Reprod. Update 20 (6), 905–923.
Vogelstein, B., Papadopoulos, N., Velculescu, V.E., Zhou, S., Diaz Jr., L.A., Kinzler, K. W., 2013. Science 339, 1546–1558.
Wijenayaka, L.A., Ivanov, M.R., Cheatum, C.M., Haes, A.J., 2015. J. Phys. Chem. C 119, 10064–10075.
Wu, W., Huang, J., Wu, L., Sun, D., Lin, L., Zhou, Y., Wang, H., Li, Q., 2013. Sep. Purif. Technol. 106, 117–122.
Xu, X., Caswell, K.K., Tucker, E., Kabisatpathy, S., Brodhacker, K.L., Scrivens, W.A., 2007. J. Chromatogr. A 1167, 35–41.

Please cite this article as: Marczak, S., et al., Biosensors and Bioelectronics (2016), http://dx.doi.org/10.1016/j.bios.2016.07.093